



THE HONG KONG
POLYTECHNIC UNIVERSITY

香港理工大學

Pao Yue-kong Library

包玉剛圖書館

Copyright Undertaking

This thesis is protected by copyright, with all rights reserved.

By reading and using the thesis, the reader understands and agrees to the following terms:

1. The reader will abide by the rules and legal ordinances governing copyright regarding the use of the thesis.
2. The reader will use the thesis for the purpose of research or private study only and not for distribution or further reproduction or any other purpose.
3. The reader agrees to indemnify and hold the University harmless from and against any loss, damage, cost, liability or expenses arising from copyright infringement or unauthorized usage.

IMPORTANT

If you have reasons to believe that any materials in this thesis are deemed not suitable to be distributed in this form, or a copyright owner having difficulty with the material being included in our database, please contact lbsys@polyu.edu.hk providing details. The Library will look into your claim and consider taking remedial action upon receipt of the written requests.

**SYNTHESIS OF SMCO FOR 3D
COMPONENTS BY METAL-ORGANIC
COMPOUNDS**

JUNFENG HUANG

PhD

The Hong Kong Polytechnic University

2019

The Hong Kong Polytechnic University

Department of Industrial and Systems Engineering

**Synthesis of SmCo for 3D components by metal-
organic compounds**

Junfeng Huang

A thesis submitted in partial fulfilment of the requirements
for the degree of Doctor of Philosophy

February 2019

CERTIFICATE OF ORIGINALITY

I hereby declare that this thesis is my own work and that, to the best of my knowledge and belief, it reproduces no material previously published or written, nor material that has been accepted for the award of any other degree or diploma, except where due acknowledgement has been made in the text.

____ (Signed)

HUANG JUNFENG (Name of student)

Abstract

Functional alloy materials are widely used for various applications. Alloys of rare-earth metals (REMs) and transition metals (TMs) are getting important due to their outstanding magnetic properties. Samarium-cobalt (SmCo) alloy is one of the most outstanding magnetic materials in this group due to its large magneto-crystalline anisotropy and high Curie temperature. In this PhD thesis, it presents my research studies on how to fabricate the three-dimensional (3D) structure of SmCo alloys.

Three technical challenges are involved in the synthesis of SmCo alloys with 3D structure:

The synthesis of SmCo alloys with 3D structure involves 3 challenges as follows:

(i) The current practice of synthesizing SmCo powders uses acetylacetonate precursors in highly volatile organic solvents. The metal (Sm and Co) acetylacetonates are toxic and the synthesis process is not environmental-friendly. (ii) The demand for magnetic materials with high flexibility in shape has increased to cater for different applications. There exist several techniques which produce the materials in 3D structure, such as laser sintering. However, laser sintering is not applicable for 3D structure fabrication of SmCo alloys due to its geometric limit: the non-spherical shape of SmCo powder does not meet the requirement of raw material for laser sintering. (iii) Before sintering to obtain final products, polymer binders are added to adjust densification and improve structural stability of the shape of 3D structure. However, the content of binder affects physical properties of products. Also, crack formation during debinding easily occurs and deforms the shape of 3D structure.

Solutions for addressing the challenges:

This research investigates and develops pathways for synthesis of SmCo alloys using metal-organic compounds and appropriate fabrication methods to form 3D structure alloys. The research consists of three parts in addressing the challenges: (1) Development of an alternative precursor, named ascorbate, from the derivation of vitamin C with water as the solvent for the sake of sustainability. (2) Development of appropriate methods to fabricate 3D structure for SmCo alloys. Laser system and inkjet printing were developed using TMs to find out the advantages and disadvantages for fabricating SmCo alloys with 3D structure. (3) Development of the control mechanism in binder content and thermal profile to enhance the crystal structure and magnetic properties of SmCo alloys.

The first part of this work was to synthesize metal-organic compounds, cobalt ascorbate and samarium ascorbate. The ratio of element and weight ratio between cobalt and samarium for the mixture were 4.3:1 and 1.8:1 respectively, which corresponded to findings in available literature. The decomposition of samarium ascorbate and cobalt ascorbate was found to occur at 326 °C and 380 °C respectively before the alloying of SmCo began. This addresses challenge (i).

The second part of this work focuses on the development of 3D structure fabrication for metals or metal-organic compounds using laser system and inkjet printing. The laser system was used to produce 3D structures of (a) copper by reducing copper oxide and copper carbonate hydroxide to form copper circuit lines with resistivity of $1.46 \times 10^{-6} \Omega\text{m}$, which is slightly higher than that of the bulk copper ($1.68 \times 10^{-8} \Omega\text{m}$); and (b) cobalt embedded within the carbon matrix by reducing ZIF-67 (a type of cobalt-based organic compound) to perform as oil absorbents. Inkjet

printing system was used to produce 3D cobalt-based material ($\text{Co(tpy)Cl}_2 \cdot \text{MeCN}$) on a silicon wafer with a droplet spacing of 110 μm . This addresses challenge (ii).

The third part of the work was to produce 3D SmCo alloys. The thermal sintering (by tube furnace) of metal-organic compounds, samarium ascorbate and cobalt ascorbate, using 6% PVA as the binder was able to produce SmCo alloys with 1:3 phase (SmCo_3). Laser sintering of SmCo powder with 1:5 phase (SmCo_5) using laser sintering parameters of 250 μm hatch space, 150 W laser power, 1270 mm/min scanning speed in one-time sintering, was able to produce 3D structure for SmCo₅ alloys with coercivity and saturation magnetization of 1586.4 Oe and 83.49 emu/g respectively, similar to the magnetic properties of SmCo₅ powders. This addresses challenge (iii).

In conclusion, this study has successfully synthesized samarium ascorbate and cobalt ascorbate as the metal-organic precursors in chemical reaction in a non-hazardous, environmental-friendly manner. SmCo alloys were fabricated into a 3D structure using the proposed precursors and thermal sintering, which can overcome the geometric limitation of SmCo powders for laser sintering. Also, the control mechanisms in binder content and thermal profile in thermal sintering were developed to improve the crystallization of SmCo alloys and avoid the crack formation in the 3D structure.

Publications Arising from the Research

Journal Papers

- (1) Winco K. C. Yung,* Bo Sun,* **Junfeng Huang**,* YingdiJin,* Zhengong Meng,* Hang Shan Choy, Zhixiang Cai, Guijun Li, Cheuk Lam Ho, Jinlong Yang and Wai Yeung Wong, “Photochemical Copper Coating on 3D Printed Thermoplastics”, *Scientific Reports*, volume 6, pages 31188 (2016). DOI: 10.1038/srep31188

- (2) Winco K. C. Yung,* Bo Sun,* Zhengong Meng,* **Junfeng Huang**,* YingdiJin,* Hang Shan Choy, Zhixiang Cai, Guijun Li, Cheuk Lam Ho, Jinlong Yang and Wai Yeung Wong, “Additive and Photochemical Manufacturing of Copper”, *Scientific Reports*, volume 6, pages 39584, (2016). DOI: 10.1038/srep39584

- (3) **Junfeng Huang**, Winco K.C. Yung, Zhengong Meng, Desmond T.C. Ang, Guijun Li, “Additive Manufacturing of Cobalt-based Organic Ferromagnetic Materials”, *IEEE Magnetics Letters*, volume 8, pages 1-5, (2017). DOI: 10.1109/LMAG.2017.2661720

- (4) **Junfeng Huang**, Winco K.C. Yung, Guijun Li, Zhuoxun Wei, Zhengong Meng, “Laser-reduced zeolite imidazole framework-67 as magnetic absorbents for oil separation in water”, *IEEE Magnetics Letters*, volume 10, pages 1-1, (2019). DOI: 10.1109/LMAG.2019.2892930

(5) **Junfeng Huang**, Winco K.C. Yung, Desmond T.C. Ang, “Magnetic properties of SmCo₅ alloy fabricated by laser sintering”, *Journal of Materials Science: Materials in Electronics*, volume 30, pages 11282–11290, (2019). DOI: 10.1007/s10854-019-01475-x

(6) **Junfeng Huang**, Winco K.C. Yung, Desmond T.C. Ang, “Environmental-friendly synthesis for samarium-cobalt alloy with three-dimensional structure”, (submitted to the *Journal of Magnetism and Magnetic Materials*, under review)

Acknowledgements

I am deeply grateful to my supervisor, Prof. Winco K.C. Yung, Professor of the Department of Industrial and System Engineering, for his valuable guidance and encouragement, instruction and support throughout the whole period of my PhD study. This project is tough for me since it is a new field I did not study before. However, with Prof. Yung's supervision and guidance, I completed this project successfully. It is a very precious experience for my research.

Besides, I also appreciate my Co supervisor, Dr. T.C. Ang, for his guidance and support and encouragement. I also sincerely appreciate Prof. Jizhao Zou, Dr. Dennis Lo and Dr. Yueyang Zou for their selfless supports and valuable guidance to my PhD research.

Furthermore, I would like to deliver my thanks to my colleagues, Ms. Xiaoyong Mo, Ms. Yue Zhang, Mr. Ran Bi, Mr. Waihoong Kok, Mr. Choyee Chan, Mr. Shaosong Zhang, Dr. Henry Choy, Dr. Bo Sun, Dr. Wenjing Wang, Ms. Tingyu Xiao, Dr. Qin Yang, Ms. Joanne Wong, Mr. Mesfin Seidibrahim, Ms. Karpagam Subramanian, Dr. Guijun Li, and all the staff in the PCB Center of The Hong Kong Polytechnic University.

I also owe sincere thanks to my friends and my family for their faith and consideration in me. I would never successfully complete this work without their understanding and patience.

Table of contents

<i>CERTIFICATE OF ORIGINALITY</i>	<i>i</i>
<i>Abstract</i>	<i>ii</i>
<i>Publications Arising from the Research</i>	<i>v</i>
<i>Acknowledgements</i>	<i>vii</i>
<i>Table of contents</i>	<i>viii</i>
<i>Lists of Figures</i>	<i>xiii</i>
<i>Lists of Tables</i>	<i>xviii</i>
<i>Nomenclature</i>	<i>xix</i>
<i>Chapter 1 Introduction</i>	<i>1</i>
1.1 Alloy materials	5
1.1.1 Rare-earth metal and transition metal alloy	6
1.2 Three-dimensional component fabricating processes	9
1.2.1 Additive manufacturing technology	10
1.2.2 Other processes for 3D component fabrication	11
1.3 Metal-organic compounds	12
1.3.1 Transition metal-organic compounds.....	13
1.3.2 Rare-earth metal-organic compounds	14
1.4 Research gaps	16

1.5 Research objectives	24
Chapter 2 Literature review	25
2.1. Transition metal and rare-earth metal-organic compounds	25
2.1.1 Transition metal-organic compounds.....	27
2.1.2 Rare-earth metal-organic compounds	29
2.2 Transition metal and rare-earth metal alloys	32
2.2.1 Rare earth-cobalt alloys	33
2.2.2 Samarium-cobalt alloys	35
2.3 Three-dimensional component fabrication technologies.....	41
2.3.1 Inkjet printing.....	44
2.3.2 Modified laser writing system	47
2.3.3 Laser sintering	53
2.4 Thermal debinding and sintering of alloy materials.....	55
2.4.1 Thermal debinding	58
2.4.2 Thermal sintering	59
2.5 Relationship between research gaps, objectives, methodologies and results and discussions	62
Chapter 3 Research Methodology.....	63
3.1 Metal-organic compounds synthesis.....	64
3.2 Three-dimensional components fabrications	67
3.2.1 Inkjet printing for metal-organic compounds	67

3.2.2 Modified laser writing system for metal reduction	68
3.2.3 Laser sintering for SmCo alloy	71
3.2.4 Compression molding	72
3.3 Thermal debinding and sintering	74
3.4 Characterization	76
3.4.1 Composition characterization	77
3.4.2 Morphology characterization	78
3.4.3 Magnetic property characterization	80
3.4.4 Thermal profile characterization	80
<i>Chapter 4 Metal-organic compound synthesis</i>	<i>81</i>
4.1 Introductory remarks	81
4.2 Experiments	84
4.2.1 Preparation of cobalt ascorbate	84
4.2.2 Preparation of samarium ascorbate	85
4.2.3 Preparation of mixture of samarium ascorbate and cobalt ascorbate	86
4.2.4 Characterizations	86
4.3 Results and discussions	90
4.3.1 Effectiveness for synthesis of metal ascorbates	91
4.3.2 Thermal profile for synthesized metal ascorbates	100
4.3 Concluding remarks	102
<i>Chapter 5 Three-dimensional components fabricating processes</i>	<i>104</i>

5.1 Laser-induced forward transfer	105
5.1.1 Introductory remarks	105
5.1.2 Experiments	107
5.1.3 Results and discussions	108
5.2 Selective laser patterning.....	116
5.2.1 Introductory remarks	116
5.2.2 Experiments	117
5.2.3 Results and discussions	120
5.3 Laser reduction on metal-organic framework.....	125
5.3.1 Introductory remarks	125
5.3.2 Experiments	126
5.3.3 Results and discussions	128
5.4 Inkjet printing.....	134
5.4.1 Introductory remarks	134
5.4.2 Experiments	135
5.4.3 Results and discussions	136
5.5 Concluding remarks	145
<i>Chapter 6 Study on crystal structure and magnetic properties of alloy</i>	
<i>materials.....</i>	<i>148</i>
6.1 Laser sintering	150
6.1.1 Introductory remarks	150

6.1.2 Experiments	150
6.1.3 Results and discussions	152
6.2 Thermal debinding and sintering	173
6.2.1 Introductory remarks	173
6.2.2 Experiments	175
6.2.3 Results and discussions	176
6.3 Concluding remarks	194
<i>Chapter 7 Conclusions and Suggestions for Future Research</i>	<i>196</i>
7.1 Overall Conclusions	196
7.2 Significance of research	201
7.3 Suggestions for future research	204
<i>References (252 references)</i>	<i>207</i>

Lists of Figures

Figure 1.1. 4f configuration of rare earth metals.

Figure 1.2. Abundance of elements in Earth's crust.

Figure 2.1. Chemical formula for referred samarium composite.

Figure 2.2. Rare-earth elements used in RE-Co magnets.

Figure 2.3. Crystal structure of SmCo_5 .

Figure 2.4. Typical category of AM process.

Figure 2.5. Schematic process of standard laser induced forward transfer.

Figure 2.6. Density change in three stages of sintering.

Figure 2.7. Thermal profile of binders.

Figure 3.1. Experiment setup for precursor synthesis.

Figure 3.2. Image of a tailor-made inkjet printing system.

Figure 3.3. Image of a tailor-made laser writing system.

Figure 4.1. Synthesized metal-organic compounds. (a) cobalt ascorbate, (b) samarium ascorbate, (c) mixture of cobalt ascorbate and samarium ascorbate.

Figure 4.2. FTIR spectra for ascorbic acid, synthesized cobalt ascorbate and samarium ascorbate.

Figure 4.3. FTIR spectra for ascorbic acid and the mixture of synthesized cobalt ascorbate and samarium ascorbate.

Figure 4.4. XRD spectra for synthesized cobalt ascorbate and samarium ascorbate.

Figure 4.5. TGA and DTG curve for synthesized (a) cobalt ascorbate and (b) samarium ascorbate.

Figure 5.1. Optical microscope images of laser printed patterns (a) before electroless plating (b) after electroless plating.

Figure 5.2. SEM images of sample surface (a) before laser treatment (b) after laser treatment (c) after electroless plating.

Figure 5.3. The EDX results of samples. (a) before laser treatment, (b) after laser treatment, (c) after electroless plating.

Figure 5.4. The XRD spectra of samples before and after laser treatment and after electroless plating.

Figure 5.5. XRD patterns of samples after laser treatment by using 1064 nm laser.

Figure 5.6. (a) Design for circuit with the connection of LEDs. (b) The detail of designed circuit pattern, with the magnification of laser writing path. The fabricated component with laser treated circuits and LEDs (c) without lighting and (d) with lighting.

Figure 5.7. Component fabricated on the substrate of FR-4 (a) without lighting and (b) with lighting. LIFT patterns transferred on (c) polyimide and (d) glass slide and (e) the magnification of that on glass slide.

Figure 5.8. 3D printed Statue of Liberty with coating of malachite. (a) schematic image; (b) real product.

Figure 5.9. 3D printed robotic hand with coating of malachite. (a) before laser treatment; (b) schematic image for laser treatment.

Figure 5.10. SEM images of sample surface (a) before and (b) after laser treatment.

Figure 5.11. XRD spectra of samples (a) before laser treatment (b) after laser treatment.

Figure 5.12. (a) XRD spectra and (b) electrical resistivity for samples treated by laser in different laser writing speeds.

Figure 5.13. (a) Testing for laser patterned circuits and blue LEDs. (b) 3D printed robotic hand with laser patterned circuits and red LEDs.

Figure 5.14. The process of oil absorption. (a) A dish of clean water. (b) a drop of dyed oil was spilled into water. (c) a spoon of samples was added to absorb oil. (d) samples absorbed oil completely. (e) a magnet was used to remove samples. (f) a dish of clean water after oil absorption.

Figure 5.15. SEM image of (a) synthesized ZIF-67 (b-f) sample A to E respectively.

Figure 5.16. (a) XRD spectra and (b) hysteresis loop of samples.

Figure 5.17. (a) Oil absorption capacity of different samples for silicone oil and castor oil. Reusability ability of different samples in (b) silicone oil and (c) castor oil respectively.

Figure 5.18. (a) multi-line patterns printed in 80 μm spacing distance (b) line patterns printed in 110 μm spacing distance.

Figure 5.19. Line pattern printed on (a) glass slide, (b) silicon wafer.

Figure 5.20. SEM images of printed patterns on (a) glass slide, (b) silicon wafer.

Figure 5.21. SEM images of printed patterns with (a) 1-time and (b) 10-times printing.

Figure 5.22. SEM images of printed patterns with 15-degree angle.

Figure 5.23. Optical surface profile images of (a) multi-drop pattern in 1000-times, (b) line pattern in 100-times.

Figure 5.24. Magnetization loop for synthesized cobalt-based organic compound.

Figure 5.25. (a) AFM images and (b) MFM image of the printed crystals. (c) cross-

section profile, (d) 3D view.

Figure 6.1. Optical microscope image of sintered surface with 450 μm hatch space.

Figure 6.2. SEM image and particle size distribution for purchased SmCo_5 powders.

Figure 6.3. (a) XRD spectrum of purchased SmCo_5 powders. (b) Magnetic hysteresis loop for purchased SmCo_5 powders.

Figure 6.4. (a) XRD spectrum of SmCo_5 sintered by different power. (b) Magnetic hysteresis loop for SmCo_5 sintered by different power.

Figure 6.5. (a) XRD spectrum of SmCo_5 sintered by different speed. (b) Magnetic hysteresis loop for SmCo_5 sintered by different speed.

Figure 6.6. (a) XRD spectrum of SmCo_5 sintered by different sintering times. (b) Magnetic hysteresis loop for SmCo_5 sintered by different sintering times.

Figure 6.7. Laser sintered sample with cylindrical shape.

Figure 6.8. (a) XRD spectrum of Sample A to C. (b) Magnetic hysteresis loop for Sample A to C.

Figure 6.9. (a) XRD spectrum of Sample A, D and E. (b) Magnetic hysteresis loop for Sample A, D and E.

Figure 6.10. (a) XRD spectrum of Sample A, F and G. (b) Magnetic hysteresis loop for Sample A, F and G.

Figure 6.11. temperature gradient on the sample during laser sintering.

Figure 6.12. SEM images for the fracture of sintered samples.

Figure 6.13. XRD spectrum of (a) Sample H to J, (c) Sample H, K and L and (e) Sample H, M and N. Magnetic hysteresis loop for (b) Sample H to J, (d) Sample H, K and L and (f) Sample H, M and N.

Figure 6.14. (a) DTG curve for the mixture of samarium ascorbate, cobalt ascorbate and PVA under nitrogen air environment. (b) TGA curve for the mixture of samarium ascorbate, cobalt ascorbate and PVA. (c) Accumulation of weight loss in percentage and weight loss for each stage.

Figure 6.15. (a) Debinding set-up. Optical microscope of sample's surface (b) before and (c) after debinding.

Figure 6.16. Optical microscope images of debinded sample (a) at 35 °C. (b) with a temperature holding time at 34 °C.

Figure 6.17. (a) Debinding set-up ranging from room temperature to 160 °C. (b) optical microscope image of debinded sample.

Figure 6.18. (a) Debinding set-up ranging from room temperature to 600 °C. (b) optical microscope image of debinded sample.

Figure 6.19. (a) Optical microscope image and (b) XRD spectrum of sample sintered at 900 °C.

Figure 6.20. (a) Optical microscope image and (b) XRD spectrum of sample sintered at 1100 °C.

Figure 6.21. Compressed samples with PVA content from 5% to 9 % (a) before and (b) after debinding and sintering.

Figure 6.22. XRD spectra of synthesized materials.

Figure 6.23. SEM images for the surface of sintered samples (a) without PVA, (b) with 5% PVA, (c) with 6% PVA, (d) with 7% PVA, (e) with 8% PVA, (f) with 9% PVA.

Figure 6.24. Hysteresis loops for sintered samples.

Lists of Tables

Table 2.1. Alloy materials for laser sintering.

Table 2.2. Resistivity of the metals and the bond dissociation energies of their corresponding oxides.

Table 4.1. Metal element measurement on synthesized samarium ascorbate.

Table 4.2. Metal element measurement on synthesized cobalt ascorbate.

Table 4.3. Metal element measurement on the mixture of synthesized cobalt ascorbate and samarium ascorbate.

Table 5.1. List of samples with different parameters and their element content.

Table 6.1. Parameter setting for laser sintering with 450 μm hatch space.

Table 6.2. Parameters setting and magnetic properties for samples sintered by laser with 350 μm hatch space.

Table 6.3. Parameters setting and magnetic properties for samples sintered by laser with 250 μm hatch space.

Table 6.4. Dimension and weight of samples after sintering in 1300 $^{\circ}\text{C}$.

Table 6.5. Metal element measurement on synthesized cobalt ascorbate and samarium ascorbate.

Table 6.6. list of coercivity and saturation magnetization for samples.

Nomenclature

TM	Transition metal
REM	Rare earth metal
3D	Three-dimensional
AM	Additive manufacturing
MOF	Metal-organic framework
ZIF	Zeolitic imidazolate framework
SLS	Selective laser sintering
LIFT	Laser-induced Forward Transfer
UV	Ultraviolet
LED	Light-emitting diode
CAD	Computer-aided design
-COOH	Carboxyl functional group
-NH ₂	Amine functional group
C ₆ H ₈ O ₆	Ascorbic acid
C ₇ H ₆ O ₃	Salicylic acid
C ₄ H ₆ O ₄	Succinic acid
EDX	Energy dispersive x-ray analysis
XRD	X-ray crystallography

FTIR Fourier transform infrared spectroscopy

ICP-OES Inductively coupled plasma-optical emission spectrometry

SEM Scanning electron microscope

AFM Atomic force microscopy

MFM Magnetic force microscopy

VSM Vibrating sample magnetometer

TGA Thermogravimetric analysis

ABS Acrylonitrile butadiene styrene

PMMA Poly(methyl methacrylate)

LR-ZIF-67 Laser reduced ZIF-67

PVA Polyvinyl alcohol

DC Direct-current

PLA Polylactic acid

DTG Derivative thermogravimetry

Chapter 1 Introduction

An alloy is a material which is composed of two or more metal elements with metallic luster and may have properties different from its parent elements. Due to their flexible properties, alloys can be applied for specific usages where pure metals are either unsuitable or expensive. Some alloys are devised for over 4,500 years, such as electrum and meteoric iron-nickel. Bronze, which is composed of copper and tin, is a typical man-made alloy. It is harder and stronger than tin and copper, and thus it is more suitable for using in weapons and tools. Another typical example of man-made alloy is steel, which is composed of iron and carbon. It is also harder and tougher than pure iron. Alteration alloying composition can change the properties of metals, including hardness, luster, tensile strength, melting point, ductility, plasticity and conductivity. Even small alteration results in large changes. Alloys and their properties are the focus for materials engineers, who study and apply these alloys to a variety of practical purposes, like vehicles, construction materials, kitchenware and other common appliances that are fabricated with various alloys.

Transition metal (TM) is a big classification of metal materials, many ordinary but important metal elements are included in this group. For example, iron, copper, aluminum and cobalt. These elements reveal strong metallic bonding, which leads to high melting point and densities. Meanwhile, because of their mechanical performance, there are a lot of applications of TMs like alloys and structural materials. Furthermore,

transition elements have been used in many fields, including industry, biomedicine, environment protection, commercial usage, strategy storage and medical field. Many synthesis approaches have been developed because of the catalytic behaviors of transition elements. Thanks to the TM catalyzed processes, the synthesis of complex organic molecules in multiple steps can be realized.

Rare-earth metals (REMs) also have aroused tremendous interest. China leads the world in reserves, productions and exports. Due to their unique electronic structure, REMs have various precious electrical, optical, magnetic and thermal properties. Due to these properties, they can be fabricated into high-performance materials. REMs are hailed as “vast treasures” and are often seen as the key elements and strategical resources in high-tech industrial development. Through comprehensive development and extensive research, REM materials have been used in numerous fields. REM alloys, as some of the most extensively applied materials, have garnered huge interest and have been developed broadly. REM alloys exhibit heavy magnetic, anti-corrosion and florescence properties, these unique physical and chemical properties resulted from their electronic configuration. Due to these advantages, REM alloys have been applied in fabricating hydrogen storage materials (Yuan et al., 2013), permanent magnetic materials (Scheunert et al., 2014) and magneto-strictive materials (Yao et al., 2015).

These alloys have the advantages of intrinsic properties of both TMs and REMs. Material engineers can combine each of these metals to create an alloy with high performance. For example, high magnetic coupling strength of magnetic moments

from transition-metal elements and strong magneto-crystalline anisotropy and high magnetic moment from rare-earth elements (Buschow, 1977). It has been reported that there is an additional focus on the investigation of REM and TM alloys. Some of these REM & TM alloys, like samarium-cobalt and neodymium iron boron, can be used as starting materials for permanent magnets. Besides, another outstanding property for some of their compounds has been discovered and shown as reversible absorption of hydrogen gas under near-atmospheric pressure and at room temperature.

Metal-organic compounds are novel materials consisting of metals and organic ligands. These compounds combine merits from both metals and organic materials and obtain strong structural and functional tunability, making their applications as one of the fastest growing fields. They also have other outstanding properties, including greater surface area, controllable pore sizes, diversified and beautiful structure (Y. Li et al., 2018). Their flexible composite property, controllable structure and various functionality make them popular in scientific research. The decomposition properties in high temperature provide potentials in alloy synthesis. Solubility in organic solvent and strong plasticity offers a path for producing alloy materials in 3d structure. Mechanical properties also can be enhanced with the addition of organic materials.

Nowadays, people are able to fabricate a variety of alloy products to meet their demands. However, complicated fabricating procedures and casting molds for certain shapes restrict the development of functional alloys. Specific mold design and fabrication are the most complex and time-consuming aspects that impede the

development of functional alloy three-dimensional (3D) component fabrication. Therefore, some novel and design-flexible methods, including additive manufacturing (AM) technology, have been developed for structural alloy fabrication. Selective laser sintering (SLS), selective laser melting and direct metal laser sintering are three types of critical AM methods for 3D structure alloy fabricating. However, nowadays only a limited choice of specific alloy powder can be applied in this technology. This means that functional alloys with 3D structure still suffer from fabrication procedure complexity, design inflexibility and time-consuming issues.

Commercially available techniques for 3D design are widely used to fulfill the global economy's endless requirements for product design, including inkjet printing, laser sintering and compression bonding. The development of these techniques addresses multiple issues related to the dimension, shape and structure of alloy materials, aiming to improve peoples' quality of life. Fused deposition modelling is commonly used in 3D designs for polymers. It is still a challenge to use metals as the raw materials for 3D component fabrication. AM processes for metal sintering or melting require an extremely long processing time and high-quality raw materials, which are expensive. Therefore, it is important to develop suitable methods for 3D structural alloy fabricating.

In summary, functional alloys, especially TM and REM alloys, are applied to a broad range of fields. The development of these functional alloys is becoming a subject of great interest. Due to the demands for special sizes, shapes and dimension, some 3D

structure fabricating processes, including AM, have been developed to fabricate design-flexible 3D components. With increasing interests on the combination of metal and organic materials, metal-organic compounds were developed and explored for widespread usage and various applications. These novel materials also tend to be considered as metal-organic precursors in alloy materials fabrication. Synthesis of alloys with 3D structure using metal-organic compound is imperative and meaningful for the long-term viability of these alloys.

1.1 Alloy materials

As mentioned previously, functional alloys are widely used and are continuously being developed for further applications. Stainless steel, for example, is commonly used for architecture and kitchen appliances, as well as in aircraft and land vehicles. TMs, which are called d block elements, serve as bridges between main groups of elements in the periodic table. These elements exhibit metallic luster and unique performance, including high toughness, high hardness and strong metallic bonding between atoms. Additionally, their various oxidation phases and magnetic behaviors can be identified by the colors of their compounds. Apart from properties mentioned above, these metals have excellent thermal and electrical conductivity and are also good carriers of thermal and electrical energy due to the motion of numerous free electrons.

As one of the most vital series of metal elements in the periodic table, REMs play a key role in functional alloys. Their specific 4f electron configuration and hexagonal crystal structure result in unique chemical properties, magnetic properties and optical properties. Therefore, REMs can be fabricated into permanent magnetic materials (Nowick, 2012), luminescent materials (Sousa Filho, Lima, & Serra, 2015), functional glass and ceramic (Zako et al., 2015), thermoelectric materials (Kinemuchi, Mimura, Towata, & Kato, 2014) and superconductor materials (Y. Gu, Halász, Robinson, & Blamire, 2015). Similarly, TMs alloys can also be applied in hydrogen sensors (Wadell et al., 2015), spin- and valley-control (G. Wang et al., 2015) and catalysis (Tedstone, Lewis, & O'Brien, 2016).

1.1.1 Rare-earth metal and transition metal alloy

REMs are defined as the elements found in the lanthanide series, including scandium and yttrium. As is shown in the periodic table, lanthanide series ranks from 57 to 71 and the scandium and yttrium list 21 and 39 respectively. Rare-earth elements all have a similar special atomic structure due to their relevant electron configuration and atom radius. Rare-earth metals exhibit plenty of unpaired electrons in 4f configuration, as shown in figure 1.1, these unpaired electrons have magnetic dipole moment, which shows magnetic properties.

表 2-5 三价镧系离子基态电子排布与光谱项

离子	4f 电子数	4f 轨道的磁量子数							L	S	J	$^{2S+1}L_J$	Δ /cm ⁻¹	ξ_{4f} /cm ⁻¹
		3	2	1	0	-1	-2	-3						
La ³⁺	0								0	0	$J=L-S$ 0	¹ S ₀		
Ce ³⁺	1	↑							3	1/2	5/2	² F _{5/2}	2200	640
Pr ³⁺	2	↑	↑						5	1	4	³ H ₄	2150	750
Nd ³⁺	3	↑	↑	↑					6	3/2	9/2	⁴ I _{9/2}	1900	900
Pm ³⁺	4	↑	↑	↑	↑				6	2	4	⁵ I ₄	1600	1070
Sm ³⁺	5	↑	↑	↑	↑	↑			5	5/2	5/2	⁶ H _{5/2}	1000	1200
Eu ³⁺	6	↑	↑	↑	↑	↑	↑		3	3	0	⁷ F ₀	350	1320
Gd ³⁺	7	↑	↑	↑	↑	↑	↑	↑	0	7/2	7/2	⁸ S _{7/2}	—	1620
Tb ³⁺	8	↑↓	↑↓	↑	↑	↑	↑	↑	3	3	6	⁷ F ₆	2000	1700
Dy ³⁺	9	↑↓	↑↓	↑	↑	↑	↑	↑	5	5/2	15/2	⁶ H _{15/2}	3300	1900
Ho ³⁺	10	↑↓	↑↓	↑↓	↑	↑	↑	↑	6	2	8	⁴ I ₈	5200	2160
Er ³⁺	11	↑↓	↑↓	↑↓	↑↓	↑	↑	↑	6	3/2	15/2	⁴ I _{15/2}	6500	2440
Tm ³⁺	12	↑↓	↑↓	↑↓	↑↓	↑↓	↑	↑	5	1	6	³ H ₆	8300	2640
Yb ³⁺	13	↑↓	↑↓	↑↓	↑↓	↑↓	↑↓	↑	3	1/2	7/2	² F _{7/2}	10300	2880
Lu ³⁺	14	↑↓	↑↓	↑↓	↑↓	↑↓	↑↓	↑↓	0	0	0	¹ S ₀	—	

注：Δ 为能级差， ξ_{4f} 为自旋-轨道耦合系数。

Figure 1.1. 4f configuration of rare-earth metals (刘光华, 2007).

The maximum storage number of unpaired electrons of the lanthanide series metal is seven in their 4f electron track, while there is only five for TM in their d-track. For this reason, REMs have the largest paramagnetic susceptibility in the periodic table, they have promising performances in magnetic application. Contrary to their defined name “rare earth”, the amount of these elements is not actually rare. As figure 1.1 shows, the amount of these elements is similar to that of copper as one of the most common metals used in daily life.

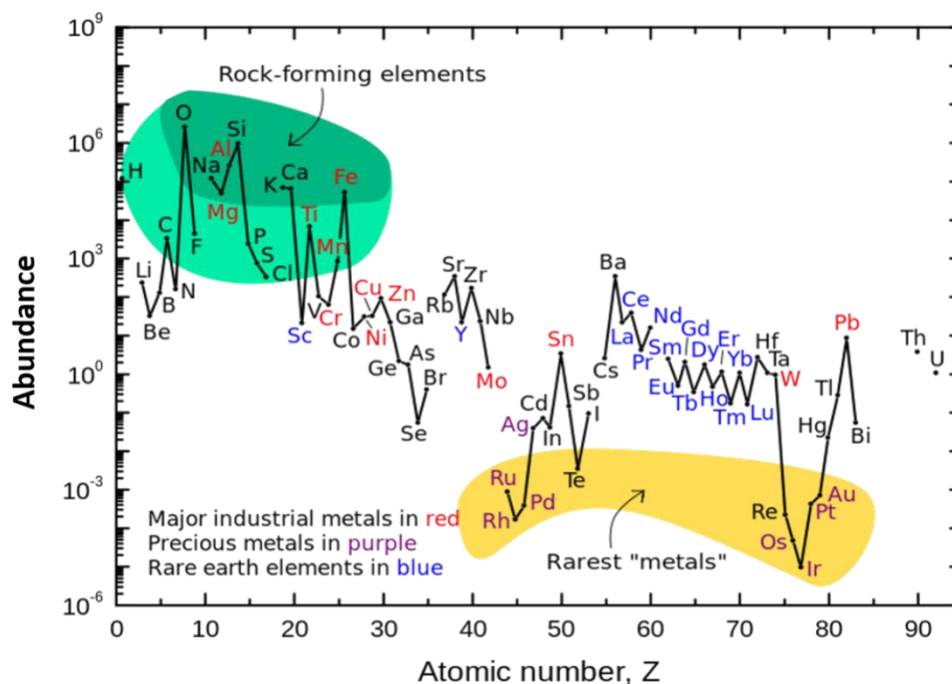


Figure 1.2. Abundance of elements in Earth's crust (Haxel, Hedrick, Orris, Stauffer, & Hendley II, 2002).

As already mentioned, TMs are one of important elements in the periodic table. Their unique properties and outstanding performance aroused wide interests in scientific researches. Additionally, their various oxidation phases and magnetic behaviors are indicated by the colors of their compounds. Besides such properties mentioned above, due to the motion of many free electrons, these metals have excellent thermal and electrical conductivity and are good carriers of thermal and electrical energy. It is easy to fabricate them into different shapes. Strong metallic bonding leads TMs to exhibit their characteristic high melting point and densities. There are a lot of applications of TMs, such as alloys, structural materials and pigments, which are used for decorative purpose and giving light color to ceramics glazes and stained glass.

Alloys consisting of REMs and TMs also attracted wide research attentions since they exhibited outstanding ferromagnetic properties, fluorescent properties, etc. The behavior of intermetallic alloys between REMs and TMs is complicated. Samarium-cobalt magnet and neodymium magnet are the typical REM and TM alloy, which are developed broadly. Furthermore, plenty of REM and TM alloys were explored and synthesized as permanent magnet materials (J. Lee et al., 2018), magneto-strictive materials (Barua et al., 2018) and hydrogen absorption materials (Sahlberg, Karlsson, Zlotea, & Jansson, 2016).

1.2 Three-dimensional component fabricating processes

3D fabricating techniques were comprehensively applied to achieve the ever-growing demands for various product designs and applications. The medical and biological fields have adopted this technology. 3D printing techniques, also called AM, are the most universal and commercial technology for 3D structure fabricating. Meanwhile, compression bonding, powder injection molding and other mature 3D component fabricating processes also play an important role in these areas. Commercially, polymers and other special materials are the major construction materials for 3D component fabricating. Nevertheless, it is still a challenge to use metal as the raw materials for 3D component fabricating. AM processes for metal sintering or melting necessitate high-quality raw materials, high cost and extremely long operation time. Hence, it is important to develop an available method to address

these issues. Meanwhile, the control of 3D structure plays a significant role in the fabrication of thin films or bulk materials which are necessary for some specific applications, such as electronics and energy conversion. However, the fabrication of thin films or bulk materials is limited to the synthesis of nanoparticles (Huang, 2018). In the next section, AM and other 3D structure fabricating processes are illustrated.

1.2.1 Additive manufacturing technology

AM is a layer-based automated fabrication approach for making scaled 3D products according to 3D-computer aided design (CAD) data without using any other tools. It is also named as “rapid prototyping” when the first time it entered the market in 1987 (Y. Gu et al., 2015).

The term additive manufacturing describes all methods of adding material to create a 3D physical form. The principle of this approach is to fabricate a 3D physical object from many layers of largely equal thickness. Each layer is identical, it will be put on top of the preceding one. Industrial applications are the main focus when discussing AM. Apart from other professional industrial techniques, more and more people are turning to AM to enhance the competitiveness of their operation and to realize their business objectives. Fascinating applications are the real drivers for new solutions and inspiration. This technology is widely adopted and developed into mature stages in many fields. For examples, automotive industries, aerospace industry,

consumer goods, toy industry and medical products have all adopted AM (Wong & Hernandez, 2012). There are many variations in the methods of AM. Individual processes will be modified according to the change of materials and machines. AM was defined and classified into 7 categories in the standard “ASTM F42 – Additive Manufacturing” by the American Society for Testing and Materials group in 2010, including photopolymerization, material extrusion, direct energy deposition, material jetting, sheet lamination, powder bed fusion and binder jetting. AM provides limitless potential in fabricating products with required features, since it can help people to fabricate products of complicated geometries, which cannot be done by traditional methods. Meanwhile, it also can be applied by different materials and even vary the properties of materials within the products. AM also changes the rules of traditional manufacturing completely. It can achieve the manufacturing of a number of parts in any required shape by any imaginable materials all over the world. Furthermore, it can be also applied based on basis of customized production rather than by using mass-production method.

1.2.2 Other processes for 3D component fabrication

Other techniques can be applied in forming 3D structure. Compression bonding is a method to fabricate 3D component with high pressure. This method only required simple and low-cost tooling and fabricated products having higher magnetic property comparing with injection molding (Ormerod & Constantinides, 1997). Metal-organic

powders and binders can be used to fabricate parts with 3D structure for required shape by applying force on compression machine. Compressed 3D structure parts suffer from debinding and sintering process is needed to reduce and eliminate binders and organic parts and finally obtaining alloys with 3D structure.

Powder injection molding is another method. It can be applied to fabricated 3D component with high precision in different shapes. Metal and ceramic are the major materials used in this method. The advantages of PIM are its flexibility in design as plastic injection molding and no limitation in material selection within the scope of powder metallurgy. These merits make it possible to combine multiple parts into a single part.

1.3 Metal-organic compounds

In modern coordination chemistry, the term “compounds” is used to describe most molecular compounds of TMs, formed by a central metal atom and its coordinated set of ligands. Any attempt to summarize the history of coordination chemistry is complicated because it has no clearly defined inception. It was not until the middle of the 19th century that coordination compounds began to be the object of chemical investigation. Coordination chemistry became an independent discipline by the end of the 19th century through Alfred Werner’s work (Blacque & Berke, 2015). To date, metal-organic compounds have aroused comprehensive attentions due to their functionality, controllable structure and superior properties (M. X. Wu & Yang, 2017).

Organic materials can be used to chelate metal to form metal-organic compound, especially for materials with strong chemistry character, like REMs (Y. Hu, Drouin, Larivière, Kleitz, & Fontaine, 2017). Metal-organic compounds have been widely studied and applied in various fields, including gas storage and separation (B. Li, Wen, Zhou, & Chen, 2014), catalysis and drug delivery (Y. Cui et al., 2016).

Direct melting of metallic raw materials requires much energy to melt materials, the energy for breaking the bond of metal and organic ligands is relatively low. Meanwhile, a mold is required during the melting process since the liquid phase metals need to cool down and shape into the mold form. However, the quality of crystal structure and properties for melted metals is better than that prepared by metal-organic precursors, because the residual carbon after sintering may affect the crystallization of metals.

1.3.1 Transition metal-organic compounds

Researchers have investigated the chemistry of transition elements for around two centuries. These metals and their compounds are considered as the main materials developed to understand structure and bonding of metal-organic compounds in the past seventy years. There is no systematic research on the chemistry of TMs until 19th century. From that time, an obvious change in transition elements studies began to overthrow the previously cognition of chemists. Secondary valency, which refers to

the number of groups attached to a metal center, was introduced by Werner in researching on cobalt complexes (Gerloch, Constable, & Kaim, 1995). Several forms of cobalt, including ammonia and chloride, complexes were developed and the term coordination number was created to describe the corresponding secondary valence inside. These complexes were also defined as coordination compound. So far, the d-block TMs represent the classical metals of coordination chemistry and these were significant and of continual interest and focus. In particular, the lighter and unusually more abundant elements of the first row, including iron, cobalt, copper and zinc, received the most attention. Meanwhile, the d-block TM elements exhibited stable oxidation phases and their d orbitals are partially filled. This behavior has an impact in both physical and chemical properties.

1.3.2 Rare-earth metal-organic compounds

Compared to many 3d-transition elements, rare-earth elements were thought to have a coordination number of six by most inorganic chemists. Owing to this reason, REs coordination chemistry was slow in development for a long time. However, a coordination number of nine has been revealed in a material of neodymium bromates in 1939 (Cotton, 2016). After performing further structural analysis on polyaminocarboxylates in 1960s, a larger coordination number reaching 10 has been confirmed (Huang, 2011). This discovery not only aroused massive interest in various fields, but also contributed to other important landmarks. Therefore, a number of

articles (Arleth et al., 2016; T. Li, Kaercher, & Roesky, 2014) covering various directions of coordination chemistry in rare-earth elements were periodically renewed. Research on metal-organic material is growing into an important part of RE chemistry.

1.4 Research gaps

Metal-organic compounds are required to be used as raw materials for the synthesis of alloys. The materials are also called precursors and are prepared using chemical methods. Researches on metal-organic coordination materials has garnered a lot of interest (H.-C. Zhou et al., 2012). Selection of the appropriate organic ligand is an important part in the whole process, since different organic ligands lead to different results in the material properties and structure. Even if small amounts of element variations in the materials are made, variation in properties may be resulted (L. J. Wang et al., 2014). Coordination Chemistry in the organic field is the science concerned with the interactions of organic and metal components. The development of the coordination chemistry of TMs began a few decades ago (T. Li et al., 2014; Saad, 2014), whereas rare-earth (RE) elements had a late start in comparison. Further developments in TMs and REMs are promising and urgent due to their unique physical and chemical properties and various applicability.

Currently, the technology for building the widely used three-dimensional alloy products is becoming mature. Complex procedures and difficult-to-manufacture mold requirements, however, are still a severe challenge in 3D structure alloy products development. As one of the novel and highly-attractive 3D component building processes, 3D printing technologies have been extensively developed in recent years. However, the researches in fabrication for 3D structure using magnetic materials were

still rare, especially for ferromagnetic materials. It is because the magnetic materials have some drawbacks, such as high thermal sensitivity and processing constrains, easy oxidation and phase distortion. REM-TM alloys are outstanding alloy materials with strong ferromagnetic behaviors, applying them in fabricating 3D structure component has potential.

Research gaps are summarized below:

- (1) Metal acetylacetonates used in current practice of synthesis of SmCo alloys are toxic and the whole process is not environmental-friendly.

For improved environmental protection, the decrease of usage of toxic raw materials and generation of waste and byproducts has been reviewed (Melchert, Reis, & Rocha, 2012). Cobalt composites, nickel composites, zinc composites and manganese composite can be synthesized in an aqueous system with hydrothermal assistance in an easy, rapid and reproducible way (Diodati, Pandolfo, Caneschi, Gialanella, & Gross, 2014). As mentioned in the previous section, organic materials with carboxylic bonds are the best ligand for the coordination chemistry. Carboxylic acids provide limitless potential for designing metal compounds to satisfy various requirements. These properties are exhibited in two ways: one is that rare-earth ions are ready to form compounds with carboxylate ligands, and the other is that the synthesis of these compounds can be completed under simple conditions, such as

aqueous system, which completely fulfills the requirements for non-hazardous synthesis (Janicki, Mondry, & Starynowicz, 2017). Simple and green organic materials with O- and N- donors are the ideal organic ligand materials for non-hazardous synthesis. The non-hazardous synthesis for REMs, however, is still not studied widely. The development in REMs and TMs organic precursor with minimum of hazardous waste and byproducts is promising and has potentials. Meanwhile, REMs have strong Lewis acid character, which can facilitate the coordination with nucleophiles to form stable complexes (Florek et al., 2015). So, there is a need to reduce and eliminate toxic raw materials, solvents and binders for the synthesis of REMs & TMs organic materials. In the metal precursor's preparation, organic materials and inorganic salts are the two major types of reaction materials. Metal oxide, metal halide and metal oxyacid are the major raw materials for the preparation of metal-organic compounds. They can react with coordinated organic materials to form metal-organic precursors. Since a great number of organic materials are capable of functioning as organic ligands, it is essential to choose an appropriate one. In view of these restrictions, an investigation for the selection of organic ligand is a significant challenge in precursor preparation.

Metal acetylacetonates are used as precursors in highly volatile organic solvents for synthesizing samarium-cobalt alloy in current methods (Fiévet et al., 2018). However, these metal acetylacetonates are toxic, and the synthesis process is not environmental-friendly. To fulfill the requirement of eliminating toxic starting

materials, waste and byproducts, starting materials should be non-hazardous and water soluble. Moreover, RE elements are desired to coordinate with organic bond with hard Lewis base donors, like O, F and N, to form coordination materials with high coordination number since they have large ionic radii and strong hard Lewis acid character (R. Wang & Zheng, 2010). Ascorbic acid, generally called Vitamin C, is a green, common and water-soluble material, which has strong chelating ability to reduce metal oxide and metal compound and form metal ascorbate complex (X. Hou et al., 2016). The generated byproducts are common metal salts, for example, sodium chloride, which is green and non-hazardous. Furthermore, only CO₂ and H₂O are produced as exhaust gases when using metal ascorbate as precursor for preparation of alloy. The related chemical equation is shown in chapter 3. During the chemical synthesis, an aqueous system, normally made up of water or ethanol, is used as the reaction solvent. In consideration of these restrictions, the selection of organic ligand is a significant challenge in precursor preparation.

(2) Laser sintering is not applicable for 3D structure fabrication of SmCo alloys due to its geometric limit.

3D alloy products are widely used in industry and daily life. This method has already reaching its saturation level. Complicated procedures and the difficult-to-manufacture mold requirement, however, are still the most severe challenges in the

development of 3D structure alloy products. Various fabricating technologies of 3D components have been developed, including gel casting, powder injection molding and AM. AM is one of the important and outstanding 3D components fabricating processes. Recently, it has been widely developed. 3D printing technology developed in the 1980's for fabricating prototypes and models with the ability to manufacture required products in 3D structure with the assistance of CAD. This novel method has been improved dramatically and has extended into almost all fields of industry (Gross et al., 2014). Its advantages include high cost effectiveness, easy-processing and good design flexibility. Although thermoplastic is the major raw materials used in this industry, metal/alloy products fabricated by using 3D printing technology still have challenges. Fabricating alloy materials with this technique was also developed through SLS. In SLS, a wide range of materials can be used, from polymers such as nylon, polycarbonate, polyvinyl chloride, acrylonitrile butadiene styrene and resin to metal and ceramic powders (J.-Y. Lee, An, & Chua, 2017). The mechanism of SLS is that laser provides sufficient energy to heat metals to their melting point to reform the shape. However, it is both time and energy consuming. Although SLS can be applied in fabricating 3D structure alloy, only a small group of materials can be successfully used (DD Gu et al., 2012). Only certain iron-, nickel-, aluminum-, copper-, titanium- and cobalt-based alloys can be used in SLS. Because of the critical requirement for the raw powders used in laser sintering, spherical shape is the ideal one for laser sintering. Spherical shape can provide lower inter-particle friction, higher flowability and strong

inter-agglomerate bonding between particles, which increase the density of products (Sing et al., 2017). Fabrication of SmCo alloy in 3D structure is limited by its geometry when applying laser sintering. Meanwhile, it is still rare for research in the fabrication of the magnetic materials with 3D structure. It is because the magnetic materials have some drawbacks, such as high thermal sensitivity and processing constrains, easy oxidation and phase distortion of magnetic materials. This seriously hinder the development for these materials applying in laser sintering (Jung et al., 2015; Matsushita et al., 2010; Zou et al., 2018). Therefore, it is important to develop appropriate methods to fabricate 3D structure for the magnetic materials, especially for SmCo alloys.

(3) Crack formation during debinding easily occurs and deforms the shape of 3D structure. Also, the content of binder affects the physical properties of products.

Binders are used to enhance the materials properties, especially for mechanical properties. Raw materials mix with binders to form a mixture for pre-pyrolysis, which is called the “green part”. The addition of binder plays the most significant role for densification through wetting, spreading and formation of agglomerates (Suh et al., 2015). Polymer binders receive more attentions since they can be completely removed from the green part by heating in an oxidizing environment. Consequently, polymer binders provide outstanding mechanical strength to the green part resulting from the

evaporation of organic materials which can connect particles (Ren, Luo, & Zhou, 2018). Furthermore, the content of binder can also affect the physical properties of products. It is easy to manipulate organic binder into materials and maintain the required shape before debinding. It also provides high driving force for sintering after debinding, which results in high density of the sample. (Shahzad et al., 2013). Extremely high temperatures can easily destroy the 3D structure of products, since shape-forming polymers have low decomposition temperature. As the temperature increases, the polymers are consumed and exhausted as gas, and the shaped 3D structures are deformed. The thermal stability of green parts during sintering is still a big challenge (Y.-S. Park et al., 2014). The crack formation during debinding can easily occur and deform the shape of the 3D structure.

Due to the low decomposition temperature of the selected polymers, high temperature sintering can easily destroy the 3D structure. As temperature rises, the polymers are consumed and exhausted as gas, and the 3D structure is easily deformed. Therefore, it is necessary to find out the effectiveness of thermal stability at low temperatures since it may cause unexpected deformation of sample's shape by uncontrollable thermal runaway. If debinding process is too fast, cracks can easily occur and thereby affect the structure of products during sintering (Belgacem, Thierry, & Jean-Claude, 2013). Controlling the temperature during sintering is also a critical challenge which can obstruct the development of 3D alloy component fabricated by 3D printing.

Meanwhile, the magnetic properties of the magnetic materials are highly sensitive to temperature during sintering process (N. Wang et al., 2018). Tremendous heat generated in sintering process increases the temperature and simultaneously weakens materials' coercivity. Furthermore, magnetic materials have limited application in laser sintering, especially for ferromagnetic materials. They were hindered by thermal sensitivity, easy oxidation and phase distortion of magnetic materials and high processing constraints (Zou et al., 2018). Owing to thermal sensitivity of magnetic materials, the intensity of laser sintering has a significant effect on their crystal structure and magnetic properties. Therefore, a controlling temperature during sintering is important for the crystal structure and magnetic properties of the magnetic materials.

1.5 Research objectives

This research aims to develop appropriate methods in fabricating 3D structure for SmCo alloys in environmental-friendly manner. According to the research gaps mentioned in section 2.5, the following three objectives are framed:

- (1) Development of an alternative precursor for the sake of environmental-friendly synthesis;
- (2) Development of appropriate methods to fabricate 3D structure for SmCo alloys;
- (3) Development of the control mechanism in binder content and thermal profile to enhance crystal structure and magnetic properties of SmCo alloys.

Chapter 2 Literature review

2.1. Transition metal and rare-earth metal-organic compounds

The synthesis of metal-organic compounds has attracted considerable attention in recent years due to their diverse functionality, versatile structure and unique physical properties. The large range of available metals and coordinated organic ligands provides a very large number of potential collocations with different structures and functions. A subclass of these materials consisting of metal ions and a multidentate organic linker with a porous structure is identified as a metal-organic framework (MOF) (James, 2003). MOFs have attracted substantial attention due to their excellent properties and easily controlled structural design (M. X. Wu & Yang, 2017). Extremely high porosity and surface area, tailorable composition and structure, multifunctionality and biocompatibility are the major advantages of MOFs. To date, MOFs have been widely studied and applied in various fields, including gas storage and separation, drug storage and delivery, catalysis and gas sensing (Bloch et al., 2012; B. Li et al., 2016; R. B. Lin, Liu, Ye, Li, & Zhang, 2016; Zheng et al., 2016).

TMs and REMs also instigated substantial interest in the application of these compounds. Many studies have focused on the coordination chemistry of chelating ligands on TM centers with multiple functionalities. For example, chelating agents were used for iron bioavailability and applied to produce cell culture media (R. B. Lin

et al., 2016). The reactivity of the metal centers mostly results from their redox-active or Lewis acids characters. Metal centers can be treated as strong Lewis acids, which can activate coordinated ligands for reactivity. Another important and widely used TM, cobalt, was also used for coordination for applications in biology and medicine (Renfrew, O'Neill, Hambley, & New, 2017). However, the coordination chemistry of rare-earth elements had a late start when compared with that of TMs. RE elements prefer to coordinate with organic bonds with hard Lewis base donors, such as O, F and N, to form coordinated materials with high coordination numbers since they have large ionic radii and strong hard Lewis acid character (Florek et al., 2015). Carboxylic acids, a group of organic materials that contain carboxyl groups, were fully studied in forming RE complexes due to their strong chelating ability (Jha et al., 2016).

Increasing environmental concerns and efficiency requirements for materials resources have emphasized the importance of improving materials savings and generating a decreased amount of harmful waste generated materials synthesis. Many methods have been developed by researchers to synthesize complicated materials. They aim to reach the efficiency provided by nature, which consists of a combination of compatible single bond-forming processes. In addition, cascade or tandem reactions (McKenna, Leimkühler, Herter, Turner, & Carnell, 2015), C–H activation (Davis, Du Bois, & Yu, 2011) and metathesis (Stoianova, Johns, & Pederson, 2015) are rather new approaches. They illustrate clean and efficient synthesis approaches available in organic chemistry. The designed natural molecules can be prepared with cascade

reactions and biomimetic strategies. In these approaches, a single event launches the change from a starting material to a product. After that, the product becomes the substrate in the next reaction until the final stage is reached. Cascade reactions and biomimetic strategies are highly desirable because of their efficiency and economy in terms of reagent purification and consumption. The challenge of developing nonhazardous synthesis approaches is leading to fundamental innovations in organic synthesis and will result in environmental, economic and social benefits in the pharmaceutical industry (Ahsan et al., 2018).

2.1.1 Transition metal-organic compounds

As mentioned previously, the synthesis of TM organic compounds has received significant attention. Various structures of metal-organic compounds with diverse functionalities can be produced through TM and coordinated organic ligands, such as carbonyl ligands (Ding & Hall, 2016). Moreover, a substantial number of applications for these materials can be identified, including luminescent chemo-sensors (L. Li, Shen, Lin, Bai, & Liu, 2017), heterogeneous selective oxidation catalysis (Paille et al., 2018) and medicinal devices (Guerriero, Peruzzini, & Gonsalvi, 2017). A large group of metal-organic compounds is referred to as a metal-organic framework (MOF), which is often porous and has special features. Cobalt-based MOFs have been widely studied because of their easily controlled structure with high porosity and multifunctional

abilities. The large specific surface area that is a result of their high porosity indicates their potential as a catalyst for cyanosilylation (X. Cui, Xu, Zhang, Yao, & Zhang, 2015); their thermal stability also makes them feasible as a precursor for cobalt nanoparticle preparation, which are encapsulated in graphene shells (Murugesan et al., 2018). Zeolitic imidazolate framework (ZIF), as one of the important subclasses of MOFs, were also studied widely. ZIF-67, a type of cobalt-based MOF, contains the advantages of high porosity, chemical stability and structural stability at high temperatures, similar to those of MOFs. However, most MOFs consist of long organic links, which often have isolated metal-based centers to prevent the generation of long-range magnetic ordering, thereby demonstrating nonmagnetic performance (Dechambenoit & Long, 2011). Hence, a single-molecule magnet was developed and inserted into the pores of MOFs to create paramagnetic materials (Das et al., 2017; Feng et al., 2015; S. Zhang et al., 2015). Additionally, to decrease the distance between metal centers, redox-active ligands were inserted into MOFs to generate strong magnetic exchanges (DeGayner, Jeon, Sun, Dincă, & Harris, 2017). Ferromagnetic MOFs are still rare, and the existing ones demonstrated small coercivity (R. Dong et al., 2018; K. Wang et al., 2018). Therefore, MOFs with strong ferromagnetic properties are in demand for magnetic applications.

Ascorbic acid is a common organic material that has strong chelating ability. It can be used to form metal-organic compounds by the reduction of metal oxide and metal compounds (X. Hou, Shen, Huang, Ai, & Zhang, 2016; Y.-T. Lin, Liang, & Yu,

2016). During the reduction process, only common metal salts are generated as waste, which are not hazardous. Normally, generated exhaust gases comprise only CO₂ and H₂O during sintering when using a metal ascorbate as the precursor. Complexes of TM ascorbates were first prepared in 1992 (Obaleye & Orjiekwe, 1992). A green solvent system with methanol and water was used as the solvent during the preparation, a modified process was conducted to replace the sodium hydroxide. Cobalt-based organic compounds can also be treated as precursors for further materials preparation (Smyrnioti & Ioannides, 2017).

2.1.2 Rare-earth metal-organic compounds

Coordination chemistry is a science that consists of process that involve an interaction between a metal center and organic or inorganic ligands. Research on the coordination chemistry of rare-earth elements (RE) has substantial interest in recent years. Rare-earth organic complexes with chelating ligands in N- donors were synthesized and characterized sequentially (J.-F. Liu et al., 2014; Y. Zhang, Yao, Li, & Mu, 2012). However, due to their unique properties, strong chemical characteristics and diverse applications, research on REMs has increased intensively in the past three decades. REM ions are apt to bond with hard Lewis base donors, including F, O, and N. Due to their hard Lewis acid character and large ion radius, they exhibit large coordination numbers (Marques et al., 2016). Carboxylic acids and

polyaminopolycarboxylic acids have O and N donors respectively, which contribute to various structures and satisfy the high coordination number requirement. Therefore, these materials are adequate ligands for REM coordination. For example, a type of samarium composite with chelating ligands of O and N donors is shown in figure 2.1 (Maria et al., 2016). Samarium chelated four N-donors and two O-donors to form a composite, and the coordination number of samarium was six.

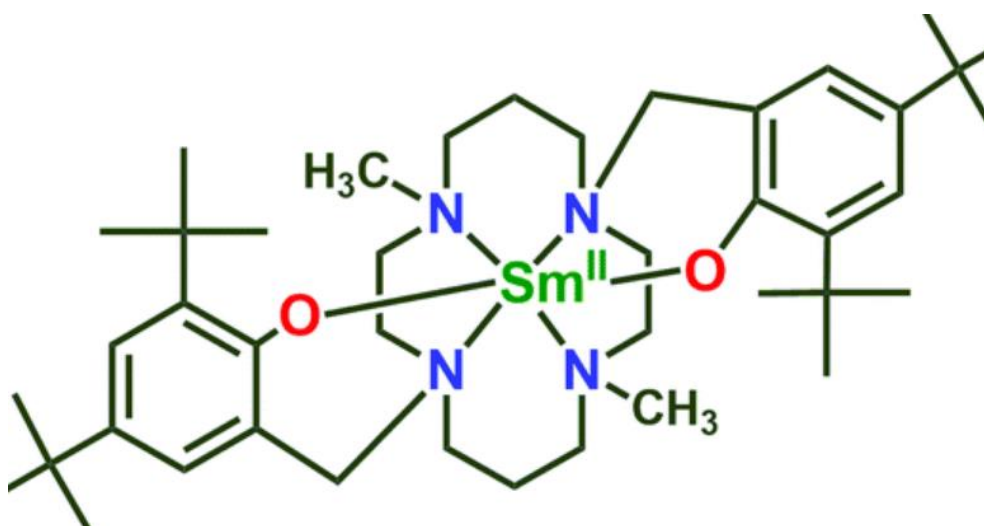


Figure 2.1. Chemical formula for referred samarium composite (Maria et al., 2016).

In the beginning, cation-exchange resins were used to separate REMs, and citrate and polyaminopolycarboxylates were applied as the raw materials (Ketelle & Boyd, 1947). The development of RE chemistry has attracted great attention in the coordination chemistry field by using organic ligands, such as carboxylic acid, amino acids and polyamino-polycarboxylic acids. REM compounds with these organic

ligands have been developed with various binding modes and applied in different fields, including nonlinear optics (He, Tan, & Zhang, 2015), organic light emitting diodes (Gaj, Fuentes-Hernandez, Zhang, Marder, & Kippelen, 2015), metal–organic frameworks (Alezi et al., 2015) and corrosion inhibitors (C. Zhu et al., 2018).

As TMs, REMs can also be used to prepare metal-organic precursors with clean organic ligands. As a type of green, common and water-soluble organic material, ascorbic acid can be used as an organic ligand for metal-organic compound preparation. Due to the chelating ability of REMs, ascorbic acid can be applied to synthesize REM ascorbates. Samarium ascorbate can be prepared by adding ascorbic acid (Yin & Lu, 1998). However, it is still a challenge to predict the structures of these species because of their relatively low stability. Detection of different materials at equilibrium is also difficult and needs to be studied systematically. These challenges represent from the major goals for the development of REM compounds in the future.

Precursor preparation is a major step in the functional alloy synthesis process when using chemistry methods. Metal composites are prepared as raw materials, also called precursors, for synthesis. Normally, the organic ligand and inorganic salt are the two primary coordination materials for metal precursors. Metal oxides, metal halides and metal oxyacids are the major metal-inorganic precursors. However, thousands of organic materials can be selected as organic ligands for metal-organic compound preparation. Therefore, the selection of organic ligands is very important. In recent years, many reports on the synthesis of meta-organic compounds have been published

(H.-C. Zhou, Long, & Yaghi, 2012). Thus, it is important to select appropriate organic materials as organic ligands because the use of different organic ligands may result in a variation in the properties and structures of the resulting materials. In addition, different elements also lead to a variation in the properties of the resulting materials (L. J. Wang et al., 2014).

2.2 Transition metal and rare-earth metal alloys

As mentioned, TM and REM alloys have reached a mature development phase. The classification of compounds formed by REMs and TMs has aroused widespread interest, and the number of these compounds is very large. Until the 1950s, metallic forms of individual REMs were almost unavailable (Froehlich, Lorenz, Martin, Brett, & Bertau, 2017). However, the significance of rare-earth (RE) alloys in nuclear fission was then published and the separation and reduction of these elements became important. It allowed elemental metals to be commercially available and instigated scientific interest in RE alloys. From 1950 to 1965, many RE-TM compounds were prepared. Their properties were also studied systematically (Wallace, 2012). A composite of one REM and one TM can generate numerous intermetallic compounds with different structures, and these compounds have attracted considerable attention. Simultaneously, these compounds can possess advantages from both of their composing elements. For example, they can attain a strong magnetic coupling strength from TMs and large magnetic crystalline anisotropy and a large magnetic moment

from rare-earth elements (Buschow, 1977). Subclass materials, such as Lu, Y, La and tetravalent Ce, do not process a magnetic moment and are not included in my research. In addition, a substantial amount of research effort has been made with regard to an enhancement in the material properties, sizes and fabrication methods of REM-TM compounds. The unique electron configuration in REMs results in strong magnetic properties, which is the major interest of rare-earth alloys. RE-cobalt magnets, neodymium iron boron and other permanent magnetic materials have been researched continuously. With different engineering properties and economic prospects, many kinds of RE-Co magnets are being produced and used today (Chongkang, Shunkang, CHENG, Xing, & Yajun, 2015). Relevant research and development activities are discussed in this chapter. The samarium-cobalt alloy is illustrated independently since it is a promising permanent magnet with outstanding performance.

2.2.1 Rare earth-cobalt alloys

Investigations of the magnetic orders in RE-TM materials played a significant role in their magnetic development. In the beginning, researchers in the Bell Telephone Laboratories (Nesbitt, Williams, Wernick, & Sherwood, 1962), the University of Pittsburgh (Nassau, Cherry, & Wallace, 1960) and the US Naval Research Laboratories (Hubbard, Adams, & Gilfrich, 1960) were the pioneers in this field. Hubbard et al. demonstrated that GdCo_5 exhibited uniaxial anisotropy and showed a coercivity of 0.64 MA/m (8 kOe). This was the first indication that RECo_5 compounds exhibited

outstanding properties as permanent magnets. $GdCo_5$ is generally ignored and disqualified as a general magnetic material owing to its low saturation magnetization.

The properties and synthesis cost were investigated for a series of RE-Co magnets as shown in figure 2.2. The basic magnetic properties and cost comparison for RE components are indicated. Samarium-cobalt magnets are the materials with the highest coercivity in this series, while lanthanum-cobalt magnets and cerium-cobalt magnets have the lowest cost. From Pr to Y, the saturation of corresponding cobalt magnets increases. The saturation magnetization decreases from Gd to Er.

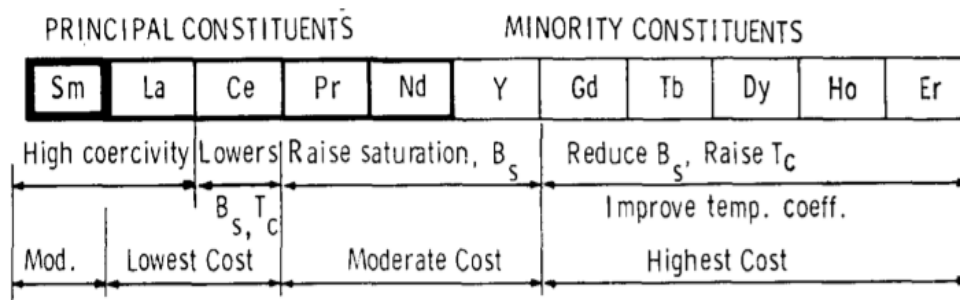


Figure 2.2. Rare-earth elements used in RE-Co magnets.

Due to the low densities in the REM series, Ce, Pr, Nd, Sm and Y were defined as "light" REs. The $RECo_5$ materials with these elements were treated as possible new permanent magnetic materials (Karl Strnat, Hoffer, Olson, Ostertag, & Becker, 1967). The RE_2Co_{17} phases were then developed as permanent magnetic materials (K Strnat, Hoffer, Ostertag, & Olson, 1966). YCo_5 and the majority of other $RECo_5$ compounds

show extremely high crystalline anisotropy along the single easy axis of magnetization. With this unique magnetic property, YCo_5 and most other RECo_5 compounds become outstanding new permanent magnets. The discovery of the unsatisfactory crystalline anisotropy of Y_2Co_{17} initially discouraged the development of 2-17 phase magnetic materials. However, in later research, $\text{Sm}_2\text{Co}_{17}$, $\text{Er}_2\text{Co}_{17}$ and $\text{Tm}_2\text{Co}_{17}$ were revealed to have high anisotropy along the easy axis (Schaller, Craig, & Wallace, 1972).

Dense and stable SmCo_5 magnets were fabricated and with the development of appropriate sintering techniques, they became the first major commercial REM-based permanent magnetic materials. Subsequently, they were further studied as a replacement of Co by Cu in SmCo_5 and CeCo_5 . This allowed the development of RECo_5 matrix precipitates with large coercivity (Chouhan & Paudyal, 2017). The high cost of the REMs, especially samarium, seriously inhibits widespread industrial use. Samarium-cobalt alloys will be discussed later in the manuscript.

2.2.2 Samarium-cobalt alloys

Nano samarium-cobalt magnetic materials have drawn substantial attention for high-performance advanced applications due to their promising physical properties and structures. Due to a large number of studies on the fabrication of nanoscale magnetic materials, many mature processes and technologies have contributed to the development of these novel and widely used materials with unique structures and outstanding functions. As one of most important REM magnetic alloys, SmCo_5 has

unique structure and performance features, such as a very large magnetic anisotropy ($K_u=2\times 10^8$ erg/cm³), high Curie temperature (1000 K) and large coercivity (Matsushita, Iwamoto, Inokuchi, & Toshima, 2010). Therefore, SmCo₅ ferromagnetic materials become one of the most popular candidates for permanent magnetic materials applications. Due to the outstanding magnetic properties of SmCo materials, SmCo can be applied in various fields, such as magnetic products, and the major and important applications include high-density recording media, permanent magnetic materials, and magnetic microelectromechanical systems (Abbas, 2017; Shen, 2018; Hannachi, 2016).

Because of the outstanding performance and substantial number of potential applications of SmCo₅, the specific structure and advanced properties of its synthesis have been widely studied. Unlike other magnetic materials, the crystal structure of SmCo₅ (figure 2.3) is hexagonal close-packed, which is also known as a CaCu₅-type structure. Samarium elements are symbolized as black spots and occur at 1a (0,0,0), cobalt elements are symbolized as white spots and occur at 2c (1/3, 1/3, 0), and the other elements occur at in 3g (0, 1/2, 1/2). Its lattice constant is a= 499 pm, c= 398 pm.

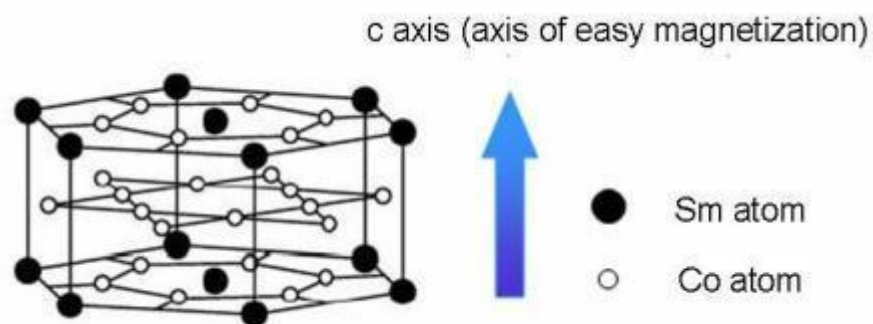


Figure 2.3. Crystal structure of SmCo₅ (Sayama, Asahi, Mizutani, & Osaka, 2003).

The high Curie temperature causes SmCo₅ to be a potential candidate to replace Nd₂Fe₁₄B as a magnetic material at room temperature, and the attendant high coercivity makes it attractive for industrial applications. Because SmCo₅ has such advanced physical properties, it is used in many high-performance applications, such as in magnetic resonance imaging and as drug carriers in biomedical technology (Ma, Yang, Zhang, & Jiang, 2016); as motors, generators, magnet sensors and separators for transportation application; telecommunication devices and microelectronic devices in MEMS applications (Baig et al., 2016) and in aerospace applications (Jingtao, Binbin, & Dongmei, 2012). Since SmCo₅ has extremely high uniaxial magnetocrystalline anisotropy, it can fulfill the requirements of excellent thermal stability and minimal stable grain size for high-density magnetic recording media; thus, it is a promising candidate for this application. According to the energetically favorable principle, the crystal structure of SmCo₅ is hexagonal close-packed (hcp), and the magnetic moment of magnetically anisotropic materials tends to align with an "easy axis". Therefore, the crystal structure of SmCo₅ in the bulk state strongly influences its magnetic properties. Furthermore, the crystalline anisotropy and 4f-3d exchange coupling between Sm and Co in this structure have important impacts on the magnetic performance (Nesbitt, 1962; Nassau, 1960). SmCo₅ nanoparticles with strong magnetic properties synthesized by chemical or physical methods have large magnetic crystalline

anisotropy. This can solve the thermal fluctuation in ultrahigh density magnetic recording media.

Many successful and mature synthesis methods for RE magnetics materials and scientific studies on their physical properties and crystallography have been reported. The synthesis of micro/nano-sized particles, the control of specified crystal structures and the enhancement of their properties have become noble research topics in recent decades (Reszczyńska et al., 2015). The miniaturization of magnetic components requires a decrease in the raw material size. The synthesis of micro/nano scale particles with the same functionality or even better performance has aroused substantial interest. Various novel fabrication methods have consequently emerged, such as high energy ball milling (Nie et al., 2013) and polyol processing (Matsushita et al., 2010). Furthermore, SmCo_5 exhibits a CaCu_5 -type structure (hexagonal close packed), which induces high magnetic anisotropy and strongly influences the magnetic properties.

Good thermal stability and the greatest anisotropy make SmCo_5 as an extraordinary candidate in the hard magnet area. Recently, the fabrication of samarium-cobalt magnets in 1:5 phase with small size and uniform phase has received remarkable interest. Accordingly, multifarious synthesis methods were developed, such as chemical methods and high energy ball milling techniques. They were reported to be the major synthesis methods.

In addition to the 1:5 phase of samarium-cobalt magnet, its 1:3 phase also aroused widespread interest for use as a permanent magnetic material. This is because SmCo_3 has large lattice anisotropy, though not as large as that of SmCo_5 . SmCo_3 also exhibited rhombohedral PuNi_3 -type structure with the magnetic moments of samarium and cobalt oriented antiparallel (Gaidukova et al., 2006). SmCo_3 is normally treated as an impurity during the synthesis of SmCo_5 because it can be isolated from SmCo_5 by replacing cobalt atoms (Bulyk, Panasyuk, & Trostianchyn, 2004). Its axial ratio $c/a > 4.5$, which endows it have large lattice anisotropy; it is therefore receiving consideration as a potential candidate for permanent magnetic material (Lu, Song, & Zhang, 2010).

Chemical synthesis for binary alloy nanoparticles has been comprehensively developed and reported, due to their unique merits of controllable particle size, unique crystal structure and extremely large magnetic isotropy (Sun, Murray, Weller, Folks, & Moser, 2000). Since the chemical process is able to manage the particle size, composition, crystal structure and interparticle spacing, it can satisfy the fundamental and technological requirements for product design. For example, the chemical process can be used to solve the thermal fluctuation problem, which is the main issue that hinders the development of magnetic recording media (Matsushita et al., 2010). The synthesis in high boiling point multivalent alcohols, called the polyol process, has been widely applied as a novel and common chemical synthesis method for nanoparticle products (H. Dong, Chen, & Feldmann, 2015). As is first reported by Fieve (H. Dong

et al., 2015), the two major advantages of the polyol process for micro sized metal particles are the simple starting materials and efficient reducibility, which were also demonstrated in later research. Making use of these advantages, super lattice nanocrystal ferromagnetic FePt nanoparticles were prepared by S. H. Sun (Sun et al., 2000), which aroused widespread interest in the magnetic materials research area. A thermally stable grain size down to 5 nm and anisotropy that reached 106 erg/cm^3 demonstrated the unique potential for the chemical synthesis of ferromagnetic nanoparticles. Due to the far-reaching implications of this work, a rich new route for magnetic particle synthesis by chemical processing has been established. SmCo_5 and other magnetic materials have been reported in succession due to the remarkable work by Sun. Chen and Nikles (M. Chen & Nikles, 2002) reported the synthesis of 3 to 10 nm spherical FeCoPt, FePd and CoPt nanoparticles in the following two years with a similar methodology; the synthesis of cobalt-platinum particles with a size of less than 10 nm was reported by Park and Cheon (J.-I. Park & Cheon, 2001); and SmCo_5 was also successfully synthesized in a chemical routine (H. Gu et al., 2003).

Although the polyol process is the commonly used chemical method for synthesizing samarium-cobalt alloys with outstanding performance, there are still some drawbacks with this method. Metal acetylacetonates were used as precursors in polyol process for synthesizing samarium-cobalt alloys, and highly volatile organic solvents were also used to dissolve materials during synthesis process (Fiévet et al., 2018). However, these metal acetylacetonates are toxic, and the synthesis process is

not environmentally friendly. The toxicity of metal acetylacetonates and the volatility of organic solvents are harmful to humans and environment. Moreover, the generated wastes/byproducts from metal acetylacetonates are organic based materials, which are also not environmentally friendly.

2.3 Three-dimensional component fabrication technologies

Due to the increasing demand for shape-flexible products for critical requirements and the tendency towards miniaturization, traditional manufacturing techniques are decreasing in popularity. An automatic manufacturing method that deposits a stack of single elements using computer aided design was created. American Society for Testing and Materials international defined this novel manufacturing technology and named it additive manufacturing. It is defined as “a process of joining materials to make objects from 3D model data, usually layer upon layer, as opposed to subtractive manufacturing methodologies” (Frazier, 2014). To date, AM has developed into a mature technology that serves very different areas with a variety of materials, and is used commercially, and the number is growing continuously.

The ability to fabricate a variety of shapes that are light weight and porous represents the unique advantage of AM which is the major reason for its popularity. Therefore, a group of AM methods were created for various requirements. It can be classified by different criteria, such as the phase of materials, material feed stock, and

energy source. Here, a typical classification criterion for the phase of materials is shown in figure 2.4. They can be liquid based, solid based and powder based. Many AM processes are sorted into these three categories, such as fused deposition modeling and SLS. Fused deposition modeling has been fully developed with various colorful polymers for both industrial and domestic use.

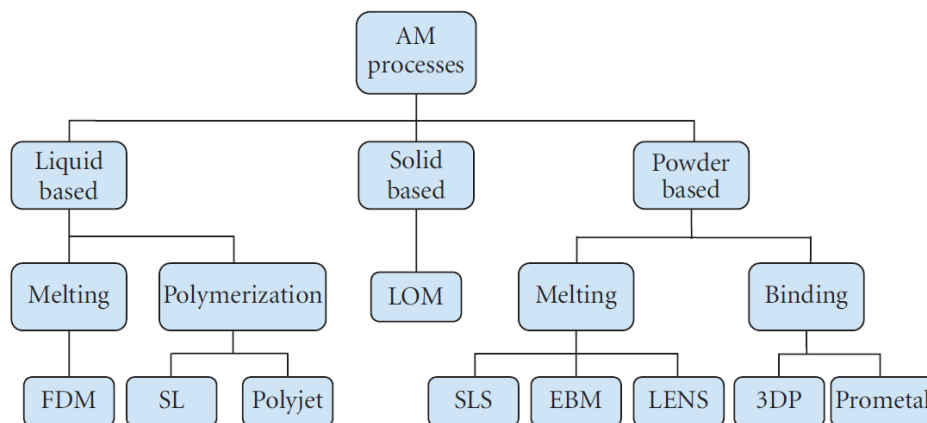


Figure 2.4. Typical category of AM process.

As AM technology has rapidly developed with the study of novel materials and approaches, numerous applications have been established, including those in the aerospace, automotive, biomedical, energy and other fields (Guo & Leu, 2013). AM technologies have been widely deployed in the aerospace field because structures with a light weight can be fabricated, and this fulfils a common requirement for aircraft and spacecraft. It is also advantageous for the vehicle industry. AM method can reproduce difficult-to-find parts, including the parts for classic cars (Frazier, 2014). However, because not every industrial material can be fabricated with AM, it has not yet become

a standard manufacturing method in industry. Because there is a very large demand for products with critical features, there is a need to further develop AM methods.

Table 2.1. Alloy materials for laser sintering (DD Gu, et al., 2012).

Alloy	Composition	Alloy	Composition
Ti based	Ti-6Al-4V	Fe based	Stainless steel 316L
	Ti-25V-15Cr-2Al-0.2C		Stainless steel Inox904L
	Ti-4Al-1.5Mn		Tool steel H13
Ni based	Inconel 625		High speed steel M2
	Waspaloy		AISI 4340 high strength low alloy steel
	Inconel 718		Fe-15Cr-2Mn-16B-4C-2Mo-1Si-1W-1Zr
	Rene 88DT	Al based	Al-40Ti-10Si
Rene 41	Al-10Si-Mg		
Co based	61.78Co-29.37Cr-6.53Mn-0.23C-0.69Mn-0.68Si	Al based	6061 Al alloy
	Co-10.10Ni-26.41Cr-7.31W-0.81C-0.44Si		Cu based
		Cu-30Ni alloy	

Materials for AM are still the major limitation. Polymers, metals and ceramics are the primary materials for AM, while there are only some potential commonly used materials for AM (Wong & Hernandez, 2012), as shown in table 2.1. The accuracy for the products fabricated by AM also needs to be improved to reach the requirements for an elevated level of precision. Moreover, limitation regarding the materials that are feasible for AM, especially alloys, has seriously obstructed the use and development of AM. Table 2.1 shows the potential alloys for state-of-the-art laser sintering in 2012. Only a few types of titanium, nickel, iron, aluminum, cobalt and copper-based alloys can be fabricated with laser sintering. There is still a very large opportunity to develop multiple alloy materials for laser sintering to satisfy ever-growing demands for AM fabrication.

2.3.1 Inkjet printing

Inkjet printing is one of the AM techniques that uses liquid-phase materials to fabricate products. These liquid-phase materials, generally called inks, contain soluble raw materials and corresponding solvents. The process has several steps: the required quantity of ink is ejected from a chamber, which then passes through a nozzle under piezoelectric control with quasi-adiabatic reduction of the chamber volume. Finally, the ink drops on the required substrate to form a certain shape. An external voltage is

applied to fill the chamber with the condensed liquid. A shock wave in the liquid is induced to eject the ink from the nozzle (Singh, Haverinen, Dhagat, & Jabbour, 2010).

Inkjet printing of magnetic materials with 3D structures has recently aroused widespread interest (G. Li, Roberts, & Tien, 2014). As one of the most attractive AM methods for the development of miniaturized 3D microscopic devices with flexible shapes, inkjet printing method has attractive properties, such as its ambient processing feature and low cost (Dixon, Ng, Fobel, Miltenburg, & Wheeler, 2016). Meanwhile, this easy-to-operate and economical method has been applied widely with drop-on demand by using nanoparticle ink. However, the agglomeration of nanoparticles resulted in severe clogging problems during processing (Yung, Wu, & Liem, 2009), it was because the low solubility of nanoparticles and the changes of dynamic viscosity as temperature increasing as well as time passing caused aggregation for dispersion and lead to ink clogging. To address these issues, metal-organic particles were developed to enhance solubility and stability since metal-organic particles in the ink have lower particle-particle interaction, which can decrease the risk of aggregation (Elgammal, Schneider, & Gradzielski, 2016; Jahn et al., 2008). The solubility of the ink increased because metal-organic particles can be dissolved completely rather than dispersed into solution, which is the case for nanoparticles. Applying this type of ink can eliminate sedimentation in inkjet nozzles and thereby increase the inkjet printability. Furthermore, it also provides excellent adhesion to different substrates and creates uniform layers (Mei, Lovell, & Mickle, 2005). Relatively high surface tension,

from 30 mN/m to 70 mN/m, contributed to the formation of a uniform and continuous layer over the substrate surface without dripping and spreading since the ink could be sufficiently held in the nozzle (Yun, Kim, Lee, Cho, & Lee, 2009). The coffee-ring effect is an unexpected phenomenon that influences the required accuracy for the patterns (J. Wu et al., 2015). Optimizing the distance between each droplet can reduce this unexpected phenomenon (J Stringer & Derby, 2009; Jonathan Stringer & Derby, 2010). Many factors can affect the determination of the droplet spacing, such as solution adhesion and substrate properties.

Inkjet printing has been applied in various fields by using promising magnetic materials. For example, superparamagnetic materials, such as SU-8 (Jacot-Descombes et al., 2014), were used to fabricate a micro electromechanical system; NiZn-ferrite, as an outstanding soft magnetic material, was used to fabricate radio-frequency passive components (Bissannagari & Kim, 2015); and ferromagnetic materials were also used to produce microscale devices (H. Lee, Tentzeris, Markondeya, Raj, & Kawahara, 2013). Furthermore, this mask-less and noncontact technique has been applied to fabricate numerous applications products, including magnetic circulating tumor cells, radio-frequency identification resonators, photonic crystal microchip and electromagnetic driven actuators (P. Chen, Huang, Bhave, Hoshino, & Zhang, 2016; Marjanović et al., 2014) (B. Ando & Marletta, 2016; J. Hou et al., 2014).

Cobalt, as one of the important TMs, has been developed and has received substantial interest for the fabrication of materials with magnetic properties. Thin films

of cobalt-based materials fabricated by using inkjet printing have been thoroughly explored (Fittschen et al., 2006; Shen, Pan, Wang, & Chang, 2006). Therefore, it is foremost to develop magnetic components with 3D structures by using cobalt-based molecular nanoparticles in inkjet printing. However, to the best of my knowledge, there is still little research on inkjet printing that uses cobalt-based materials with high solubility and ferromagnetic behavior.

2.3.2 Modified laser writing system

Metal materials for AM have been studied to fabricate electronics devices via the aid of computer (Ladd, So, Muth, & Dickey, 2013; Visser et al., 2015). SLS (Hong et al., 2013) and inkjet printing (Chao, Qi, Xiao, Luo, & Zhou, 2012; Vaezi, Seitz, & Yang, 2013) have been widely investigated to overcome their drawbacks. SLS is a time-consuming and energy-intensive technique that heats metal or alloy powders to their melting points. Additionally, inks consisting of nanoparticles easily clog nozzles, which continuously hinder the development of inkjet printing. Therefore, high-yield and low-cost production of electrodes, electrical circuits and antennas is still a challenge for the AM approach (Frazier, 2014).

To obtain target materials on any required substrate, a novel AM method was developed and was referred to as laser-induced forward transfer (LIFT) method (J. Shaw-Stewart, Lippert, Nagel, Nüesch, & Wokaun, 2011). Applying laser system in LIFT for metal materials aroused widespread attentions (Kattamis, Brown, & Arnold,

2011). Normally, there are three layers used in the LIFT method for the traditional noncontact mode. As shown in figure 2.5, these layers are transparent carrier, donor and acceptor. Laser goes through a transparent carrier and illuminates on the donor, donor absorbs laser power, expands its volume and finally transfers onto the acceptor. Optimizing laser power and the distance between donor and acceptor can uniformly transfer the expanded droplet onto the donor.

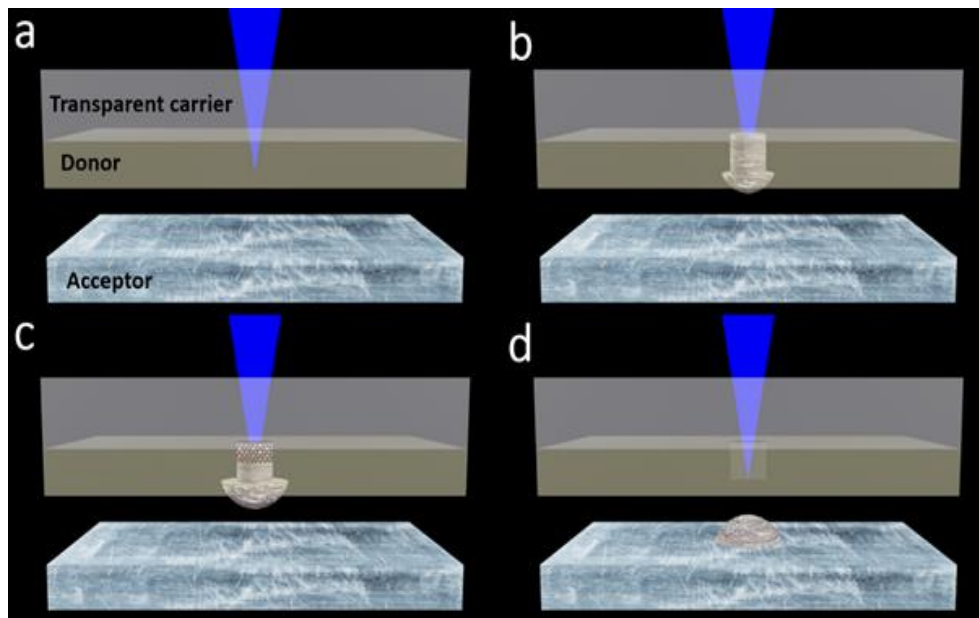


Figure 2.5. Schematic process of standard laser induced forward transfer.

LIFT method becomes an outstanding method for functional material deposition due to the rapid development of laser techniques. Moreover, it is also time-saving and energy-saving because of the merits of thermal expansion of materials compared with

laser sintering, which usually needs very high temperatures (W. K. Yung, B. Sun, Z. Meng, et al., 2016). LIFT method has been developed for many metal elements, such as gold (Unger, Koch, Overmeyer, & Chichkov, 2012), silver (Di Pietrantonio et al., 2012), copper, aluminum, and silicon (Zywietz, Evlyukhin, Reinhardt, & Chichkov, 2014), for the fabrication of numerous products, such as emerging energy devices (Zenou, Sa'ar, & Kotler, 2015). Vacuum deposition methods can be used to fabricate metal thin films on transparent carriers, however, these methods are usually time-consuming and expensive. In contrast, it is cheaper to use solution-based methods to prepare donors on transparent carriers (Rapp, Cibert, Alloncle, & Delaporte, 2009). However, it is still difficult to obtain thick metal layers by using solution-based method. Moreover, it is also easy to oxidize nano sized metals in the solution since the ratio of surface area to volume is high. Furthermore, it is also expensive for pulsed laser systems.

Metals can be reduced from their oxidation state by chemical methods, for example, by using photochemical methods (Jakus, Taylor, Geisendorfer, Dunand, & Shah, 2015). Photochemical methods use light to reduce metal oxides based on homolysis effect and photo-thermal effect. It has been proven that copper oxide can be reduced to metallic copper by the emerging intense pulsed light through local heating with pre-defined patterns (Paglia et al., 2015). Usually, ultraviolet (UV) light is used for photochemical method through homolysis effect. The minimum energy for homolysis effect in photochemical method is defined as the bond dissociation energy.

The bond dissociation energy and the resistivity of metals commonly used for the photochemical method were collected and are shown in table 2.2. Silver presented the lowest resistivity compared with that of other metals. Its bond dissociation energy is 221 kJ/mol, which can be transferred to photon energy with a wavelength of 541 nm. However, silver is too expensive to be used in mass production. Copper also have a very low resistivity, and its bond dissociation energy is 287.4 kJ/mol, which can be transferred to photon energy with a wavelength of 416 nm. Therefore, a GaN laser with wavelength of 405 nm can activate the homolysis effect of copper oxide. Moreover, this laser and copper oxide have a low cost in comparison with that of silver. Owing to the cost, resistivity and bond dissociation energy of a variety of materials, copper is an outstanding candidate for synthesis through homolysis.

Table 2.2. Resistivity of the metals and the bond dissociation energies of their corresponding oxides.

Element	Resistivity ($\Omega \cdot m$) (20 °C)	Oxide Bond	Bond Dissociation Energies (kJ mol ⁻¹)
Silver	1.59×10^{-8}	Ag-O	221 ± 21
Copper	1.68×10^{-8}	Cu-O	287.4 ± 11.6
Gold	2.44×10^{-8}	Au-O	223 ± 21
Alumina	2.82×10^{-8}	Al-O	501.9 ± 10.6

Cobalt	6.24×10^{-8}	Co-O	397.4 ± 8.7
Nickel	6.99×10^{-8}	Ni-O	366 ± 30
Iron	1.00×10^{-7}	Fe-O	407.0 ± 1.0
Platinum	1.06×10^{-7}	Pt-O	418.6 ± 11.6
Titanium	4.20×10^{-7}	Ti-O	666.5 ± 5.6

A dynamic release layer, also called a sacrificial layer, is necessary to eject donor to the acceptor. The momentum for this process is called the ejection momentum (Pohl et al., 2015). With the support of ejection momentum, the dynamic release layer expands and escapes from donor to acceptor (Meshcheryakov, Shugaev, Mattle, Lippert, & Bulgakova, 2013). Organic dynamic releases layer is better for metal materials by using LIFT method because of the low boiling temperature and sublimation temperature of organic materials. Acrylonitrile butadiene styrene (ABS), a commercial and cheap organic thermoplastic, is an outstanding candidate for LIFT since its relatively high thermal expansion ($73.8 \times 10^{-6} \text{ K}^{-1}$) and low decomposition temperature ($400 \text{ }^\circ\text{C}$). Meanwhile, generated gas during LIFT for this organic material is CO_2 under ambient conditions, which can increase the expansion of volume and thereby increase the ejection momentum for donor.

Thermoplastics materials used in 3D printing have been fully studied for application in modelling, prototyping and production applications (Ladd et al., 2013).

Millions of 3D printed objects have been fabricated in recent years. A metal coating on the surface of these objects can make them multi-functional. This is because metals provide higher thermal conductivity and better wear resistance and luster than nonmetallic coating materials (Torgerson et al., 2018). Furthermore, electronic devices or circuits can be fabricated by selectively coated with metallic materials (Aminuzzaman, Watanabe, & Miyashita, 2010). Electronic circuits were successfully fabricated by inkjet printing on flat surfaces with large areas (Y. Lee, Choi, Lee, Stott, & Kim, 2008). However, it is still rare to coat metals on the surface of 3D printed objects directly. This is because that thermoplastic is insulating, which makes it difficult to electroplate metallic coatings on them (Green et al., 2015). Owing to their low melting point, thermoplastic objects cannot be cast by metals without damaging their shapes at high temperatures (Takemori, 1979). Therefore, it is still important to develop a novel method to coat metals on the surface of 3D printed thermoplastic objects.

Painting is a common method to coat functional materials onto the surface of target substrate (W. h. Zhou et al., 2016). Malachite, also called copper carbonate hydroxide, has been used since ancient Egyptians time (Burgio & Clark, 2000). However, the low applicability of oxide phase has resulted in this material receiving a small amount of attention. Therefore, it is necessary to use photochemical methods to reduce the oxides into metals.

2.3.3 Laser sintering

Three-dimensional alloy products are widely used in common industrial and commercial applications. Three-dimensional fabrication is reaching a mature stage. Complicated procedures and molds that are difficult to manufacture, however, are still the most severe challenges in 3D structural alloy product development. Various 3D component fabrication technologies have been developed, including gel casting, powder injection molding and AM. As one of the novel and highly attractive 3D component fabrication technologies, AM, also called 3D printing, has been extensively developed in recent years. 3D printing technology was developed in the 1980s for creating models and prototypes with the ability to create a 3D object layer by layer using CAD. This novel method has been improved dramatically and has spread into nearly all industrial fields (Gross, Erkal, Lockwood, Chen, & Spence, 2014). Its advantages are cost effectiveness, easy-processing and design flexibility. Although thermoplastics are the major raw materials used in AM, the fabrication of metal/alloy products by using 3D printing technology still represents a challenge. Fabricating alloy materials with this technique was also developed with SLS.

Laser sintering is a promising technique for fabricating 3D alloy components with flexible shapes and without the need for a mold. For SLS, a wide range of materials can be used, from polymers, such as nylon, polycarbonate, polyvinyl chloride, acrylonitrile butadiene styrene and resin, to metal and ceramic powders (Gross et al.,

2014). SLS involves heating the metal to its melting point, which is both energy-intensive and time-consuming. Thus, although SLS can be used to fabricate 3D structure alloys, only a small group of materials can be successfully used (DD Gu et al., 2012). Stainless steel, cobalt-based, titanium-based and aluminum-based alloys were the major materials fabricated with laser sintering (AlMangour, Grzesiak, & Yang, 2017; Hadadzadeh, Baxter, Amirkhiz, & Mohammadi, 2018; M. Sharma, Bansal, Panthi, Malik, & Sharma, 2017; Zhao, Iyer, Promoppatum, & Yao, 2017). Prealloyed powders were used to fabricate net shaped parts layer by layer to obtain final product with required properties and showed great potential for various applications, like those in the medical, aerospace and automotive fields (Attar, Ehtemam-Haghighi, Kent, & Dargusch, 2018; Bawane, Srinivasan, & Banerjee, 2018). However, the geometric requirements for raw powders for laser sintering still hinder the development of laser sintering. Spherical powder shape is ideal for laser sintering because this shape provides high flowability and low interparticle friction, which results in products with higher density (Sing et al., 2017; H. Zhu, Fuh, & Lu, 2007). Meanwhile, sintering neck between spherical powders formed with laser sintering also provides strong inter-agglomerate bonding (Dongdong Gu & Shen, 2009). Furthermore, the exploration of magnetic materials applied in laser sintering was still limited, especially for ferromagnetic materials. High thermal sensitivity and processing constraints, easy oxidation and phase distortion of magnetic materials severely restrict the development of laser sintering (Jung et al., 2015; Matsushita et al., 2010; Zou et al., 2018). To date,

few studies of laser sintering of soft ferromagnetic materials have been published (Garibaldi, Ashcroft, Simonelli, & Hague, 2016; Shongwe et al., 2016). Compared to those of soft ferromagnetic materials, permanent ferromagnetic materials have high coercivity and stable domain walls, which are very sensitive to temperature (Jiang et al., 2018; Y. Wang et al., 2018). Therefore, studies of permanent ferromagnetic materials fabricated with laser sintering are still challenging. The feasibility of preparing 3D structures of comprising REM alloys is important due to their unique properties and outstanding performance. Furthermore, it is also important to understand the reasons why the 3D synthesis of REM alloys fails.

2.4 Thermal debinding and sintering of alloy materials

Before obtaining alloys with 3D structures by sintering, polymers are commonly used to support materials during the shaping of 3D structures. These polymers are called binders, and when binders are mixed with raw materials to form the required 3D shapes for a fabrication technique, the mixture is called a “green part” (Enneti, Park, German, & Atre, 2012). The addition of binders can increase the ability to shape structures and provide a high driving force. The process of binder burnout is called debinding. In this process, binder can be removed, and the constructed shape can be maintained. After debinding, sintering is performed to obtain final alloy products with higher density and attractive mechanical properties.

Sintering is a process that compacts materials and forms a solid mass by heat or pressure without reaching the melting point of the targeted alloys. The density of sintered materials increases from the initial stage to the final stage, generally increasing more than 92% of the integrated density (Fang, 2010). Figure 2.6 shows density change during sintering.

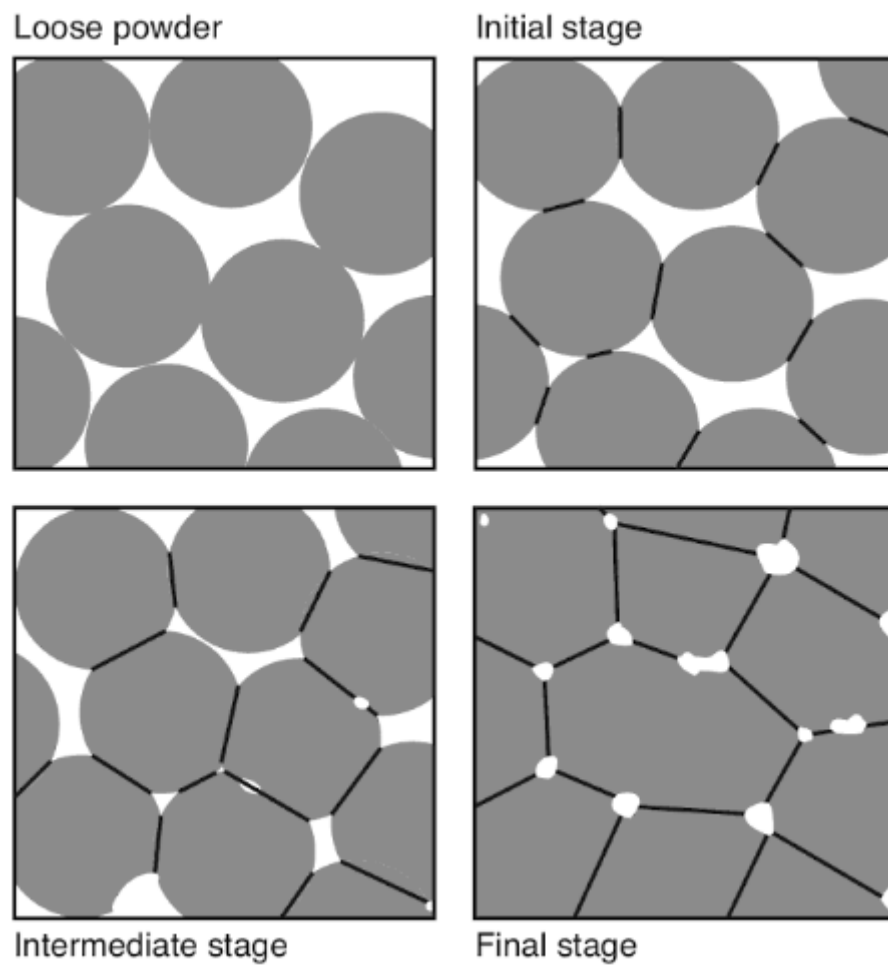


Figure 2.6. Density change in three stages of sintering (Fang, 2010).

A process to consolidate powders is called sintering which has been carried out for more than 6000 years in the manufacturing of bricks and ceramic products and in the

consolidation of precious metals in pre-Columbian South American (Burke, 1984). A decrease in the grain boundary and surface energies leads to the thermal activation of mass transport processes. This is because the consolidation can be achieved without melting. High temperature is required to obtain a high density with corresponding strength and thermal activation, which is related to the melting point of the material. To reduce cost and increase efficiency, efforts have been directed towards different types of activation to attain a high density in shorter time and at lower temperatures. Pulsed electric current sintering, spark plasma sintering, field-activated sintering and current-activated densification are the major forms that have been used in recent years. Sintering with assistance of field activation has increased dramatically, which also plays an important role in applied and fundamental levels (Munir, Quach, & Ohyanagi, 2011).

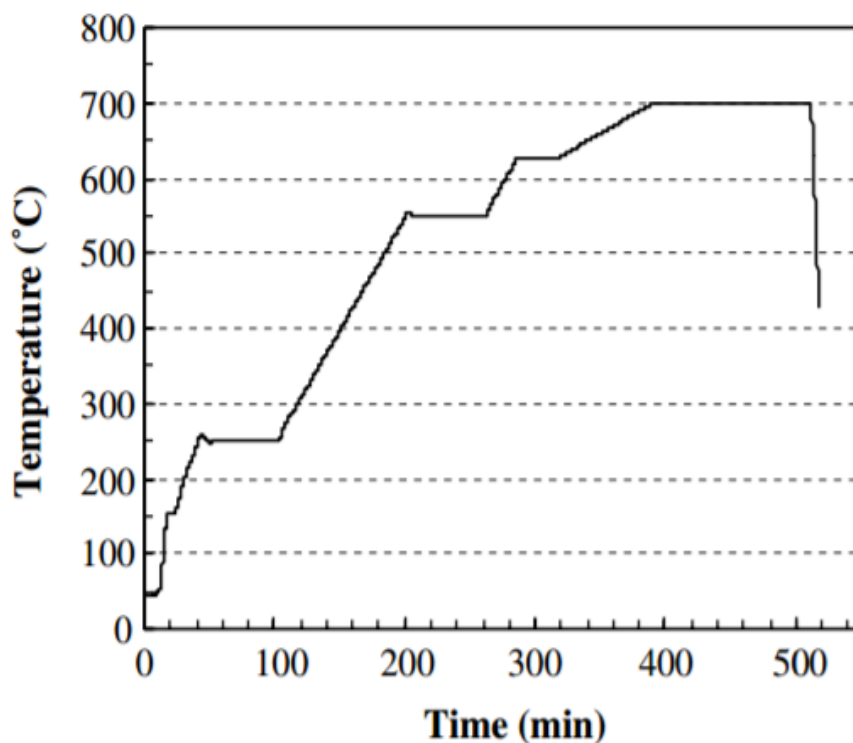


Figure 2.7. Thermal profile of binders (K.-H. Lin et al., 2007).

According to thermal profile, which can be identified by thermal gravimetric analysis, 3D green part undergoes a debinding stage and a sintering stage. The debinding stage is a period of burnout of relevant polymers. A similar reference thermal profile is shown in figure 2.7. The debinding stage comprised heating at 5 °C/min to 250 °C, holding for 60 min for burnout of the first polymer (paraffin wax) and then ramping up at 3 °C/min to 500 °C and holding for 60 min for the pyrolysis of another polymer (poly(butyl methacrylate)) (K.-H. Lin, Peng, & Lin, 2007).

By using this modified sintering technique, a 3D structural alloy component can be sintered directly from raw materials to produce components that maintains their shape and dimension. Only certain alloy compositions can be fabricated into 3D components through traditional sintering processes, but all alloy compositions can be sintered with this modified method.

2.4.1 Thermal debinding

Binders can be used to form green parts and adjust densification through wetting, spreading and forming agglomerates during sintering (Suh, Shin, & Bae, 2015). The content of added binder can also affect the crystallization and magnetic properties of magnetic materials (Y. Liu, Yi, Shao, & Shao, 2013). Normally, organic and inorganic materials can both be used as binders. However, organic binders receive more attention

that inorganic binders because they can be completely removed during sintering. Meanwhile, addition of organic binder plays a vital role in enhancement of mechanical strength between particles. Furthermore, binder content can also affect the physical properties of the resulting products (Y. Liu et al., 2013).

With addition of organic binder, it is easier to form the target shape for a given material. Meanwhile, sintered samples have high density since organic binder provides high driving force (Shahzad, Deckers, Kruth, & Vleugels, 2013). In debinding process, the strength of component decreases in the initial stage since the loss of binder which is caused by heat. The following sintering stage can densify the component and enhance the mechanical properties. However, organic binders for shape formation normally have low decomposition temperature. As temperature increases during sintering, binders are consumed into exhaust gas and the shape of sample is deformed. The uncontrollable thermal runaway may cause unexpected deformation the sample shape (Y.-S. Park, Oh, & Lee, 2014), therefore, it is important to investigate thermal profile of green parts to enhance the stability of samples.

2.4.2 Thermal sintering

Small ceramic components with complicated shapes can be produced by the powder injection molding method with high dimensional precision. During sintering, deformation caused by non-uniform shrinkage affects the dimension precision of components. It is very common to see differential sintering since it may be caused by

agglomeration, and the differences in temperature gradients near the surface during sintering. However, the deformation in some sintered ceramic materials reveals a correlation between powders and alignment (Krug, Evans, & Ter Maat, 2002).

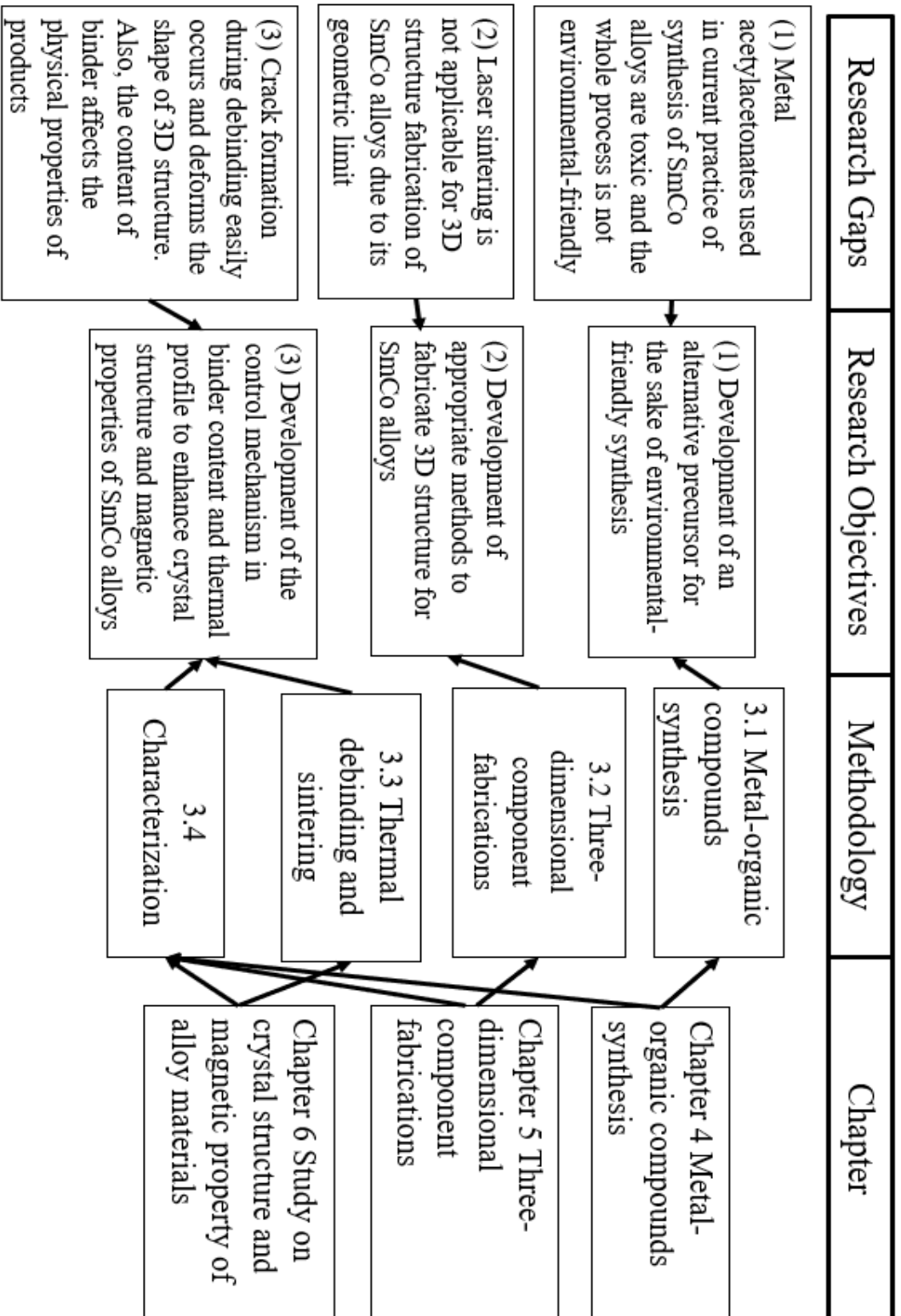
Particles with an anisotropic shape, such as fibers, whiskers or platelet particles, that cause a preferred orientation, were studied. A preferred fiber orientation, for example, can be achieved with ceramic materials and metal matrix materials by using injection molding in flow-induced fiber alignment with double-gated and open-ended modulated pressure (Tao Zhang, Evans, & Bevis, 1996). An orientated layer in the same direction as the flow in the sub-skin area can be produced by conventional injection molding, which is comparable to polymer composite molding. The oriented area is increased by increasing the alternating melting flow during solidification. The fibers are perpendicular to the flow direction in the center.

The microstructure of alumina powder and the correlations between it and sintering processes were studied by Roosen and Bowen (Roosen & Bowen, 1988). They revealed that pore size distribution is strongly influenced by the initial and intermediate stages of sintering. The effects on the variation of the initial structure were also observed in the sintered microstructure. Their works demonstrated that different forming techniques lead to different sintered microstructures and densities despite using the same starting powders and sintering procedure

Zhang et al. (T Zhang, Blackburn, & Bridgwater, 1997) used different alumina powders to study the effects of differential shrinkage and particle morphology during sintering. Gate position, mold geometry and particle shape were the major factors in the shrinkage of ceramic materials using the injection molding method. They speculated that the particle orientation was caused during mold filling. The plate-shape alumina particles tended to be perpendicular to the mold wall in the molding center and aligned parallel to the mold wall at the surface of the fiber-composites. The alumina particles reduced the shrinkage compared to normal shrinkage.

Uematsu et al. (Uematsu et al., 1995) explored a different direction and used nearly identically shaped alumina powders. Orientation effects were not present with conventional characterization methods. Orientation effects can be easily measured by immersing the sample in a liquid and using an optical method that relies on the refractive index. This is because the slightly extended axes of particles align parallel to the flow direction, although the alumina powder only deviates slightly from spherical symmetry. In their work, particle alignment caused anisotropic shrinkage during sintering. Furthermore, their work involved the design of powders in injection molding.

2.5 Relationship between research gaps, objectives, methodologies and results and discussions



Chapter 3 Research Methodology

This chapter illustrates the research method and work flow for the fabrication of SmCo alloys with 3D structures. It consists of four sections. The first section introduces the synthesis of metal ascorbates in an environmental-friendly method, which can fully fulfill objective 1 of the research. In section 3.1, the selection criteria for starting materials and coordinated ligands for the synthesis of precursors for SmCo alloys are explained. After the synthesis of metal ascorbates as metal-organic precursors, the 3D structure for the materials is constructed before binding and sintering. In the second section (3.2), many fabrication processes for 3D structures, including the use of laser systems, inkjet printing and laser sintering, are discussed. Metals, metal-organic compounds and alloys are fabricated into a 3D structure by using the fabrication processes. In the third section (3.3), 3D structural parts using the synthesized metal ascorbates and binder are debinded and sintered into SmCo alloys by thermal debinding and sintering. In the last section (3.4), the characterization techniques for the synthesized materials, fabricated 3D structure and final products are illustrated. The characterization techniques for the synthesized materials, including fourier transform infrared spectroscopy (FTIR), inductively coupled plasma-optical emission spectrometry (ICP-OES) and thermogravimetric analysis (TGA), demonstrate the success of the synthesized materials and also provide the required information for the debinding and sintering process. Meanwhile, the characterization

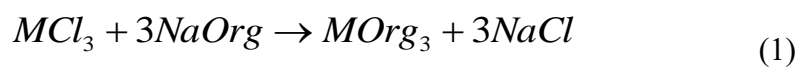
techniques for the fabricated 3D structure, including scanning electron microscopy (SEM), atomic force microscopy (AFM) and surface profiler, show the effectiveness for the fabrication of 3D structure of metals, metal-organic compounds and alloys. The characterization techniques for final products, including x-ray crystallography (XRD), magnetic force microscopy (MFM) and vibrating sample magnetometer (VSM), investigate the crystallization and magnetic properties of SmCo alloys and the effect of the binder and thermal profile on the crystal structure and magnetic properties of SmCo alloys.

3.1 Metal-organic compounds synthesis

Because of environmental protection and sustainable development considerations, coordinated organic materials should be non-hazardous and the waste and byproducts are green and recyclable. The electron configuration of REMs and TM resulted in typical coordination characterization, requiring coordination materials with strong chelating ability. It was demonstrated that oxygen bonds and nitrogen bonds have a strong chelating ability to coordinate with REMs and TMs. The carboxyl functional group (-COOH) and amine functional group (-NH₂) are among the best organic coordinated ligands in REM coordination materials and TM coordination materials. Accordingly, organic materials with these functional groups are ideal choices as coordination ligands in the synthesis of REM organic materials and TM organic

materials. In the debinding stage, carbon, oxygen, hydrogen and other inorganic elements are expected to be degassed. Therefore, oxygen is the better choice comparing with nitrogen since oxygen easily reacts with carbon and generates carbon dioxide. With this concern, the carboxyl function group is the better choice. With conjugation of debinding process and the consideration of non-hazardous synthesis, simple organic materials with carboxyl function groups are preferred. These organic materials include ascorbic acid ($C_6H_8O_6$), salicylic acid ($C_7H_6O_3$), succinic acid ($C_4H_6O_4$), etc. Ascorbic acid, also known as vitamin C, is one of the most common organic materials. Because of its simplicity and ordinariness, ascorbic acid is selected to be the organic ligand.

Samarium and cobalt are selected as the REM and TM for research, because samarium-cobalt alloy is a widely used magnetic material with extraordinary coercivity and can be applied in various fields. The samarium organic precursor and cobalt organic precursor should be prepared for the synthesis of the samarium-cobalt alloy. An aqueous system is used in precursor preparation to fulfill the requirement for non-hazardous synthesis. Generally, the aqueous system is a water, water-ethanol or water-methanol system. As water soluble materials, samarium chloride and cobalt chloride were selected as raw materials to prepare the samarium organic precursor and cobalt organic precursor. For metal-organic precursor preparation, the basic reaction is as follows:



where M denotes a metal and Org denotes the organic ligand. The formula assumes that the metal is positive trivalent.

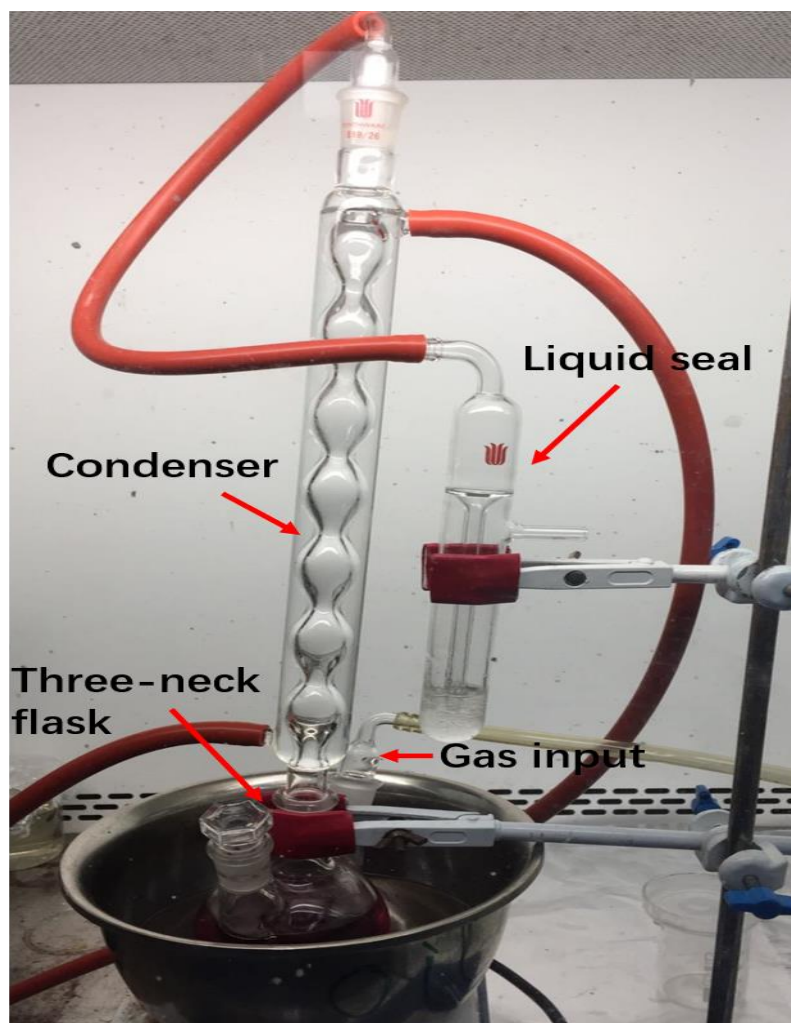


Figure 3.1. Experiment setup for precursor synthesis.

Some fundamental synthesis apparatuses are used for metal-organic precursor synthesis, including three-neck flask, condenser and liquid seal. The setup for chemical

reaction is shown in figure 3.1. The three-neck flask is the main reaction container, covered by silicon oil to maintain uniform heating. A hot plate is placed underneath a stainless-steel container with silicon oil to provide the appropriate temperature for synthesis. The center neck is fixed by the condenser to prevent liquid evaporation. Meanwhile, protection gas, like nitrogen gas, is input through the gas input connecting with right neck. The top of the condenser is connected to a liquid seal to prevent gas explosion and reflux. The left neck is blocked for gas protection in the system. A centrifuge machine and oven are used to purify and dry the samples respectively.

3.2 Three-dimensional components fabrications

3.2.1 Inkjet printing for metal-organic compounds

Inkjet printing is one of the most important AM methods in fabricating 3D components by using soluble material ink due to its simplicity, convenience and easy-controlling. Synthesized metal-organic materials are dissolved in an aqueous system or an organic solvent to produce printing ink. The 3D components with functional materials are fabricated by inkjet printing technology on a particular substrate. The heated substrate accelerates the solvent evaporation speed. The required materials accumulate with multi-printing and thereby form ideal 3D components.

An inkjet printing system is shown in figure 3.2. A standard micro-dispenser system was set to control the printing parameters, including printing period, delay and drive voltage switch. An inkjet printer was fixed to a tailor-made X-Y table with a moving

controller, which was controlled by two motors. The inkjet printed patterns were drawn by AutoCAD. The speed of pattern writing can be adjusted by the moving table. A hot plate was laid underneath the printer for substrate heating.

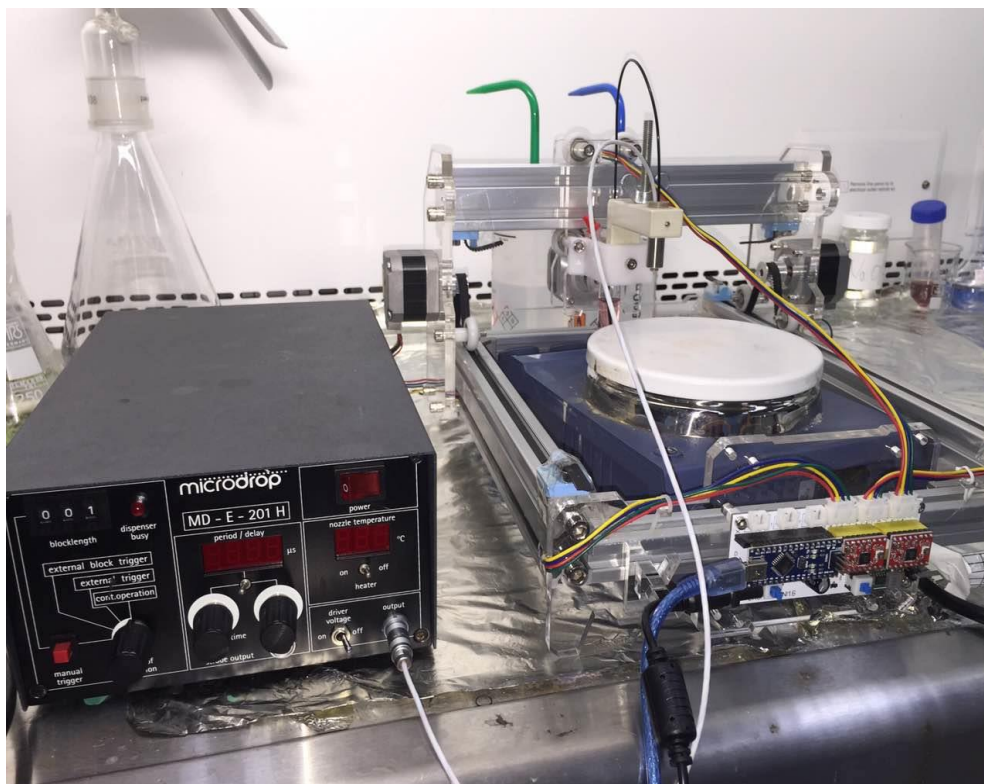


Figure 3.2. Image of a tailor-made inkjet printing system.

3.2.2 Modified laser writing system for metal reduction

Laser-assisted additive manufacturing is another popular method to fabricate 3D components. A laser can provide a large amount of energy instantaneously to melt, sinter or be treated on materials for 3D structure fabricating.

Laser writing system is constructed as shown in figure 3.3 (W. K. C. Yung et al., 2016). The laser with a 405 nm wavelength is fixed on the tailor-made X-Y table with a moving controller. The power of laser is 0.4 W, and the laser beam size is measured as 200 μm . The laser treated circuit patterns were designed by AutoCAD.

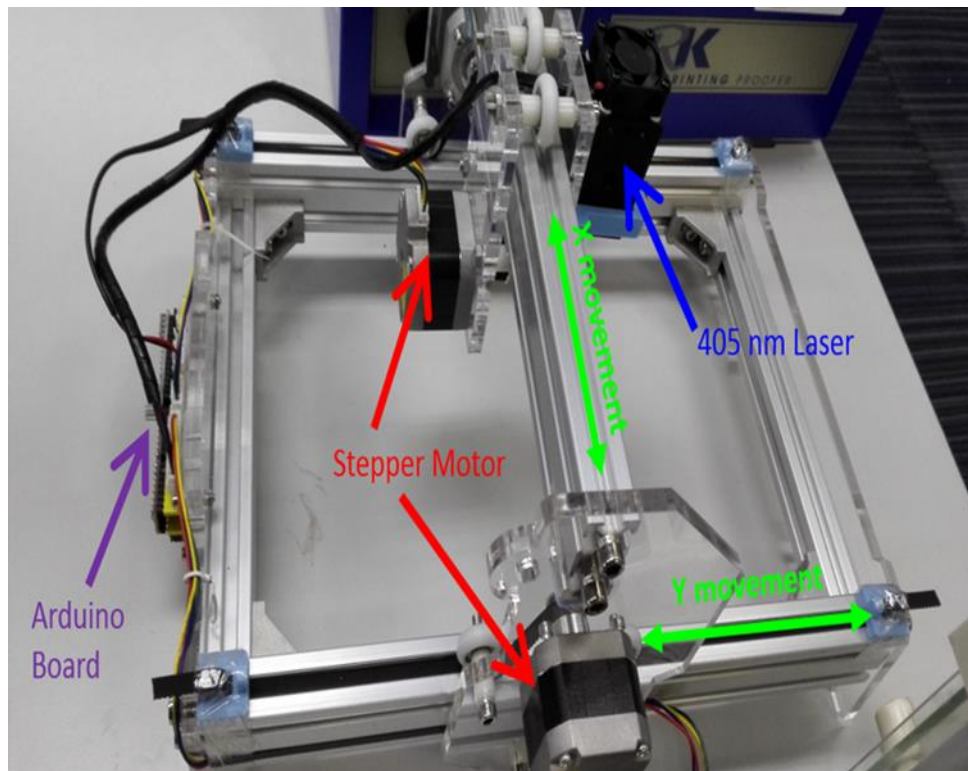


Figure 3.3. Image of a tailor-made laser writing system.

(1) Laser treatment on copper carbonate hydroxide

Thermoplastic materials applied for 3D printing have received wide attentions recently. However, it is a challenge to coat metals on the surface of 3D objects without using expensive and specialized tools. Hence, a novel paint material consisting of

malachite and thermoplastic materials is developed. It can be directly transferred by laser into the copper on the target surface. Some common polymers, including ABS and Poly(methyl methacrylate) (PMMA), were selected as the transformer. These polymers were dissolved by organic solvent and mixed with the required materials. Mixed gel type materials were spread on particular substrates layer by layer.

(2) Laser induced forwards transfer on copper oxide

3D printing methods were developed to fabricate the prototype rapidly based on conceptual design. However, the existing technique for metallic materials is still expensive and time-consuming. Therefore, it is necessary to develop a novel platform to fabricate metallic materials by using photochemical reaction and LIFT at low cost.

(3) Laser reduction on cobalt based organic compound

Modification in the structure and properties of materials by laser reduction has aroused comprehensive attention recently. However, they are still rarely applied by researchers on the laser reduction of MOFs materials. ZIF, as one of the important subclass materials of MOFs, is selected as the initial material. In this study, the zeolite imidazole framework-67 (ZIF-67) is reduced by laser to obtain cobalt nanoparticles which are embedded into the porous carbon matrix.

The oil adsorption capacities of the samples were measured and calculated as

$$Ca \text{ (g/g)} = (Wa - Wb) / Wc \quad (1)$$

Where W_a is the weight of the dish of water with oil in the initial state, W_b is the weight of the dish of water with oil after oil absorption and particles removal, and W_c is the mass of particles.

3.2.3 Laser sintering for SmCo alloy

Samarium-cobalt magnets have attracted significant attention as promising ferromagnetic materials. However, fabrication of these materials in flexible shapes still limits its development due to the high thermal sensitivity and processing constraints, easy oxidation and phase distortion of magnetic materials. Herein, the 3D part of the SmCo₅ materials is fabricated by laser sintering.

For laser sintering, an Optomec LENS MR-7 laser machine with 1070-nm laser under argon gas protection was used, as shown in figure 3.4. The purchased SmCo₅ powders (Alfa, Sm 33 wt%) were measured in accurate amounts and uniformly spread on the stainless-steel substrate by applying compression. The first layer was sintered using high power (200 W) as the sacrificial layer – it acted as the interface between the substrate and sample to enhance the combining force. At this stage, a series of parameters were studied, such as laser power, scanning speed, hatch space and laser sintering time. The laser spot size was set as 450 μm , but the effective area for the laser was measured at 350 μm width for the studied materials. This was due to the elliptical shape of the laser beam in laser sintering which lands on the sample surface; the outermost part of the laser does not have sufficient intensity to sinter the SmCo₅

materials. meanwhile, the affected area is depicted two small verge areas on two sides, this phenomenon resulted based on the nature of distribution of laser energy. The resultant verge areas were measured to be around 50 μm . In order to compensate for the loss of energy from these areas, the hatch space was reduced to 250 μm . The laser power, laser scanning speed, sintering time were studied from 100 W to 150 W, 1270 mm/min to 1778 mm/min and 1 to 3 times respectively.

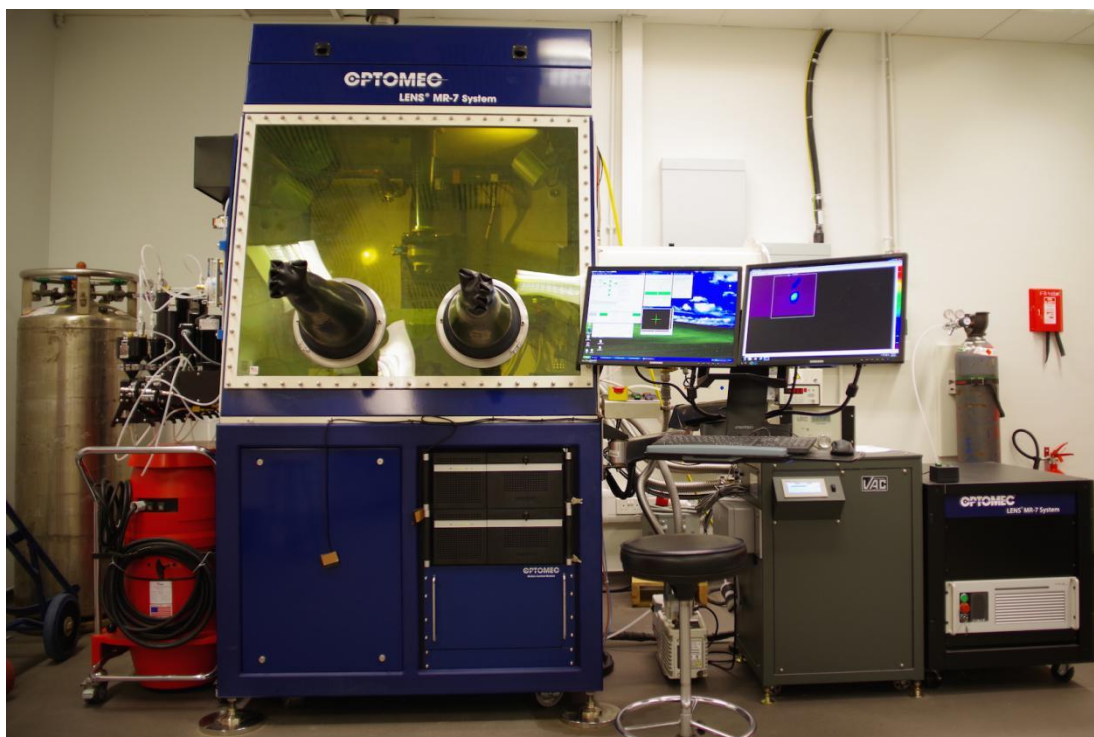


Figure 3.4. Image of laser sintering system.

3.2.4 Compression molding

Compression molding is a common molding method because of its time-saving, simplicity and cost-effectiveness. It is suitable for plastic or organic compounds which

are easier to form into the required shape. Meanwhile, this manufacturing method only requires simple equipment, which is quite convenient for research into structure fabrication. The equipment used for compression molding is a tableting machine, which is shown in figure 3.5.

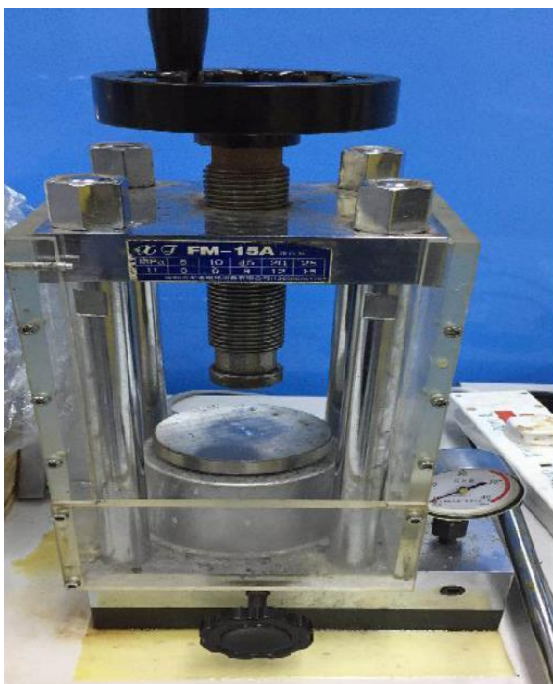


Figure 3.5. Image of tableting machine.

The viscosity and flowability of the target materials are necessarily required to reach the certain level for structure fabrication, however, owing to the nature of the target powders, binders are added to modify the viscosity and flowability for structure fabrication. Normally, some common polymers, such as Polyvinyl alcohol (PVA), are typical binders for 3D structure fabrication since these materials provide strong

wetting ability for the homogeneous formation and flexibility for tunable structure fabrication. Furthermore, consideration for non-hazardous synthesis, simple and clean polymers are applied in this project.

However, the debinding process is also an inevitable challenge for researchers since an inappropriate process may lead to crack formation and even destruction of the samples. Therefore, thermal measurements for both the target materials and binder are required for elimination of any negative impacts.

3.3 Thermal debinding and sintering

Pre-debinding products are fabricated by a 3D structure fabrication process with the addition of the binder. The organic ligands and binder should be removed during the debinding process. Therefore, the thermal profile should be performed to find the information and details for the decomposition of the materials from room temperature to high temperature until the materials are completely decomposed.

Pre-debinding materials are measured by TGA to acquire the thermal profile. Based on this thermal profile, a ladder-type heating process is designed to obtain the required alloy. The decomposition temperatures for the materials are analyzed, and the temperature holding stages are added at the decomposition temperature for the complete decomposition of the materials. Meanwhile, the heating rate near the

decomposition temperature also decreases, providing sufficient time for the decomposition of materials and avoids cracks formation.

During the debinding and sintering process, protective gas is added to maintain the sintering environment as an oxidation preventer. The 3D component fabricating technique as described earlier in the introduction section is applied here to produce 3D components for further investigation. As mentioned previously, the synthesis methods in this work only use a basic aqueous environment, such as a water-ethanol system, to prepare all the basic complexes for the next step in the 3D structure fabrication. Compressed pellets are debinded in a tube furnace with argon gas protection according to the thermal profile. Post-sintering products are fabricated using debinding, and organic ligands and binders are removed as carbon, oxygen and hydrogen with carbon dioxide and waste vapor phase.

Thermal sintering is performed after the debinding process for densification of the products and the enhancement of the crystal structure of sintered materials. During this process, protection gas is also needed to prevent the oxidation of materials. After sintering, the space and cavities in the products decrease and shrink. Therefore, the density of the products is increased.

3.4 Characterization

In this section, many characterization techniques are discussed for measuring and characterizing the synthesized materials, fabricated 3D structures and final products. These techniques contain four aspects: composition characterization, morphology characterization, thermal profile characterization and magnetic property characterization. Composition characterization techniques measure the synthesized metal ascorbates and show the effectiveness of success of the synthesis with the functional groups and metal elements concentrations of the synthesized materials. The characterization techniques are also used to measure and find the composition of the final products (SmCo alloys). After the authentication, the quality of the synthesis of metal-organic precursors, a fabrication process of 3D structure, is used to form 3D structure using metal-organic precursors. Morphology characterization techniques are used to measure the morphologies of these 3D structures for metal-organic precursors and also for final products. Debinding and sintering are necessary to inspect the quality of the final products after the 3D structure fabrication. Therefore, the thermal profile for metal-organic precursors is required to be measured in advance. In the last stage, the sintered final products are characterized by the magnetic property characterization technique in order to obtain the results for their magnetic properties.

3.4.1 Composition characterization

Composition characterizations are conducted to measure the materials' composition in the element phase, functional group phase and crystalline structure phase, including EDX, XRD, FTIR and ICP-OES.

(1) Energy dispersive x-ray analysis

EDX is applied to analyze the elementary composition for laser treated samples and sintered samples. EDX can measure the content of elements on the surface which can help to analyze the elementary composition and the ratio of laser treated samples or sintered samples. Tescan VEGA3 and LEO 1530 were used in this research.

(2) X-ray crystallography

XRD is a common technique used for phase detection of crystalline materials. It can identify atomic as well as molecular structures, and measures angles and intensities of diffracted beams caused by crystalline atoms. In the work of this research, XRD (Rigaku SmartLab) was used to measure the crystalline structure of the laser treated sample and sintered sample, identifying the crystal structure.

(3) Fourier transform infrared spectroscopy

FTIR is used as the leading detector equipment to measure the function groups of materials. FTIR can obtain the infrared spectrum of photoconductivity, emission, absorption or Raman scattering of organic mixtures, and simultaneously collects a

wide spectral range data with high spectral resolution. In the research, FTIR (BRUKER) is used to measure function groups of synthesized metal-organic compounds and analyzes their composition.

(4) Inductively coupled plasma-optical emission spectrometry

ICP-OES is an analytical technique used for elemental determination. It has superior detection capabilities, particularly for the rare-earth elements. Due to the nature of rare-earth metals, REMs are easily oxidized and remain stable at this state. When materials are dissolved into a solution to form the liquid phase, REMs become in an ionic state, and the issue of easy oxidized can be solved. Compared to other detecting processes, such as EDX, ICP can detect the content of metals entirely rather than only the surface as in EDX. Therefore, ICP is particularly good for detecting rare-earth elements.

In the work of my research, ICP was used to identify the synthesized metal-organic compounds.

3.4.2 Morphology characterization

SEM and optical microscopy were used to identify the morphology of the printing surface, and thereby analyzed the optimum printing parameters and 3D structure fabrication situation. Besides, AFM and SP are used to characterize the surface with vertical difference. 3D profiles can be obtained using AFM and SP, and no pretreatment is needed for sample preparation.

(1) Optical microscopy

Optical microscopy is used to measure and characterize the morphology of laser treated samples, inkjet printing samples and sintered samples. Inject printed patterns, surface change and cracks generation can be observed by optical microscope.

(2) Scanning electron microscopy

SEM is a type of electron microscope which can scan samples surfaces to obtain images by a focused beam of electrons. It is normally used to measure the surface morphology of materials. In this research, SEM (Tescan VEGA3 and LEO 1530) is used to measure the surface morphology of laser treated samples, inkjet printing samples and sintered samples.

(3) Atomic force microscope

AFM is a type of scanning probe microscopy with very high resolution to measure the samples' surface topography and magnetic structure. In this research, AFM (Bruker NanoScope 8) is used to measure the topography of the inkjet printed samples.

(4) Surface profiler

A surface profiler is a surface profile measurement machine for surface profile and irregularity measurement. SP (Zygo Nexview) was used to obtain the 3D morphology of the inkjet printed samples.

3.4.3 Magnetic property characterization

MFM and VSM were used to analyze the magnetic properties of samples.

(1) Magnetic force microscopy

MFM (Bruker NanoScope 8) was applied to measure the magnetic properties and magnetic structure of surface of inkjet printed samples.

(2) Vibrating sample magnetometer

VSM (LAKESHORE) was applied to measure magnetic hysteresis loop of laser treated sample, inkjet printed samples and sintered samples.

3.4.4 Thermal profile characterization

TGA is a method of thermal analysis. Thermal profile data for 3D green-component materials collected from TGA are used as a guideline in designing sintering processes. The physical and chemical reactions of materials can be measured by TGA as the temperature or time increases. Besides, it can provide information about the physical change of materials, such as second-order phase transitions, including sublimation, desorption, absorption and vaporization. These are the key parameters in thermal profiling.

Mettler Toledo TGA/DSC3+ was applied for TGA measurement, and the protection gas was nitrogen.

Chapter 4 Metal-organic compound synthesis

4.1 Introductory remarks

Metal-organic compounds are materials consisting of metal ions and coordinated organic ligands that exhibit versatile functionality and controllable structures. The diversity of metals and coordinated organic ligands provides tremendous potential for numerous material combinations. TMs and REMs, which play important roles as metal elements, are the foremost candidates for the formation of metal-organic compounds. TMs contain unfilled d orbital, which endows them with unique physical and chemical properties so that they have potential applications in various fields. The nature of TMs also makes them exhibit a strong ability to form metal-organic compounds with the coordinated organic materials. The coordination chemistry of TMs has aroused comprehensive attention since synthesized TM organic compounds exhibit outstanding performance and can be applied in various fields (Bellemin-Laponnaz & Dagorne, 2014), such as catalysis, gas storage, sensing and drug delivery (H. B. Wu, Xia, Yu, Yu, & Lou, 2015). In contrast, studies of REM metal-organic compounds began later than those of TMs because of the unique nature of REMs for coordination and oxidation. Their strong chemical character and large ion radius results in strong chelating ability in coordination with relevant organic materials. Carboxylic acid, a type of organic material, contains one or more carboxyl groups (-COOH), and is

considered as an outstanding candidate for coordinated organic materials during the formation of metal-organic compounds due to its strong chelating ability. The strong chelating ability of these organic materials can easily chelate metals, especially REMs, and form metal-organic compounds with strong stability.

Applying metal-organic compounds to synthesize alloys is considered a wise option since the addition of organic materials can strongly enhance the stability of the structure and mechanical properties. Meanwhile, the exhaust gas or waste generated during the debinding and sintering process are green and clean, since their formation elements are carbon, oxygen and hydrogen. Making use of these merits, alloy materials can be prepared by using metal-organic compounds which can maintain the required shape under appropriate debinding and sintering process.

REMs and TMs are well known due to their multi-functional and unique properties, especially the magnetic field. As one of the REM and TM alloys with high performance in magnetic properties, samarium-cobalt alloys have attracted significant attention in application on magnetic recording media, micro-electro-mechanical systems and the aerospace field because of large magneto-crystalline anisotropy ($K_u=2\times 10^8$ erg/cm³) and high Curie temperature (Ma et al., 2016; Ma, Zhang, & Jiang, 2015; Qiu et al., 2018). With the ever-growing demands for permanent magnets components with 3D structure, various technologies were studied to overcome the manufacturing restrictions (Caputo & Solomon, 2017). Laser sintering is an outstanding method for fabricating alloy materials with 3D structures. However,

expensive but type-limited alloy powders, as raw materials, and the requirement for certain shape, size and dimension of particles still restricts its developments (DD Gu et al., 2012; Shirazi et al., 2015; Sing et al., 2017). Meanwhile, research in laser sintering of ferromagnetic materials is still rare due to the nature of the thermal sensitivity and the easy oxidation of magnetic materials (Matsushita et al., 2010; Zou et al., 2018).

Environmental concerns and energy resource sustainability was raised massive consideration in materials synthesis and in research with limited waste and byproducts. Non-hazardous synthesis, aiming at the reduction of byproducts and hazardous waste, was explored recently in the synthesis of metal-organic precursors (Cioc, Ruijter, & Orru, 2014; R. Sharma, Sharma, Dutta, Zboril, & Gawande, 2015). Owing to the strong Lewis acid character of REMs, using organic materials with strong chelating ability to form RE-complex is economically and environmentally sustainable (Y. Hu et al., 2017). Ascorbic acid has strong chelating ability and it is common and non-hazardous. It can be used to chelate metal oxides or metal compounds to form metal ascorbate (X. Hou et al., 2016; Y.-T. Lin et al., 2016). Meanwhile, during the synthesis of metal ascorbate, the generated byproduct is only sodium chloride if the starting materials is metal chloride, which is a common and green metal salt. Furthermore, during the debinding process, the generated exhaust gases are only CO₂ and H₂O.

In the present study, samarium and cobalt were selected as the metal elements to form a metal-organic precursor with ascorbic acid for the preparation of samarium-

cobalt alloys with 3D structures. Owing to its strong chelating ability and green and simple nature, ascorbic acid was selected as the coordinated organic material. Samarium ascorbate and cobalt ascorbate were synthesized in an aqueous system under a nitrogen gas atmosphere. FTIR and ICP-OES were used to identify the compositions of synthesized metal-organic compounds. XRD was used to determine the crystal structures of the synthesized metal-organic compounds. TGA was used to obtain the thermal profiles of the synthesized materials.

In this chapter, the synthesis of metal-organic compounds and their effectiveness are discussed; these compounds provide provides the primary materials for 3D structure fabrication and alloy sintering that is discussed in next two chapters. The motivation of this chapter is to describe the non-hazardous and environmentally friendly materials that were selected to form metal-organic compounds for alloy synthesis.

4.2 Experiments

4.2.1 Preparation of cobalt ascorbate

The solving solution was made up by 80% v/v methanol and 20% v/v distilled water. Cobalt chloride (10 mmole) and ascorbic acid (20 mmole) were measured and dissolved into 30 mL methanol-water solution with moderate stirring respectively.

These two solutions were then mixed. Sodium hydroxide solution (0.1 mole/L) was added drop by drop into the mixture to adjust the PH value to 8. The color changed from light red into light purple. Nitrogen gas was ventilated continuously for half an hour to get rid of any oxygen before the reaction. The mixture was then refluxed at 60 °C for 6 hours with continuous stirring using a magnetic stirrer. A purple precipitate was collected and washed by methanol-water solution with centrifugation at 4000 rpm in 20 minutes. Samples were dried at 30 °C.

4.2.2 Preparation of samarium ascorbate

The synthesis procedure for samarium ascorbate is similar to that of cobalt ascorbate, and the molar ratio of samarium chloride and ascorbic acid changed to 1:3 since the ion charge of samarium is three instead of two as in the case of cobalt. Methanol-water solution was prepared as reaction solvent and purification solution. 10 mmole samarium chloride and 30 mmole ascorbic acid were dissolved into the methanol-water solution respectively and then mixed. The mixture solution was adjusted PH value to 8 by 0.1 mole/L sodium hydroxide solution. The mixture was heated at 60 °C for 6 hours. The precipitate was then washed and dried for further steps.

4.2.3 Preparation of mixture of samarium ascorbate and cobalt ascorbate

The synthesis procedure is similar to what in the previous illustration. The elemental ratio of samarium and cobalt was set as 1:5, because the ratio of the final product, samarium-cobalt magnet, is in the ratio of 1:5. The amount of ascorbic acid should be prepared according to the ion charges of the samarium and cobalt. Therefore, 10 mmole samarium chloride, 50 mmole cobalt chloride and 130 mmole ascorbic acid were measured and dissolved into methanol-water solution respectively. These solutions were then mixed and adjusted to a PH value of 8 by using 0.1 mole/L sodium hydroxide solution. The mixture solution was then heated at 60 °C with stirring for 6 hours. The precipitate was then washed out and dried as a metal-organic compound precursor for alloy materials synthesis.

4.2.4 Characterizations

(1) Fourier transform infrared spectroscopy characterization

The composition characterization of the functional group of the synthesized metal-organic compounds was identified by Fourier transform infrared spectroscopy (Perkin Elmer Paragon 1000 PC). Synthesized samples, including cobalt ascorbate, samarium ascorbate and the mixture of cobalt ascorbate and samarium ascorbate, were dried at 60 °C for 1 hour to remove moisture before measurement. Potassium bromide (KBr) was used in addition to form the pellet to be measured, since its refractive index

is very low and it does not contain bands in the mid-IR region of the spectrum. 20mg synthesized materials were measured and mixed with 1000mg KBr powders for dilution. The mixture was then ground uniformly into micro-size and compressed in a cylindrical mold with 5 tonnes of pressure for 2 minutes to form a thin film (pellet) for FTIR measurement. This pellet was put into a fixture and measured in surroundings without light. The scanning range was from 400 cm^{-1} to 4000 cm^{-1} , and the scanning mode was transmittance.

(2) Inductively coupled plasma-optical emission spectrometry characterization

An Agilent Technologies 700 ICP-OES was used for quantitative determination of the ion concentration. A blank solution, standard solution and test solution of synthesized materials were prepared before testing. Standard solutions with different ion concentrations were prepared for the instrument's calibration curve. Since hydrochloric acid was used to dissolve the synthesized materials, metal chloride was used to prepare the standard solution. Therefore, cobalt chloride and samarium chloride were used to prepare the standard solution for ICP measurement. A low concentration of hydrochloric acid solution with 1% nitric acid was prepared as a blank solution for test adjustment. Relative metal ascorbates were used to prepare the test solution for ICP respectively with addition of hydrochloric acid and 1% nitric acid. 228.615, 230.786, 238.892 analyte wavelengths were set to characterize the cobalt element, and 356.827, 359.259 and 360.949 analyte wavelengths were set for the samarium element.

In the ICP test for samarium ascorbate, a standard solution and test solution were prepared, as below. For standard solution preparation, 5 ppm, 10 ppm and 15 ppm metal chloride solution were prepared respectively, and hydrochloric acid and 1% nitric acid were added to ensure the complete dissolution. 0.606mg, 1.213mg and 1.820mg samarium chloride were measured and dissolved into 50 ml DI water to prepare 5 ppm 10 ppm and 15 ppm standard solutions respectively. Similarly, for the test solution preparation, 0.225mg, 0.674mg and 1.123mg samarium ascorbate were used to prepare 1 ppm, 3 ppm and 5 ppm test solution respectively.

In the ICP test for samarium ascorbate, the standard solution and test solution were prepared as shown below. For standard solution preparation, 5 ppm, 10 ppm and 15 ppm metal chloride solutions were prepared respectively, and hydrochloric acid and 1% nitric acid were added to ensure the complete dissolution. 1.001mg, 2.020mg and 3.030mg cobalt chloride were measured and dissolved into 50 ml DI water to prepare 5 ppm 10 ppm and 15 ppm standard solutions respectively. Similarly, for test solution preparation, 0.347mg, 1.041mg and 1.736mg cobalt ascorbate were used to prepare 1 ppm, 3 ppm and 5 ppm test solutions respectively.

In the ICP test for the mixture of samarium ascorbate and cobalt ascorbate, the standard solution and test solution were prepared as shown below. For standard solution preparation, 5 ppm, 10 ppm and 15 ppm metal chloride solution were prepared respectively, and hydrochloric acid and 1% nitric acid were added to ensure complete dissolution. 0.606mg, 1.213mg and 1.820mg samarium chloride and 1.188mg,

2.377mg and 3.567mg cobalt chloride (Sm:Co=1:1.9596) were measured and dissolved into 50 ml DI water to prepare 5 ppm 10 ppm and 15 ppm standard solutions respectively. Similarly, for test solution preparation, 0.225mg, 0.674mg and 1.123mg samarium ascorbate and 0.441mg, 1.321mg and 2.201mg cobalt ascorbate (Sm:Co=1:1.9596) were used to prepare 1 ppm, 3 ppm and 5 ppm test solutions respectively.

In this research, the ratio of Sm and Co was evaluated by ICP-OES. The content of the intake of samarium and cobalt determines the ratio of Sm and Co in SmCo alloy during the synthesis process.

(3) Thermogravimetric analysis characterization

Decomposition of the synthesized metal-organic precursors was characterized using thermal gravimetric analysis (Mettler Toledo TGA/DSC3+). The thermal profile of the synthesized cobalt ascorbate, samarium ascorbate and the mixture of samarium ascorbate and cobalt ascorbate were obtained respectively.

In test of cobalt ascorbate, 5g cobalt ascorbate was measured and loaded into an alumina crucible for testing. A standard sample was used to do the alignment. TGA was performed in the range from 25 °C to 700 °C, with a heating rate at 10 °C/min in N₂ gas atmosphere with 20 ml/min flow rate.

Similarly, the same amount (5g) of samarium ascorbate or the mixture of samarium ascorbate and cobalt ascorbate were measured respectively for the TGA test.

The temperature range in TGA was also from 25 °C to 700 °C and the heating rate was 10 °C/min. The TGA tests are performed under N₂ gas with a 20 ml/min flow rate.

(4) X-ray diffraction characterization

X-ray diffraction was used to measure the crystal structure of the synthesized cobalt ascorbate, samarium ascorbate and the mixture of samarium ascorbate and cobalt ascorbate. For the XRD measurement of cobalt ascorbate, 500mg cobalt ascorbate was put in the sample container, and a glass slide was used to flatten the surface of samples. Samples were then put into the chamber to do XRD measurement. The scanning range was from 20° to 80°, and the scanning speed was 0.1°/min. For the XRD measurement of samarium ascorbate and the mixture of samarium ascorbate and cobalt ascorbate, the same amount of samples was measured and put in the sample container with flattening using a glass slide. The scanning range and scanning speed were also from 20° to 80° and 0.1°/min respectively.

4.3 Results and discussions

Synthesized metal-organic compounds are shown in figure 4.1. Figure 4.1 a, b show synthesized cobalt ascorbate and samarium ascorbate respectively. They exhibited deep red and light-yellow color respectively, corresponding to those in the literature (Obaleye & Orjiekwe, 1992; Yin & Lu, 1998). Figure 4.1 c shows the mixture

of cobalt ascorbate and samarium ascorbate. The mixture powder is shown dark red in color.

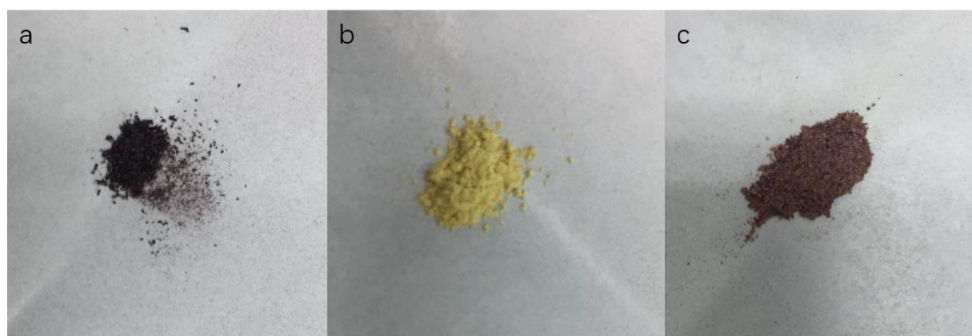


Figure 4.1. Synthesized metal-organic compounds. (a) cobalt ascorbate, (b) samarium ascorbate, (c) mixture of cobalt ascorbate and samarium ascorbate.

4.3.1 Effectiveness for synthesis of metal ascorbates

(1) Functional groups detection for synthesized materials

The effectiveness of the synthesis of metal ascorbate was confirmed by comparing the FTIR spectra of ascorbic acid and the synthesized metal ascorbates. It was also used to identify the functional group of ascorbic acid and synthesized materials, as shown in figure 4.2. A typical FTIR spectrum of ascorbic acid is shown in the figure. Four weak absorption bands obtained in the range from 3527 cm^{-1} to 3221 cm^{-1} corresponded to the different hydroxyl groups, which showed the moisture in the ascorbic acid. Another weak absorption peak at 3035 cm^{-1} presented the C-H stretching band. The strong absorptions at 1755 cm^{-1} and at 1672 cm^{-1} are attributed

to the C=O stretching of the five-membered lactone ring and the C=C stretching vibrations respectively. The absorption at 1322 cm^{-1} , 1118 cm^{-1} and 1024 cm^{-1} corresponded to the C-H bending band (wagging), the C-O-C stretching band, and the C-O-H bending band respectively. The absorption at 757 cm^{-1} was related to the O-H out-of-plane deformation band (Panicker, Varghese, & Philip, 2006). The FTIR spectra of the synthesized cobalt ascorbate and samarium ascorbate exhibited similar results, as shown in figure 4.2. In the range from 3600 cm^{-1} to 3200 cm^{-1} , the absorption bands for the hydroxyl groups for synthesized materials showed a wide peak after synthesis. Meanwhile, the stretching vibrations of the C-H band and C=O band at 3035 cm^{-1} and 1755 cm^{-1} disappeared after synthesis as well (Farias et al., 2018; Sreeja, Jayaprabha, & Joy, 2015). In contrast, the peaks for the C-H bending band, C-O-C stretching band and C-O-H bending band were observed clearly in the spectra for the synthesized materials. Since the replacement of the cobalt or samarium element during the synthesis process, the absorption band for the O-H deformation band was replaced by M-O band (M means metal). The M-O bands of synthesized cobalt ascorbate and samarium ascorbate were shown at around 490 cm^{-1} , which were consistent in the result in the paper published previously (Patel, Patel, Dholariya, Patel, & Patel, 2012).

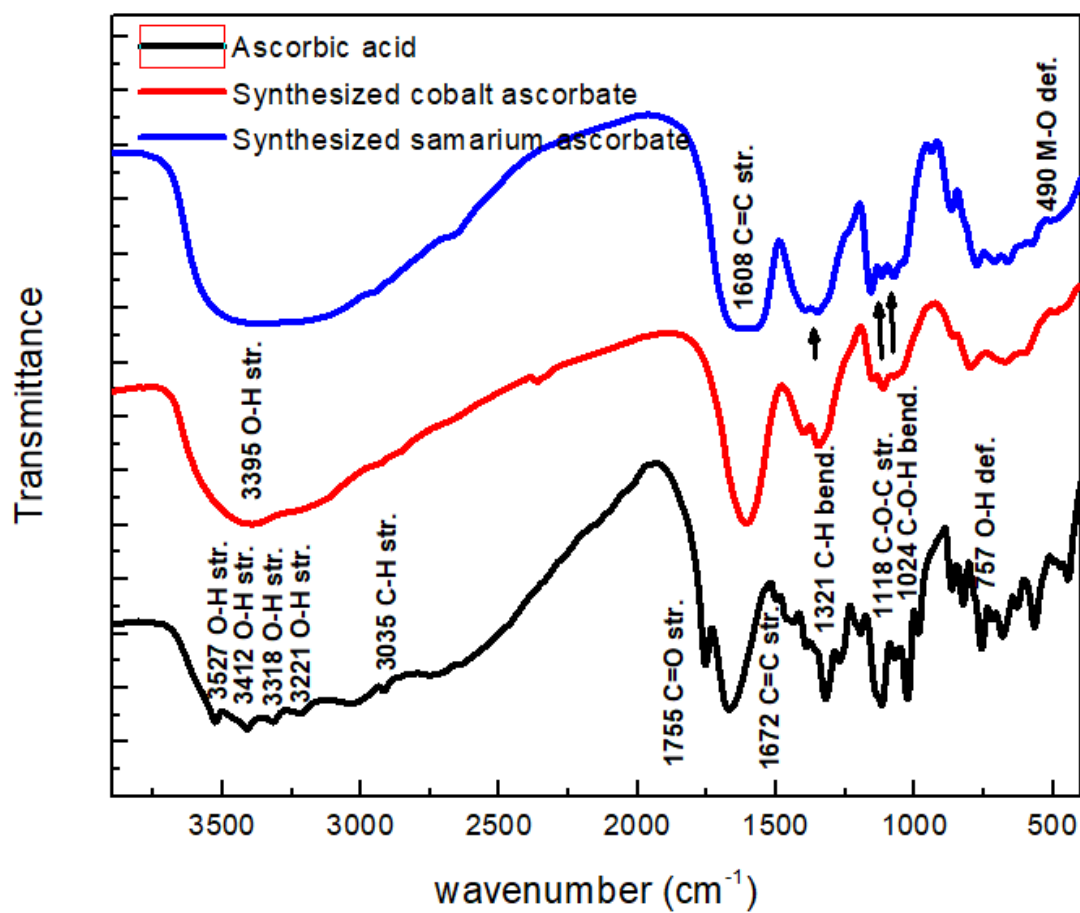


Figure 4.2. FTIR spectra for ascorbic acid, synthesized cobalt ascorbate and samarium ascorbate.

The spectrum of the mixture of synthesized cobalt ascorbate and samarium ascorbate is shown in figure 4.3. The FTIR spectrum of ascorbic acid is also attached in the figure for comparison. The spectra of the mixture of synthesized samarium ascorbate and cobalt ascorbate presented a similar curve as that of ascorbic acid, which demonstrated that synthesized materials have similar functional groups. Similarly, the absorption bands for the hydroxyl groups for synthesized materials became a wide peak after synthesis at 3395 cm^{-1} . The stretching vibrations of the C=O band at 1755

cm^{-1} disappeared after synthesis as well. Other peaks for the C-H bend band, C-O-C stretch band and C-O-H bend band were obtained in the spectra for the synthesized materials. Furthermore, as mentioned before, the replacement of cobalt or samarium during the synthesis process led to the change in the absorption band from O-H deformation band to M-O band. The absorption band exhibited a peak at around 490 cm^{-1} , consistent with the result in the previous paper.

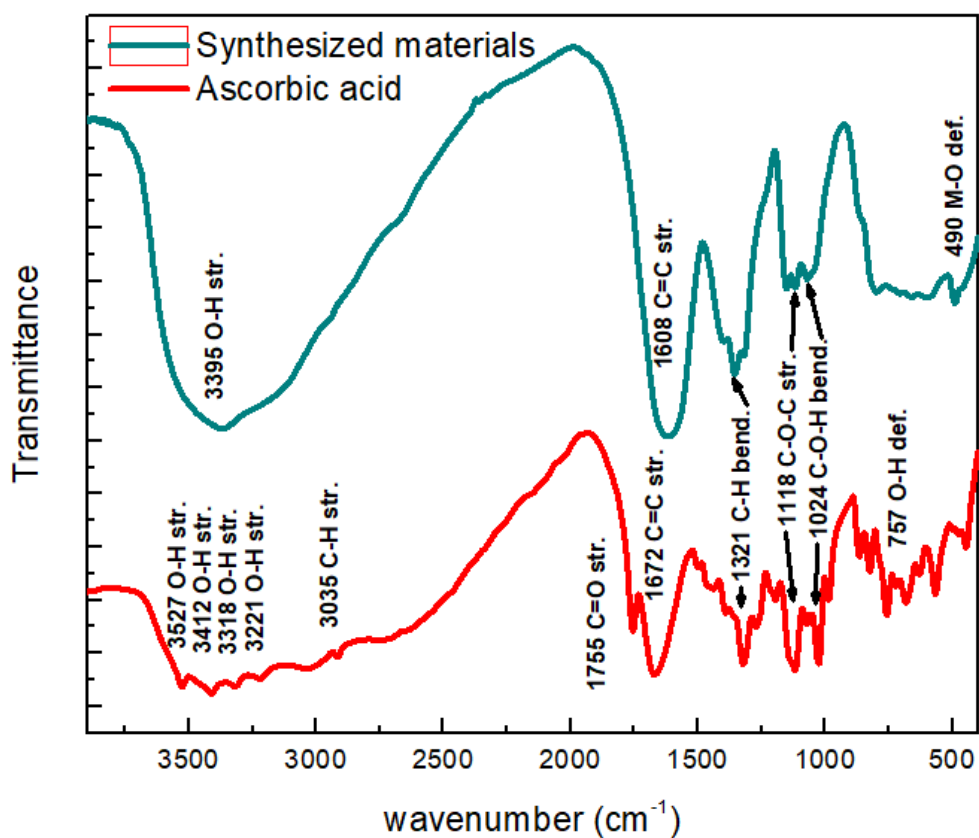


Figure 4.3. FTIR spectra for ascorbic acid and the mixture of synthesized cobalt ascorbate and samarium ascorbate.

(2) Metal element composition characterization for synthesized materials.

ICP-OES can be used to identify the metallic elements of materials. Therefore, synthesized materials were measured by ICP-OES.

The result of synthesized samarium ascorbate is shown in Table 4.1. The standard solution for samarium was samarium chloride. 5ppm, 10 ppm and 15 ppm standard solutions were tested by ICP-OES. 1ppm, 3ppm and 5ppm test solutions of synthesized samarium ascorbate were measured by ICP-OES as well. The proportion of samples in testing solution was relatively low compared with the standard solution, because the testing solution with a higher proportion of samples (5ppm to 15 ppm) cannot be measured completely. This may be caused by the limitation of the machine range. Based on the results of metal element measurement, the samarium content was around 1.9 times that of the predicted content. It demonstrated samarium ascorbate was not very high. The potential impurity contained in the synthesized materials was samarium oxide. If the impurity was only samarium oxide, the production yield of samarium ascorbate can be calculated as 68.66%.

Table 4.1. Metal element measurement on synthesized samarium ascorbate.

Selected spectral line (nm)		Sm (356.827)	Sm (359.259)	Sm (360.949)
Condition				
Standard	5ppm	4.95681	5.00359	5.09026
	10ppm	10.07461	10.08022	10.05633
	15ppm	14.96463	14.94533	14.93236
Replicates Concentration	1ppm	1.84927	1.90388	1.86536

	3ppm	5.72256	5.76600	5.79399
	5ppm	9.5573	9.53556	9.53148

Similarly, the standard solution for cobalt was cobalt chloride. The result of the synthesized cobalt ascorbate is shown in Table 4.2. 5ppm, 10 ppm and 15 ppm standard solutions were tested by ICP-OES. 1ppm, 3ppm and 5ppm test solutions of synthesized cobalt ascorbate were measured by ICP-OES as well. Based on the results of the metal element measurement, the cobalt content was around 1.27 times that of the predicted one. It demonstrated that cobalt ascorbate was relatively high. The potential impurity contained in the synthesized materials was cobalt oxide. If the impurity was only cobalt oxide, the production yield of cobalt ascorbate can be calculated as 68.66%. 94.02%, which is much larger than that in the literature (52%) (Obaleye & Orjiekwe, 1992). It showed that the production yield of synthesized materials is relatively high.

Table 4.2. Metal element measurement on synthesized cobalt ascorbate.

Selected spectral line (nm)		Co (228.615)	Co (230.786)	Co (238.892)
Condition				
Standard	5ppm	5.26813	5.29748	5.31514
	10ppm	9.67213	9.72522	9.76049
	15ppm	14.75027	14.8439	14.87507
Replicates Concentration	1ppm	1.6849	1.69625	1.69999
	3ppm	3.32335	3.3401	3.36298
	5ppm	5.16883	5.18778	5.21872

The mixture of cobalt ascorbate and samarium ascorbate was also measured by ICP-OES to identical metal elements and their ratio. Standard solutions for cobalt and samarium elements were cobalt chloride and samarium chloride respectively. The elemental ratio between cobalt and samarium was 5:1, which corresponded to the ratio of the required final product. The weight ratio was 1.9596:1. The standard solution was prepared in the same ratio. Based on the proportion of samarium element, 5ppm to 15 ppm standard solutions and 1ppm to 5 ppm test solutions were prepared and measured respectively. Results are shown in table 4.3.

Table 4.3. Metal element measurement on the mixture of synthesized cobalt ascorbate and samarium ascorbate.

Selected spectral line (nm) Condition		Sm (356.827)	Sm (359.259)	Sm (360.949)	Co (228.615)	Co (230.786)	Co (238.892)
Standard	5ppm	5.12979	5.20102	5.27658	10.15063	10.14153	10.16150
	10ppm	10.08410	10.09696	10.07845	19.73707	19.71777	19.76540
	15ppm	14.90063	14.86833	14.85547	29.13207	29.14797	29.10950
Replicates Concentration	1ppm	1.66121	1.75355	1.73695	3.29937	3.30353	3.28906
	3ppm	5.49978	5.56535	5.61837	10.20293	10.22257	10.25307
	5ppm	9.28966	9.28363	9.28077	17.10903	17.13617	17.12993

The content of samarium was around 1.8 times of the predicted concentration, demonstrating that there were some impurities in the synthesized material. Samarium oxide was considered as the impurity due to the nature of the oxidation for samarium. The production yield of samarium ascorbate in this mixture was 72.18% if the impurity was samarium oxide only. Similarly, the content of cobalt element was around 1.7 times. Because cobalt was also easy oxidized, cobalt oxide was treated as the impurity. The production yield of cobalt ascorbate was 84.30% if the impurity was cobalt

ascorbate only. The weight ratio between cobalt and samarium for the mixture was 1.87:1. It demonstrated that some cobalt was lost during the synthesis. The elemental ratio between them was 4.35:1. According to Sun's research, the Co:Sm ratio of the metal-organic precursor for SmCo_5 was determined as around 4.17:1 with a ratio of reduce of 1:1.2 due to the loss of Sm during sintering (H. Zhang et al., 2011). The ratio of Co:Sm for synthesized materials were similar to that in Sun's paper.

(3) Crystal structure characterization for synthesized materials

XRD spectra of synthesized samarium ascorbate and cobalt ascorbate are shown in figure 4.4. There were not any obvious peaks that could be observed, demonstrating that these two synthesized materials represented the amorphous phase. After the synthesis process, the original peaks for the starting materials, cobalt chloride and samarium chloride, cannot be observed.

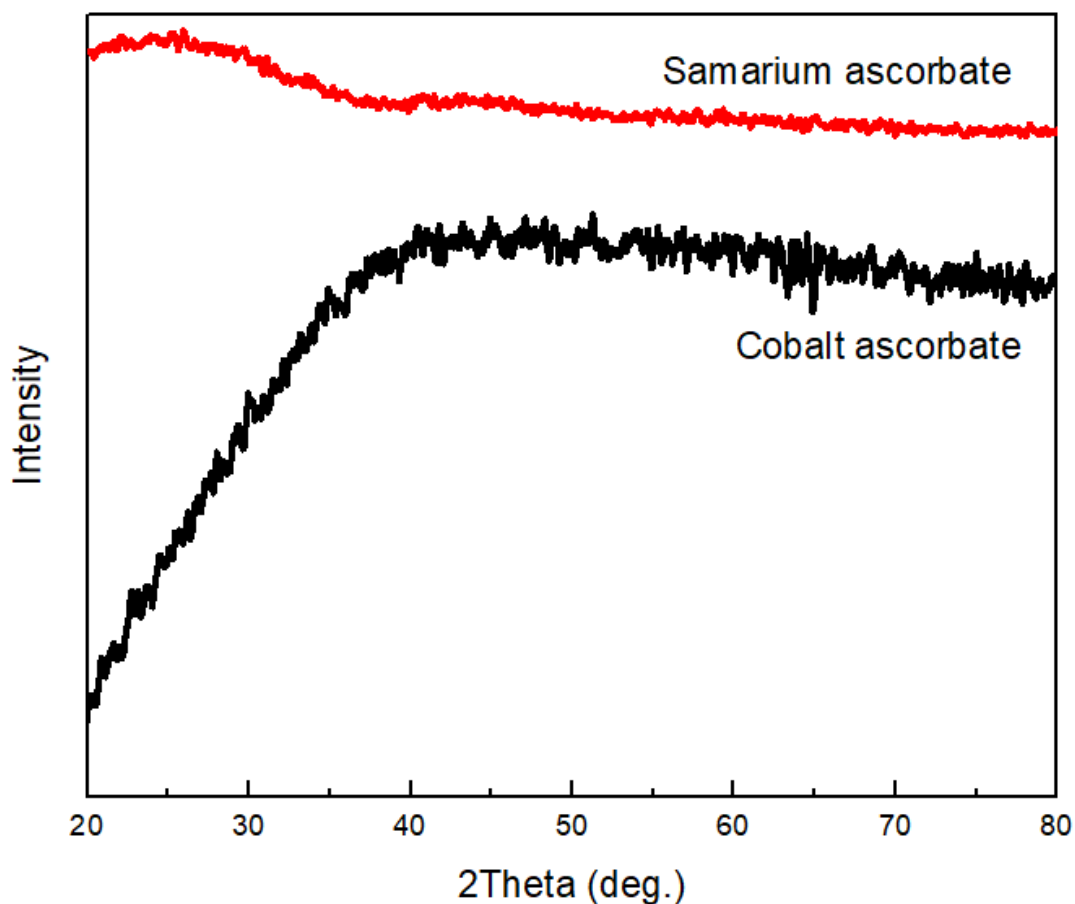


Figure 4.4. XRD spectra for synthesized cobalt ascorbate and samarium ascorbate.

In the XRD spectrum of cobalt ascorbate, the peaks for cobalt chloride cannot be observed, demonstrating cobalt chloride was transferred into cobalt ascorbate completely, and no impurities were produced with a crystal structure (de la Osa, Romero, Dorado, Valverde, & Sánchez, 2016). Similarly, in the XRD spectrum of samarium ascorbate, the peaks for samarium chloride also cannot be observed, demonstrating samarium chloride was completely transferred into cobalt ascorbate, and no any impurities produced were during the synthesis process.

4.3.2 Thermal profile for synthesized metal ascorbates

The TGA results of samarium ascorbate and cobalt ascorbate were obtained so as to perform the thermal profiles respectively. Nitrogen was used as the protection gas during the TGA measurement, and the flow rate was 20 ml/min. They are shown in figure 4.5. The derivative thermogravimetry (DTG) curves were also obtained by derivation of the TGA results for samarium ascorbate and cobalt ascorbate respectively.

As shown in figure 4.5a, the synthesized cobalt ascorbate started to lose weight at the beginning, caused by the evaporation of moisture. Water vapor easily attached on the synthesized cobalt ascorbate although the cobalt ascorbate was stored in the dry box. It can be observed that around 14% weight loss was occurred in this process, which demonstrated that the content of the attached water vapor was relatively high. When the temperature reached 326 °C, a typical decrease occurred as the cobalt ascorbate tended to decompose. This sharp decrease stopped at 426 °C, showing that the decomposition in this stage was ended. With the assistance of the DTG curve (blue one), the largest weight losses in this period occurred at 333 °C, 384 °C and 431 °C, the peaks in the DTG curve represented them. It demonstrated that the decomposition rate of cobalt ascorbate at these temperatures was the highest. The three temperature may be caused by the decomposition of cobalt ascorbate in different organic bonds. The fastest rate of weight loss of sample was at 384 °C, and demonstrated that the decomposition rate of cobalt ascorbate was the highest at this temperature. The weight

loss of cobalt ascorbate was around 34.7%. A large part of the organic ligands was decomposed during this stage. These decomposition temperatures provide information in the setting for the debinding and sintering processes. The heating rate should provide enough time to decompose cobalt ascorbate. Meanwhile, the temperature holding time at these decomposition temperatures should also be set to allow sufficient decomposition without crack formation during debinding and sintering (Qu, Zhu, Li, & Ouyang, 2012). After the sharp decrease in weight loss, the weight of cobalt ascorbate did not undergo any obvious change although there was a small fluctuation before weight loss stopped. This fluctuation may be caused by the oxidation of cobalt. Decomposed cobalt reacts with the oxygen generated from the decomposition, thus the weight underwent a small increase. The change of weight stopped at around 465 °C, showing that the decomposition was completed. The total weight loss was 52.5%, which demonstrates that there is still some carbon that cannot be removed.

Figure 4.5b presents the TGA curve and DTG curve for samarium ascorbate. The same as for cobalt ascorbate, samarium ascorbate also started to lose weight in the beginning due to the evaporation of the moisture. The weight loss in this stage was 15%, which was similar to that of cobalt ascorbate. Samarium ascorbate underwent a sharp decrease at 380 °C, which was slower than that of cobalt ascorbate. Meanwhile, there was only one apparent peak in the DTG curve, showing samarium ascorbate decomposing rapidly and completely in one time. The temperature for the fastest decomposition was 408 °C. The weight loss in this stage was around 24%. However,

there was still a small sharp from 565 °C to 650 °C. It demonstrated that there was still a decomposition for samarium ascorbate. The weight loss for decomposition period was 33% in total, which was also similar to that for cobalt ascorbate. The total weight loss was 52 %. There was also some carbon remaining after decomposition. The heating rate during this sharp decrease period should be designed as slow as possible to provide sufficient time for the decomposition of samarium ascorbate. A holding time at this decomposition temperature was also needed for the confirmation of complete decomposition.

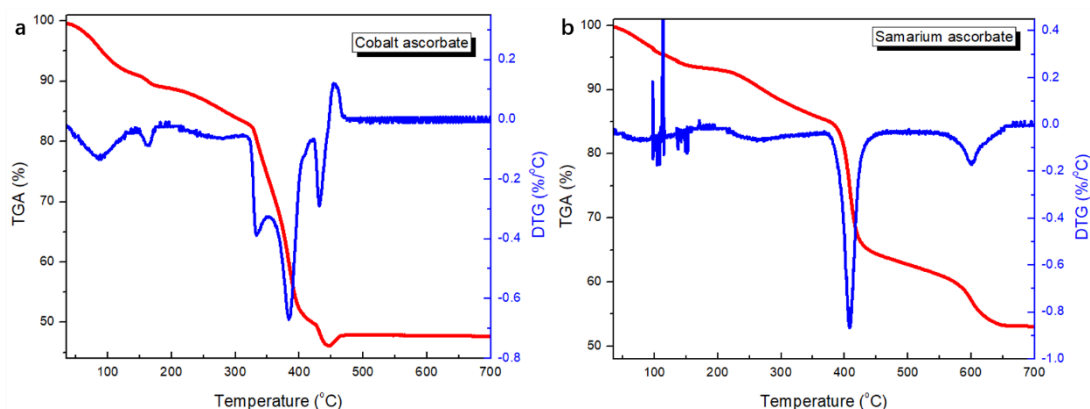


Figure 4.5. TGA and DTG curve for synthesized (a) cobalt ascorbate and (b) samarium ascorbate.

4.3 Concluding remarks

Cobalt and samarium were selected to form the ideal REM-TM alloy due to the outstanding properties of cobalt samarium alloy. Ascorbic acid, one of the common

and green organic ligands, was selected as the coordination ligand. Cobalt ascorbate and samarium ascorbate were successfully synthesized. These synthesized materials were prepared as metal-organic compounds precursors for alloy synthesis. Meanwhile, the FTIR spectra and ICP-OES results showed the effectiveness of producing cobalt ascorbate and samarium ascorbate. Synthesized samarium ascorbate and cobalt ascorbate reached 68.66 % and 94.01% yield respectively. The yield of their mixture was 84.30%, which showed that the yield can be affected by any of them alone. The elemental ratio and weight ratio between cobalt and samarium for the mixture was 4.35:1 and 1.87:1 respectively, which corresponded to the findings in the literature. The thermal profiles of samarium ascorbate and cobalt ascorbate were studied. These synthesized materials started to decompose at 326 °C and 380 °C respectively. The decomposition temperature can assist in developing the sintering profile for the alloys.

Chapter 5 Three-dimensional components fabricating processes

The increasing demands being placed on 3D components have caused concern and encourage the development of technologies and materials for 3D component fabrication. As discussed in the previous chapter, AM, such as inkjet printing and laser sintering, in addition to other 3D component fabrication processes, were thoroughly explored. Furthermore, fabrication of 3D metal components has been intensively studied using AM methods. However, high-cost and energy requirement of lasers were the major disadvantages for additive manufacturing approaches. Therefore, a modified laser writing system was built to achieve 3D component comprising metal materials. An inexpensive and low-power laser (0.4 W) was used as laser head, tailor-made X-Y movement system driven by 2 stepper motors was used to control laser writing direction and speed. A computer was used to control this modified laser system to build required patterns with Autodesk AutoCAD software. Relevant details for modified laser writing system are presented in Chapter 3. By using this system, LIFT, selective laser patterning and laser reduction were conducted to construct 3D metal components. Meanwhile, inkjet printing and compression bonding were also used to fabricate ferromagnetic multilayer patterns with 3D structures and pellets of mixture of PVA, cobalt ascorbate and samarium ascorbate for alloy sintering.

In this chapter, 3D structure fabrication methods, such as inkjet printing and modified laser systems, are used to fabricate 3D structures using metal composites or metal-organic compounds. The development of these 3D structure fabrication methods can provide 3D structures for target materials, including the synthesized materials mentioned in Chapter 4, and for alloys synthesis, as shown in Chapter 6. The motivation for this chapter is that the research for 3D structure fabrication methods can solve some critical problems for typical materials in 3D structure fabrication, crystal structure and magnetic properties for materials.

5.1 Laser-induced forward transfer

5.1.1 Introductory remarks

LIFT is an alternative AM method for transferring required materials on top of target substrates. The mechanism of LIFT is illustrated in detail in the chapter 2. As the rapid development of laser techniques, LIFT method attracted much attentions and used as materials deposition method for functional materials. By comparing with other method, such as laser sintering, LIFT is time-saving and energy-saving owing to the thermal expansion of materials (W. K. Yung, B. Sun, Z. Meng, et al., 2016). Meanwhile, vacuum deposition methods, including sputtering, and solution-based methods are the major competitors in functional materials deposition (Sametoglu, Sauer, & Tsui, 2013) (Rapp et al., 2009). While the disadvantage of cost and consuming time for these

methods, LIFT is the better choice. In the LIFT method, scarified layer is important. Generally, inorganic-metal layer and organic layer can be adopted as the scarified layers. For example, inorganic titanium layer was used as the scarified layer in facilitation of silver nanoparticle ink owing to its relatively low melting temperature (Boutopoulos, Kalpyris, Serpetzoglou, & Zergioti, 2014). By comparing with inorganic-metal layer, organic sacrificial layer attracted more attentions due to its relatively low sublimation and boiling temperature and the absence of metal contamination (J. R. Shaw-Stewart, Lippert, Nagel, Nüesch, & Wokaun, 2012). During LIFT process, organic layer reacts with O² under ambient conditions, and then giving out CO² in the gas phase and further increasing the volume expansion. Organic materials are completely removed under laser illumination and leaving metals on the substrates. Acrylonitrile butadiene styrene (ABS), as a common polymer, has a thermal expansion of $73.8 \times 10^{-6} \text{ K}^{-1}$ and a relatively low decomposition temperature of 400 °C, which is a good choice as a sacrificial layer for LIFT method. As mentioned in the chapter 2, copper is an optimized candidate in applying LIFT for fabrication 3D metal objects owing to its high electrical conductivity, low bond dissociation energy and low cost. Herein, in the work of my research, copper circuit lines were successfully fabricated by using LIFT method. The mixture of copper oxide and ABS was prepared as the sacrificial layer. Copper oxide was reduced into copper by laser illumination with photochemical reduction. Morphology, elemental composition and crystal structure of laser reduced materials were studied by SEM, EDX and XRD respectively.

5.1.2 Experiments

ABS (PA-707) was purchased from Taiwan (Chi Mei Co.) and copper oxide was purchased from USA (International Laboratory Co.). 1 mol ABS and same molar weight of CuO were measured and dissolved into chloroform with stirring for 1 h, hot plate was used to provide heat to dissolve ABS at 60 °C. The homogenous gel-type mixture was then painted onto glass slides using brush. After that, this mixture was then heated continuously on a hot plate at 60 °C for evaporation of the chloroform solution to form a coating on the glass. The coating cooled down to room temperature and was treated as the donor layer. The thickness of the donor layer was 100 µm. The donor layer was placed above the acceptor layer with a 50 µm space between the donor and acceptor layers. Laser treated patterns were designed with AutoCAD software for the test of laser treatment and for certain applications, such as circuit lines for LEDs. Since the laser beam size was measured as 200 µm, the width between each line was set at 50 µm to ensure the connection between each line. Designed patterns were then transformed into G-code by using GRBL software for laser writing. The 0.5 W laser focused on the donor layer which coated on the glass slide, the laser writing speed was set at 10 mm/min. After the photon energies are absorbed by CuO, the photo-reduction of CuO and volume expansion would occur simultaneously. Reduced products would be forward transferred onto the acceptor layer and obtaining required patterns with reduced copper. Electroless plating was then performed selectively to enhance the electrical conductivity. The electroless plating solution was ECM-100, which was

purchased from Teamly Chemicals Corporation. The ratio of cupric sulfate and edetic acid was 16:5 in the solution. Electroless plating was performed in four hours at 60 °C.

The morphology of laser treated lines were observed by using optical microscopy (Leica Microscope) with a 50x object lens and charge-coupled devices. The microstructures and element compositions for brushed coating, laser treated patterns and samples after electroless plating were analyzed by FESEM (LEO 1530) and EDX respectively. The crystalline structures were studied by XRD (Bruker D8). The resistivity of the sample circuits was determined by standard four-probe measurement using an Agilent 4338B milliohm meter.

5.1.3 Results and discussions

Electrical circuit line transferred by laser was shown in figure 5.1a. The width of pattern line in bronzing color is 200 μm . Some random black dots are shown as well. The thickness of pattern is determined by profilometer and measured as 13.67 μm . Electrical resistivity is measured by standard four-probe measurement as $1.46 \times 10^{-6} \Omega\text{m}$, which is 87 times larger compared with that of bulk copper ($1.68 \times 10^{-8} \Omega\text{m}$). Since the high porosity of the surface, four-point measurement is not reproducible. The porous structure can be easily destroyed by the pressure during four-point measurement. However, the electrical resistivity was high comparing to the recent work from Visser (Visser et al., 2015), who used pulsed laser to trigger LIFT, electroless plating was used to reduce electrical resistivity and thereby improve

electrical performance. Electroless plated sample is shown in figure 5.1b. Electroless plated sample presents brighter and fewer black dots compared with that without electroless plating. After electroless plating, sample's height increases to 20.54 μm and its resistivity decreases to $1.29 \times 10^{-7} \Omega\text{m}$, which is only 7.7 times larger than that of copper. It is obvious that copper selectively grows on the laser treated part rather than the whole substrate.

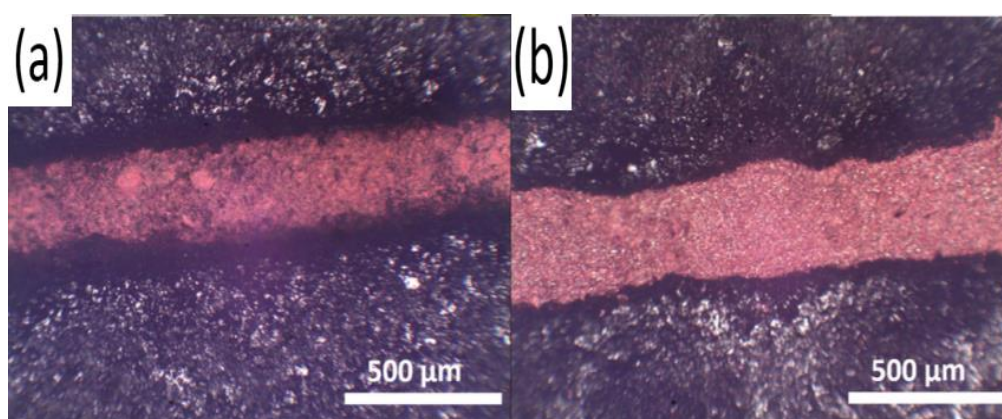


Figure 5.1. Optical microscope images of laser printed patterns (a) before electroless plating (b) after electroless plating.

SEM images for plan-view are shown in figure 5.2a-c to present the microstructures of CuO/ABS composite without and with laser treatment and after electroless plating, respectively. The raw sample without laser treatment shows dense film with clusters in micro-size, as shown in figure 5.2a. Its surface is smooth as shown in the insets. Sample surface becomes porous after LIFT, as shown in figure 5.2b. Based on the EDX result, as shown in figure 5.3, the clusters should be the aggregated CuO. And later, they became copper after laser treatment. After laser treatment, as

shown in figure 5.2b, micro-size clusters and holes are randomly distributed on the surface of sample. This rough surface was corresponding to the darker bronzing color as shown in figure 5.1a. Sample's surface became smoother after electroless plating as shown in figure 5.2c, which is also corresponding to the brighter surface as shown in figure 5.1b. It demonstrates that copper grows on the laser treated part, filling and sheathing porous structures.

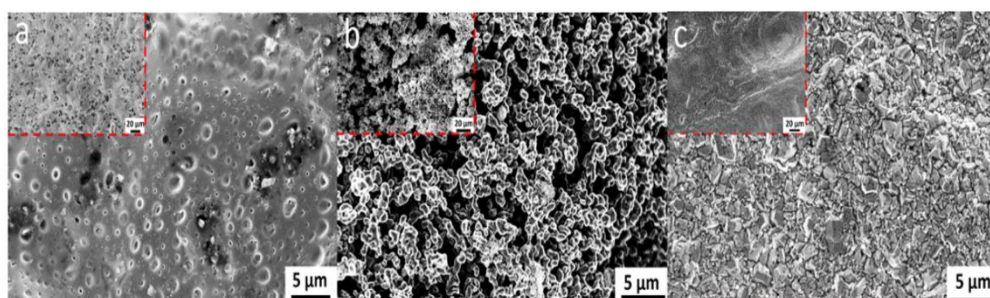


Figure 5.2. SEM images of sample surface (a) before laser treatment (b) after laser treatment (c) after electroless plating.

EDX results of the samples are shown in figure 5.3a-c. Sample without laser treatment is detected with 93.15% carbon in atomic ratio, as shown in figure 5.3a. The rest of elements, copper and oxygen only took up 3.7% and 3.2% respectively. It proved that the main compositions of sample were CuO and ABS. The elementary compositions changed after laser treatment, as shown in figure 5.3b. The proportion of carbon decreased from 93.15% to 58.4%, which demonstrated that part of carbon was removed after laser treatment. The reaction of carbon and oxygen generated CO₂ gas and thereby led to the weight loss of carbon. After electroless plating, the only element was detected for the sample was copper, as shown in figure 5.3c. Hence, it

demonstrated that electroless plating deposited copper above laser treated part, which was corresponding with the result of electrical resistivity.

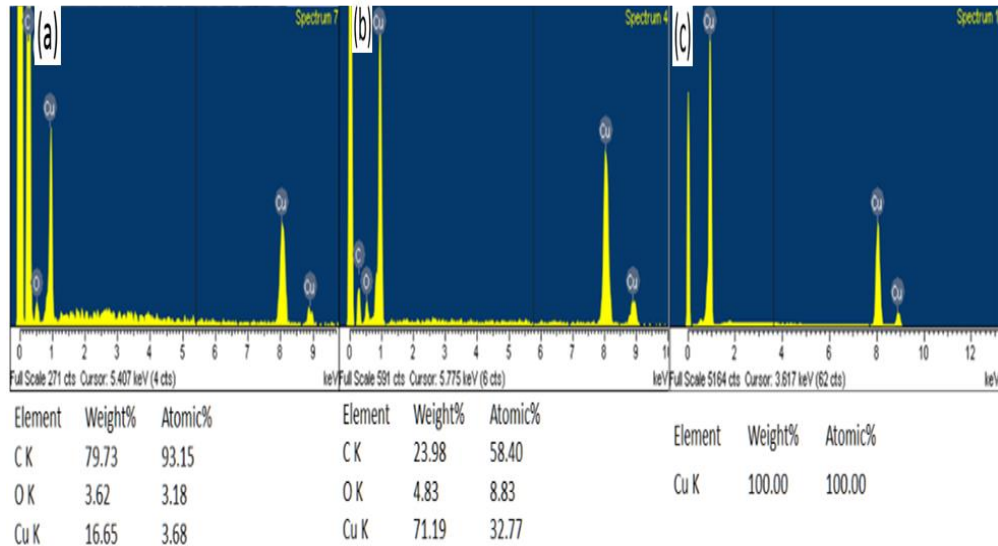


Figure 5.3. The EDX results of samples. (a) before laser treatment, (b) after laser treatment, (c) after electroless plating.

XRD was used to further confirm chemical composition with and without laser treatment and electroless plating, as shown in figure 5.4. Sample without laser treatment exhibited typical XRD spectrum of copper oxide (Meyer et al., 2012). Sample with laser treatment exhibited copper identification peaks in face centered cubic phase and weaker intensities for copper oxide identification peaks. It demonstrated that copper oxide was reduced partially into copper with homolysis effect. Meanwhile, very weak intensity of signal for cuprous oxide was detected. It

demonstrated the incomplete reduction of copper oxide. Therefore, laser in 405 nm wavelength was proved to be able to reduce copper oxide into copper effectively.

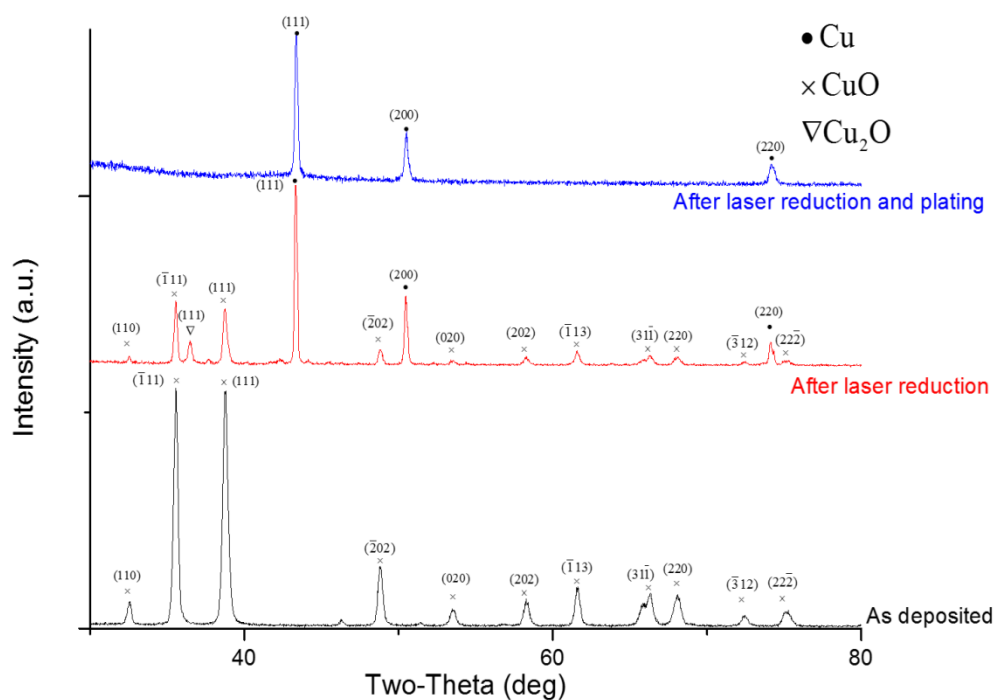


Figure 5.4. The XRD spectra of samples before and after laser treatment and after electroless plating.

The transformation of reduced copper using LIFT process contains two coinstantaneous ways, photochemical reaction and thermal expansion. Copper oxide can effectively absorb the photon energy and dissociate into copper and cuprous oxide (Cu₂O) with the illumination of the 405 nm laser, as showed in the XRD results. Although the laser power of the 405 nm laser was low (0.5 W), laser treated patterns also exhibited copper. It was because the incident light was absorbed by materials to initiate a reaction according to Grotthuss-Draper law (Y. S. Zhou et al., 2015). The

wavelength of laser provided sufficient photon energy to perform photochemical reduction. In other words, the crucial factor of LIFT is laser wavelength rather than laser power, which normally is the key parameter of traditional LIFT (Brown, Kattamis, & Arnold, 2010; Pohl et al., 2015). A comparison experiment was performed to evidence the importance of wavelength of laser. A 1064 nm fiber laser with 10 W was used to illuminate the identical donor layer. The XRD result for the laser treated samples was shown in figure 5.5. It was obviously that there was not any reduced copper can be observed although the laser power was much high than that for the 405 nm laser. It demonstrated the laser wavelength was more important than laser power for laser energy absorption.

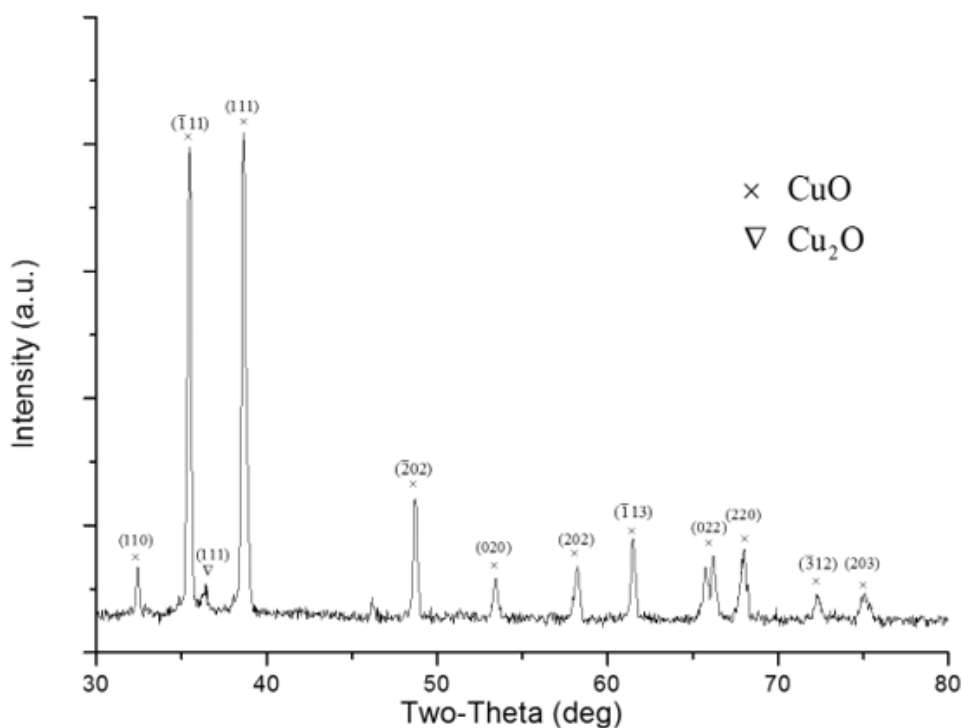


Figure 5.5. XRD patterns of samples after laser treatment by using 1064 nm laser.

The thermal expansion stage for LIFT was illustrated as below. The ABS polymer absorbs the heat from the photon energy and thus was decomposed and expanded to increase the volume, which generated momentum for the transformation from the donor layer to acceptor layer. This ejection mechanism based on the driving mechanism from the expansion of the donor layer and the evaporation caused by the decomposition (Brown et al., 2010).

It has been proved that copper circuits can be successfully fabricated by the transformation from ABS/CuO donor by LIFT. Simple device with (light-emitting diode) LED was fabricated with copper circuits as connection by LIFT to demonstrate the potential application, as shown in figure 5.6.

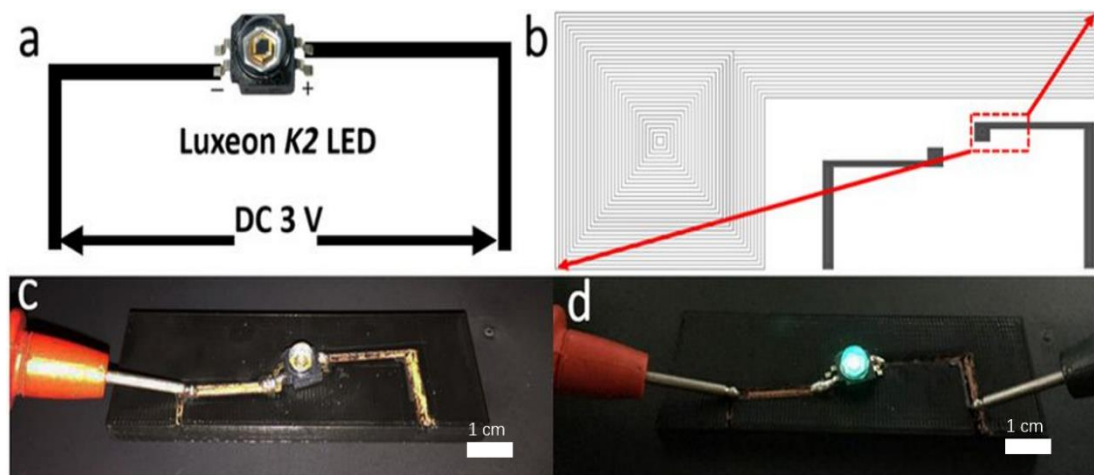


Figure 5.6. (a) Design for circuit with the connection of LEDs. (b) The detail of designed circuit pattern, with the magnification of laser writing path. The fabricated component with laser treated circuits and LEDs (c) without lighting and (d) with lighting.

The design scheme was shown in figure 5.6a, LED connected with direct-current (DC) power in 3V. The connecting circuit can be fabricated by selective transformation from donor on any target substrates, such as polylactic acid (PLA), glass and FR-4. For example, PLA was used as substrate and shown in figure 5.6c. LED was lighted up when power was supplied, as shown in figure 5.6d. It demonstrated that LIFT copper circuits can be simply treated as electronic circuits.

As mentioned previously, any other target substrates can be transferred. As shown in figure 5.7, FR-4, polyimide and glass were used as substrates and they were all proved that copper can be transferred by LIFT successfully.

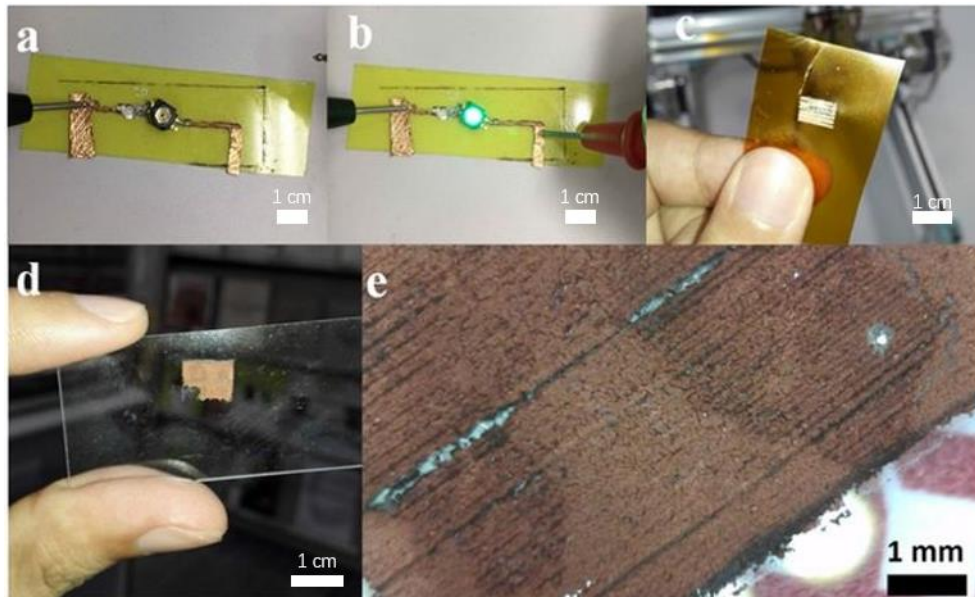


Figure 5.7. Component fabricated on the substrate of FR-4 (a) without lighting and (b) with lighting. LIFT patterns transferred on (c) polyimide and (d) glass slide and (e) the magnification of that on glass slide.

For LIFT process, sample can also be fabricated into 3D structure as the printing time increase since the reduced materials accumulates layer by layer. In my research, LIFT was used to fabricate the electrical circuit for LED device, which only shows the fabrication of 2D structure. Electrical circuits were fabricated using LIFT in one time because electrical circuits with higher thickness have lower electrical conductivity.

5.2 Selective laser patterning

5.2.1 Introductory remarks

3D printing methods has been explosively developed, while massive 3D printed objects are fabricated by thermoplastic materials. 3D printed objects with metal coating has aroused comprehensive concerns since stronger wear resistance, higher thermal conductivity and better aesthetic appearance (Torgerson et al., 2018). Meanwhile, selective patterning of metals on the surface can be utilized as electronic circuits, antennas and radiofrequency identification (Aminuzzaman et al., 2010). Lee et al used inkjet printing patterned circuits with copper nanoparticles on flat surface (Y. Lee et al., 2008), while it is still a challenge to directly coat metals on 3D printed thermoplastic since the low adhesion force between substrate and metals. Meanwhile, electroplating and casting cannot be used to directly fabricate metal patterns on thermoplastic surface owing to the insulating characters and low decomposition temperature (Green et al., 2015). Painting is one of the most exhaustively used methods

to coat functional materials on objects, which is suitable for 3D printed thermoplastic objects (W. h. Zhou et al., 2016). Malachite, as a historic and common paint material, can be used for surface coating, since malachite can be reduced into copper with photochemical reduction of laser, and then required patterns can be fabricated. In my research, selective laser patterning was conducted by using modified laser system to fabricate copper patterns with brushed malachite coating on 3D printed thermoplastic objects. The morphology and crystal structure of laser reduced materials were studied by SEM and XRD respectively. The optimum laser writing speed was studied for better crystallization of reduced materials.

5.2.2 Experiments

PMMA powders and malachite were purchased from Mitsubishi and Alfa Aesar respectively. 2 g PMMA and 5g malachite were measured and dissolved into 100 mL ethyl acetate with stirring, hot plate was used to provide heat to dissolve PMMA at 60 °C. The mixture was then coated on the surface of 3D printed objects by using brush. The thickness of coating was 50 µm. A 405 nm laser then selectively treated on the coating after the paint dried. Laser treatment can be performed selectively or across-the-board. Laser treated areas were transferred to copper by photochemical reaction. The circuit patterns were designed using AutoCAD software, the CAD files were then transformed into G-code to control laser patterning. Because the laser beam size was

200 μm , the width between each line for laser patterning was set at 50 μm to ensure the connection of each line. The laser patterning speed was set at 10 mm/min.

The overall workflow for patterning the Statue of Liberty is shown in figure 5.8a. The coating area after the laser treatment became natural bronze while the untreated part still showed in green. Prototypes were fabricated and shown in figure 5.8b. During the laser patterning process, laser spot should focus on the surface and illuminate it. When laser spot is out of focus, there is not enough laser energy to trigger photochemical reaction for the materials. Therefore, the laser spot on the curved surface of the sample should be controlled at the same focal plane to maintain resolution.



Figure 5.8. 3D printed Statue of Liberty with coating of malachite. (a) schematic image; (b) real product.

Copper tracks were also fabricated on 3D printed thermoplastics with same method. As shown in figure 5.9, an emulated robot hand was fabricated by 3D printing, electronic circuits were fabricated for connecting microchips and LEDs. The Statue of Liberty and robot hand were printed using fused deposition modeling.

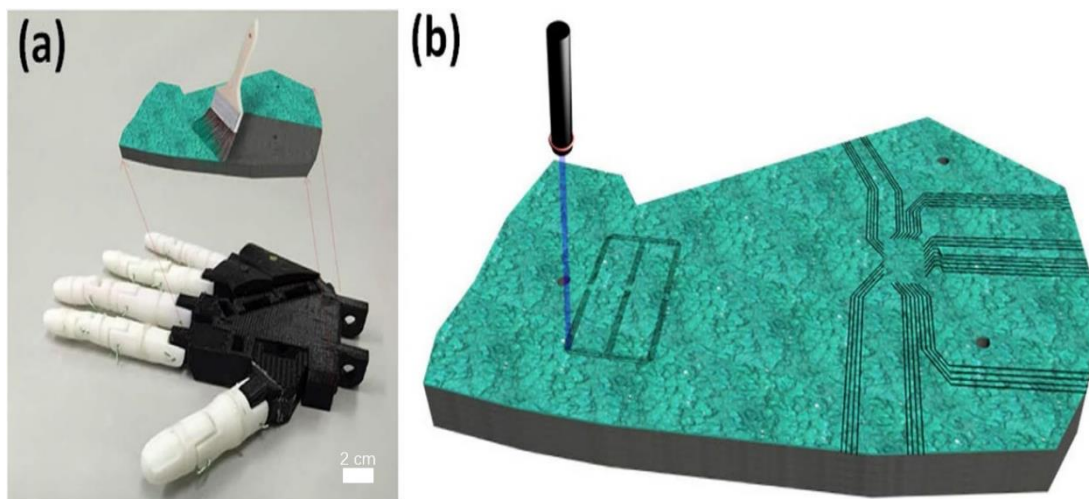


Figure 5.9. 3D printed robotic hand with coating of malachite. (a) before laser treatment; (b) schematic image for laser treatment.

The raw materials for them was 1.75 mm polylactic acid filament. The infill rate was 10% and the feeding rate was 41 mm/s. The thickness for each layer was 0.27 mm. The crystalline structures and morphology of malachite before and after laser treatment were studied by XRD (Bruker D8) and SEM (LEO 1530) respectively.

5.2.3 Results and discussions

Since malachite is one of the major compositions of the surface of the Statue of Liberty in New York, the prototype of the Statue of Liberty was fabricated using PLA polylactic acid filament and the coating of malachite and PMMA. The prototype of the Statue of Liberty was then scanned by laser line by line, the surface was reduced into copper with a natural bronze color, which similar to the real Statue of Liberty shipped to New York in 1886 (Matyi & Baboian, 1986). It demonstrated that copper can be coated on the surface of 3D printed thermoplastics using these two-step process of painting and post laser treatment.

As SEM images shown, due to the porous microstructures, the surface of the malachite with PMMA was smooth as prepared by doctor blade coater. However, the surface became highly porous as shown in figure 5.10a. It was because that the PMMA paint was evaporated during the laser treatment and this evaporation was likely a very volatile process. Besides, instantaneous power with extremely high temperature evaporated PMMA paint, other materials cannot fill up the holes immediately. Decreasing the containing proportion of PMMA paint was a strategy to reduce the porosity. The holes between the copper clusters should be the reason that the synthesized copper had lower conductivity than bulk copper.

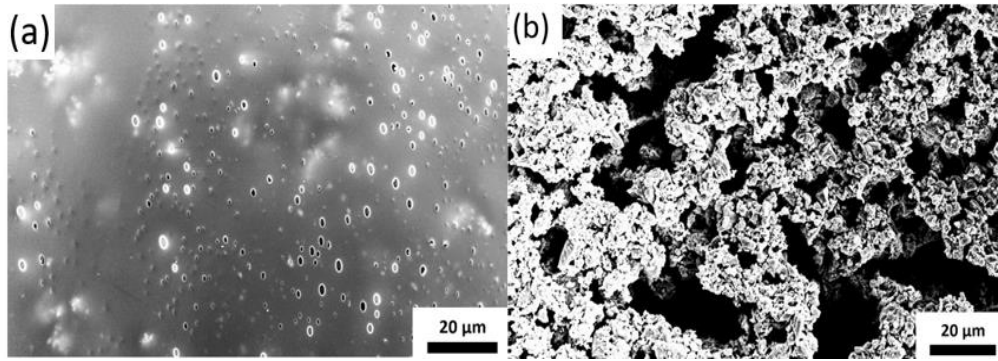


Figure 5.10. SEM images of sample surface (a) before and (b) after laser treatment.

XRD was performed to identify samples before and after laser treatment, as shown in figure 5.11. Sample before laser treatment exhibited typical malachite with monoclinic prismatic crystalline structures (JCPDS-ICDD 41-1390), as in figure 5.11a. In contrast, sample after the laser treatment exhibited typical copper crystal structure (JCPDS-ICDD 04-0836) in face centered cubic rather than malachite crystal structure, as shown in figure 5.11b. It demonstrated that laser in 405 nm wavelength can directly transfer malachite into copper.

The coating of malachite and PMMA can absorb photons with sufficient energy to reduce copper composite. The copper atoms in copper composite can be cleaved from the copper-oxygen bonds and form pure copper when they absorb sufficient photon energy (W. Ando & Moro-oka, 1988). The photon energy of laser in 405 nm wavelength is 3.06 eV. The bond dissociated energy of malachite is 2.99 eV, which

was lower than 3.06 eV. It means that laser at 405 nm wavelength is sufficiently high to break the copper-oxygen bond with homolysis effect (Y.-R. Luo, 2007).

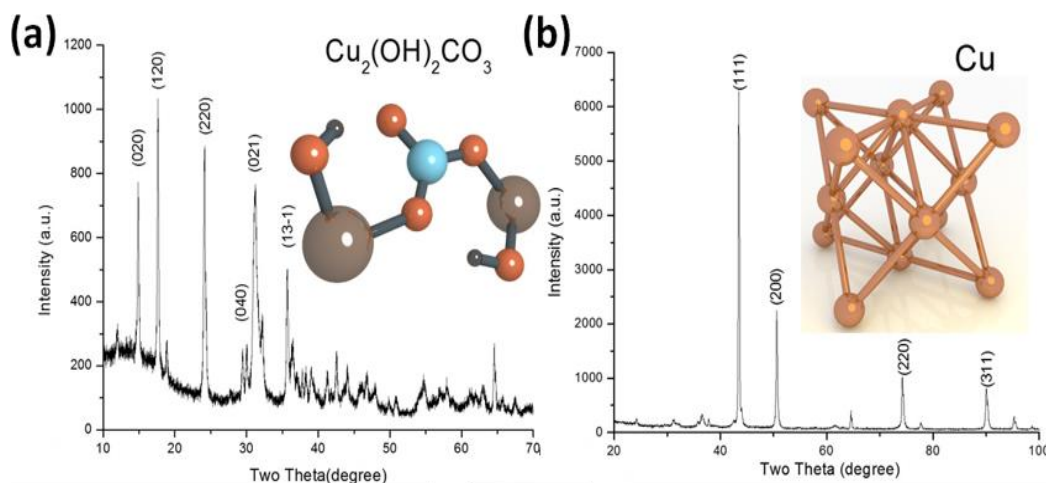


Figure 5.11. XRD spectra of samples (a) before laser treatment (b) after laser treatment.

The XRD spectra for laser treated materials with different writing speed were shown in figure 5.12a. The XRD results demonstrated laser treated materials can be reduced into copper, while reduction cannot be performed completely as the writing speed increased. Meanwhile, the crystallization of copper also weakened. The amount of these two phases can be compared using the order parameters, which defined as the ratio of their intensity (Q. Dong et al., 2012). The equation was:

$$\alpha = I_{111} / I_{120} \quad (5.1)$$

Where I_{111} and I_{120} corresponded to the copper (111) peak and malachite (120), respectively since (111) peak and (120) peak are the main peak for copper and

malachite. Order parameter increased as the laser writing speed decreased from 1000 mm/min to 200 mm/min. The electrical resistivity of samples treated by laser in different writing speed was shown in figure 5.12b. The electrical resistivity of sample treated by laser in 200 mm/min was the lowest ($4.3 \times 10^{-7} \Omega\text{m}$), which was corresponding to the best crystallization of copper shown in XRD spectra. The electrical resistivity was almost as low as that for the copper with electroless plating ($1.29 \times 10^{-7} \Omega\text{m}$) in the previous work (W. K. Yung, B. Sun, Z. Meng, et al., 2016).

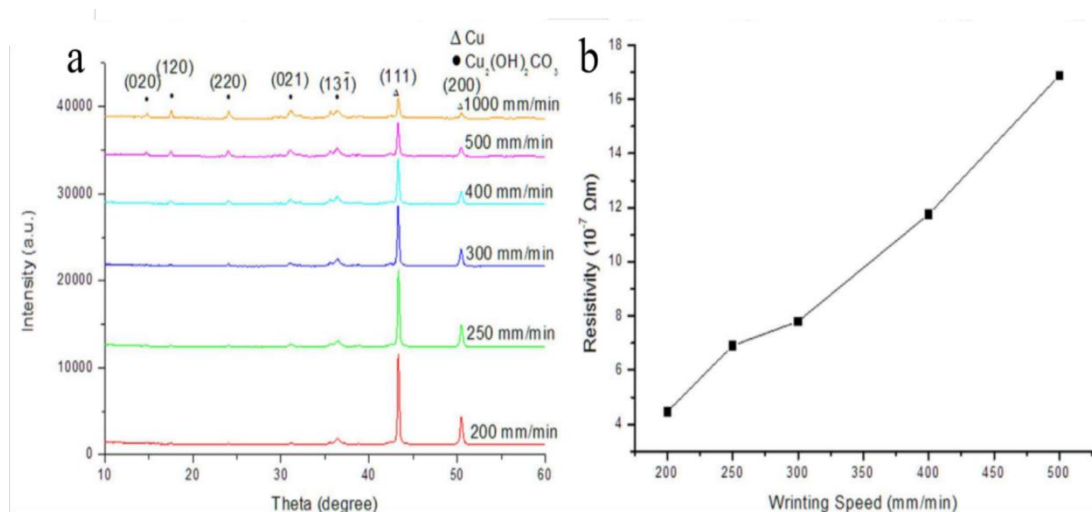


Figure 5.12. (a) XRD spectra and (b) electrical resistivity for samples treated by laser in different laser writing speeds.

LED device connected with batteries was designed and fabricated by laser treatment, as shown in figure 5.13. LEDs were lighted up by batteries. The voltage across LEDs was measured by multimeter as 2.99 V. It almost reached the original

voltage of batteries (3 V). It demonstrated that LEDs can be lighted up through the fabricated circuit.

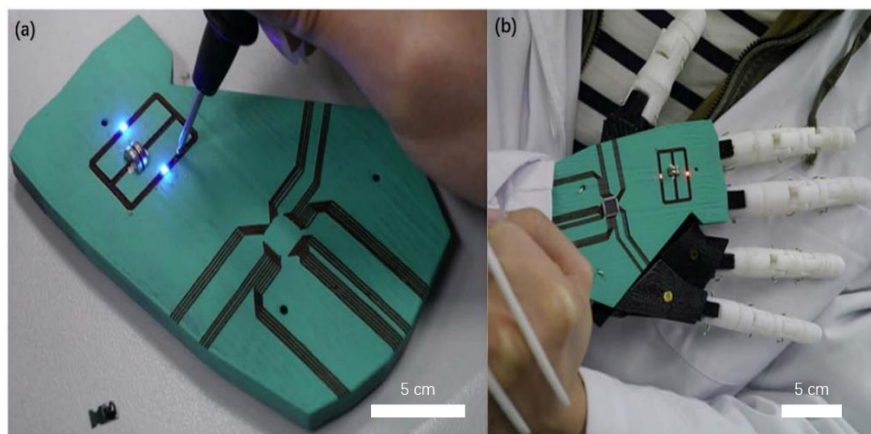


Figure 5.13. (a) Testing for laser patterned circuits and blue LEDs. (b) 3D printed robotic hand with laser patterned circuits and red LEDs.

The conventional precursors for coating onto the thermoplastic was copper powders, while the required energy for separating copper was high, which may damage the shape of the thermoplastic substrate (Visser et al., 2015). Using malachite as the precursor required much lower energy through photochemical reaction rather than thermal effect. It is more suitable to coat copper on the thermoplastic materials using malachite.

5.3 Laser reduction on metal-organic framework

5.3.1 Introductory remarks

It is avoidable for the rapid increase of the usage of fossil fuel in social and industrial development. While concomitant oil spillages during transportation and production result in ecological and environmental issues. To solve these unexpected problems, various materials were developed, such as graphene aerogels (X. Xu et al., 2015) and polyurethane sponges (Tran & Lee, 2017). Among these materials, hydrophobic polymers with relatively large porosity are the major absorbents for oil absorption. However, the low porosity, irregular pore size and poor thermal stability are the major drawbacks for these materials. In contrast, metal-organic frameworks (MOFs) present high porosity, which bring them limitless potential in physical absorption (M. X. Wu & Yang, 2017). Additionally, thermal stability in high temperature makes MOFs more competitive compared with polymer materials. Heat is easy to separate the inserted magnetic particles in polymer materials, while MOFs are structural stable owing to their carbon framework. Combining with the advantages of MOFs, the applications in magnetic field received wide attentions (Kurmoo, 2009). However, researches on MOFs with ferromagnetic behavior were still rare, and the existing ones revealed small coercivity (R. Dong et al., 2018). Furthermore, researches on laser reduction for materials modification has been studied comprehensively recently (El-Kady, Strong, Dubin, & Kaner, 2012). Owing to the merits of easy control,

low cost and time-saving, laser reduction became an outstanding candidate in scientific development. Laser reduced MOFs exhibited strong ferromagnetic properties and maintained large porosity and strong thermal stability. As one of the important MOFs materials, ZIF received comprehensive attentions. Since its thermal stability and large porosity, ZIF-67 was selected as the initial material (Shi, Chen, Song, Li, & Dong, 2011).

In the work of my research, modified laser system was applied to fabricate porous carbon materials with ferromagnetic behavior by the reduction of ZIF-67. The influence of parameters of laser system toward materials' structure and properties were comprehensively explored. The crystalline structure, morphology and magnetic properties of laser reduced ZIF-67 (LR-ZIF-67) and ZIF-67 and were also measured.

5.3.2 Experiments

ZIF-67 is dispersed in ethanol and then dropped on silicon wafers. Laser reduction was performed after the evaporation of ethanol with the hotplate at 50 °C. Laser system was used for laser reduction. A 405 nm laser with 0.5 W was installed on a tailor-made X-Y moving table, which was controlled by computer. ZIF-67 was reduced by laser at different writing speed (1500 mm/min to 1000 mm/min) and hatch space (60 μm to 10 μm). Acetic acid was used to remove the residual ZIF-67 particles. After that, laser treated samples washed by deionized water and ethanol respectively. Samples were then dried in oven at 100 °C to remove residual solution.

Iron oxide pigments were used to dye oil in red for distinct observation. Castor oil and silicone oil were selected for oil absorption. The process of oil absorption and recycling for samples is shown in figure 5.14. Firstly, a drop of dyed oil was poured on water as oil spill. Subsequently, a spoon of samples was added as absorbents to absorb the spilled oil. A magnet covered by weighing paper was applied to absorb samples and remove them. Oil-absorbed samples were then washed by water and ethanol respectively with the support of ultrasonication to remove absorbed oil. Collected samples were then dried at 65 °C for 6 hours in oven for recycling.

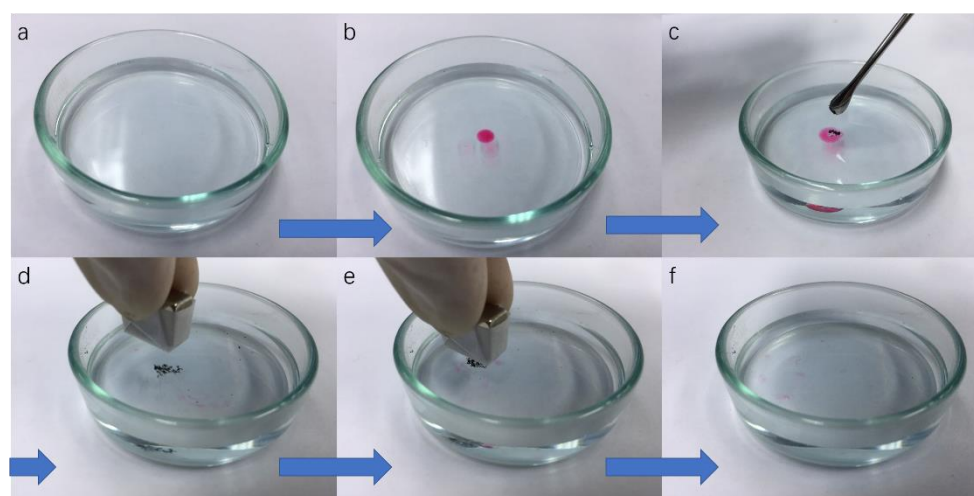


Figure 5.14. The process of oil absorption. (a) A dish of clean water. (b) a drop of dyed oil was spilled into water. (c) a spoon of samples was added to absorb oil. (d) samples absorbed oil completely. (e) a magnet was used to remove samples. (f) a dish of clean water after oil absorption.

The crystal structures of samples were identified by XRD with Cu K radiation (Rigaku SmartLab). The morphology and composition were studied by using SEM and

EDX spectroscopy (LEO 1530). For measuring magnetic properties, VSM (Lakeshore) was used to measure the magnetic hysteresis loop at room temperature.

5.3.3 Results and discussions

SEM was used to measure the morphology and microstructure of LR-ZIF-67 and ZIF-67, as shown in figure 5.15. It showed that the shape of ZIF-67 changed from regular dodecahedral shape to partially deformed shape after laser reduction. It was because laser generated tremendous energy, which breaks down the chemical bonds in organic frameworks. Numerous metal cores were decomposed and deposited on the particles' surface. This phenomenon was caused by both laser irradiation and thermal effect. Massive energy generated by laser irradiation broke down chemical bonds between organic ligand and cobalt (W. K. Yung, B. Sun, J. Huang, et al., 2016). The energy which can break down chemical bonds was defended as bond dissociation energy. Furthermore, heat generated by laser can carbonize ZIF-67 and simultaneously decompose and deposit cobalt particles into carbon matrix (Torad et al., 2014). Meanwhile, the structure of reduced samples was still stable after laser reduction. Some cavities were generated during this process. The larger porosity, cavity volume and pore size of LR-ZIF-67 resulted in larger absorption ability (Zhong, Liu, & Zhang, 2018). Samples tended to deform as writing speed decreased, while the deformation was not heavy, the structure still maintained polyhedral structure, as shown in figure 5.15c, d. ZIF-67 suffered from laser treatment in one time when the spot size was 60

μm . Residual carbon on sample provided protection of oxidation of particles core, thereby the oxidation only occurred on the surface. In contrast, when hatch space decreased to lower than $60\ \mu\text{m}$, samples suffered from laser treatment more than one time, which promoted the oxidation of inner part of particles and thereby changing the structure.

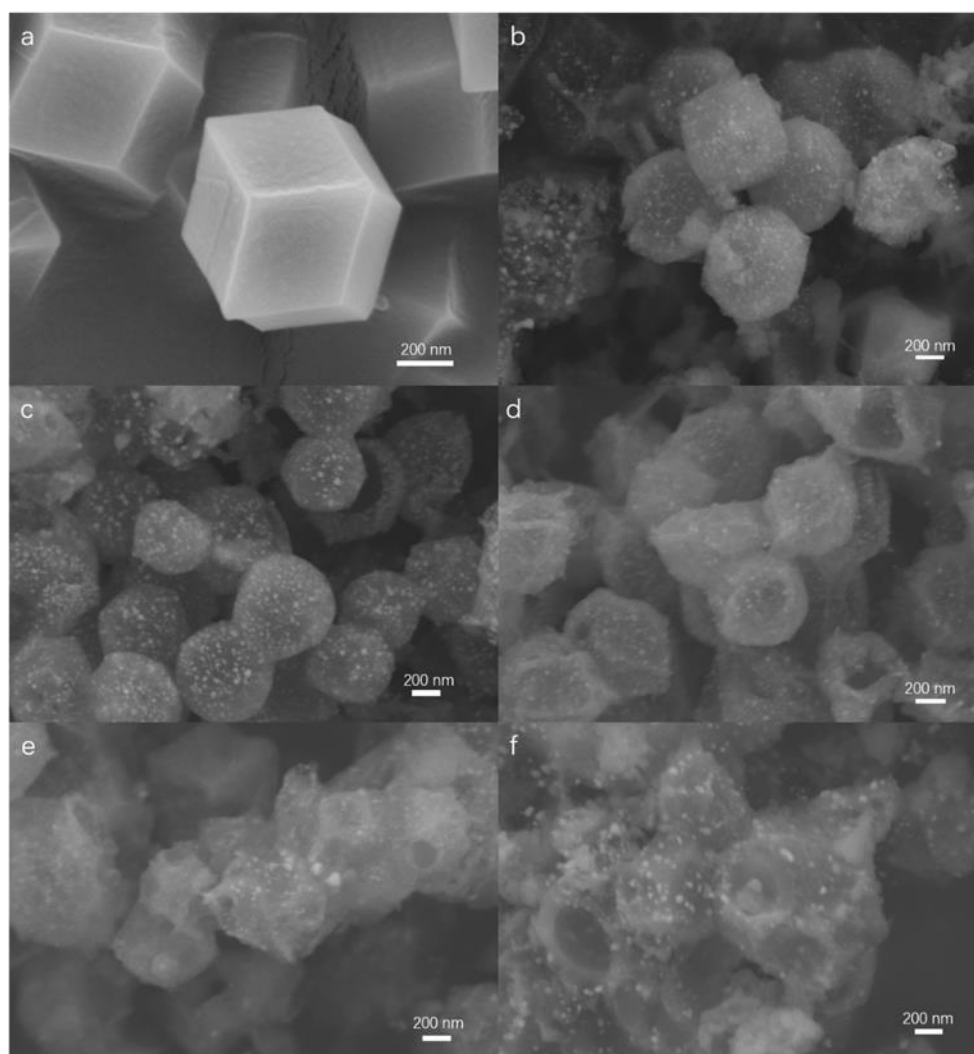


Figure 5.15. SEM image of (a) synthesized ZIF-67 (b-f) sample A to E respectively.

Table 5.1 displayed the results of EDX for the elemental content of samples. There were not any signal of oxygen can be detected since the low concentration in ZIF-67 and sample A. For sample B to sample E, the content of cobalt and oxygen increased with the decrease of that of carbon when hatch space and writing speed decreased. It was because the decrease of writing speed generated more energy by increasing the retention time, the connection for organic bond and metal was broke down, which resulted in the decrease of the content of carbon. Cavities were generated simultaneously, which provided paths for oxygen transportation.

Table 5.1. List of samples with different parameters and their element content.

Sample		ZIF-67	A	B	C	D	E
Hatch space (μm)		N/A	60	60	60	40	10
Writing speed (mm/min)		N/A	1500	1200	1000	1000	1000
Cobalt (%)	W	34.35	33.69	36.98	40.19	28	51.36
	A	9.64	9.38	11.07	12.5	7.59	18.65
Carbon (%)	W	65.65	66.31	53.23	48.81	61.72	36.69
	A	90.36	90.62	78.14	74.8	82.17	65.36
Oxygen (%)	W	N/A	N/A	9.79	11	10.25	11.95
	A			10.79	12.65	10.24	15.99

XRD was used to identify the crystal structures of LR-ZIF-67 and ZIF-67, as shown in figure 5.16a. XRD spectrum of synthesized ZIF-67 exhibited clear peaks, like (011) phase and (112) phase, for typical ZIF-67 crystal. Laser treatment on ZIF-67 completely changed the crystal structure, LR-ZIF-67 only exhibited the signal of

cobalt. Laser treatment on samples broke down the connection for organic bond and cobalt, baring the decomposed cobalt atom on top of sample's surface. This was similar to thermal reduction while the heat was generated by laser (Nishikawa, Nakajima, Kumagai, Okutani, & Tsuchiya, 2011). The intensity of signal for (200) phase for LR-ZIF-67 treated by laser with 60 μm hatch space was strong while that for sample treated by lower hatch space hid in background noise. It demonstrated that the crystal structure of samples was destroyed by laser treatment in multiple time.

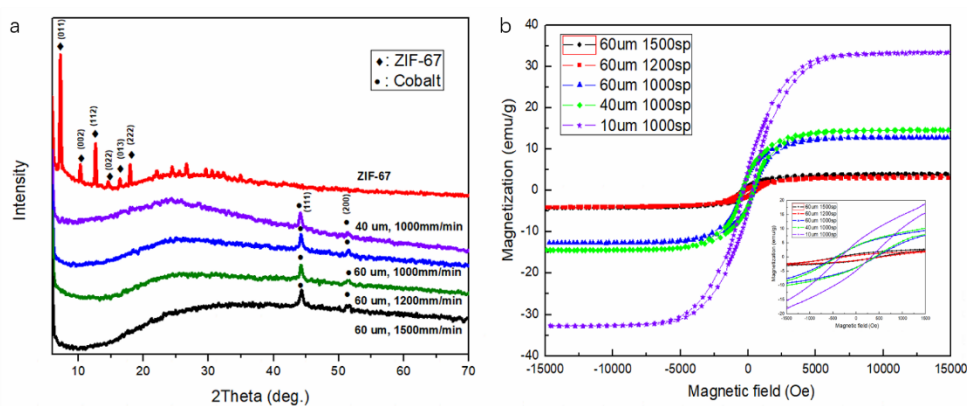


Figure 5.16. (a) XRD spectra and (b) hysteresis loop of samples.

Figure 5.16b showed the hysteresis loop of samples. The coercivity of sample A, B and C were 433.16 Oe, 410.91 Oe and 436.13 Oe, respectively. The change of writing speed did not affect magnetic properties of samples significantly. The value of saturation magnetization also displayed similar situation. While the value of saturation magnetization of sample C underwent a sharp increase to 12.78 emu/g by compared

with those of sample A (3.93 emu/g) and B (3.38 emu/g). It presented slower laser writing speed (1000 mm/min) can increase saturation magnetization by the increase of induced magnetic dipole moments. In contrast, the change of hatch space affected samples obviously on magnetic properties. As hatch space decreased, saturation magnetization increased while coercivity decreased. Coercivity of sample D and E were 410.91 Oe and 329.32 Oe, respectively. The extent of decrease of coercivity was high. When hatch space decreased to 10 μm , saturation magnetization increased to 33.35 emu/g. It was because the generation of magnetic domains inside cobalt increased. Meanwhile, the increase of cobalt resulted in the increase of magnetic phase, generating a stronger exchange in coupling interaction, therefore the remanent magnetization increased (S. Xu et al., 2018). Meanwhile, the increase in the extent of crystallization and density of domains also contributed to the increase in magnetization (M.-Q. Liu, Shen, Meng, SONG, & XIANG, 2010).

ZIF-67 reduced by laser showed magnetic behaviours and very high porosity. As a good oil absorbent, it requires high porosity and magnetic property. Therefore, reduced ZIF-67 is considered to absorb oil. Silicone oil and castor oil were selected for the test of oil absorption. Iron oxide pigments were used to dyed oil in red for distinct observation. The results of oil absorption capacity for samples is shown in figure 5.17a. It was clear that the capacity of oil absorption for silicone oil was much lower than that of castor oil. The values of capacity were 22.58 g/g and 37.96 g/g for silicone oil and castor oil respectively in average. Although the oil absorption capacity

of silicone oil was not as high as that of castor oil, it was almost as high as that for sponge in the literature (X. Zhou, Zhang, Xu, Men, & Zhu, 2013). Sample C has stronger ability for oil absorption for castor oil while sample B showed stronger ability for silicone oil. Overall, slower laser writing speed can enhance oil absorption capacity. The reusability of samples for castor oil and silicone oil was shown in figure 5.17b, c, respectively. The ability of repeatability of samples was relatively strong since the thermal stability of MOFs materials.

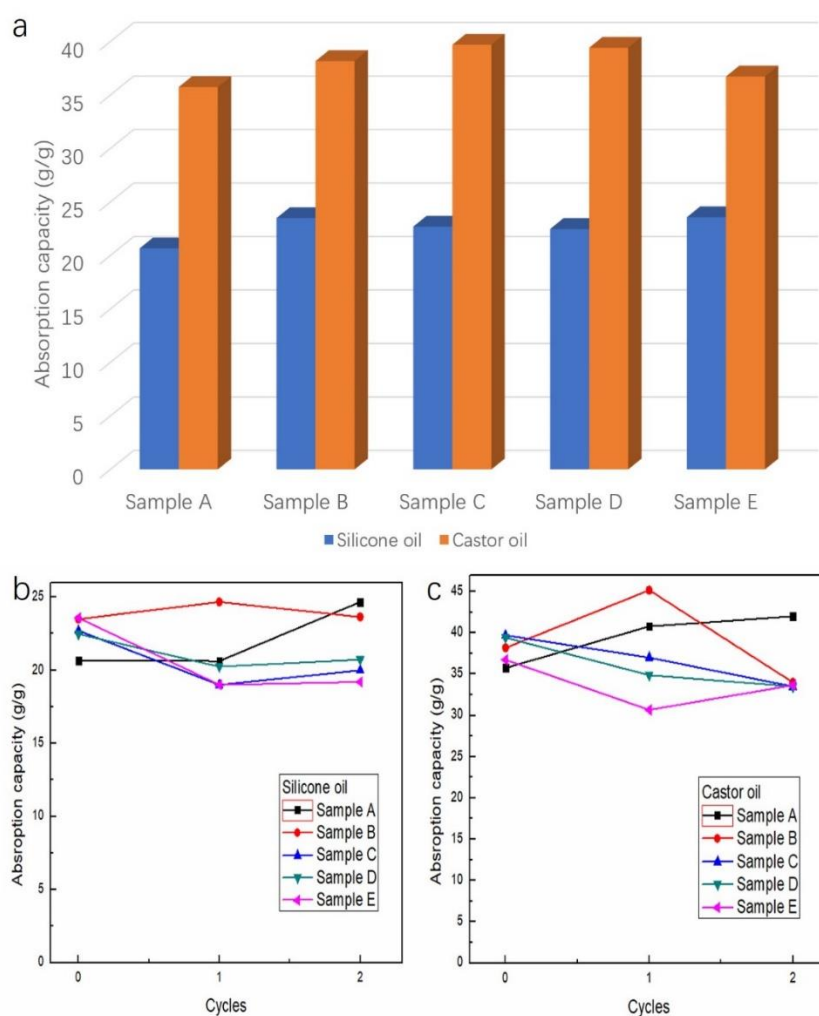


Figure 5.17. (a) oil absorption capacity of different samples for silicone oil and castor oil. Reusability ability of different samples in (b) silicone oil and (c) castor oil respectively.

Sample A was considered as the best sample with highest oil absorption capacity after recycling for both oils, as shown in the figure. Unfortunately, the ability of oil absorption tended to weaken when the recycling number was two. It was because that the cavity volume decreased due to the deformations of samples' structure resulting from the decrease of hatch speed and writing speed.

5.4 Inkjet printing

5.4.1 Introductory remarks

Inkjet printing is one of the AM methods for fabricating products with 3D structure by using ink, which is consisting of soluble materials and corresponding solvent. Inkjet printing of magnetic materials for 3D structure fabrication was widely explored recently. Its merits of low cost and ambient processing features endow it as promising AM method for fabricating 3D component, for example, flexible and miniaturized 3D micro devices (Dixon et al., 2016). Nanoparticle ink was proved to be the ink for inkjet printing method to fabricate 3D structural devices and applied in various applications. However, clogging issues still impede the development of inkjet printing with nanoparticle ink owing to the change of solubility and dynamic viscosity when time and temperature changes (Yung et al., 2009). Metal-organic material is applied as the ink for inkjet printing since this material can be completely dissolved into organic solvent, preventing sedimentation in the inkjet nozzle. Meanwhile, cobalt,

as one of the most important TMs with ferromagnetic properties, was widely studied in magnetic components. Cobalt-based thin films based on inkjet printing have been comprehensively studied. Therefore, applying inkjet printing method to fabricate magnetic devices by using cobalt-based metal-organic materials is promising and has become a priority.

In the work of my research, inkjet printing method was used to construct 2.5D structure multilayer patterns with ferromagnetic properties. Cobalt-based materials was used as raw materials and was dissolved into organic solvent to solve the material agglomeration issue. Microstructures, magnetic properties, and the optimum parameters of printed patterns were systemically studied by VSM, SEM, AFM, MFM and optical surface profiler.

5.4.2 Experiments

0.5 mmol $\text{Co}(\text{tpy})\text{Cl}_2$ MeCN was measured and dissolved into 1.5 ml dimethylformamide (DMF). The mixture solution was then filtered by a 0.22 μm size syringe filter after 30-mins ultrasonication. Glass slides and silicon wafers were used as substrates for research. They were cleaned by acetone, water and methanol in sequence with ultrasonication. The inkjet printing head with 30 μm width nozzle was fixed in a tailor-made X-Y moving table for patterning. The table was controlled by computer, the printing patterns were designed by AutoCAD software. The step spacing and the distance between nozzle and substrate were fixed at 0.15 μm and 0.4 mm

respectively. The speed for the moving stage was fixed at 500 mm/min. Printing delay and printing period for droplets were set as 704 μ s and 9650 μ s respectively. Hot plate was used to heat up substrates to 100 °C.

Revealed by VSM (Lakeshore), SEM (LEO 1530), AFM (Bruker NanoScope 8), MFM and optical surface profiler (Zygo), the microstructures, magnetic properties, and the optimum parameters of printed patterns were systemically studied.

5.4.3 Results and discussions

(1) Optimization of parameters

To optimize the dropping distance, patterns for overlapping individual drops were performed on the glass slides as substrates, as shown in figure 5.18. The droplet spaces were set as 80 μ m and 110 μ m as shown in figure 5.18a and figure 5.18b, respectively. The printing directions and the distances between each line were changed to distinguish the intersection for each drop. The diameter of the droplet was measured as 240 μ m in average. It was obviously to observe the coffee ring effect in the figure (Denneulin, Bras, Carcone, Neuman, & Blayo, 2011). Crystal-like materials were dispersed on the boundary of drop and produced distinct marks during solution drying.

Cobalt-based nanoparticles were dispersed on the boundary of drop primarily, the latter droplet dropped on the substrate and overlapped the former droplet's circle with intersection. Intersection areas were generated intensively since the diameter of droplet was larger than the distance between each line. Over-intersection of droplet generated

numerous partial-ring marks, resulting in worse accuracy of patterns. Additionally, printing direction did not show any significant influence for the patterns.

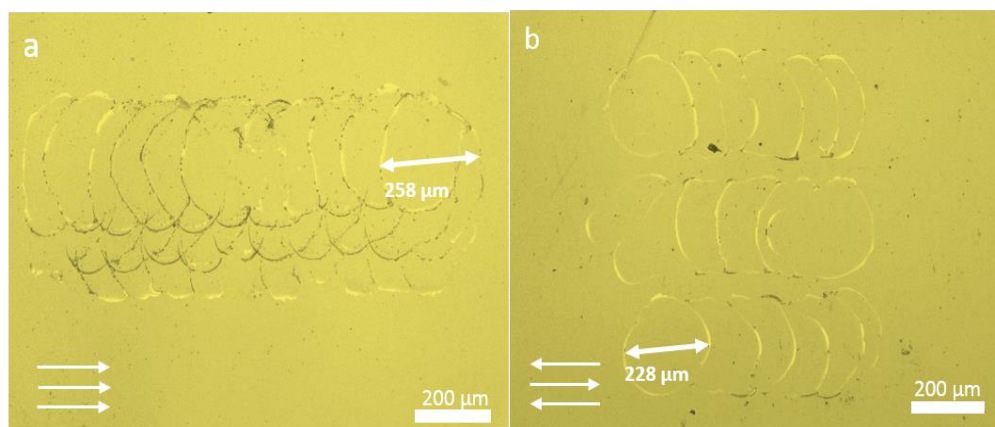


Figure 5.18. (a) multi-line patterns printed in 80 μm spacing distance (b) line patterns printed in 110 μm spacing distance.

Glass and silicon wafer were selected to investigate the influence of substrates. Cobalt-based nanoparticles were printed on these two substrates in identical parameters to ensure variables. The contact angles of the ink were measured as 16.2° and 17.6° for silicon wafer and glass respectively. The spreading ratio β can be calculated based on the spreading ratio equation (T. Lim et al., 2009). The ratio β for silicon and glass were 2.650 and 2.576 respectively. Figure 5.19 showed the optical microscopy images for glass and silicon wafer. The width of printed patterns was 804 μm and 513 μm for silicon wafer and glass slides respectively. Printed pattern in figure 5.19a revealed higher contrast to that in figure 5.19b. Glass slides still showed some inevitable darkness even they were cleaned systematically. While silicon wafer did not

show similar condition, because of the poor polishing of glass slide (Le Houerou, Sangleboeuf, & Rouxel, 2005). Meanwhile, the printing contrast can be enhanced by the increase of spreading ratio since evaporation time decreased. In addition to use appropriate substrate to enhance resolution, increasing the temperature of substrate also obtained similar results (Girard, Antoni, Faure, & Steinchen, 2006). Since the rise of temperature, the saturated vapor concentration increases consequently, thereby the evaporation time decreases. Based on certain spreading ratio, lower evaporation time leads to decrease for printing unit dimension, thereby enhances the printing resolution.

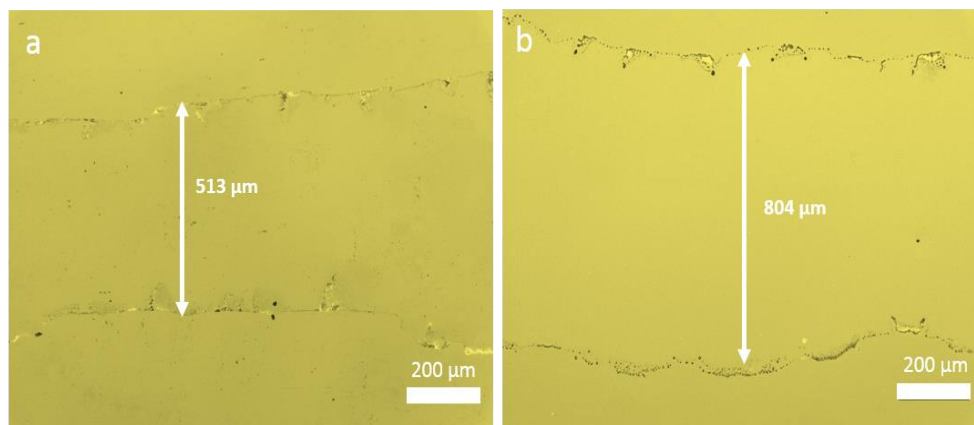


Figure 5.19. line pattern printed on (a) glass slide, (b) silicon wafer.

The morphology of printed patterns was measured by SEM, as shown in figure 5.20. Figure 5.20a, b showed printed patterns on glass and silicon wafer under same condition respectively. Cobalt-based materials exhibited cuboid structures as shown in the figure, ranging from 300 nm to 3 μm in length. It was obviously that cobalt-based

materials distributed on the substrate in ladder shape, increasing from center to edge. It was corresponding to the coffee-ring effects as mentioned before. However, some unexpected spot-type marks were observed on the substrate. There were more unexpected marks on the glass by compared to that on silicon wafer, which was caused by poor quality of surface and lower spreading ratio of glass. Meanwhile, the different thermal conductivity of these two substrates was also the reason for the different quality of printed patterns (Lim, Jeong, Chung, & Chung, 2009). It demonstrated that silicon wafer was the better substrate and it was used in the following study.

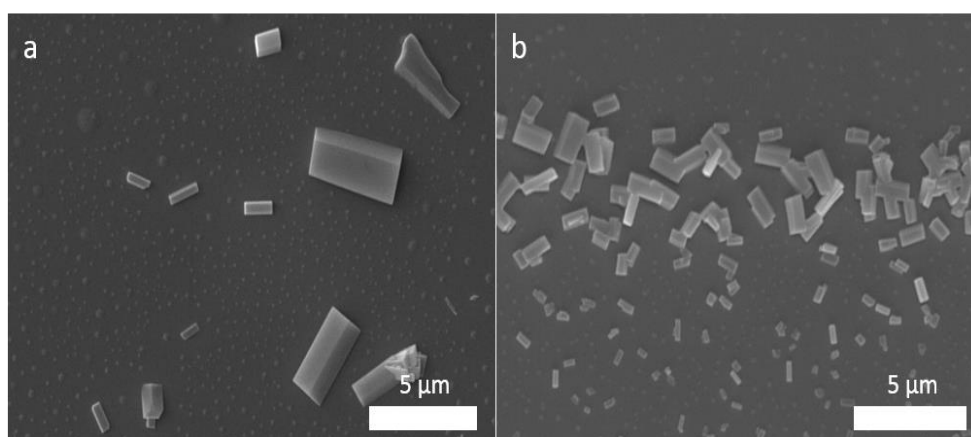


Figure 5.20. SEM images of printed patterns on (a) glass slide, (b) silicon wafer.

After the repeatedly printing, SEM image of a straight-line pattern on silicon wafers with 10-times repetitive printing was shown (figure 5.21b). As comparison, the image with one-time printing was also presented in figure 5.21a. Cobalt-based materials were dispersed on the substrate from boundary to center with a decreased

profile because of the coffee effects. As shown in figure 5.21a, cobalt-based materials recrystallized near the boundary and tended to mild aggregation. Figure 5.21b showed the printed pattern after 10-times printing, materials were superimposed vertically to form in 3D structure. The boundary showed critical superimposition and center part bestrewed concentrated nanoparticles. Materials in the boundary part mixed together and tended to agglomerate with substantial accumulation, as shown in the inset in figure 5.21b.

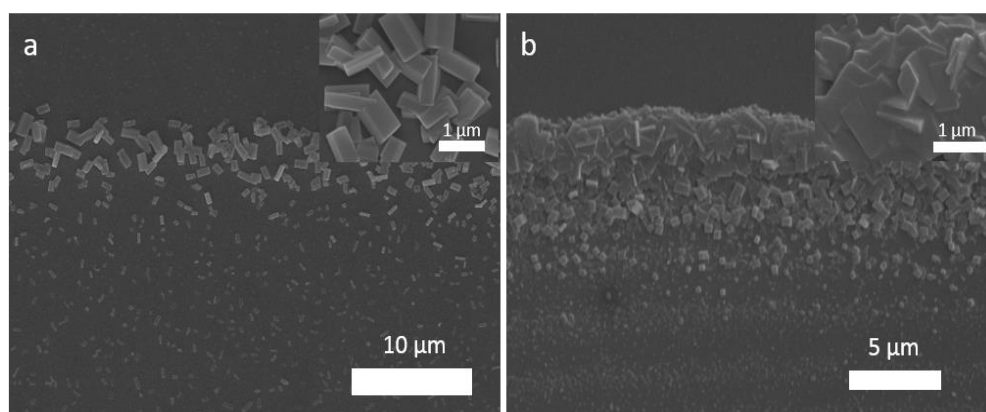


Figure 5.21. SEM images of printed patterns with (a) 1-time and (b) 10-times printing.

Printed pattern in multiple times with 3D structure was measured by SEM with a 15° incident angle view, as shown in figure 5.22a. A distinct line with considerable height was observed, which was constructed by inkjet printing in 200 times. With heating by hot plate, materials recrystallized rapidly and form in irregular shape. The accumulation of these irregular crystals constructed 3D structure. The magnified

image for this area was shown in figure 5.22b. The 3D structure of printed pattern was showed more distinct, the height of pattern was 10 μm .

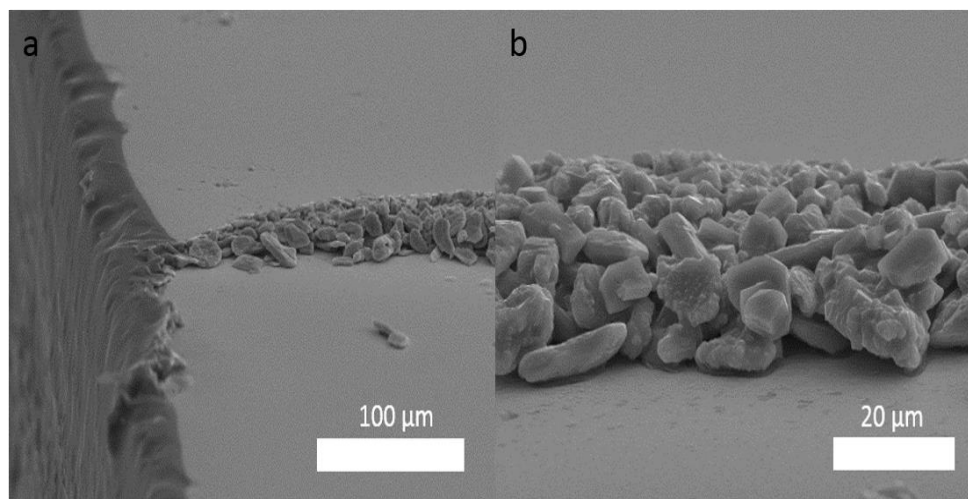


Figure 5.22. SEM images of printed patterns with 15-degree angle.

(2) Characterization for fabricated 3D structure of cobalt-based organic compound

3D morphologies of printed patterns were obtained by optical surface profiler (Zygo Nexview), as shown in figure 5.23. Multi-drop pattern in figure 5.23a was fabricated by 1000-times printing. The height of printed pattern was determined as around 20 μm . It demonstrated that the increase of printing time can continuously increase the height of pattern and fabricate 3D structure, which was correspondent to the mechanism of AM. Line pattern printed in 100 times was shown in figure 5.23b, its height was measured as 12 μm . 100-times printing can reach 12 μm height while

1000-times printing can only reach 20 μm , it demonstrated that the relationship between height and printing times was nonlinear, which was against the relationship between the thickness of printed samples and printing time (Shin, Hong, & Jang, 2011). As printing times increase, printed patterns tended to enlarge, which required more droplet adding to obtain higher thickness. In other words, it was because of the lateral development of sample. Printed droplets spread quickly and formed into mountain-shape. Heat transfer spread from the substrate surface to droplets. The bottom part of droplet, near the substrate, was easier evaporated. Due to high spreading ratio, droplets preferred to spread through horizontal directions. The heat transfer ratio decreased during the fabrication of materials. Accordingly, the growth speed of thickness decreases with the increase of printing time. This phenomenon can be reduced or eliminated with the increase of spreading ratio and substrate temperature. Accumulation in horizontal direction severely affected vertical 3D component fabrication.

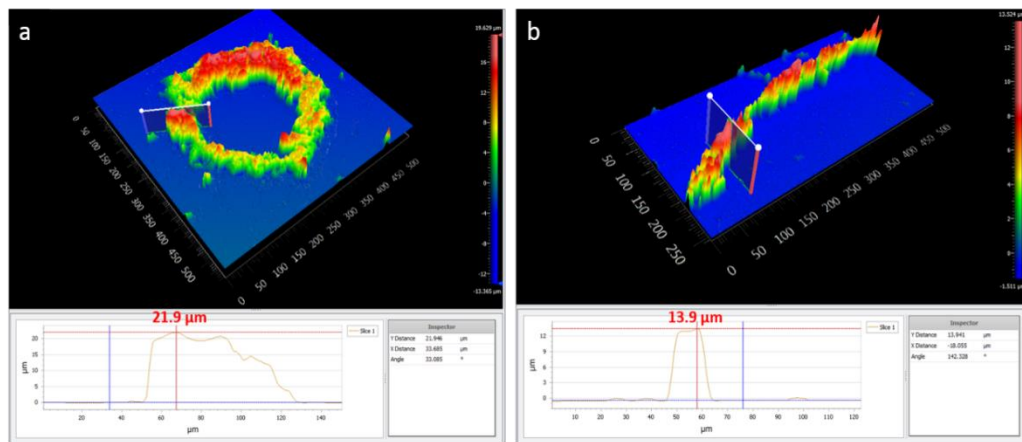


Figure 5.23. Optical surface profile images of (a) multi-drop pattern in 1000-times, (b) line pattern in 100-times.

The ferromagnetic properties of this material were characterized by VSM at room temperature as shown in figure 5.24. The result shows that the particles behave ferromagnetic with magnetic moments at 0.24 emu/g. The coercivity is approximate 50 Oe as in the zoom-in figure as the inset image of figure 5.24.

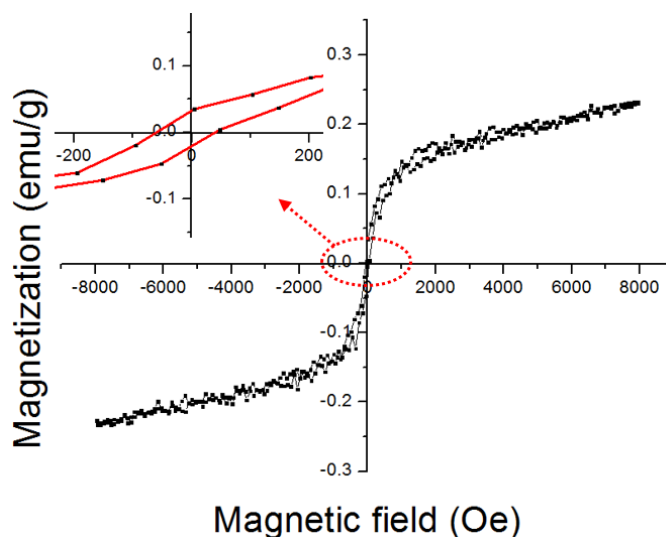


Figure 5.24. Magnetization loop for synthesized cobalt-based organic compound.

AFM and MFM were used to measure the topography and magnetic behavior for the pattern in one-time printing, respectively, as shown in figure 5.25. Magnetic contrast of MFM was consistent to that of AFM in bright and dark areas. It was obviously that materials tended to overlap and form circle shape. As shown in figure 5.23a, this overlapped samples showed 300 nm height. In figure 5.25b, magnetic contrast in MFM was corresponding to the topography in AFM. It demonstrated that printed cobalt-based materials exhibited strong magnetic signal, and they can accumulate proportionally as the increase of the amount of materials. It also proved

that sample's topography and magnetic property were homogenous. As shown in figure 5.25c, the cross-section profile of sample was measured as the white line shown in figure 5.25a to present height information. The non-uniform profile revealed that materials aggregated by nanoparticles rather than single crystals, which was different from what was observed in SEM images.

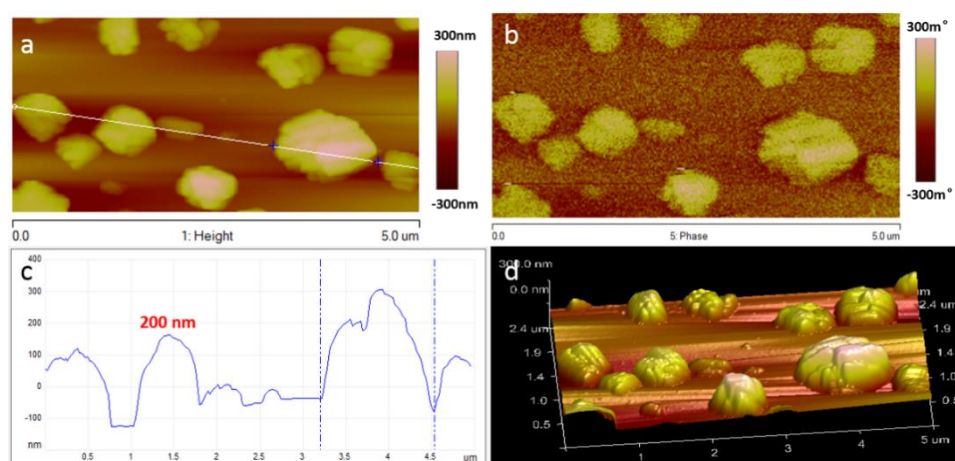


Figure 5.25. (a) AFM images and (b) MFM image of the printed crystals. (c) cross-section profile, (d) 3D view.

The aggregation of particles resulted from the break of the force balance caused by the evaporation of solvent (Vaseem, Lee, Hong, & Hahn, 2012). The average height of samples was measured as 200 nm. Figure 5.25d showed the 3D view of AFM image. Samples tended to aggregate on the surface spatially. The pattern showed on the substrate can be identified as accumulation of several particles rather than single particles based on the images of height profile and 3D view. It again demonstrated that magnetic contrast of MFM was corresponding to the topography of AFM.

Printed materials accumulate as printing time increases in inkjet printing process, which contributes to the fabrication of 3D structure layer by layer. However, the relationship between printing time and height of sample is not linear since the lateral extension of materials. This seriously affects the efficiency of 3D structure fabrication. Meanwhile, the “coffee ring” morphology should be eliminated in the future by an increase of the temperature in the substrate (J. Wu et al., 2015).

5.5 Concluding remarks

In this chapter, laser system and inkjet printing method were developed to fabricate 3D structures for copper, cobalt and cobalt-based organic compounds. In the study of these 3D structure fabrication processes, the following were found:

(1) Modified SLS was used to fabricate copper circuit lines with a 0.5 W and 405 nm laser. Electrical resistivity of reduced copper reached $1.46 \times 10^{-6} \Omega\text{m}$, which is slightly larger than that of bulk copper ($1.68 \times 10^{-8} \Omega\text{m}$). Electroless plating was used to decrease the electrical resistivity to $1.29 \times 10^{-7} \Omega\text{m}$ by coating the laser treated area. XRD and EDX were used to confirm the photochemical reduction of samples. By applying this method, various substrates, including PLA, FR-4, polyimide and glass, can be used to fabricate copper circuit in 3D structure.

(2) A mixture of PMMA and malachite was developed as a coating material used for 3D printed objects. Copper was reduced by laser in one step. The photochemical

transformation processes and material properties were comprehensively studied. Laser selectively transferred coating on 3D printed objects into copper as an electronic circuit. XRD was used to identify the laser reduced materials. This approach can provide a novel solution for providing metal coatings on 3D printed objects.

(3) ZIF-67 was successfully reduced by laser to obtain ferromagnetic porous carbon materials and the optimized parameters, such as hatch space and writing speed, was determined. The laser treated samples still maintained a polyhedral structure with embedded cobalt particles. The capacity for castor oil (37.96 g/g) was higher than that for silicone oil (22.58 g/g). The optimized parameters for the oil absorption capacity consisted of a 60 μm hatch space and 1000 mm/min, and 1200 mm/min for castor oil and silicone oil, respectively. 1500 mm/min writing speed was the optimum parameter for reusability after recycling.

(4) Cobalt-based materials ($\text{Co}(\text{tpy})\text{Cl}_2 \cdot \text{MeCN}$) were used and completely dissolved in DMF as an ink for inkjet printing. The optimum droplet spacing for inkjet printing on silicon substrates was 110 μm according to the optical surface profiler results that demonstrated the fabrication of a printed pattern with a 3D structure. Magnetic behavior printed sample was measured, and the results indicated that they corresponded to the topography.

The investigation of 3D structure fabrication using laser system and inkjet printing revealed advantages and disadvantages for fabricating SmCo alloys by using

these two processes. If laser system is used to fabricate 3D structure comprising SmCo alloy, SmCo alloy can be selectively fabricated on target substrate or on target objects as a coating. The effectiveness of sufficient laser energy on the reduction of samarium ascorbate and cobalt ascorbate is essential to be evidenced. Meanwhile, the adhesive force between alloy and substrate is low. Furthermore, the waste of un-pattered parts by laser is high. If inkjet printing is used to fabricate 3D structures comprising SmCo alloy, samarium ascorbate and cobalt ascorbate can be fabricated into 3D structures before sintering. However, the thickness of fabricated product is low.

Chapter 6 Study on crystal structure and magnetic properties of alloy materials

Alloy materials play irreplaceable roles nowadays in industrial and commercial applications, and many devices, pieces of equipment and commodities comprise functional alloy materials. Alloy materials with magnetic behavior also arouse attention since they present limitless potential for application in electronic instruments, magnetic storage, permanent magnets and catalysis (Akhtar et al., 2017; Bu et al., 2018; Z. Zhang et al., 2015). However, fabrication of magnetic alloy materials with 3D structure is still explored limited. Laser sintering, as an outstanding AM method, can be applied to fabricate alloy materials with 3D structures. Due to the thermal sensitivity of magnetic materials, laser power, laser scanning speed, hatch space and sintering times are necessarily studied. Furthermore, the inner magnetic dipole interaction of magnetic materials has a significant effect on the crystal structure, therefore, the correlation between them is necessary to be studied.

Moreover, environmental concerns are widespread, and the consideration of non-hazardous synthesis was proposed. The method for synthesizing required materials without further waste or hazardous byproducts has been thoroughly studied recently. Metal-organic compounds can be used as precursors to synthesize alloys by using green and non-hazardous starting materials and solvents. However, the decomposition of metal-organic compounds is always accompanied by exhaust gas, such as CO₂ and

H₂O. Temperature control during debinding and sintering is important since inappropriate operation results in cracks on the sample surface or even a break down. Therefore, research on optimum parameters for laser sintering of magnetic materials and thermal effects on 3D alloy preparation were studied in my work.

In previous chapters (chapter 4 & 5), the synthesis of metal-organic compounds and the 3D structure fabrication technologies were illustrated and studied. As a result of these approaches, fabricated samples with 3D structures can be sintered into alloy forms for further application and research. Therefore, in this chapter, samples with 3D structures are sintered into alloy forms and the crystal structure and magnetic properties are also studied with parameter optimization.

The crystal structure and magnetic properties impacted by heat generated during sintering process, and their exploration motivated this chapter. Therefore, control laser sintering and thermal sintering parameters is significant important in the optimization of crystal structure and magnetic properties. Furthermore, crack formation and structure destruction are also other problems that occur during the sintering process that need to be eliminated.

6.1 Laser sintering

6.1.1 Introductory remarks

Samarium-cobalt magnets have attracted significant attention as promising ferromagnetic materials, and they can be applied in various areas, such as in aerospace, micro-electro-mechanical systems and automotive industries. However, fabrication of samarium-cobalt magnets into flexible shapes still limits their development due to their easy oxidation and phase distortion, processing constraints and high thermal sensitivity. Herein, laser sintering was used to fabricate 3D parts with cylindrical shapes of SmCo₅ materials successfully. Meanwhile, the impact for the parameters on materials' magnetic properties and crystal structure of the materials during laser sintering was also studied systematically. These parameters included sintering times, scanning speed, laser power and hatch space.

6.1.2 Experiments

Laser sintering processed in the Optomec LENS MR-7 laser machine with argon gas protection. The laser wavelength was 1070-nm. Oxygen content was lower than 200 ppm. 0.5g purchased SmCo₅ powders (Sm 33 wt%, Alfa) were spread on the substrate (stainless-steel board) uniformly with compression for pre-sintering preparation. The thickness of each powder layer is 200 μ m. Since the thickness of powder layer can affect the density of sintered samples and it is also dependent on

penetration depth of laser radiation, the thickness is required to be determined for the efficient connection for the upper and lower layers during laser sintering.

The first layer was the sacrificial layer. This layer was comprised of sintered SmCo₅ powders at 200W. The function of this layer was the enhancement of combining force between substrate and sample. In other words, this layer acted as the compatible interface. Equivalent amount of SmCo₅ powders were measured and compressed with 8 Mpa pressure for densification. After that, SmCo₅ was spread on the substrate and sintered by laser. In this study, a group of parameters were studied, they were hatch space, scanning speed, laser power and laser sintering times.

The spot size for laser head was 450 μm . However, as shown in figure 6.1, the effective area for laser on materials was only 350 μm width. It is because that the typical temperature field on sample surface in laser sintering is in ellipses shape, the outmost part of laser does not generate sufficient energy to sinter SmCo₅ materials (Zeng, Pal, & Stucker, 2012). Meanwhile, as shown in figure 6.1, there were two small verge areas on two sides of effective area. This phenomenon resulted from the nature of laser energy distribution. These verge areas around 50 μm as figure shown. In order to compensate the energy loss of these areas, hatch space was changed to 250 μm . Therefore, to explore this factor systematically, hatch space for laser sintering was set as 450 μm , 350 μm and 250 μm respectively. Meanwhile, other parameters, such as laser scanning speed, laser power and sintering times, were studied ranging from 1270

mm/min to 1778 mm/min, from 100W to 200 W, and from 1 time to 3 times, respectively. The details were shown in table 6.1, table 6.2 and table 6.3 respectively.

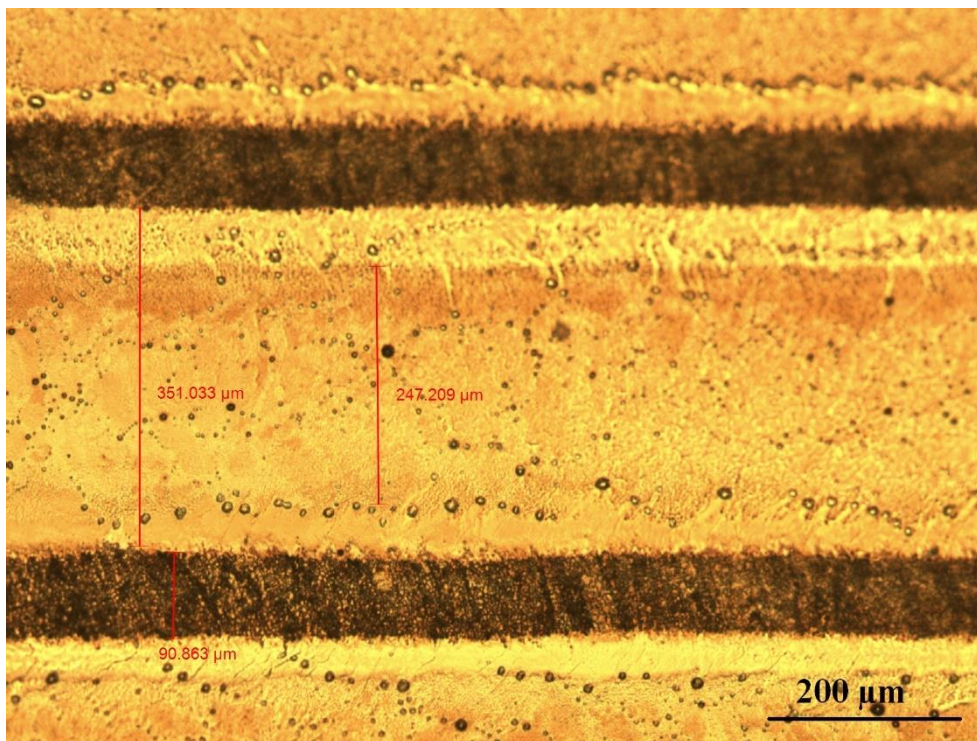


Figure 6.1. Optical microscope image of sintered surface with 450 μm hatch space.

Crystal structures of samples were identified by XRD with Cu K radiation (Rigaku SmartLab). The morphology and magnetic properties were measured by SEM and VSM (Lakeshore) respectively.

6.1.3 Results and discussions

The SEM image and particle size distribution for purchased SmCo_5 powders were shown in figure 6.2a and b respectively. Obviously the purchased SmCo_5 powders

presented irregular shapes, and they tended to agglomerate in to small part randomly. However, normal raw materials for laser sintering are demanded with spherical shape because this shape provides strong flowability and ensures minimal contact between particles causing a reduction in friction (Berretta, Ghita, Evans, Anderson, & Newman, 2013). Irregular shape of purchased powders impeded the ability of conveying and replenishment seriously during laser sintering. In order to solve this problem, powders were spread layer by layer rather than dusting directly during laser sintering. As shown in figure 6.2b, the average particle size was 5.41 μm . The unsymmetrical distribution is potentially caused by the irregular powder morphology, and the potential agglomeration of the powder particles during the measurement. However, owing to the magnetic behavior of the particles, some small particles agglomerated and formed large parts, which leading to some large particles in the SEM images.

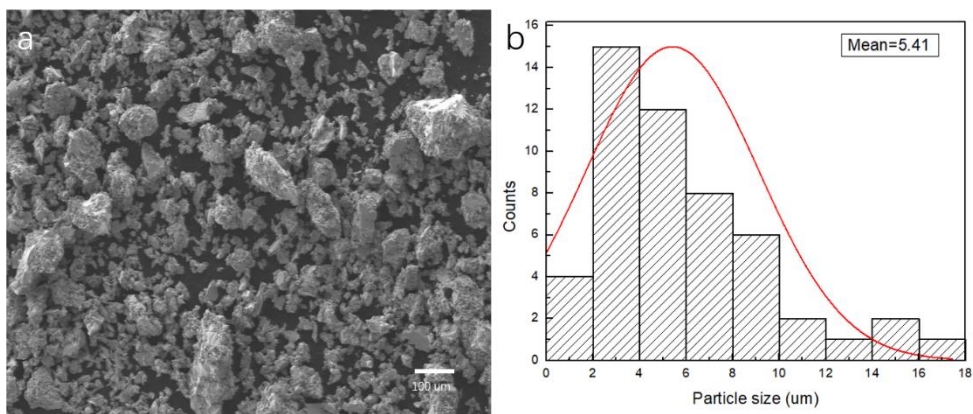


Figure 6.2. (a) Morphology and (b) particle size distribution, for purchased SmCo_5 powders.

The purchased SmCo_5 powders were identified by XRD and VSM, respectively, for crystal structure and magnetic properties characterization (Figure 6.3). The XRD spectrum showed in figure 6.3a exhibited distinct typical SmCo_5 crystal structure, such as (101), (110), (200) and so on. All the peaks of SmCo_5 are clear. The relevant magnetic behavior was also characterized and shown in Figure 6.3 b. The SmCo_5 powder exhibited typical ferromagnetic behavior with saturation magnetization of 102.58 emu/g and strong coercivity of 1589.38 Oe, as presented in the figure.

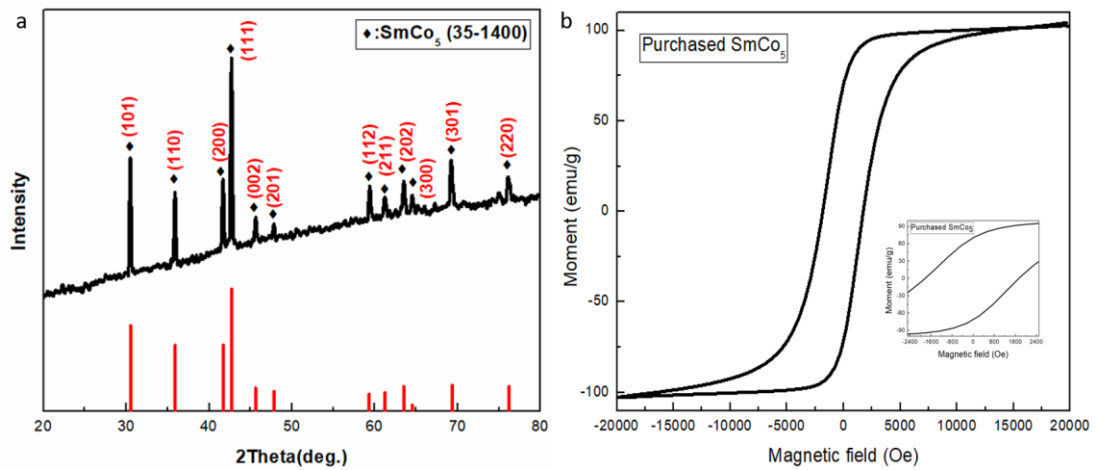


Figure 6.3. (a) XRD spectrum and (b) Magnetic properties, for purchased SmCo_5 powders.

(1) 450 μm hatch space

Since the spot size of laser was 500 μm , hatch space was set to 450 μm to eliminate the gap between sintered line. Parameter setting was shown in table 6.1. In this section, laser scanning speed, laser power and sintering times are the major variables to be studied.

Table 6.1. Parameter setting for laser sintering in 450 μm hatch space.

Sample	Laser power (w)	Laser scanning speed (mm/min)	Sintering times	Coercivity (Oe)	Saturation magnetization (emu/g)
1	100	1270	1	1295.5	69.8
2	150	1270	1	460.3	41.5
3	200	1270	1	890.5	26.0
4	100	1270	2	1566.0	58.0
5	100	1524	2	755.4	67.0
6	100	1778	2	770.1	43.0
7	100	1270	3	1126.9	64.6

The influence of laser power on crystal structure and magnetic properties of SmCo_5 was studied. Laser power ranged from 100 W to 200 W as table 6.2 shown. Laser scanning speed and sintering times were set as 1270 mm/min and 1 time respectively to ensure only one variable in this research. When laser power was 200 W, sintered sample started deforming and the color turned into black. Based on XRD spectrum, it presented that SmCo_5 cannot suffer from large laser power as 200 W. Such high laser power can provide massive heat as thermal effect, which tended to melt SmCo_5 into liquid phase. Small amount of SmCo_5 was melted and became cobalt and samarium oxide. Samarium was easier oxidized since it has negative standard potential comparing to cobalt (Gómez, Cojocar, Magagnin, & Valles, 2011). The crystal structure and magnetic hysteresis loop were shown in figure 6.4. SmCo_5 sintered by laser under 100W still exhibited obvious crystalline peaks of SmCo_5 in (101), (110), (200) and (111) phases. When laser power increased to 150W, sample exhibited crystalline peak of SmCo_5 with weak intensity. Sample sintered by laser with 200W

exhibited strong crystalline distortion, obvious crystalline signals of Sm_2O_3 and Co were showed. It was corresponding to sample's color, sample tended to turn into black presenting distortion began. 200W laser power caused deforming for SmCo_5 and decomposed into Sm and Co. Owing to the stronger oxidation ability of RE element by compared with that of transition element, samarium was oxidized into samarium oxide. Laser power was proved as a sensitive parameter in laser sintering for SmCo_5 , and it was corresponding to the nature of magnetic materials for their thermal sensitivity. As shown in figure 6.4 (b), saturation magnetization decreased as laser power increased, which was caused by heavy distortion of crystal structure of SmCo_5 . Coercivity of samples also decreased as laser power increased. While coercivity of sample sintered in 200 W larger than that in 150 W. It was because the full distortion recrystallized sample into cobalt, which also revealed relatively high coercivity.

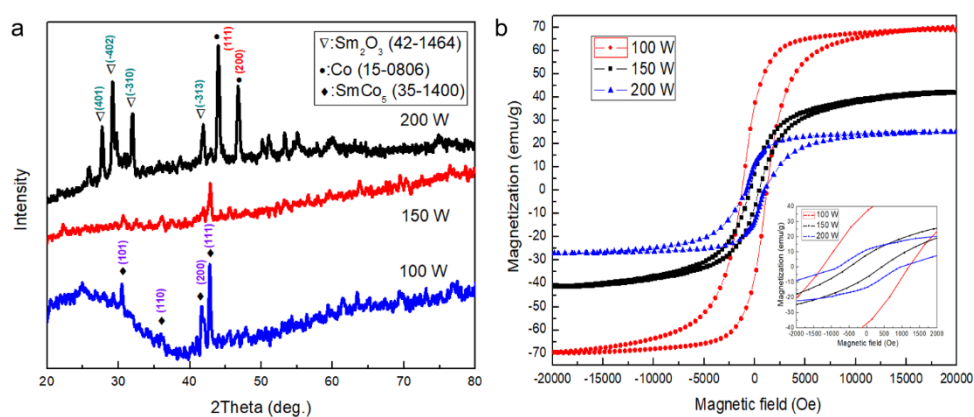


Figure 6.4. (a) XRD spectrum of SmCo_5 sintered by different power. (b) Magnetic hysteresis loop for SmCo_5 sintered by different power.

The XRD spectrum and hysteresis loop of samples sintered by different scanning speed were shown in figure 6.5. Laser power and laser sintering times were set as 100 W and 2 times respectively. Based on XRD spectra showed in figure 6.5 (a), samples exhibited clear typical crystalline signal of SmCo_5 materials, it demonstrated sintering speed was not a sensitive parameter in laser sintering for SmCo_5 by compared with laser power. However, the decrease of laser scanning speed also brought obvious influence on crystal structure and magnetic properties of SmCo_5 . Intensity of signal for sample became stronger as scanning speed increased to 1524 mm/min, while it dropped down when the speed continuously increased.

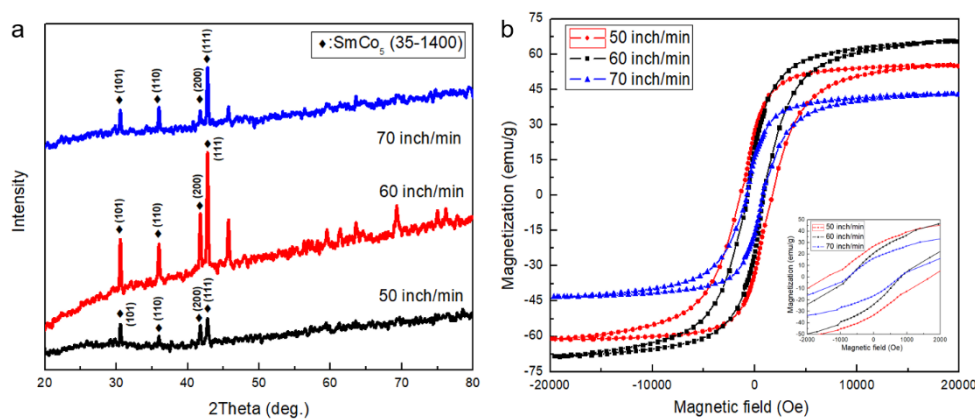


Figure 6.5. (a) XRD spectrum of SmCo_5 sintered by different speed. (b) Magnetic hysteresis loop for SmCo_5 sintered by different speed.

Faster laser scanning speed resulted in shorter illumination time of laser on samples, which thereby reduced thermal distortion on samples. However, when laser scanning speed decreased to 1778 mm/min, weaker laser power caused by shorter laser

illumination time could not bring adequate power to diffuse heat uniformly. Therefore, the crystallization of sample sintered by laser in 1524 mm/min was better than that of sample sintered by laser in 1778 mm/min. The vibration of saturation magnetization of samples was corresponding to the crystallization level of samples. The value of saturation magnetization of samples suffered from a fluctuation with a maximum value when speed was in 1524 mm/min. The increase of magnetization led to the decrease of inter-particle dipole interaction, and thereby decreased coercivity (Pramanik & Banerjee, 2010). Samples sintered by laser in 1778 mm/min did not exhibit high coercivity, it was because the uneven heat for the sample affected the crystallization of SmCo_5 materials and then decreased the coercivity of sample.

Sintering times was another parameter to be discussed. Figure 6.6 showed XRD spectrum and hysteresis loop of samples sintered by different sintering times. Laser power and scanning speed were 100 W and 1270 mm/min respectively. The increase of sintering times distorted crystal structure.

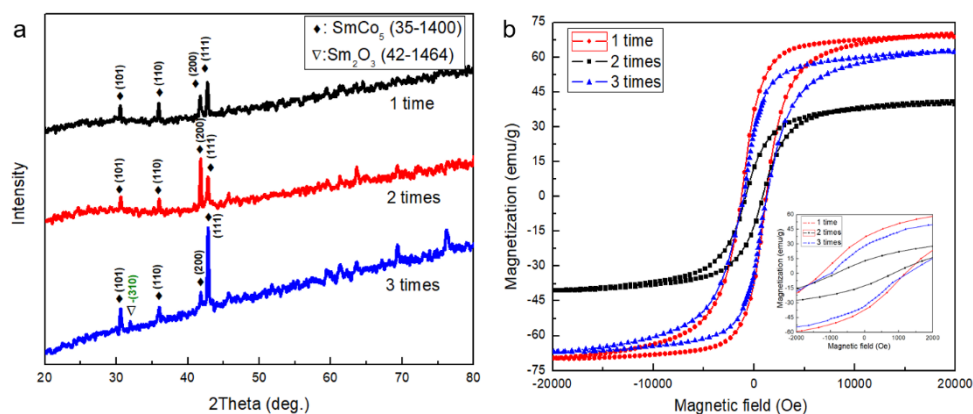


Figure 6.6. (a) XRD spectrum of SmCo_5 sintered by different sintering times. (b) Magnetic hysteresis loop for SmCo_5 sintered by different sintering times.

When sintering times was two-times, intensity of signal for (200) phase was larger than that for (111) phase while the whole XRD spectrum still present obvious crystalline structure of SmCo_5 materials. When sintering times increased to three, a weak signal of Sm_2O_3 was detected. Sample overheated by laser, part of samarium was separated and oxidized into samarium oxide. Furthermore, increase of sintering times also brought negative influence on magnetic behaviors. Coercivity and saturation magnetization of samples decreased as sintering times increased, except the sample sintered in 3 times, which revealed better saturation magnetization than that of sample sintered in 2 times. To sum up, increase of sintering times brought negative influence in both crystallization and magnetic behaviors.

Optical microscope was used to observe samples' surface. As figure 6.1 shown, laser treatment did not cover the whole substrate. Some thin dark lines, which was considered as untreated area, can be observed. It presented that laser scanning area was only around $350\ \mu\text{m}$, which was smaller than laser spot size ($500\ \mu\text{m}$). It was because laser curing area was $500\ \mu\text{m}$ while the heating distribution was not uniform, the central part was the higher, the boundary was lower, as we mentioned previously. The input of laser power determined the thermal history, influencing the energy density for the sample surface. Heat lost due to convection and radiation during lasering sintering also reduced energy density. This energy density was determined by laser power, scanning speed, laser beam spot size, layer thickness and hatch spacing (Z. Liu, Li, Fang, & Guo, 2018). These factors simultaneously influenced the heat transfer from

laser to sample, and thus, resulting in smaller sintered area by compared with the width of spot size. The influence area for laser sintering was around 350 μm . These untreated lines exhibited 90 μm width. In other words, the clearance between each laser scanned mark was around 90 μm . To eliminate untreated area, laser hatch space reduced from 450 μm into 350 μm . Due to the nature of laser energy distribution, the verge sections of laser energy were relatively low (Nerush et al., 2011). Based on figure 6.1, the verge area of laser was around 50 μm at each side. Therefore, to compensate the energy loss of the area, the hatch space reduced to 250 μm .

(2) 350 μm and 250 μm hatch space

In the coming part, the research on the thermal effect on magnetic properties and crystal structure focuses on two hatch spaces, 350 μm and 250 μm , respectively. As mentioned previously, the effective area for laser on SmCo_5 powders was 350 μm . The width for the verge area with lower energy was 50 μm . The other parameters in the study were scanning speed, laser power and laser sintering times. Detail studies on parameters setting were showed in table 6.2 and table 6.3 respectively.

Table 6.2. Parameters setting for laser sintering and magnetic properties for sintered samples (350 μm hatch space).

Sample	Laser power (w)	Laser sintering speed (mm/min)	Sintering times	Coercivity (Oe)	Saturation magnetization (emu/g)
A	100	1270	1	720.9	68.7
B	120	1270	1	770.5	64.3
C	150	1270	1	424.5	68.8
D	100	1524	1	803.4	52.2
E	100	1778	1	629.6	42.6
F	100	1270	2	783.5	67.4
G	100	1270	3	502.6	61.8

Table 6.3. Parameters setting for laser sintering and magnetic properties for sintered samples (250 μm hatch space).

Sample	Laser power (w)	Laser sintering speed (mm/min)	Sintering times	Coercivity (Oe)	Saturation magnetization (emu/g)
H	100	1270	1	755.8	86.5
I	120	1270	1	1209.2	34.7
J	150	1270	1	1586.4	83.5
K	100	1524	1	638.2	72.4
L	100	1778	1	640.9	71.4
M	100	1270	2	888.2	81.3
N	100	1270	3	508.5	56.6

SmCo₅ powders were sintered by laser into a small part successfully as shown in figure 6.7. Sintered part still maintained cylindrical structure as required. However, some spots were occurred on the surface, it was because that SmCo₅ powders absorbed massive laser energy, and then they expanded and formed many small spots by the agglomeration.



Figure 6.7. Laser sintered sample with cylindrical shape.

Firstly, hatch space was set as 350 μm . XRD spectrum and magnetic hysteresis loop of sample A to C were displayed in figure 6.8 Laser sintering times and scanning speed were set as 1 time and 1270 mm/min respectively to make sure one variable in this serial research. The first variable is laser powers, it ranged from 100 W to 150W. As shown in XRD spectrum (figure 6.8a), sample A to C still exhibited distinct characteristic peak of SmCo_5 materials. While the intensity of signal for (101) and (200) phases were very weak. It demonstrated that if laser power larger than 150 W, crystal structure of SmCo_5 materials may seriously be distorted, and the worse, deformed into oxidation status. When 100W laser treated on SmCo_5 materials, heat generated by laser did not bring significant negative influence on materials' crystal structure. Similar situation happened when laser power increased to 120 W. Interestingly, signal of (200) phase mildly weakened while signal of (101) phase

strengthened relatively when laser power increased. Larger heat generated from laser with larger power persistently affected the exhibition of (200) phase of crystal of SmCo₅ materials. As laser power continuously increased (150 W), intensity of signal for (200) phase strongly weakened. In contrast, intensity of signal for (101) phase also strongly weakened. It demonstrated that mild heat treated on SmCo₅ materials can relative enhanced intensity of signal for (101) phase, while crystalline structure tended to deform with continuous increase of heat. Magnetic property of samples was shown in figure 6.8 b. The value of coercivity and saturation magnetization for samples were shown in table 6.2 and table 6.3 for better observation and analysis. The coercivity of sample A to C were 720.9 Oe, 770.5 Oe and 424.5 Oe respectively. Obviously, they were significantly lower than those of original one, since magnetic property of materials is very sensitive to temperature (N. Wang et al., 2018). Plenty of heat generated by laser rose up the temperature of sample instantaneously and thereby weakened coercivity of SmCo₅ materials. Similarly, saturation magnetization of sample A to C dropped to 68.7 emu/g, 64.3 emu/g and 68.8 emu/g respectively. It was apparently the relationship between laser power and magnetic was not linear. As laser power increased (120 W), coercivity of sample grew up to 770.5 Oe while saturation magnetization declined to 64.3 emu/g. Mild rise of laser power resulted in the increase of coercivity owing to the increase of inter-particle dipole interaction resulting from better crystallization of (101) phase and (110) phase. Furthermore, stronger dipole interaction can suppress coupling interaction of materials, which leads to the decline

of magnetization (S. Xu et al., 2018). When laser power dropped to 150 W, larger power seriously distorted crystalline structure and weakened dipole interaction between particles, which thereby decreased coercivity.

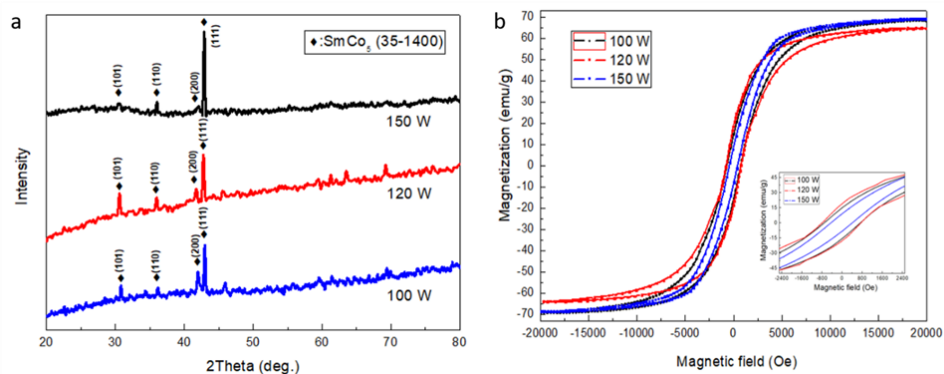


Figure 6.8. (a) XRD spectrum and (b) magnetic hysteresis loop, for sample A to C.

XRD spectra and magnetic hysteresis loops were shown in figure 6.9 for the analysis of the influence of laser scanning speed on SmCo₅ materials during laser sintering. Laser sintering times and laser power were set as 1 time and 100 W respectively. As shown in XRD spectra, sample A, D and E exhibited typical crystalline signal of SmCo₅ materials clearly. The change of scanning speed brought apparent influence on intensity of signals. While the crystal structure did not suffer from a clear deformation as the change of laser power, especially for (110), (200) and (111) phases. As scanning speed increased, intensity of signal of (200) and (111) weakened continuously. Duration of laser on SmCo₅ materials decreased as the scanning speed increased. Since laser power remained 100 W, the momentary energy

generated by laser was identical. Figure showed that shorter duration of laser on materials displayed a fade of crystallization in both (111) and (200) phase. It proved adequate heat produced by laser resulted in better crystallization and formation of energy self-diffusion homogeneously (Mirzadeh & Parsa, 2014). Shorter duration of laser brought negative influence in crystal structure. It was because rapid cooling rate resulted from low duration time of laser because of worse crystallization (Krüger & Deubener, 2016). The coercivity of sample D increased to 803.4 Oe while the saturation magnetization decreased to 52.2 emu/g by comparing with those of sample A. Shorter duration time for laser mildly increased inter-particle dipole interaction, which lead to the increase of coercivity and the decline of magnetization. When scanning speed grew to 1778 mm/min, sample E showed lowest coercivity (629.6 Oe) and magnetization (42.6 emu/g). As a whole, faster scanning speed weakened materials' magnetic properties and crystallization.

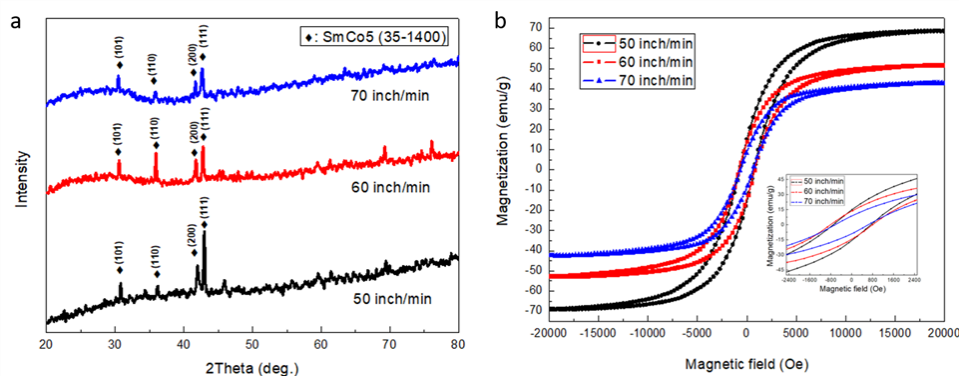


Figure 6.9. (a) XRD spectrum and (b) magnetic hysteresis loop, for sample A, D and E.

In this study, the third parameter was the number of laser sintering. Sintering times for SmCo₅ materials play an important role in crystal structure and magnetic properties. As shown in figure 6.10 a, increase of laser sintering times persistently decreased crystallization. The intensity of signal for (111) and (200) phase weakened dramatically. The other major peaks, such as (110) and (101) phase, did not show a typical weakening, but the intensity of signal still exhibited low. It demonstrated laser sintering on SmCo₅ in multiple times weakened materials' crystallization. It was because heat produced by multiple-times laser sintering gradually distorted SmCo₅ materials' crystalline structure. Besides, magnetic properties of sintered SmCo₅ were weakened as laser sintering times increased entirely. The saturation magnetization and coercivity for sample F and G were 67.4 emu/g and 783.5 Oe, and 61.8 emu/g and 502.6 Oe, respectively. The coercivity rose mildly as the sintering times changed to two and then decreased heavily to 502.6 Oe when the number increased to three. The mild increase of coercivity may be caused by the enhancement of dipole interaction with twice sintering. Saturation magnetization decreased gradually as the sintering times increased from two to three. The rise of laser sintering times seriously weakened materials' crystallization, resulting in the decrease of saturation of magnetization. Meanwhile, the thermal sensitivity of ferromagnetic materials is also the reason for the decrease of magnetic properties of SmCo₅ materials.

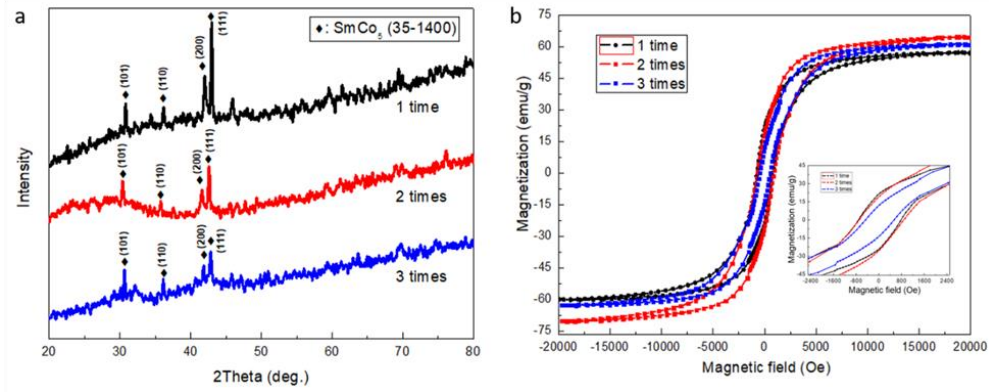


Figure 6.10. (a) XRD spectrum and (b) magnetic hysteresis loop, for Sample A, F and G.

To explore the mechanism of temperature gradient of laser, the measurement was conducted and shown in figure 6.11. In the figure, the temperature in the center of laser spot was around 1500 °C, while it decreased from the center to the boundary gradually, it is because of the nature of laser energy distribution. Laser generated then heat and temperature to sinter SmCo₅ powders into bulk section, the generated heat also leads to re-crystallization of the samples and thus changing the structure of crystal. Furthermore, crystallization of samples can be enhanced by energy diffusion through sintering process, which also affected the magnetic properties of samples simultaneously.

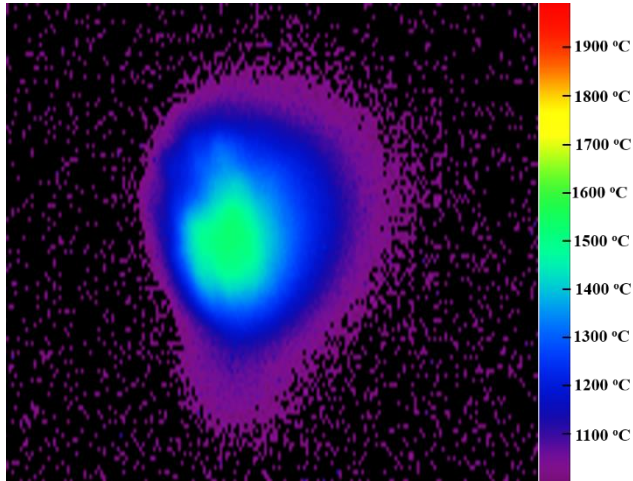


Figure 6.11. temperature gradient on the sample during laser sintering.

Figure 6.12 showed the morphology for fracture section of sintered SmCo_5 . It was distinct that majority of SmCo_5 powders formed into bulk section after sintering by laser, although some small agglomeration or particles were occurred, as shown in the figure. Meanwhile, even if some small gaps between fracture occurred, the density of sintered part was still relatively high. Figure 6.12b was the magnification image for the connection section of fracture between each powder layer. It showed that SmCo_5 powders were sintered into bulk section in connection part and the connection was stiff.

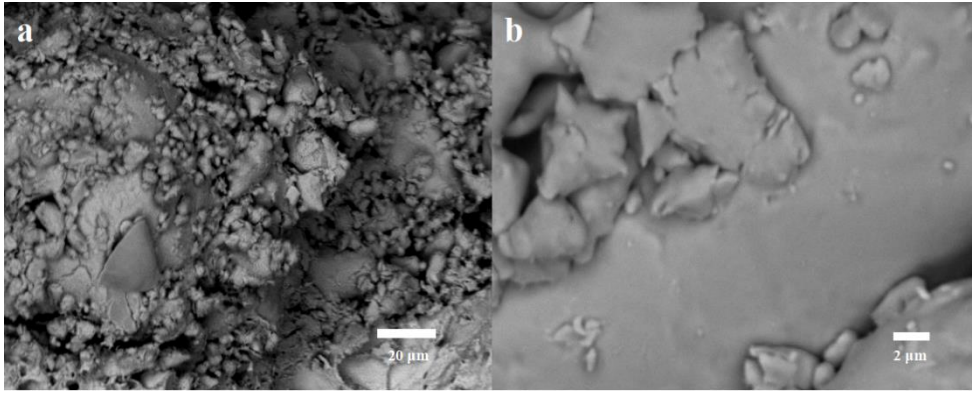


Figure 6.12. SEM images for the fracture of sintered samples

Generally speaking, increase of laser sintering times, laser scanning speed and laser power weakened the magnetic properties of sintered samples, which was corresponding to the fade of crystallization of SmCo_5 materials. Comparing to sintering times and scanning speed, laser power played more important role in the effect on laser for magnetic properties and crystal structure.

In the next part, to compensate the effect from low energy of laser in the verge parts, hatch space was changed to $250 \mu\text{m}$. Therefore, identical parameter setting was set up expect hatch space (table 6.3). Result was shown in figure 6.13. When laser power changed, crystallization of sintered samples did not suffer from apparent distortion when hatch space decrease to $250 \mu\text{m}$. Increase of laser power brought positive influence in crystal structure, which was completely to the opposite for the result of $350 \mu\text{m}$. It was because the original low-energy sections undergone twice laser sintering when the hatch space reduced. The energy diffusion on samples' surface became more uniform, crystallization of samples became better. When laser power

increased, however, XRD spectra of sintered samples showed completely opposite situation by comparing with those of samples sintered in 350 μm hatch space. Meanwhile, when laser power increased, intensity of signal for (200) phase became stronger. Since overlapped area suffered from laser sintering in two times when hatch space decreased to 250 μm , nonuniform areas were removed. Increase of laser power brought much more energy for self-diffusion of samples, which like heat treatment, and led samples to be more homogeneous, which promoted the crystallization of samples (Saadatkia, Mirzadeh, & Cabrera, 2015). Overlapped parts created a path for energy rotation. Therefore, increase of laser power brought completely opposite effect on crystallization. Intensity of signals for typical SmCo_5 crystalline peaks increased as a whole when laser power increased. Magnetic properties in the same times became stronger, which was corresponding to crystallization of samples. Coercivity of sample H to J were 755.8 Oe, 1209.2 Oe and 1586.4 Oe respectively. Sample J exhibited almost the same value of coercivity as that of the original one. It demonstrated that larger laser power promoted energy distribution on sample and made it more homogenous and simultaneously enhanced magnetic properties and crystallization. Saturation magnetization of sample H to J were 86.5 emu/g, 34.7 emu/g and 83.5 emu/g, respectively. As laser power increased (120 W), saturation magnetization of samples did not tend to increase since the thermal sensitivity of SmCo_5 materials is much stronger than the influence of energy self-diffusion when laser power increased to 120 W. When laser power excessively increased (150w), the influence of energy

self-diffusion was quite stronger than the impact for thermal sensitivity. Therefore, magnetization of samples increased to 83.5 emu/g. Scanning speed brought opposite influence on crystal structure and magnetic properties when hatch space reduced to 250 μm comparing to laser power. Intensity of signal for (111) phase tended to increase when scanning speed increased while that of samples was completely opposite when hatch space was 350 μm . This situation was also because laser energy spreading on samples became more homogeneous. However, both coercivity and saturation magnetization undergone decrease when scanning speed increased. Saturation magnetization and coercivity of sample K and L were 72.4 emu/g and 638.2 Oe, and 71.35 emu/g and 640.9 Oe, respectively. It again demonstrated that rapid cooling rate resulted from low duration time of laser caused by worse crystallization.

Unfortunately, increase of number of sintering times also played a negative role on SmCo_5 materials when hatch space reduced to 250 μm . Entirely, intensity of signal for peaks weakened when sintering times increased entirely. Negative influence on crystal structure was heavy, as shown in figure 6.13 e. However, magnetic properties of samples did not be affected dramatically. Saturation magnetization and coercivity of sample M and N were 81.3 emu/g and 888.2 Oe, and 56.6 emu/g and 508.5 Oe, respectively. Coercivity of sample M undergone slightly increase and saturation magnetization reduced mildly. Decrease of hatch space contributed to a way for self-diffusion of energy, and thus, which attenuated the negative effect of increase of

number of sintering times. As laser sintering times changed to three times, saturation magnetization and coercivity dropped to only 56.6 emu/g and 508.5 Oe.

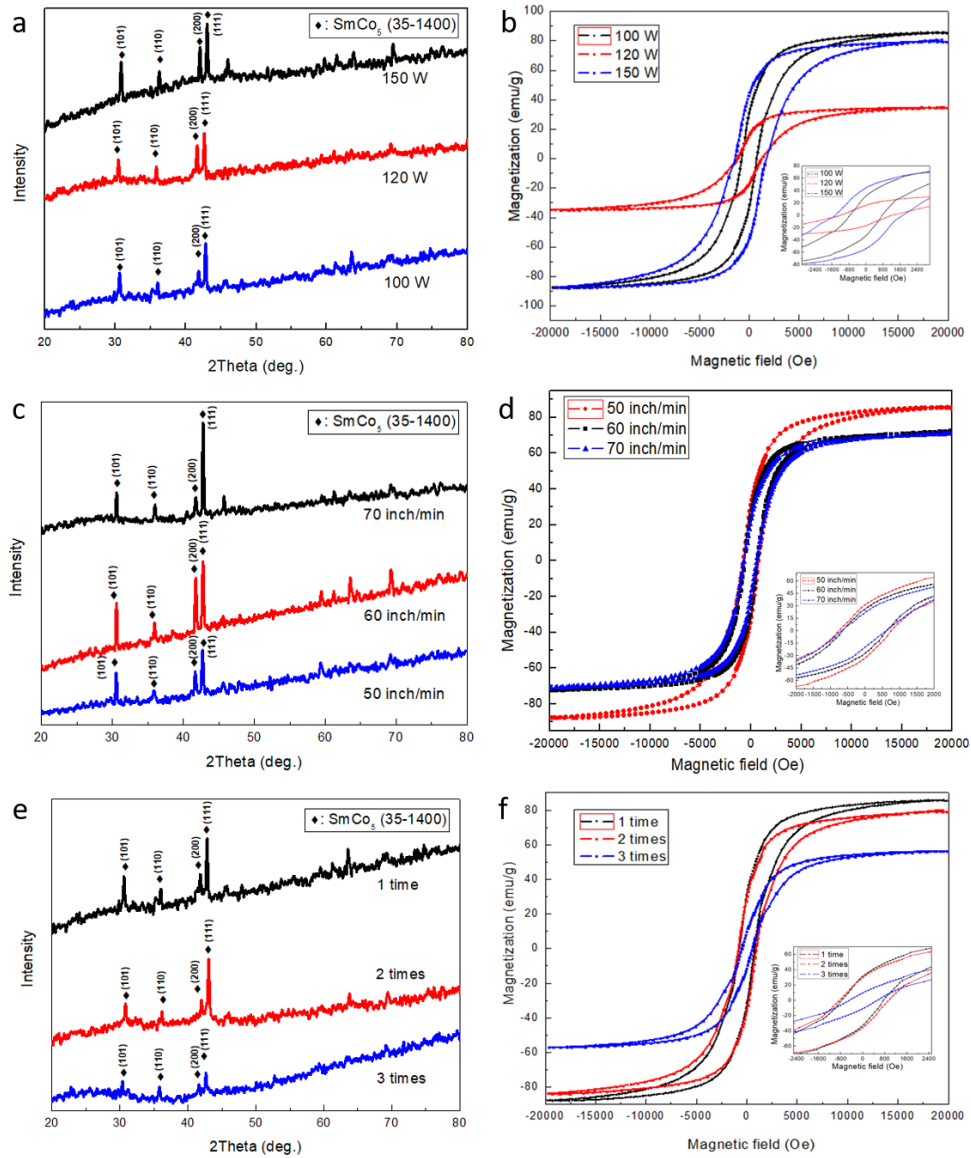


Figure 6.13. (a) XRD spectrum of and (b) magnetic hysteresis loop for Sample H to J; (c) XRD spectrum of and (d) magnetic hysteresis loop for Sample H K and L; (e) XRD spectrum of and (f) magnetic hysteresis loop for Sample H , M and N.

6.2 Thermal debinding and sintering

6.2.1 Introductory remarks

With the increasing demands of permanent magnet components with 3D structures, various technologies have been studied to overcome manufacturing restrictions in recent years. Laser sintering is one of the best methods for fabricating alloy materials with 3D structures. However, the raw materials are expensive and limited, and the shape, size and dimension requirements still hinder the development of laser sintering. Moreover, research on laser sintering on ferromagnetic materials is still rare due to the thermal sensitivity and easy oxidation for magnetic materials.

Concerns about the environment and sustainability of energy resources have encouraged the development of materials synthesis methods with minimum waste and byproducts. Synthesis approaches for metal-organic compounds with non-hazardous starting materials have recently been developed. Ascorbic acid, generally called vitamin C, is a green, common and water-soluble material that has a strong chelating ability to reduce metal oxide and metal compounds and then form a metal ascorbate complex. The byproducts generated during reaction are common metal salts, such as sodium chloride, which is green and non-hazardous. Furthermore, only CO₂ and H₂O are produced as exhaust gases when using metal ascorbate as a precursor for preparing alloy.

Binders are generally used to form the “green part” before sintering, since they play the most significant role in densification by wetting, spreading and forming agglomerates. Polymer binders receive attention because they can be completely removed from the green part by heating. Moreover, polymer binders provide outstanding mechanical strength to the green part after evaporation of the solvent through the formation of organic bridges between materials. Controlling the temperature and content of added binder are important factors to retain the shape of samples and eliminate the generation of cracks, which can decrease the density of samples and their mechanical strength. Polyvinyl alcohol (PVA) is a common, simple and green polymer that is frequently used as a binder since it exhibits excellent printability, biocompatibility, mechanical properties and structural properties.

Compression bonding is a method to fabricate 3D components with high pressure. This method only requires simple and low-cost tooling and fabricates products with higher magnetic properties than injection molding (Ormerod & Constantinides, 1997). Metal-organic powders and binders can be used to fabricate parts with 3D structures in required shape by applying force to compression machine. Compressed 3D structural parts undergo debinding and sintering processes. In this process, binders and organic parts are reduced and eliminated alloys with 3D structures are obtained. In my research, synthesized cobalt ascorbate and samarium ascorbate and a certain proportion of PVA were compressed into pellets using compression bonding machine for alloy sintering.

6.2.2 Experiments

Polyvinyl alcohol (PVA), as a typical thermalplastic material, is selected as the binder since it is common, simple and easy-removed. Certain amount of PVA (from 5%-7%) is dissolved in water at 90 °C for 1 hour in water-bath. Dissolved PVA solution is dropped into the synthesized mixture powders of samarium ascorbate and cobalt ascorbate to form a pre-debinding mixture materias for debinding treatment with grinding in a quartz mortar. This mixture is measured and molded into cylindrical shape by using tableting machine with 8 kPa pressure in 15 minutes compression time. The compressed pellets are used for debinding and sintering. The mixture of PVA, samarium ascorbate and cobalt ascorbate was used to measure TGA to obtain the thermal profile, the content of PVA was 6 wt%. Debinding and sintering process was set based on TGA result.

The shrinkage and weight loss of samples were calculated by using dimension and weight measurements, which can be expressed as

$$V = \pi (D/2)^2 * T \quad (6.1)$$

$$S = (V_I - V_F) / V_I \quad (6.2)$$

$$WL = (W_I - W_F) / W_I \quad (6.3)$$

Where D, T, V, S and WL are the diameter, thickness, volume, shrinkage and weight loss, respectively. V_I , V_F , W_I and W_F are the initial volume, final volume, initial weight

and final weight of samples, respectively. Where W_a and W_b are the weight of the dish of water with oil in the initial state and after oil absorption and particles removal respectively, and W_c is the mass of particles

Optical microscope, XRD and VSM were used to measure grain size, crystal structure and magnetic properties of samples respectively.

6.2.3 Results and discussions

(1) Thermal debinding

Thermal profile for the mixture of PVA, cobalt ascorbate and samarium ascorbate was obtained by TGA measurement. The results are shown in figure 6.14a. Twenty milliliters/min nitrogen gas was used to prevent oxidation of samples during TGA measurement. Sample underwent multiple steps of weight loss and started to stabilize at approximately 600 °C, the heating rate was 5 °C/min. To display typical weight loss at certain temperature intuitively, the DTG curve was obtained from a derivation of the TGA data, as shown in figure 6.14b. Based on the extent of weight loss shown in the figure, debinding process can be divided into seven parts. The detailed division is shown in figure 6.14a. In the first part, weight loss was caused by evaporation of the moisture inside sample. The second typical weight loss, ranging from 160 °C to 207 °C, resulted from the decomposition of PVA, which is consistent with the literature (S.-Y. Lee et al., 2009). The third and fourth typical peaks for weight loss shown in DTG curve indicated the decomposition of samarium ascorbate and cobalt ascorbate

respectively, which corresponds to those measured by TGA that are shown in the Chapter 4.

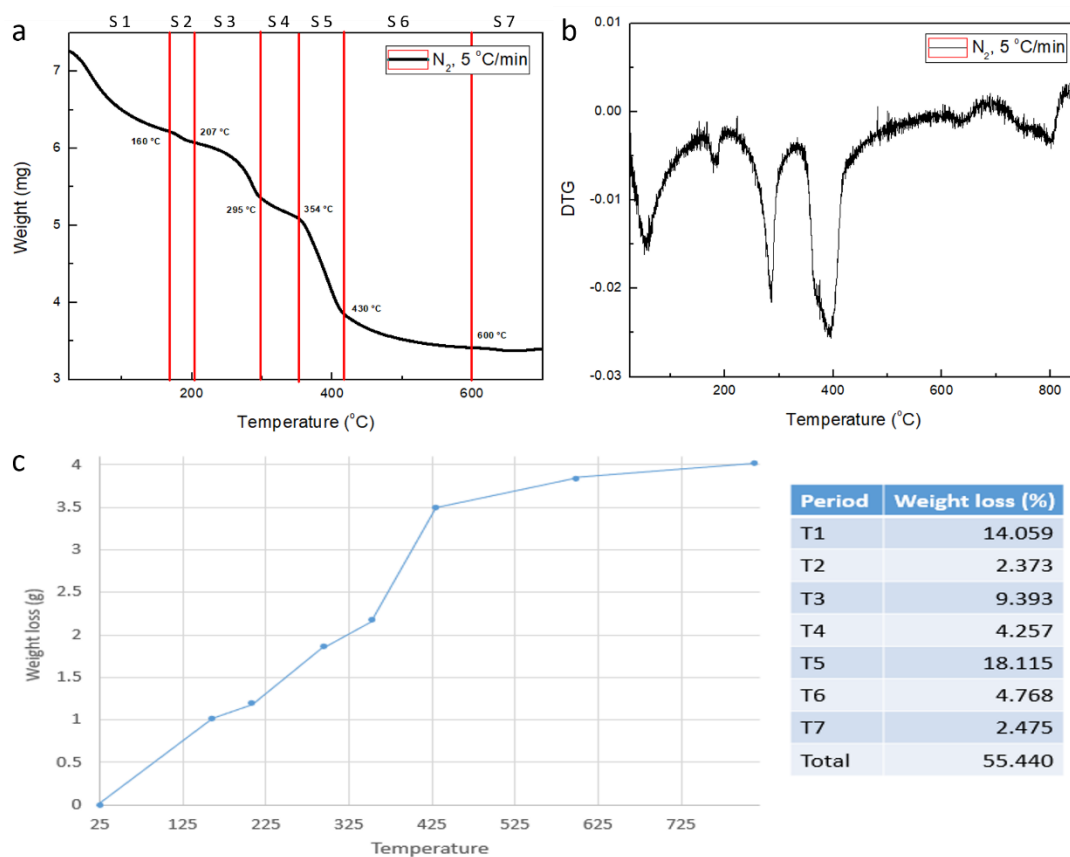


Figure 6.14. (a) DTG curve for the mixture of samarium ascorbate, cobalt ascorbate and PVA under nitrogen air environment. (b) TGA curve for the mixture of samarium ascorbate, cobalt ascorbate and PVA. (c) Accumulation of weight loss in percentage and weight loss for each stage.

The weight of samples was maintained at 47% when temperature was 600 °C and above, indicating that the debinding process ended at 600 °C since PVA binder can be completely burnt out when temperature reaches 600 °C under N₂ atmosphere (Tao, Li, & Zhou, 2013), which is also consistent with the result shown in TGA curve.

Based on the weight-loss processes in the TGA curve, the relevant weight loss in each stage is summarized in figure 6.14c. Stage 1, 3 and 5 had the largest weight loss, which was caused by decomposition of PVA, samarium ascorbate and cobalt ascorbate, respectively. The accumulation of weight loss in percentage is also shown in figure 6.14c. The total weight loss of final part reached 55.44%.

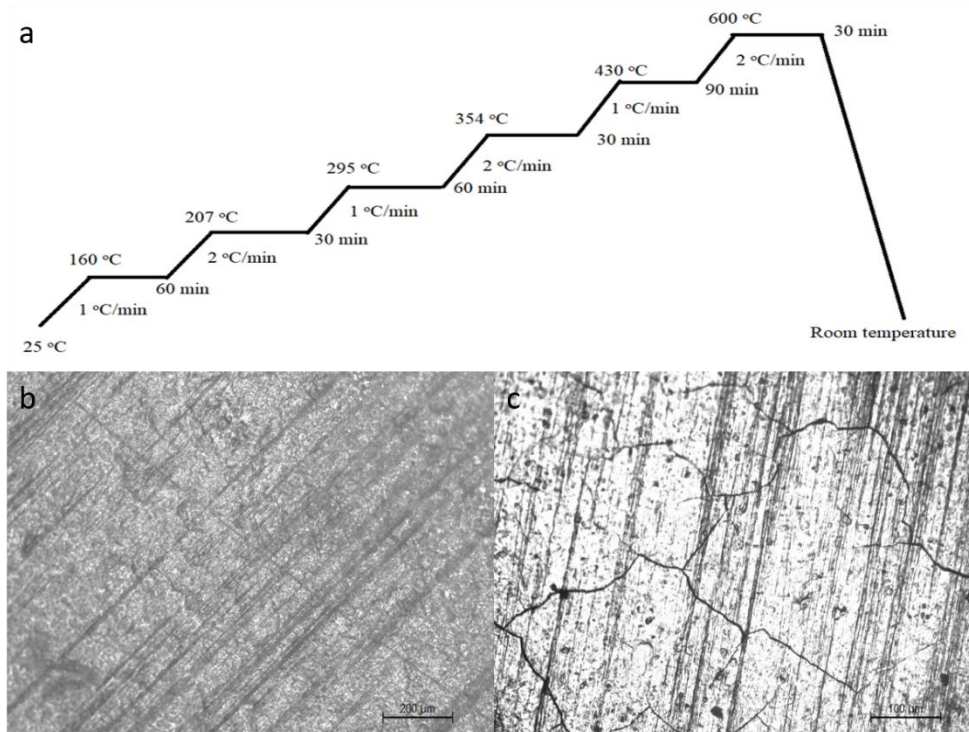


Figure 6.15. (a) Debinding set-up. Optical microscope of sample's surface (b) before and (c) after debinding.

Based on the weight loss situation, the heating rate and temperature holding time for different stages were set to debind sample gradually, as shown in figure 6.15a. Initially, heating rate in each step was set as 2 °C/min. The relatively slow heating rate

can prevent crack generation due to rapid decomposition resulting from rapid temperature changes (Belgacem et al., 2013). The long temperature holding time at typical temperature for decomposition can achieve complete decomposition during each step.

Optical microscopy images of the sample surface are shown in figure 6.15b, c. Obvious cracks occurred after debinding. These cracks may be caused by rapid decomposition of PVA, which resulted from fast heating rate and short temperature holding time. Therefore, temperature control during the first stage was very important. This was because rapid decomposition of PVA generated large amounts of CO₂ and H₂O gases. If evaporation rate of these gases was too fast, additional space was required for gas to escape, which forced sample to generate cracks to release the gas (Belgacem et al., 2013). To eliminate or decrease the generation of cracks, heating rate in the first stage was set to the minimum value of 0.1 °C/min. To determine the starting temperature for generation of cracks, the debinding process was monitored. When the temperature increased to 35 °C, sample began to generate cracks, as shown in figure 6.16a. A temperature holding step for this temperature was needed to eliminate or decrease generation of cracks. Figure 6.16b shows the sample surface after debinding at 35 °C with an addition of temperature holding step at 34 °C. No cracks were observed. The additional setup for temperature holding step successfully eliminated the generation of cracks.

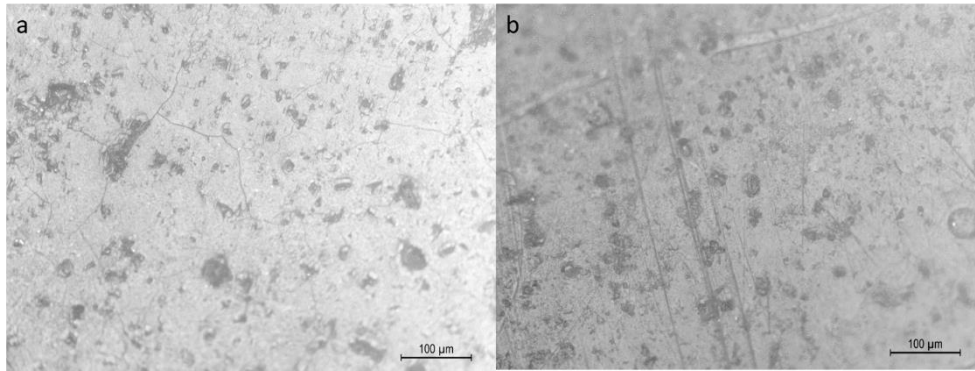


Figure 6.16. Optical microscope images of debinded sample (a) at 35 °C. (b) with a temperature holding time at 34 °C.

To determine the required steps for holding temperature, similar processes were conducted. Based on the results, there were still four more steps needed to decrease or eliminate the generation of cracks. Therefore, a 30-minute temperature holding step was set at 45 °C, 60 °C, 80 °C and 100 °C respectively. However, there were still small cracks that could not be avoided when the temperature was 45 °C, even when the heating rate reached the minimum value and the additional temperature holding steps were added. The new debinding approach included these six steps for holding temperature, as shown in figure 6.17a. The sample surface that underwent debinding process in the first stage of the six steps is shown in figure 6.17b. The sample showed small cracks on the surface while it was still relatively flat on the whole. Since these small cracks were inevitable, this debinding approach was utilized for debinding process in the first stage.

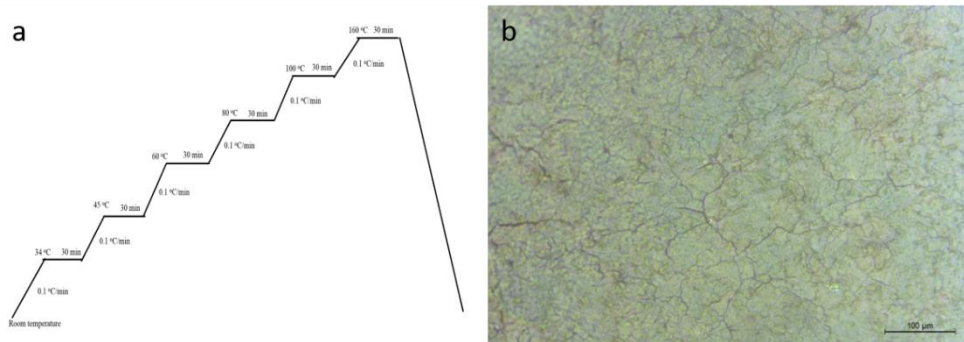


Figure 6.17. (a) Debinding set-up ranging from room temperature to 160 °C. (b) optical microscope image of debinded sample.

Based on the optimum debinding setting for the stage one, a debinding process was set to obtain final part, as shown in figure 6.18a. An optical microscope image of the sample surface after debinding process is shown in figure 6.18b. Only some small cracks were observed. The persistent debinding process decomposed PVA, samarium ascorbate and cobalt ascorbate, and it generated gases, like CO₂ and H₂O, which primarily evaporated through the generated small cracks. These small cracks provided a pathway for evaporated gases to escape and thus prevented further large crack generation and even breaks. These results indicated that the debinding process was suitable and outstanding.

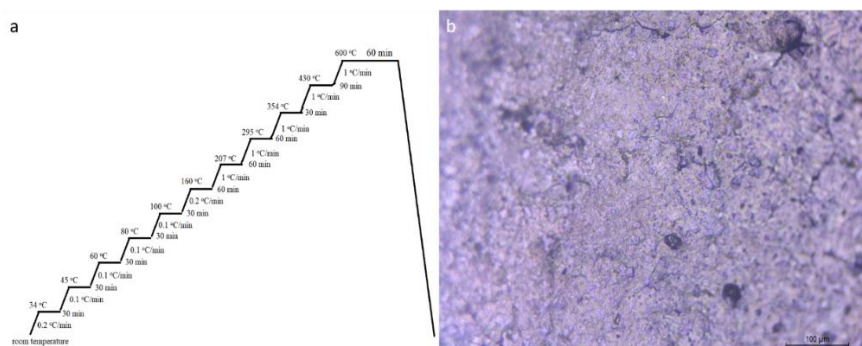


Figure 6.18. (a) Debinding set-up ranging from room temperature to 600 °C. (b) optical microscope image of debinded sample.

(2) Thermal sintering

Debinded samples were then processed for the sintering stage to obtain the final alloy part. The sintering temperatures were set at 900 °C, 1100 °C and 1300 °C to determine the optimum sintering temperature. Heating rate was set to 1 °C/min. The optical microscopy images and XRD spectra for samples sintered at 900 °C and 1100 °C are shown in figure 6.19 and figure 6.20, respectively. Sample sintered at 900 °C exhibited many apparent cracks on the surface, as shown in figure 6.19a. This sintering process did not successfully increase the density. Crack propagation was caused by large gradient in the binder in sample with a thick 3D structure, and the densification cannot be completely performed when the temperature was higher enough (D. J. Lee, Oh, & Bae, 2010). It presented the temperature of sintering was low. The XRD spectrum presented only very weak signal of SmCo₅ materials, while the signals of cobalt and samarium oxide were relatively high. The large width of cracks provided spaces for oxygen to hide, and this small amount of oxygen can easily oxidize a portion of samarium into samarium oxide. Owing to the negative standard potential of samarium compared to that of cobalt, samarium tends to oxidize prior to cobalt (Gómez et al., 2011). The low temperature did not fully sinter sample into alloy phase.

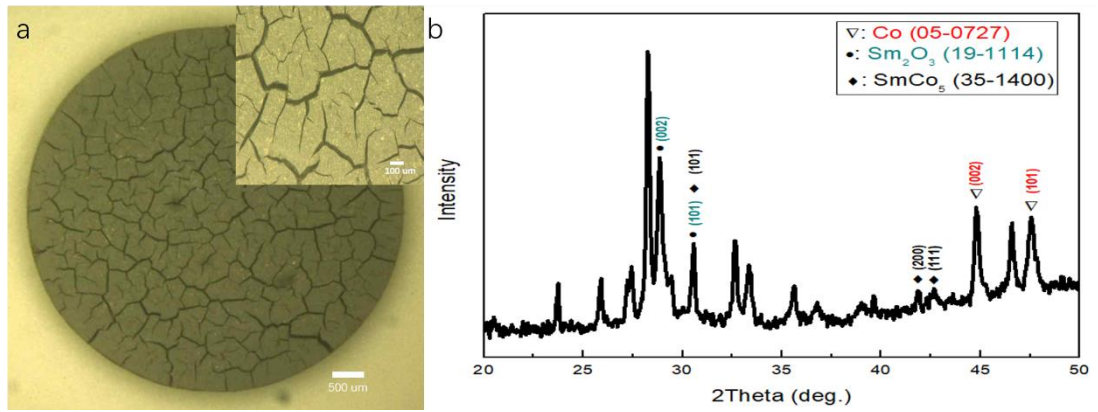


Figure 6.19. (a) Optical microscope image and (b) XRD spectrum of sample sintered at 900 °C.

As shown in figure 6.20a, when the sintering temperature increased to 1100 °C, sample surface became more uniform and no cracks were observed. This high temperature (1100 °C) increased the densification of sample.

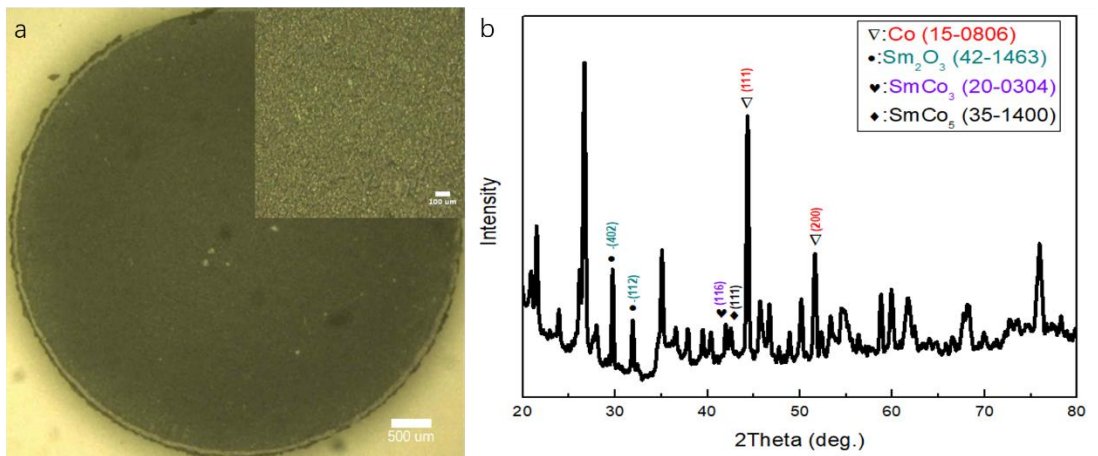


Figure 6.20. (a) Optical microscope image and (b) XRD spectrum of sample sintered at 1100 °C.

However, the XRD spectrum did not show better crystallization of sample. The signal of SmCo_5 was very weak. Meanwhile, the signal for SmCo_3 was observed. It presented samarium-cobalt alloy tended to form 1:3 phase as temperature increased. This phenomenon may also be caused by a decrease in ratio of cobalt due to the formation of pure cobalt. To perform better crystallization of sample, higher sintering temperature was required.

When sintering temperature increased to 1300 °C, crystallization and densification of sample improved (details will be discussed below). Therefore, in the following section, samples with different PVA contents (from 5%-9% and no PVA addition) were used to analyze the influence of sintering temperature and binder content on samples. Samples before and after debinding and sintering (1300 °C) were arranged in the crucible, as shown in figure 6.21. Cylindrical samples in red became small black pellets after debinding and sintering, while the shape of samples remained cylindrical. The presented samples can maintain their original shape after debinding and sintering, even though the dimension decreased. Continuous sintering at higher temperatures continuously solidified samples and thus increased the sample density.

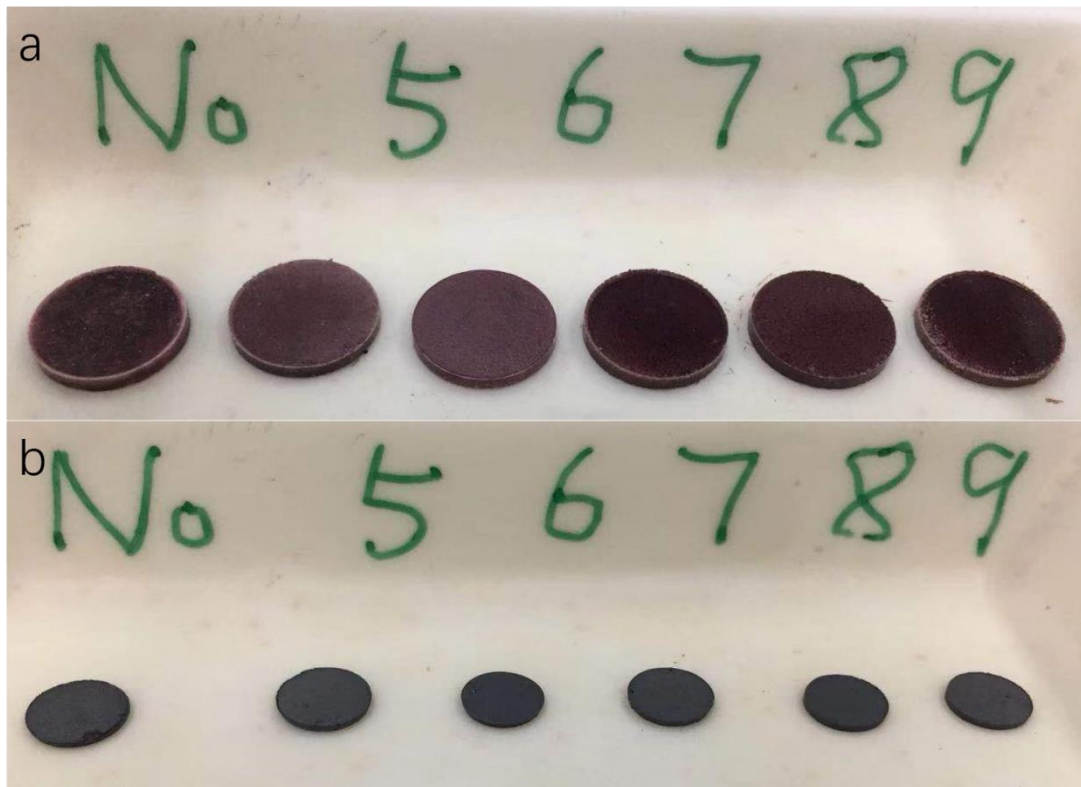


Figure 6.21. Compressed samples without with PVA content from 5% to 9 % (a) before and (b) after debinding and sintering.

XRD spectra of synthesized materials after sintering in 1300 °C were shown in figure 6.22. The signal for samarium-cobalt magnet in 1:5 phase was completely disappeared, while that of 1:3 phase can be observed apparently. It presented that the crystallization of samples was improved while the phase of samarium-cobalt alloys was changed as the sintering temperature increased to 1300 °C. Because high temperature sintering promoted grain growth and therefore improved the crystallization of samples (Y. Liu et al., 2013). The signal for cobalt was simultaneously occurred with relatively strong intensity. Although the mixture of samarium ascorbate and cobalt ascorbate was homogenous before debinding and

sintering, organic bond for metal-organic compounds still hindered the combination of samarium elements and cobalt elements. Large amount of cobalt tended to form pure cobalt rather than combined with samarium to form samarium-cobalt alloy. Meanwhile, since the loss of samarium during sintering (Ma et al., 2015), the absence for samarium atoms which surrounded cobalt atoms resulted in the vacancy on the surrounding of cobalt atoms, therefore, cobalt atoms was only sintered into pure cobalt. The addition of PVA binder did not show apparent influence of crystallization of alloys. The intensity of signal for cobalt was strong without the adding of PVA, comparing with those of sample with the addition of PVA binder. As PVA binder adding increased, the intensity of cobalt increased gradually. While small amount of addition of PVA (5% wt) weakened the signal of cobalt, simultaneously, the signal of samarium-cobalt magnet did not undergo any apparent change. It presented small amount of addition of PVA can mildly hinder the crystallization of pure cobalt while affecting the crystallization of samarium-cobalt magnet hardly. The intensity of signal for samarium-cobalt magnet was strongest for the sample with addition of PVA binder in 6%, it presented moderate addition of PVA binder brought positive influence on the crystallization of samarium-cobalt magnet.

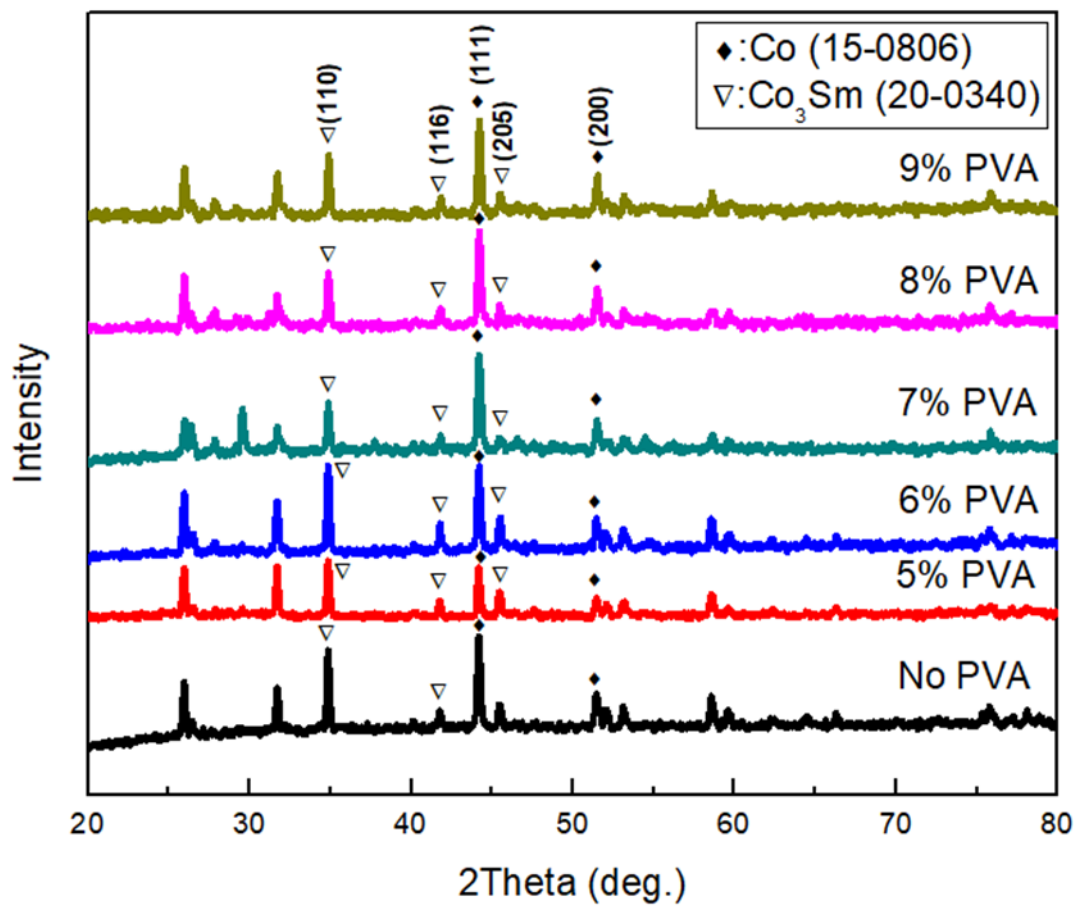


Figure 6.22. XRD spectra of synthesized materials.

The dimension and weight of them were also measured to analyze the shrinkage ratio and weight loss of samples. Details were shown in table 6.4. As table shown, the shrinkage of samples was around 68% to 84%. As the increase of binder adding, shrinkage tended to increase. There was not any obvious deformation occurred for the shape of sintered samples. It demonstrated the adding of binder brought positive influence in shape and dimension maintenance. The more adding of binder, the more shrinkage of samples. It presented binder played a role in improving densification

thereby the shrinkage increased. The appropriate debinding improves the results after sintering, therefore the sintering (1300 °C) increase the shrinkage of sample by the improvement of densification (Enneti et al., 2012). The weight loss of samples also tended to increase as the increase of binder adding. Meanwhile, the weight loss of samples was larger than that of predicted one based on TGA result (55.4%), it may be caused by the loss of samarium during sintering (H. Zhang et al., 2011).

Table 6.4. Dimension and weight of samples after sintering in 1300 °C.

Stage PVA proportion	Initial stage			Final stage			Shrinkage (%)	Weight loss (%)
	Diameter (mm)	Thickness (mm)	Weight (mg)	Diameter (mm)	Thickness (mm)	Weight (mg)		
No	10.17	1.01	153.2	6.16	0.89	61.8	67.67%	59.66%
5%	10.34	1.2	160.9	6.03	0.88	58.2	75.06%	63.83%
6%	10.11	1.16	155.1	5.42	0.79	53.1	80.43%	65.76%
7%	10.15	1.26	158.4	5.69	0.81	53.4	79.80%	66.29%
8%	10.08	1.15	144.4	5.44	0.73	51.9	81.51%	64.06%
9%	10.13	1.12	154.1	5.53	0.61	49.1	83.77%	68.14%

SEM images for the surface of sintered samples were shown in figure 6.23. There were not any apparent cracks can be observed in the samples' surface. Samples' surface exhibited a successive region with irregular grains, while the porosity was relatively high since there were not any apparent hole can be observed. It is because thermal sintering increased the densification of samples with higher sintering temperature

(Nandwana et al., 2017). Figure 6.23a showed the SEM image of the surface of sample without adding of PVA binder. The surface exhibited relatively flat and many small irregular particles distributed on the surface. According to the EDX results (table 6.5) and XRD spectrum, these particles were cobalt, samarium-cobalt and carbon matrix. Comparing to the sample without binder, those samples with different amount of PVA binder (from 5% to 9%) exhibited many crystal-types particles on the surface after sintering. These particles showed in cuboid shape. When the content of PVA binder was 5%, these cuboid shape particles were slenderer. As adding of binder increase, these cuboid shape particles tended to become larger and cubic shape. The average aspect ratio of particles decreased with the increase of binder, the aggregation of these particles also increased (Yu, Zheng, Liu, Zheng, & Xiong, 2010). It demonstrated the adding of binder played a role in improving crystallization of samples although it was not apparent according to the XRD spectra. As the content of PVA binder increased, the porosity of samples tended to increase since some cavities generated on the surface. This phenomenon was caused by the increase of the agglomeration of particles, which performed negative influence in microstructure formation (Ibrahim, Johari, Rahman, & Maslehuddin, 2017).

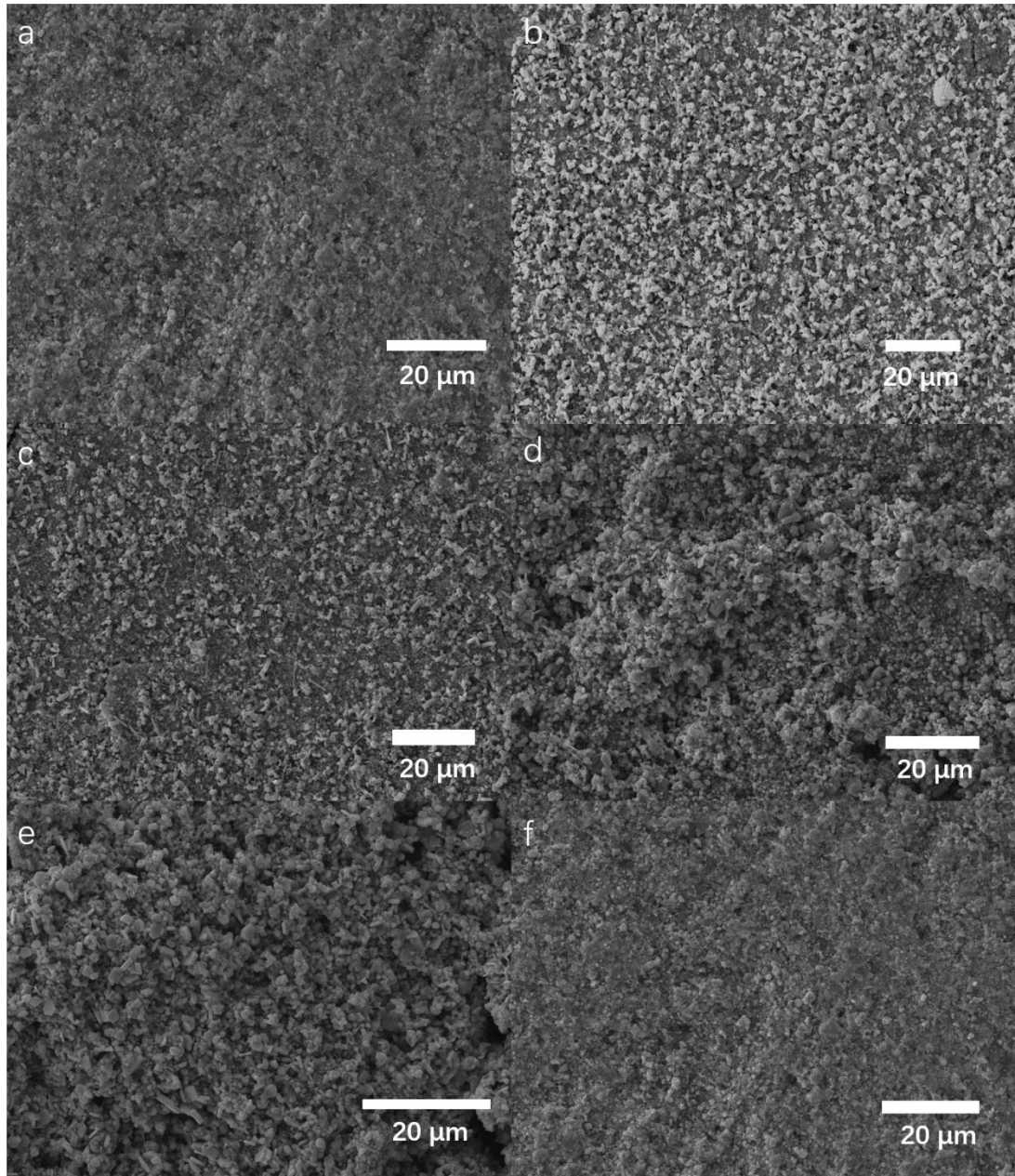


Figure 6.23. SEM images for the surface of sintered samples (a) without PVA, (b) with 5% PVA, (c) with 6% PVA, (d) with 7% PVA, (e) with 8% PVA, (f) with 9% PVA.

Table 6.5 showed the element content of samples with different PVA content. As increase of addition of PVA binder, the content of carbon tended to increase while those of oxygen, cobalt and samarium tended to decrease. It was corresponding to the

addition of organic binder which was mainly consisting of carbon. Meanwhile, four hydrogen atoms in PVA per unit can react with two oxygen atoms into water vapor and run out, therefore, they can not only react with one oxygen atom in PVA, but also react with another one atom in metal ascorbate, and finally the content of oxygen decreased. While the content of cobalt underwent a relatively sharp drop when the addition of PVA was 6%. The relative high content of samarium resulted in the better crystallization of samarium-cobalt magnet rather than that of pure cobalt. Furthermore, sample without addition of PVA binder presented relatively low content of carbon, oxygen while relatively high content of cobalt and samarium. It is because organic binders showed more fixed carbon (Q. Hu et al., 2015). It presented the addition of PVA may led to oxidation in a certain extent.

Table 6.5. Metal element measurement on synthesized cobalt ascorbate and samarium ascorbate.

Sample		A	B	C	D	E	F
PVA content (%)		5	6	7	8	9	N/A
Carbon (%)	A	58.02	65.35	68.23	74.58	71.74	63.59
	W	18.98	25.17	27.6	33.03	32.3	22.13
Oxygen (%)	A	11.21	10.55	8.31	6.51	8.30	8.95
	W	4.88	5.41	4.48	3.84	4.98	4.15
Cobalt (%)	A	20.02	15.96	16.54	12.35	14.51	17.33
	W	32.13	30.16	32.83	26.84	32.06	29.59
Samarium (%)	A	10.75	8.14	6.93	6.55	5.44	10.13
	W	44.01	39.25	35.09	36.29	30.66	44.13

Magnetic properties of sintered samples were measured and shown in figure 6.24. The inset was the magnified image for capturing coercivity of samples. The detailed values of coercivity and saturation magnetization were shown in table 6.6. The saturation magnetization of sample without PVA binder addition was almost the lowest (71.58 emu/g), although that of sample with 5% binder was only 71 emu/g. When the content of binder increased to 6%, the saturation magnetization increased to 91.19 emu/g, which was the highest one. The saturation magnetization was higher than that was reported (35.5 emu/g) (Lu et al., 2010). However, as the content of binder increased continuously, the value of saturation magnetization decreased gradually. It presented that the content of PVA binder was optimized as 6% in enhancing the saturation magnetic properties. Because appropriate amount of binders played a role in densification of samples, which can enhance magnetic properties of samples (Y. Liu et al., 2013). It was completely corresponding to optimization of content of binder (6%) for enhancing crystallization of samples. The improvement of crystallization of samples led to stronger exchange in coupling interaction, thereby increased the saturation magnetization (S. Xu et al., 2018). Comparing to the high saturation magnetization, the coercivity for sintered samples was relatively low. It was because the content of cobalt was high, and the coercivity of pure cobalt was relatively low (10 Oe) compared to samarium-cobalt alloys (H. Luo, Wang, He, & Lu, 2005). Although the coercivity of samples was low, the influence for PVA binder on coercivity of

samples was similar to that on saturation magnetization. 6% PVA binder also resulted in the highest coercivity of samples (55.04 Oe) compared to other content of binder.

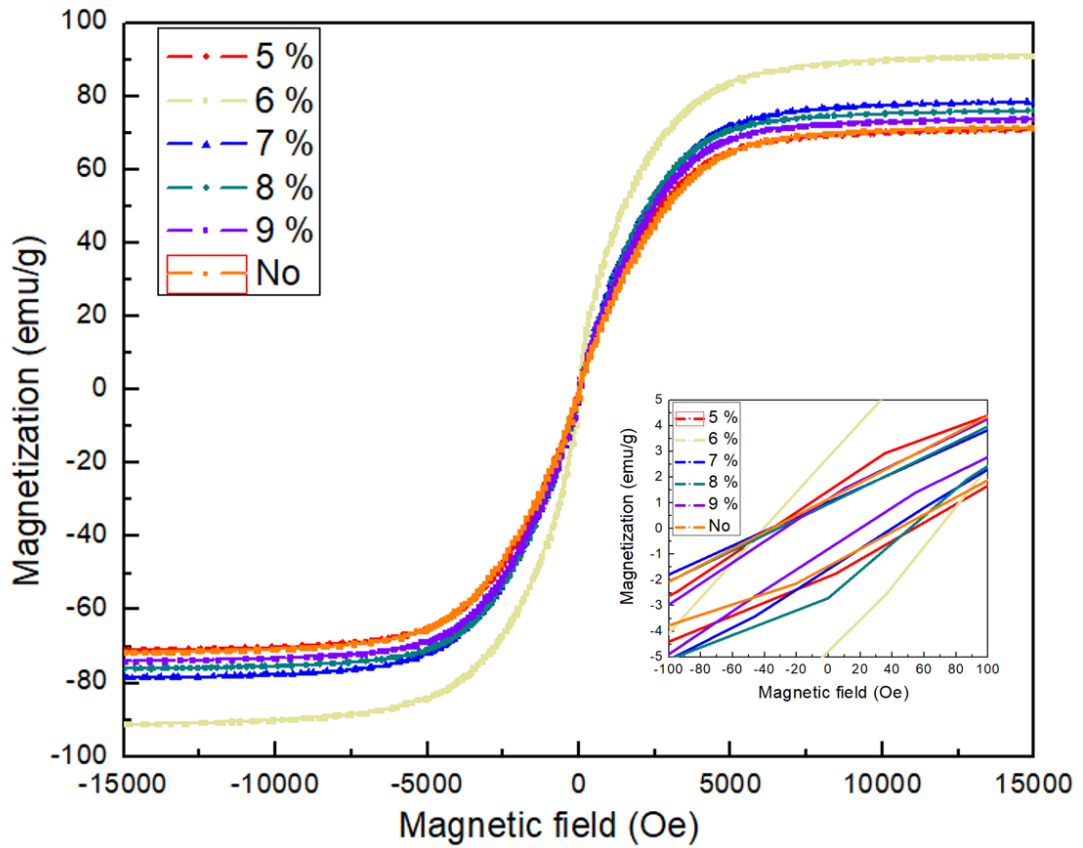


Figure 6.24. Hysteresis loops for sintered samples.

Comparing to the SmCo alloy fabricated by laser sintering, the SmCo alloy fabricated by thermal sintering exhibited the phase of 1:3 (SmCo₃), the impurity of Co was also occurred. Although the coercivity for the sample fabricated by thermal sintering was lower than that for the sample fabricated by laser sintering, while the saturation magnetization (91.19 emu/g) was higher than that for the sample fabricated by laser sintering (83.49 emu/g).

Table 6.6. list of coercivity and saturation magnetization for samples.

Content of binder	5%	6%	7%	8%	9%	No
Coercivity (Oe)	44.67	55.04	38.24	41.46	23.94	39.67
Saturation magnetization (emu/g)	71.00	91.19	78.52	76.08	73.91	71.58

Although the final sample is SmCo alloy in 1:3 phase, SmCo alloy is obtained after sintering using metal-organic precursors, which proves that using metal-organic precursors can help to synthesize the alloy successfully. The crystal structure showed that SmCo alloy was in 1:3 phase rather than in 1:5 phase, some adjustments should be made to obtain SmCo alloy in 1:5 phase in the future.

6.3 Concluding remarks

In this chapter, laser sintering and thermal sintering were used to fabricate SmCo alloys, and the crystal structure and magnetic properties were characterized. The major findings are as follows:

- (1) SmCo₅ was successfully sintered by laser into a small part with a cylindrical shape, and the effect of sintering parameters on the magnetic properties and crystal structure of the material was thoroughly explored. Overall, larger laser power, faster scanning speed and more sintering times weakened crystallization and decreased

saturation magnetization and coercivity of SmCo₅ materials as hatch space was 350 μm . In contrast, when hatch space changed to 250 μm , the homogeneity of the self-diffusion energy of samples increased because a change in hatch space compensated for the low-energy verge sections, which had a significantly positive influence on the magnetic properties and crystallization of the materials. Furthermore, the effect of scanning speed and laser power on magnetic properties and crystal structure reversed when compared with those for 350 μm hatch space. The optimum parameters for laser sintering on SmCo₅ materials was 250 μm hatch space, 150 W laser power, 1270 mm/min scanning speed and one-time sintering. Saturation magnetization and coercivity of sintered samples reached 83.49 emu/g and 1586.4 Oe, respectively.

(2) Samarium-cobalt magnet in 3D structure was successfully fabricated by using metal-organic compounds. Ascorbic acid was used as the organic precursor for synthesis of metal-organic compounds in an environmentally friendly process. Thermal profile of synthesized metal-organic compounds with the addition of PVA binder was performed to improve the debinding and sintering process and therefore improve the performance of samples. XRD spectra were obtained and identified the synthesized sample as a samarium-cobalt magnet in 1:3 phase, although pure cobalt impurities were observed. It was found that addition of 6% PVA binder resulted in improved crystallization and magnetic properties. The saturation magnetization reached 91.19 emu/g, which was higher than that for the sample fabricated by laser sintering.

Chapter 7 Conclusions and Suggestions for Future Research

7.1 Overall Conclusions

Metal-organic compounds were synthesized by using a non-hazardous process as metal-organic precursors for SmCo alloys synthesis. The fabricating technologies of the 3D component were fully studied for the fabrication of the 3D structure for alloy materials or metal-organic compounds. The crystal structure and relevant properties for the final products were also studied.

(1) Formation and investigation of REM and TM organic compounds

Samarium and cobalt were selected as metal elements for the preparation of the metal-organic compounds. Ascorbic acid was used to synthesize the metal-organic compounds for alloy production preparation. Their composition was identified by FTIR and ICP. FTIR spectra for the synthesized materials and original materials were measured. The comparison results of their spectra proved that the functional groups for the synthesized materials were similar to the original one (ascorbic acid). It demonstrated that the synthesized materials were metal ascorbates, as required. ICP-OES was used to measure the composition of metal elements for synthesized samarium ascorbate and cobalt ascorbate. The results showed that samarium and cobalt were

detected and the production yield of the target materials for samarium ascorbate and cobalt ascorbate were 68.66 % and 94.01% respectively. The mixture of synthesized cobalt ascorbate and samarium ascorbate gave a 84.3% production yield and 4.3:1 for the elemental ratio.

(2) Development for 3D structure fabrication processes

A laser system and inkjet printing were developed for fabricating metals or metal-organic compounds. The advantages and disadvantages for using these methods to fabricate SmCo alloys are also summarized. Using laser system to fabricate 3D structures for SmCo alloys can directly transfer the reduced metals/alloys on the substrates, while the effectiveness for the energy of the laser on reducing samarium ascorbate and cobalt ascorbate is essential to be verified. Furthermore, the adhesive force between the alloy and substrate is low. Using inkjet printing to fabricate 3D structure for SmCo alloys can fabricate 3D structures for samarium ascorbate and cobalt ascorbate before sintering, while the thickness of the fabricated product is small. The major findings are shown below:

(a) Metal patterns fabrication in 3D structure by Laser induced forward transfer

A modified laser system was built up to fabricate the metal patterns in 3D structures. The mixture of copper oxide and ABS was used as a sacrificial layer for pre-laser treatment. Selective copper patterns can be fabricated by this laser system.

EDX and XRD results for the laser treated patterns presented the reduction of copper oxide. The copper patterns exhibited relatively low conductive resistivity of $1.46 \times 10^{-6} \Omega\text{m}$. Post electroless plating can enhance the conductive resistivity selectively, and its value can reach $1.29 \times 10^{-7} \Omega\text{m}$. This method can be used for 3D printing of metal circuits onto various substrates.

(b) Metal patterns fabrication by selective laser treatment on thermoplastic coating

A thermoplastic coating fabricated by PMMA material and malachite was used as a coating for fabricating 3D metal patterns by using modified laser system. The laser treatment on coating transformed malachite into copper as conductive metal patterns. The EDX and XRD results for the laser treated patterns showed that malachite was reduced into copper. This material can provide a novel solution for coating metals on 3D printed objects and selectively transforming the coating into copper after the laser writing process.

(c) Laser reduction on cobalt based organic compound

Cobalt based organic compounds were reduced by laser into cobalt ions as ferromagnetic materials and maintained a porous structure to absorb oil. The laser parameters were optimized to get the best oil absorption for the samples. The XRD results showed that the laser successfully reduced ZIF-67 into cobalt. SEM images showed that the porous structure of the samples was maintained, and that this porous structure made samples having strong ability in oil absorption. The optimum

parameters of the laser were studied. LR-ZIF-67 in 60 μm hatch space and 1200 mm/min and 1000 mm/min showed optimum oil absorption capacity for silicone oil and castor oil, but LR-ZIF-67 in 1500 mm/min writing speed exhibited optimum reusability after recycling.

(d) Inkjet printing for cobalt based organic materials

The inkjet printing method was used to construct 2.5D structure multilayer patterns with ferromagnetic properties. Cobalt-based materials were used as raw materials and they were dissolved in organic solvent to address the agglomeration issue. 3D structured patterns were successfully fabricated by inkjet printing on the silicon wafer, as revealed by optical surface profiler. The magnetic properties of cobalt based organic materials after printing were characterized, and they were in consistent with the relevant surface morphology of the samples.

(3) Control mechanism in binder content and thermal profile to enhance the crystal structure and magnetic properties of SmCo alloys

The debinding and sintering processes were controlled to avoid crack formation based on the thermal profile of the synthesized metal-organic precursors. An investigation of the effect on the binder content for the crystal structure and magnetic properties of SmCo alloys is also discussed. Laser sintering for SmCo powders is used to fabricate 3D structures for the comparison of crystal structures and magnetic

properties for SmCo alloys fabricated from the metal-organic precursors using thermal sintering. The major findings are shown below:

(a) Laser sintering for SmCo alloys

Samarium-cobalt magnet powders were used to fabricate 3D components by using laser sintering. The parameters of laser were optimized to achieve better crystal structures and magnetic properties. SmCo₅ materials were sintered by laser and the materials were formed into a small part with cylindrical shape successfully. Larger laser power, faster scanning speed and increased sintering times weakened the crystallization and decreased coercivity and saturation magnetization of SmCo₅ materials when the hatch space was 350 μm. When hatch space was reduced to 250 μm to compensate low-energy verge sections, the energy distribution of the samples became more homogenous, which brought significant positive influence on the materials' crystallization and magnetic properties. In this hatch space, the influence of laser power and scanning speed on the crystal structure and magnetic properties became the opposite in comparison with those for the 350 μm hatch space. The optimum parameters for laser sintering on SmCo₅ materials was 250 μm hatch space, 150 W laser power, 1270 mm/min scanning speed and one-time sintering.

(b) Thermal sintering for SmCo alloys

A samarium-cobalt magnet in a 3D structure was successfully fabricated by using metal-organic compounds. Ascorbic acid was used as the organic precursor for the synthesis of metal-organic compounds in an environmental-friendly process. Thermal profiling of synthesized metal-organic compounds and the addition of PVA binder was performed to improve the debinding and sintering process, and therefore improve the crystallization and magnetic performance of the samples. XRD spectra were measured to identify the synthesized sample as samarium-cobalt magnet in 1:3 phase, although some pure cobalt impurity was observed. It was found that the addition of a 6% PVA binder can give better crystallization and magnetic properties. The saturation magnetization can reach 91.19 emu/g, which was higher than that for the sample fabricated by laser sintering.

7.2 Significance of research

The success of the synthesis of samarium ascorbate and cobalt ascorbate metal-organic precursors provides a new path to produce SmCo alloys in a non-hazardous and environmental-friendly manner. The usage of metal-organic compounds in the alloy synthesis can minimize or even eliminate the usage of toxic and hazardous materials and organic solvents during synthesis and eliminate generation of hazardous wastes. Since construction elements in metal-organic compounds are carbon, oxygen, hydrogen (except metals), when the temperature increased, the metal-organic

compounds burned out with the formation of water vapor and carbon dioxide, which are non-hazardous. The synthesis process reacts in water solutions, which is quite environmental-friendly compared to organic solvents. Traditionally, metal acetylacetonates are used to synthesize SmCo alloys in organic solvents for chemical processes (Fiévet et al., 2018), while the toxicity of metal acetylacetonates and the volatility of organic solvents brings substantial harm to human beings and the environment. The generated wastes/byproducts from metal acetylacetonates are organic based materials, which are also not environmental-friendly. Alternatively, metal ascorbates can be used as precursors, because the starting materials are non-hazardous and the solvent used for the synthesis of SmCo alloys is water only. The generated wastes/byproducts from metal ascorbates are only sodium chloride during precursor synthesis. Meanwhile, the exhaust gases during thermal sintering of metal ascorbates are only CO₂ and H₂O, which are non-hazardous. Therefore, the use of metal ascorbates as metal-organic precursors for synthesizing SmCo alloys can effectively decrease the harm to human beings and the environment in a certain extent.

Using the proposed precursors and thermal sintering to fabricate SmCo alloys into a 3D structure can overcome the geometric limitation of SmCo powders for laser sintering. This is due to the use of the proposed metal-organic precursors and a method that can exclude consideration of the geometric limitation of SmCo powders. Besides, the addition of a binder decreases the interaction of the powders according to the strong ability in wetting and spreading (Suh et al., 2015). In comparison, laser sintering of

SmCo powders was used to fabricate 3D structures. SmCo powders were compressed into a small pellet with a certain 3D structural shape before laser sintering, which also helps to decrease the negative effects of the geometric limitation of SmCo powders. Furthermore, the research work for laser system and inkjet printing of metals or metal-organic compounds also provides potential applications for the fabrication of SmCo alloys with 3D structures.

The study of the control mechanisms in the binder content and thermal profile in thermal sintering can minimize the crack formation in the 3D structure and improve the crystallization and magnetic properties of SmCo alloys (Y. Liu et al., 2013). The added binder can enhance the structural stability of 3D structure, while it decreases densification and thereby weakens the crystallization and magnetic properties of SmCo alloys. The study successfully balances the negative effect and positive effect of the added binder and the obtain optimized crystal structure and magnetic properties of SmCo alloys. Rapid decomposition and evaporation of the binder can easily deform the shape of the 3D structure and generate cracks (Belgacem et al., 2013), a study of the control mechanism of the thermal profile in thermal sintering is useful to provide appropriate sintering conditions to avoid the above problems occurring.

7.3 Suggestions for future research

Although this study provides some processes to fabricate alloy materials or metal-organic materials in 3D structure, synthesized materials and components are characterized, and the objectives have been achieved, there is still further related research that can be undertaken.

(1) In this work, samarium and cobalt were used to synthesize their metal-organic compounds for alloy production preparation, while there were still many elements for REMs and TMs that can be adopted to synthesize metal-organic compounds, and these compounds can also be applied in alloy synthesis. For example, gadolinium, neodymium, iron and nickel. Collocation for these elements are limitless, so binary, ternary and even poly-basic alloys can be synthesized by using these elements. Furthermore, the same as for metal selection, various organic materials are also can be used to synthesize metal-organic compounds for further research to enhance the material properties or change the material structure. Carboxylate, amino and other types of organic materials can be used as coordinate ligands for metal-organic compounds. The difference in functional groups and chains for these materials results in different properties of metal-organic compounds and alloy materials. The different usage of organic materials for coordinated ligands may causes different properties in the alloy materials, and this

also can be studied in the future. There is still a large space for collocation of these elements and organic materials.

- (2) Some 3D structure fabricating technologies were studied in this work. The advantages and disadvantages for these techniques were summarized as well. However, these techniques were not used to fabricate SmCo alloys using synthesized metal-organic compounds, so such study should be performed in the future. Especially the effectiveness for reducing synthesized metal-organic materials into metals/alloys should be investigated. Meanwhile, the requirement of particle size for inkjet printing is 0.22 μm , so further measurement for synthesized metal-organic compounds should be performed to confirm the particle size of synthesized metal-organic compounds that can achieve this requirement. Furthermore, the limitation of thickness of inkjet printed products should be addressed in the future in order that this technique can be completely applied for fabricating 3D structures.
- (3) The geometric limitation of SmCo powders should be addressed in the future by using other synthesis methods to control the shape and size of the powders and achieve the requirement for laser sintering. In my study, SmCo powders were compressed before sintering to decrease the negative influence of geometric limits. However, only a thin pellet-type product can be fabricated by laser sintering, so products with flexible shape and size are still difficult to fabricate.

(4) The proposed method has some limitations, for example, the dislodgement of impurities for sintered SmCo materials, and the relatively low coercivity of samarium-cobalt alloy. SmCo alloys were fabricated into 3D structures using thermal sintering, while SmCo alloys only presented the 1:3 phase (SmCo_3), which presents relatively low magnetic properties. Meanwhile, large amounts of impurities for cobalt occurred in the SmCo alloy, which also affects the magnetic properties of the products. Dislodgement of cobalt impurities and enhancement of the crystallization of products are necessary to be studied in the future. Meanwhile, PVA was selected as the binder in this study, while different binder usage causes different crystallization and properties of products. This also needs to be studied. Further, measurement of mechanical properties can also be conducted in the future.

References (252 references)

Abbas, N., Ding, J., Liu J. P., Du J., Xia W., Yan A., . . . Zhang J. (2017). Well protected SmCo nanoclusters: fabrication and transformation to single crystals. *RSC Advances*, 7(81), 51695-51701.

Ahsan, M. A., Jabbari, V., Islam, M. T., Kim, H., Hernandez-Viezcas, J. A., Lin, Y., . . . Noveron, J. C. (2018). Green synthesis of a highly efficient biosorbent for organic, pharmaceutical, and heavy metal pollutants removal: Engineering surface chemistry of polymeric biomass of spent coffee waste. *Journal of Water Process Engineering*, 25, 309-319.

Akhtar, M. N., Khan, M. A., Ahmad, M., Nazir, M., Imran, M., Ali, A., . . . Murtaza, G. (2017). Evaluation of structural, morphological and magnetic properties of CuZnNi ($\text{Cu}_x\text{Zn}_{0.5-x}\text{Ni}_{0.5}\text{Fe}_2\text{O}_4$) nanocrystalline ferrites for core, switching and MLCI's applications. *Journal of magnetism and magnetic materials*, 421, 260-268.

Alezi, D., Peedikakkal, A. M. P., Weseliński, Ł. J., Guillerm, V., Belmabkhout, Y., Cairns, A. J., . . . Eddaoudi, M. (2015). Quest for highly connected metal–organic framework platforms: rare-earth polynuclear clusters versatility meets net topology needs. *Journal of the American Chemical Society*, 137(16), 5421-5430.

AlMangour, B., Grzesiak, D., & Yang, J.-M. (2017). In-situ formation of novel TiC-particle-reinforced 316L stainless steel bulk-form composites by selective laser melting. *Journal of Alloys and Compounds*, 706, 409-418.

Aminuzzaman, M., Watanabe, A., & Miyashita, T. (2010). Direct writing of conductive silver micropatterns on flexible polyimide film by laser-induced pyrolysis of silver nanoparticle-dispersed film. *Journal of Nanoparticle Research*, 12(3), 931-938.

Ando, B., & Marletta, V. (2016). *An all-inkjet printed bending actuator with embedded sensing feature and an electromagnetic driving mechanism*. Paper presented at the Actuators.

Ando, W., & Moro-oka, Y. (1988). The role of oxygen in chemistry and biochemistry.

Arleth, N., Gamer, M. T., Köppe, R., Konchenko, S. N., Fleischmann, M., Scheer, M., & Roesky, P. W. (2016). Molecular Polyarsenides of the Rare-Earth Elements. *Angewandte Chemie International Edition*, 55(4), 1557-1560.

Attar, H., Ehtemam-Haghighi, S., Kent, D., & Dargusch, M. S. (2018). Recent developments and opportunities in additive manufacturing of titanium-based matrix composites: A review. *International Journal of Machine Tools and Manufacture*, 133, 85-102.

- Baig, M. K., Atiq, S., Bashir, S., Riaz, S., Naseem, S., Soleimani, H., & Yahya, N. (2016). Pulsed laser deposition of SmCo thin films for MEMS applications. *Journal of applied research and technology*, 14(5), 287-292.
- Barua, R., Taheri, P., Chen, Y., Koblishka-Veneva, A., Koblishka, M., Jiang, L., & Harris, V. (2018). Giant Enhancement of Magnetostrictive Response in Directionally-Solidified Fe₈₃Ga₁₇Er_x Compounds. *Materials*, 11(6), 1039.
- Bawane, K. K., Srinivasan, D., & Banerjee, D. (2018). Microstructural Evolution and Mechanical Properties of Direct Metal Laser-Sintered (DMLS) CoCrMo After Heat Treatment. *Metallurgical and Materials Transactions A*, 49(9), 3793-3811.
- Belgacem, M., Thierry, B., & Jean-Claude, G. (2013). Investigations on thermal debinding process for fine 316L stainless steel feedstocks and identification of kinetic parameters from coupling experiments and finite element simulations. *Powder Technology*, 235, 192-202.
- Bellemin-Lapponnaz, S., & Dagorne, S. (2014). Group 1 and 2 and early transition metal complexes bearing N-heterocyclic carbene ligands: coordination chemistry, reactivity, and applications. *Chemical reviews*, 114(18), 8747-8774.
- Berretta, S., Ghita, O., Evans, K. E., Anderson, A., & Newman, C. (2013). Size, shape and flow of powders for use in Selective Laser Sintering (SLS).
- Bissannagari, M., & Kim, J. (2015). Inkjet printing of NiZn-ferrite films and their magnetic properties. *Ceramics International*, 41(6), 8023-8027.

Blacque, O., & Berke, H. (2015). Spontaneously resolving chiral cis-[dinitrotris(ethylenediamine) cobalt] X complexes (X= Cl, Br) from the Alfred Werner collection of original samples at the University of Zurich—Alfred Werner's missed opportunity to become the 'Louis Pasteur' of coordination compounds. *Educación Química*, 26(4), 330-345.

Bloch, E. D., Queen, W. L., Krishna, R., Zadrozny, J. M., Brown, C. M., & Long, J. R. (2012). Hydrocarbon separations in a metal-organic framework with open iron (II) coordination sites. *science*, 335(6076), 1606-1610.

Boutopoulos, C., Kalpyris, I., Serpetzoglou, E., & Zergioti, I. (2014). Laser-induced forward transfer of silver nanoparticle ink: time-resolved imaging of the jetting dynamics and correlation with the printing quality. *Microfluidics and nanofluidics*, 16(3), 493-500.

Brown, M. S., Kattamis, N. T., & Arnold, C. B. (2010). Time-resolved study of polyimide absorption layers for blister-actuated laser-induced forward transfer. *Journal of Applied Physics*, 107(8), 083103.

Bu, F., Xue, X., Wang, J., Kou, H., Li, C., Zhang, P., . . . Li, J. (2018). Effect of strong static magnetic field on the microstructure and transformation temperature of Co–Ni–Al ferromagnetic shape memory alloy. *Journal of Materials Science: Materials in Electronics*, 29(22), 19491-19498.

Bulyk, I., Panasyuk, V., & Trostianchyn, A. (2004). Features of the HDDR process in alloys based on the SmCo₅ compound. *Journal of Alloys and Compounds*, 379(1-2), 154-160.

Burgio, L., & Clark, R. J. (2000). Comparative pigment analysis of six modern Egyptian papyri and an authentic one of the 13th century BC by Raman microscopy and other techniques. *Journal of Raman Spectroscopy*, 31(5), 395-401.

Burke, J. (1984). A History of the Development of a Science of Sintering. *Ancient Technology to Modern Science*, 315.

Buschow, K. (1977). Intermetallic compounds of rare-earth and 3d transition metals. *Reports on Progress in Physics*, 40(10), 1179.

Caputo, M., & Solomon, C. (2017). A facile method for producing porous parts with complex geometries from ferromagnetic Ni-Mn-Ga shape memory alloys. *Materials Letters*, 200, 87-89.

Chao, Y.-p., Qi, L.-h., Xiao, Y., Luo, J., & Zhou, J.-m. (2012). Manufacturing of micro thin-walled metal parts by micro-droplet deposition. *Journal of Materials Processing Technology*, 212(2), 484-491.

Chen, M., & Nikles, D. E. (2002). Synthesis of spherical FePd and CoPt nanoparticles. *Journal of Applied Physics*, 91(10), 8477-8479.

Chen, P., Huang, Y.-Y., Bhave, G., Hoshino, K., & Zhang, X. (2016). Inkjet-print micromagnet array on glass slides for immunomagnetic enrichment of circulating tumor cells. *Annals of biomedical engineering*, *44*(5), 1710-1720.

Chongkang, H., Shunkang, P., CHENG, L., Xing, L., & Yajun, W. (2015). Effect of rare earths on microwave absorbing properties of RE-Co alloys. *Journal of Rare Earths*, *33*(3), 271-276.

Chouhan, R. K., & Paudyal, D. (2017). Cu substituted CeCo₅: New optimal permanent magnetic material with reduced criticality. *Journal of Alloys and Compounds*, *723*, 208-212.

Cioc, R. C., Ruijter, E., & Orru, R. V. (2014). Multicomponent reactions: advanced tools for sustainable organic synthesis. *Green Chemistry*, *16*(6), 2958-2975.

Cotton, S. A. (2016). A Perspective on Lanthanide Chemistry. In *Upconverting Nanomaterials* (pp. 27-42): CRC Press.

Cui, X., Xu, M.-C., Zhang, L.-J., Yao, R.-X., & Zhang, X.-M. (2015). Solvent-free heterogeneous catalysis for cyanosilylation in a dynamic cobalt-MOF. *Dalton Transactions*, *44*(28), 12711-12716.

Cui, Y., Li, B., He, H., Zhou, W., Chen, B., & Qian, G. (2016). Metal-organic frameworks as platforms for functional materials. *Accounts of chemical research*, *49*(3), 483-493.

Das, S. K., Chatterjee, S., Bhunia, S., Mondal, A., Mitra, P., Kumari, V., . . . Bhaumik, A. (2017). A new strongly paramagnetic cerium-containing microporous MOF for CO₂ fixation under ambient conditions. *Dalton Transactions*, 46(40), 13783-13792.

Davis, H., Du Bois, J., & Yu, J. (2011). CH functionalization in organic synthesis. *Chem. Soc. Rev*, 40, 1855-1856.

de la Osa, A., Romero, A., Dorado, F., Valverde, J., & Sánchez, P. (2016). Influence of cobalt precursor on efficient production of commercial fuels over FTS Co/SiC catalyst. *Catalysts*, 6(7), 98.

Dechambenoit, P., & Long, J. R. (2011). Microporous magnets. *Chemical Society Reviews*, 40(6), 3249-3265.

DeGayner, J. A., Jeon, I.-R., Sun, L., Dincă, M., & Harris, T. D. (2017). 2D Conductive Iron-Quinoid Magnets Ordering up to T_c = 105 K via Heterogenous Redox Chemistry. *Journal of the American Chemical Society*, 139(11), 4175-4184.

Denneulin, A., Bras, J., Carcone, F., Neuman, C., & Blayo, A. (2011). Impact of ink formulation on carbon nanotube network organization within inkjet printed conductive films. *Carbon*, 49(8), 2603-2614. doi:10.1016/j.carbon.2011.02.012

Di Pietrantonio, F., Benetti, M., Cannata, D., Verona, E., Palla-Papavlu, A., Dinca, V., . . . Lippert, T. (2012). Volatile toxic compound detection by surface acoustic wave sensor array coated with chemoselective polymers deposited by laser

induced forward transfer: Application to sarin. *Sensors and Actuators B: Chemical*, *174*, 158-167.

Ding, S., & Hall, M. B. (2016). The rich structural chemistry displayed by the carbon monoxide as a ligand to metal complexes. In *The Chemical Bond I* (pp. 199-248): Springer.

Diodati, S., Pandolfo, L., Caneschi, A., Gialanella, S., & Gross, S. (2014). Green and low temperature synthesis of nanocrystalline transition metal ferrites by simple wet chemistry routes. *Nano Research*, *7*(7), 1027-1042.

Dixon, C., Ng, A. H., Fobel, R., Miltenburg, M. B., & Wheeler, A. R. (2016). An inkjet printed, roll-coated digital microfluidic device for inexpensive, miniaturized diagnostic assays. *Lab on a Chip*, *16*(23), 4560-4568.

Dong, H., Chen, Y.-C., & Feldmann, C. (2015). Polyol synthesis of nanoparticles: status and options regarding metals, oxides, chalcogenides, and non-metal elements. *Green Chemistry*, *17*(8), 4107-4132.

Dong, Q., Li, G., Ho, C. L., Faisal, M., Leung, C. W., Pong, P. W. T., . . . Wong, W. Y. (2012). A Polyferroplatinyne Precursor for the Rapid Fabrication of L10-FePt-type Bit Patterned Media by Nanoimprint Lithography. *Advanced Materials*, *24*(8), 1034-1040.

Dong, R., Zhang, Z., Tranca, D. C., Zhou, S., Wang, M., Adler, P., . . . Shi, W. (2018). A coronene-based semiconducting two-dimensional metal-organic framework with ferromagnetic behavior. *Nature communications*, 9(1), 2637.

El-Kady, M. F., Strong, V., Dubin, S., & Kaner, R. B. (2012). Laser scribing of high-performance and flexible graphene-based electrochemical capacitors. *science*, 335(6074), 1326-1330.

Elgammal, M., Schneider, R., & Gradzielski, M. (2016). Development of self-curable hybrid pigment inks by miniemulsion polymerization for inkjet printing of cotton fabrics. *Dyes and Pigments*, 133, 467-478.

Enneti, R. K., Park, S. J., German, R. M., & Atre, S. V. (2012). Thermal debinding process in particulate materials processing. *Materials and Manufacturing Processes*, 27(2), 103-118.

Fang, Z. Z. (2010). *Sintering of advanced materials*: Elsevier.

Farias, M. D., Albuquerque, P. B., Soares, P. A., de Sá, D. M., Vicente, A. A., & Carneiro-da-Cunha, M. G. (2018). Xyloglucan from *Hymenaea courbaril* var. *courbaril* seeds as encapsulating agent of l-ascorbic acid. *International journal of biological macromolecules*, 107, 1559-1566.

Feng, Y., Wang, T., Li, Y., Li, J., Wu, J., Wu, B., . . . Wang, C. (2015). Steering metallofullerene electron spin in porous metal-organic framework. *Journal of the American Chemical Society*, 137(47), 15055-15060.

Fiévet, F., Ammar-Merah, S., Brayner, R., Chau, F., Giraud, M., Mammeri, F., . . . Viau, G. (2018). The polyol process: a unique method for easy access to metal nanoparticles with tailored sizes, shapes and compositions. *Chemical Society Reviews*.

Fittschen, U. E. A., Hauschild, S., Amberger, M., Lammel, G., Strelt, C., Förster, S., . . . Falkenberg, G. (2006). A new technique for the deposition of standard solutions in total reflection X-ray fluorescence spectrometry (TXRF) using picodroplets generated by inkjet printers and its applicability for aerosol analysis with SR-TXRF. *Spectrochimica Acta Part B: Atomic Spectroscopy*, 61(10-11), 1098-1104.

Florek, J., Mushtaq, A., Larivière, D., Cantin, G., Fontaine, F.-G., & Kleitz, F. (2015). Selective recovery of rare earth elements using chelating ligands grafted on mesoporous surfaces. *RSC Advances*, 5(126), 103782-103789.

Frazier, W. E. (2014). Metal additive manufacturing: a review. *Journal of Materials Engineering and Performance*, 23(6), 1917-1928.

Froehlich, P., Lorenz, T., Martin, G., Brett, B., & Bertau, M. (2017). Valuable metals—recovery processes, current trends, and recycling strategies. *Angewandte Chemie International Edition*, 56(10), 2544-2580.

Gaidukova, I. Y., Granovsky, S., Markosyan, A., Petropavlovsky, A., Rodimin, V., & Uryvaev, V. (2006). The cobalt magnetic state in RCo₃ intermetallics with light

rare earth studied by thermal expansion. *Journal of magnetism and magnetic materials*, 300(1), e452-e454.

Gaj, M. P., Fuentes-Hernandez, C., Zhang, Y., Marder, S. R., & Kippelen, B. (2015). Highly efficient organic light-emitting diodes from thermally activated delayed fluorescence using a sulfone-carbazole host material. *Organic Electronics*, 16, 109-112.

Garibaldi, M., Ashcroft, I., Simonelli, M., & Hague, R. (2016). Metallurgy of high-silicon steel parts produced using Selective Laser Melting. *Acta Materialia*, 110, 207-216.

Gerloch, M., Constable, E., & Kaim, W. (1995). Transition Metal Chemistry. *Angewandte Chemie-German Edition*, 107(20), 2481-2481.

Girard, F., Antoni, M., Faure, S., & Steinchen, A. (2006). Evaporation and Marangoni driven convection in small heated water droplets. *Langmuir*, 22(26), 11085-11091.

Gómez, E., Cojocar, P., Magagnin, L., & Valles, E. (2011). Electrodeposition of Co, Sm and SmCo from a deep eutectic solvent. *Journal of Electroanalytical Chemistry*, 658(1-2), 18-24.

Green, C., Vaughan, A., Stevens, G., Pye, A., Sutton, S., Geussens, T., & Fairhurst, M. (2015). Thermoplastic cable insulation comprising a blend of isotactic

polypropylene and a propylene-ethylene copolymer. *IEEE Transactions on Dielectrics and Electrical Insulation*, 22(2), 639-648.

Gross, B. C., Erkal, J. L., Lockwood, S. Y., Chen, C., & Spence, D. M. (2014). Evaluation of 3D printing and its potential impact on biotechnology and the chemical sciences. In: ACS Publications.

Gu, D., Meiners, W., Wissenbach, K., & Poprawe, R. (2012). Laser additive manufacturing of metallic components: materials, processes and mechanisms. *International materials reviews*, 57(3), 133-164.

Gu, D., & Shen, Y. (2009). Balling phenomena in direct laser sintering of stainless steel powder: Metallurgical mechanisms and control methods. *Materials & Design*, 30(8), 2903-2910.

Gu, H., Zheng, R., Rao, J., Zhang, X., Fung, K., & Xu, B. (2003). *Chemical synthesis and magnetization measurement of SmCo₅ magnetic nanoparticles*. Paper presented at the 225th ACS National Meeting, New Orleans, March.

Gu, Y., Halász, G. B., Robinson, J., & Blamire, M. G. (2015). Large superconducting spin valve effect and ultrasmall exchange splitting in epitaxial rare-earth-niobium trilayers. *Physical review letters*, 115(6), 067201.

Guerriero, A., Peruzzini, M., & Gonsalvi, L. (2017). Coordination chemistry of 1, 3, 5-triaza-7-phosphatricyclo decane (PTA) and derivatives. Part III. Variations on

a theme: Novel architectures, materials and applications. *Coordination Chemistry Reviews*.

Guo, N., & Leu, M. C. (2013). Additive manufacturing: technology, applications and research needs. *Frontiers of Mechanical Engineering*, 8(3), 215-243.

Hadadzadeh, A., Baxter, C., Amirkhiz, B. S., & Mohammadi, M. (2018). Strengthening mechanisms in direct metal laser sintered AlSi10Mg: Comparison between virgin and recycled powders. *Additive Manufacturing*, 23, 108-120.

Hannachi, M., Belkacem, W., Bessais, L., & Mliki, N. (2016). Investigations of SmCo thin films grown on kapton substrate. *Journal of Superconductivity and Novel Magnetism*, 29(2), 383-388.

Haxel, G. B., Hedrick, J. B., Orris, G. J., Stauffer, P. H., & Hendley II, J. W. (2002). *Rare earth elements: critical resources for high technology (2327-6932)*. Retrieved from

He, Y.-P., Tan, Y.-X., & Zhang, J. (2015). Gas Sorption, Second-Order Nonlinear Optics, and Luminescence Properties of a Multifunctional srs-Type Metal–Organic Framework Built by Tris (4-carboxylphenylduryl) amine. *Inorganic chemistry*, 54(13), 6653-6656.

Hong, S., Yeo, J., Kim, G., Kim, D., Lee, H., Kwon, J., . . . Ko, S. H. (2013). Nonvacuum, maskless fabrication of a flexible metal grid transparent conductor

by low-temperature selective laser sintering of nanoparticle ink. *ACS nano*, 7(6), 5024-5031.

Hou, J., Zhang, H., Yang, Q., Li, M., Song, Y., & Jiang, L. (2014). Bio-inspired photonic-crystal microchip for fluorescent ultratrace detection. *Angewandte Chemie International Edition*, 53(23), 5791-5795.

Hou, X., Shen, W., Huang, X., Ai, Z., & Zhang, L. (2016). Ascorbic acid enhanced activation of oxygen by ferrous iron: a case of aerobic degradation of rhodamine B. *Journal of hazardous materials*, 308, 67-74.

Hu, Q., Shao, J., Yang, H., Yao, D., Wang, X., & Chen, H. (2015). Effects of binders on the properties of bio-char pellets. *Applied energy*, 157, 508-516.

Hu, Y., Drouin, E., Larivière, D., Kleitz, F., & Fontaine, F. d. r.-G. (2017). Highly Efficient and Selective Recovery of Rare Earth Elements Using Mesoporous Silica Functionalized by Preorganized Chelating Ligands. *ACS applied materials & interfaces*, 9(44), 38584-38593.

Huang, C.-H. (2011). *Rare earth coordination chemistry: fundamentals and applications*: John Wiley & Sons.

Huang, G., Li, X., Lou, L., Hua, Y., Zhu, G., Li, M., . . . Yue, M. (2018). Engineering bulk, layered, multicomponent nanostructures with high energy density. *Small*, 14(22), 1800619.

Hubbard, W. M., Adams, E., & Gilfrich, J. (1960). Magnetic moments of alloys of gadolinium with some of the transition elements. *Journal of Applied Physics*, 31(5), S368-S369.

Ibrahim, M., Johari, M. A. M., Rahman, M. K., & Maslehuddin, M. (2017). Effect of alkaline activators and binder content on the properties of natural pozzolan-based alkali activated concrete. *Construction and Building Materials*, 147, 648-660.

Jacot-Descombes, L., Gullo, M. R., Cadarso, V. J., Mastrangeli, M., Ergeneman, O., Peters, C., . . . Nelson, B. J. (2014). Inkjet printing of high aspect ratio superparamagnetic SU-8 microstructures with preferential magnetic directions. *Micromachines*, 5(3), 583-593.

Jahn, S. F., Jakob, A., Reinhold, I., Engisch, L., Lang, H., & Baumann, R. R. (2008). *Structuring of flexible substrates by the use of an aqueous solution based silver ink*. Paper presented at the NIP & Digital Fabrication Conference.

Jakus, A. E., Taylor, S. L., Geisendorfer, N. R., Dunand, D. C., & Shah, R. N. (2015). Metallic architectures from 3D-printed powder-based liquid inks. *Advanced Functional Materials*, 25(45), 6985-6995.

James, S. L. (2003). Metal-organic frameworks. *Chemical Society Reviews*, 32(5), 276-288.

Janicki, R., Mondry, A., & Starynowicz, P. (2017). Carboxylates of rare earth elements. *Coordination Chemistry Reviews*, 340, 98-133.

Jha, M. K., Kumari, A., Panda, R., Kumar, J. R., Yoo, K., & Lee, J. Y. (2016). Review on hydrometallurgical recovery of rare earth metals. *Hydrometallurgy*, 165, 2-26.

Jiang, Q., Lei, W., Zeng, Q., Quan, Q., Zhang, L., Liu, R., . . . Ju, Z. (2018). Improved magnetic properties and thermal stabilities of Pr-Nd-Fe-B sintered magnets by Hf addition. *AIP Advances*, 8(5), 056203.

Jingtao, D., Binbin, Z., & Dongmei, C. (2012). Synthesis and Characterization of Magnetic Nanoparticles SmCo₅. *RARE METAL MATERIALS AND ENGINEERING*, 41(12), 2215-2218.

Jung, H. Y., Choi, S. J., Prashanth, K. G., Stoica, M., Scudino, S., Yi, S., . . . Eckert, J. (2015). Fabrication of Fe-based bulk metallic glass by selective laser melting: A parameter study. *Materials & Design*, 86, 703-708.

Kattamis, N. T., Brown, M. S., & Arnold, C. B. (2011). Finite element analysis of blister formation in laser-induced forward transfer. *Journal of Materials Research*, 26(18), 2438-2449.

Ketelle, B., & Boyd, G. (1947). The Exchange Adsorption of Ions from Aqueous Solutions by Organic Zeolites. IV. The Separation of the Yttrium Group Rare Earths¹. *Journal of the American Chemical Society*, 69(11), 2800-2812.

Kinemuchi, Y., Mimura, K.-i., Towata, A., & Kato, K. (2014). Thermoelectric Properties of Rare Earth-Doped SrTiO₃ Nanocubes. *Journal of Electronic Materials*, 43(6), 2011-2016.

Krug, S., Evans, J., & Ter Maat, J. (2002). Differential sintering in ceramic injection moulding: particle orientation effects. *Journal of the European Ceramic Society*, 22(2), 173-181.

Krüger, S., & Deubener, J. (2016). The TTT curves of the heterogeneous and homogeneous crystallization of lithium disilicate—a stochastic approach to crystal nucleation. *Frontiers in Materials*, 3, 42.

Kurmoo, M. (2009). Magnetic metal–organic frameworks. *Chemical Society Reviews*, 38(5), 1353-1379.

Ladd, C., So, J. H., Muth, J., & Dickey, M. D. (2013). 3D printing of free standing liquid metal microstructures. *Advanced Materials*, 25(36), 5081-5085.

Le Houerou, V., Sangleboeuf, J. C., & Rouxel, T. (2005). Scratchability of soda-lime silica (SLS) glasses: Dynamic fracture analysis. *Fractography of Advanced Ceramics Ii*, 290, 31-38.

Lee, D. J., Oh, J. H., & Bae, H. S. (2010). Crack formation and substrate effects on electrical resistivity of inkjet-printed Ag lines. *Materials Letters*, 64(9), 1069-1072.

- Lee, H., Tentzeris, M. M., Markondeya, P., Raj, M. K., & Kawahara, Y. (2013). *Inkjet-printed ferromagnetic nanoparticles for miniaturization of flexible printed RF inductors*. Paper presented at the Antennas and Propagation Society International Symposium (APSURSI), 2013 IEEE.
- Lee, J.-Y., An, J., & Chua, C. K. (2017). Fundamentals and applications of 3D printing for novel materials. *Applied Materials Today*, 7, 120-133.
- Lee, J., Hwang, T.-Y., Kang, M. K., Cho, H.-B., Kim, J., Myung, N. V., & Choa, Y.-H. (2018). Synthesis of Samarium-Cobalt Sub-micron Fibers and Their Excellent Hard Magnetic Properties. *Frontiers in chemistry*, 6, 18.
- Lee, S.-Y., Mohan, D. J., Kang, I.-A., Doh, G.-H., Lee, S., & Han, S. O. (2009). Nanocellulose reinforced PVA composite films: effects of acid treatment and filler loading. *Fibers and Polymers*, 10(1), 77-82.
- Lee, Y., Choi, J.-r., Lee, K. J., Stott, N. E., & Kim, D. (2008). Large-scale synthesis of copper nanoparticles by chemically controlled reduction for applications of inkjet-printed electronics. *Nanotechnology*, 19(41), 415604.
- Li, B., Wen, H.-M., Zhou, W., & Chen, B. (2014). Porous metal–organic frameworks for gas storage and separation: what, how, and why? *The journal of physical chemistry letters*, 5(20), 3468-3479.

Li, B., Wen, H. M., Cui, Y., Zhou, W., Qian, G., & Chen, B. (2016). Emerging multifunctional metal–organic framework materials. *Advanced Materials*, 28(40), 8819-8860.

Li, G., Roberts, R. C., & Tien, N. C. (2014). *Interlacing method for micro-patterning silver via inkjet printing*. Paper presented at the SENSORS, 2014 IEEE.

Li, L., Shen, S., Lin, R., Bai, Y., & Liu, H. (2017). Rapid and specific luminescence sensing of Cu (ii) ions with a porphyrinic metal–organic framework. *Chemical Communications*, 53(72), 9986-9989.

Li, T., Kaercher, S., & Roesky, P. W. (2014). Synthesis, structure and reactivity of rare-earth metal complexes containing anionic phosphorus ligands. *Chemical Society Reviews*, 43(1), 42-57.

Li, Y., Liu, Y., Yamauchi, Y., Kaneti, Y., Alsheri, S., Ahamad, T., . . . Wu, N. (2018). Micelle-Assisted Strategy for the Direct Synthesis of Large-Sized Mesoporous Platinum Catalysts by Vapor Infiltration of a Reducing Agent. *Nanomaterials*, 8(10), 841.

Lim, T., Han, S., Chung, J., Chung, J. T., Ko, S., & Grigoropoulos, C. P. (2009). Experimental study on spreading and evaporation of inkjet printed pico-liter droplet on a heated substrate. *International Journal of Heat and Mass Transfer*, 52(1-2), 431-441. doi:10.1016/j.ijheatmasstransfer.2008.05.028

Lim, T., Jeong, J., Chung, J., & Chung, J. T. (2009). Evaporation of inkjet printed pico-liter droplet on heated substrates with different thermal conductivity. *Journal of mechanical science and technology*, 23(7), 1788-1794.

Lin, K.-H., Peng, S.-F., & Lin, S.-T. (2007). Sintering parameters and wear performances of vitrified bond diamond grinding wheels. *International Journal of Refractory Metals and Hard Materials*, 25(1), 25-31.

Lin, R. B., Liu, S. Y., Ye, J. W., Li, X. Y., & Zhang, J. P. (2016). Photoluminescent metal–organic frameworks for gas sensing. *Advanced Science*, 3(7), 1500434.

Lin, Y.-T., Liang, C., & Yu, C.-W. (2016). Trichloroethylene degradation by various forms of iron activated persulfate oxidation with or without the assistance of ascorbic acid. *Industrial & Engineering Chemistry Research*, 55(8), 2302-2308.

Liu, J.-F., Pan, F.-X., Yao, S., Min, X., Cui, D., & Sun, Z.-M. (2014). Syntheses, Structure, and Properties of Mixed Cp–Amidinate Rare-Earth-Metal (III) Complexes. *Organometallics*, 33(6), 1374-1381.

Liu, M.-Q., Shen, X.-Q., Meng, X.-F., SONG, F.-Z., & XIANG, J. (2010). Fabrication and magnetic property of M-type strontium ferrite nanofibers by electrospinning. *Journal of Inorganic Materials*, 1, 014.

Liu, Y., Yi, Y., Shao, W., & Shao, Y. (2013). Microstructure and magnetic properties of soft magnetic powder cores of amorphous and nanocrystalline alloys. *Journal of Magnetism and Magnetic Materials*, 330, 119-133.

- Liu, Z., Li, C., Fang, X., & Guo, Y. (2018). Energy Consumption in Additive Manufacturing of Metal Parts. *Procedia Manufacturing*, 26, 834-845.
- Lu, N., Song, X., & Zhang, J. (2010). Crystal structure and magnetic properties of ultrafine nanocrystalline SmCo₃ compound. *Nanotechnology*, 21(11), 115708.
- Luo, H., Wang, D., He, J., & Lu, Y. (2005). Magnetic cobalt nanowire thin films. *The Journal of Physical Chemistry B*, 109(5), 1919-1922.
- Luo, Y.-R. (2007). *Comprehensive handbook of chemical bond energies*: CRC press.
- Ma, Z., Yang, S., Zhang, T., & Jiang, C. (2016). The chemical synthesis of SmCo₅ single-crystal particles with small size and high performance. *Chemical Engineering Journal*, 304, 993-999.
- Ma, Z., Zhang, T., & Jiang, C. (2015). A facile synthesis of high performance SmCo₅ nanoparticles. *Chemical Engineering Journal*, 264, 610-616.
- Maria, L., Soares, M., Santos, I. C., Sousa, V. R., Mora, E., Marçalo, J., & Luzyanin, K. V. (2016). A novel samarium (II) complex bearing a dianionic bis (phenolate) cyclam ligand: synthesis, structure and electron-transfer reactions. *Dalton Transactions*, 45(9), 3778-3790.
- Marjanović, N., Chiolerio, A., Kus, M., Ozel, F., Tilki, S., Ivanović, N., . . . Baumann, R. R. (2014). Magnetite nanoparticles: synthesis, thin film properties

and inkjet printing of magnetic cores for inductor applications. *Thin Solid Films*, 570, 38-44.

Marques, L. F., Santos, H. P., Correa, C. C., Resende, J. A., da Silva, R. R., Ribeiro, S. J., & Machado, F. C. (2016). Construction of a series of rare earth metal-organic frameworks supported by thiophenedicarboxylate linker: Synthesis, characterization, crystal structures and near-infrared/visible luminescence. *Inorganica Chimica Acta*, 451, 41-51.

Matsushita, T., Iwamoto, T., Inokuchi, M., & Toshima, N. (2010). Novel ferromagnetic materials of SmCo₅ nanoparticles in single-nanometer size: chemical syntheses and characterizations. *Nanotechnology*, 21(9), 095603.

Matyi, R., & Baboian, R. (1986). An X-ray diffraction analysis of the patina of the Statue of Liberty. *Powder diffraction*, 1(4), 299-304.

McKenna, S. M., Leimkühler, S., Herter, S., Turner, N. J., & Carnell, A. J. (2015). Enzyme cascade reactions: synthesis of furandicarboxylic acid (FDCA) and carboxylic acids using oxidases in tandem. *Green Chemistry*, 17(6), 3271-3275.

Mei, J., Lovell, M. R., & Mickle, M. H. (2005). Formulation and processing of novel conductive solution inks in continuous inkjet printing of 3-D electric circuits. *IEEE transactions on electronics packaging manufacturing*, 28(3), 265-273.

Melchert, W. R., Reis, B. F., & Rocha, F. R. (2012). Green chemistry and the evolution of flow analysis. A review. *Analytica Chimica Acta*, 714, 8-19.

Meshcheryakov, Y. P., Shugaev, M. V., Mattle, T., Lippert, T., & Bulgakova, N. M. (2013). Role of thermal stresses on pulsed laser irradiation of thin films under conditions of microbump formation and nonvaporization forward transfer. *Applied Physics A*, 113(2), 521-529.

Meyer, B., Polity, A., Reppin, D., Becker, M., Hering, P., Klar, P., . . . Eickhoff, M. (2012). Binary copper oxide semiconductors: From materials towards devices. *physica status solidi (b)*, 249(8), 1487-1509.

Mirzadeh, H., & Parsa, M. (2014). Hot deformation and dynamic recrystallization of NiTi intermetallic compound. *Journal of Alloys and Compounds*, 614, 56-59.

Munir, Z. A., Quach, D. V., & Ohyanagi, M. (2011). Electric current activation of sintering: a review of the pulsed electric current sintering process. *Journal of the American Ceramic Society*, 94(1), 1-19.

Murugesan, K., Senthamarai, T., Sohail, M., Alshammari, A. S., Pohl, M.-M., Beller, M., & Jagadeesh, R. V. (2018). Cobalt-based nanoparticles prepared from MOF-carbon templates as efficient hydrogenation catalysts. *Chemical Science*.

Nandwana, P., Elliott, A. M., Siddel, D., Merriman, A., Peter, W. H., & Babu, S. S. (2017). Powder bed binder jet 3D printing of Inconel 718: Densification, microstructural evolution and challenges☆. *Current Opinion in Solid State and Materials Science*, 21(4), 207-218.

Nassau, K., Cherry, L., & Wallace, W. (1960). Intermetallic compounds between lanthanons and transition metals of the first long period: I—Preparation, existence and structural studies. *Journal of Physics and Chemistry of Solids*, 16(1-2), 123-130.

Nerush, E., Kostyukov, I. Y., Fedotov, A., Narozhny, N., Elkina, N., & Ruhl, H. (2011). Laser field absorption in self-generated electron-positron pair plasma. *Physical review letters*, 106(3), 035001.

Nesbitt, E., Williams, H., Wernick, J., & Sherwood, R. (1962). Magnetic Moments of Intermetallic Compounds of Transition and Rare-Earth Elements. *Journal of Applied Physics*, 33(5), 1674-1678.

Nie, J., Han, X., Du, J., Xia, W., Zhang, J., Guo, Z., . . . Liu, J. P. (2013). Structure and magnetism of SmCo₅ nanoflakes prepared by surfactant-assisted ball milling with different ball sizes. *Journal of magnetism and magnetic materials*, 347, 116-123.

Nishikawa, M., Nakajima, T., Kumagai, T., Okutani, T., & Tsuchiya, T. (2011). Ti-doped VO₂ films grown on glass substrates by excimer-laser-assisted metal-organic deposition process. *Japanese Journal of Applied Physics*, 50(1S2), 01BE04.

Nowick, A. (2012). *Rare earth permanent magnets*: Elsevier.

Obaleye, J. A., & Orjiekwe, C. L. (1992). Synthesis and Characterization of Some Metal Complexes of Vitamin C. Part 21—Ascorbate Complexes of Mn (II), Fe (III) and Co (II). *Synthesis and Reactivity in Inorganic and Metal-Organic Chemistry*, 22(7), 1015-1029.

Ormerod, J., & Constantinides, S. (1997). Bonded permanent magnets: current status and future opportunities. *Journal of Applied Physics*, 81(8), 4816-4820.

Paglia, F., Vak, D., van Embden, J., Chesman, A. S., Martucci, A., Jasieniak, J. J., & Della Gaspera, E. (2015). Photonic sintering of copper through the controlled reduction of printed CuO nanocrystals. *ACS applied materials & interfaces*, 7(45), 25473-25478.

Paille, G. g., Gomez-Mingot, M., Roch-Marchal, C., Lassalle-Kaiser, B., Mialane, P., Fontecave, M., . . . Dolbecq, A. (2018). A Fully Noble Metal-Free Photosystem Based on Cobalt-Polyoxometalates Immobilized in a Porphyrinic Metal-Organic Framework for Water Oxidation. *Journal of the American Chemical Society*.

Panicker, C. Y., Varghese, H. T., & Philip, D. (2006). FT-IR, FT-Raman and SERS spectra of Vitamin C. *Spectrochimica Acta Part A: Molecular and Biomolecular Spectroscopy*, 65(3-4), 802-804.

Park, J.-I., & Cheon, J. (2001). Synthesis of “solid solution” and “core-shell” type cobalt– platinum magnetic nanoparticles via transmetalation reactions. *Journal of the American Chemical Society*, 123(24), 5743-5746.

Park, Y.-S., Oh, E.-S., & Lee, S.-M. (2014). Effect of polymeric binder type on the thermal stability and tolerance to roll-pressing of spherical natural graphite anodes for Li-ion batteries. *Journal of Power Sources*, 248, 1191-1196.

Patel, K. S., Patel, J. C., Dholariya, H. R., Patel, V. K., & Patel, K. D. (2012). Synthesis of Cu (II), Ni (II), Co (II), and Mn (II) complexes with ciprofloxacin and their evaluation of antimicrobial, antioxidant and anti-tubercular activity. *Open Journal of Metal*, 2(3), 49.

Pohl, R., Visser, C. W., Römer, G.-W., Lohse, D., Sun, C., & Huis, B. (2015). Ejection regimes in picosecond laser-induced forward transfer of metals. *Physical review applied*, 3(2), 024001.

Pramanik, A., & Banerjee, A. (2010). Interparticle interaction and crossover in critical lines on field-temperature plane in Pr_{0.5}Sr_{0.5}MnO₃ nanoparticles. *Physical Review B*, 82(9), 094402.

Qiu, Z., Liu, J. P., Yu, H., Poudyal, N., Han, G., Zeng, D., & Hong, Y. (2018). Atomic diffusion and microstructure of SmCo₅ multilayers with high coercivity. *Journal of Alloys and Compounds*, 733, 45-52.

Qu, H., Zhu, S., Li, Q., & Ouyang, C. (2012). Influence of sintering temperature and holding time on the densification, phase transformation, microstructure and properties of hot pressing WC-40 vol.% Al₂O₃ composites. *Ceramics International*, 38(2), 1371-1380.

Rapp, L., Cibert, C., Alloncle, A. P., & Delaporte, P. (2009). Characterization of organic material micro-structures transferred by laser in nanosecond and picosecond regimes. *Applied surface science*, 255(10), 5439-5443.

Ren, L., Luo, X., & Zhou, H. (2018). The tape casting process for manufacturing low-temperature co-fired ceramic green sheets: A review. *Journal of the American Ceramic Society*, 101(9), 3874-3889.

Renfrew, A. K., O'Neill, E. S., Hambley, T. W., & New, E. J. (2017). Harnessing the properties of cobalt coordination complexes for biological application. *Coordination Chemistry Reviews*.

Reszczyńska, J., Grzyb, T., Sobczak, J. W., Lisowski, W., Gazda, M., Ohtani, B., & Zaleska, A. (2015). Visible light activity of rare earth metal doped (Er³⁺, Yb³⁺ or Er³⁺/Yb³⁺) titania photocatalysts. *Applied Catalysis B: Environmental*, 163, 40-49.

Roosen, A., & Bowen, H. K. (1988). Influence of various consolidation techniques on the green microstructure and sintering behavior of alumina powders. *Journal of the American Ceramic Society*, 71(11), 970-977.

Saad, F. A. (2014). Co-ordination chemistry of some first row transition metal complexes with multi-dentate ligand (1-benzoyl-3-(4-methylpyridin-2-yl) thiourea), spectral, electrochemical and X-ray single crystal studies. *Int. J. Electrochem. Sci*, 9, 4761-4775.

- Saadatkia, S., Mirzadeh, H., & Cabrera, J.-M. (2015). Hot deformation behavior, dynamic recrystallization, and physically-based constitutive modeling of plain carbon steels. *Materials Science and Engineering: A*, 636, 196-202.
- Sahlberg, M., Karlsson, D., Zlotea, C., & Jansson, U. (2016). Superior hydrogen storage in high entropy alloys. *Scientific reports*, 6, 36770.
- Sametoglu, V., Sauer, V. T., & Tsui, Y. Y. (2013). Production of 70-nm Cr dots by laser-induced forward transfer. *Optics express*, 21(15), 18525-18531.
- Sayama, J., Asahi, T., Mizutani, K., & Osaka, T. (2003). Newly developed SmCo₅ thin film with perpendicular magnetic anisotropy. *Journal of Physics D: Applied Physics*, 37(1), L1.
- Schaller, H., Craig, R., & Wallace, W. (1972). Magnetic characteristics of some binary and ternary 2–17 compounds. *Journal of Applied Physics*, 43(7), 3161-3164.
- Scheunert, G., Ward, C., Hendren, W., Lapicki, A., Hardeman, R., Mooney, M., . . . Bowman, R. (2014). Influence of strain and polycrystalline ordering on magnetic properties of high moment rare earth metals and alloys. *Journal of Physics D: Applied Physics*, 47(41), 415005.
- Shahzad, K., Deckers, J., Kruth, J.-P., & Vleugels, J. (2013). Additive manufacturing of alumina parts by indirect selective laser sintering and post processing. *Journal of Materials Processing Technology*, 213(9), 1484-1494.

Sharma, M., Bansal, A., Panthi, S., Malik, S. S., & Sharma, A. (2017). To Evaluate the Marginal Fit of Metal Copings Fabricated by Conventional Casting Procedure and Direct Metal Laser Sintering Technology—an In Vitro Study. *Dental Journal of Advance Studies*, 5(01), 039-046.

Sharma, R., Sharma, S., Dutta, S., Zboril, R., & Gawande, M. B. (2015). Silica-nanosphere-based organic–inorganic hybrid nanomaterials: synthesis, functionalization and applications in catalysis. *Green Chemistry*, 17(6), 3207-3230.

Shaw-Stewart, J., Lippert, T., Nagel, M., Nüesch, F., & Wokaun, A. (2011). Laser-induced forward transfer of polymer light-emitting diode pixels with increased charge injection. *ACS applied materials & interfaces*, 3(2), 309-316.

Shaw-Stewart, J. R., Lippert, T. K., Nagel, M., Nüesch, F. A., & Wokaun, A. (2012). Sequential printing by laser-induced forward transfer to fabricate a polymer light-emitting diode pixel. *ACS applied materials & interfaces*, 4(7), 3535-3541.

Shen, B., Yu, C., Su, D., Yin, Z., Li, J., Xi, Z., & Sun, S. (2018). A new strategy to synthesize anisotropic SmCo 5 nanomagnets. *Nanoscale*, 10(18), 8735-8740.

Shen, S., Pan, C., Wang, Y., & Chang, C. (2006). Fabrication of integrated nozzle plates for inkjet print head using microinjection process. *Sensors and Actuators A: Physical*, 127(2), 241-247.

Shi, Q., Chen, Z., Song, Z., Li, J., & Dong, J. (2011). Synthesis of ZIF-8 and ZIF-67 by Steam-Assisted Conversion and an Investigation of Their Tribological Behaviors. *Angewandte Chemie*, 123(3), 698-701.

Shin, K.-Y., Hong, J.-Y., & Jang, J. (2011). Flexible and transparent graphene films as acoustic actuator electrodes using inkjet printing. *Chemical Communications*, 47(30), 8527-8529.

Shirazi, S. F. S., Gharekhani, S., Mehrali, M., Yarmand, H., Metselaar, H. S. C., Kadri, N. A., & Osman, N. A. A. (2015). A review on powder-based additive manufacturing for tissue engineering: selective laser sintering and inkjet 3D printing. *Science and Technology of Advanced Materials*, 16(3), 033502.

Shongwe, M., Ramakokovhu, M., Diouf, S., Durowoju, M., Obadele, B., Sule, R., . . . Olubambi, P. (2016). Effect of starting powder particle size and heating rate on spark plasma sintering of FeNi alloys. *Journal of Alloys and Compounds*, 678, 241-248.

Sing, S. L., Yeong, W. Y., Wiria, F. E., Tay, B. Y., Zhao, Z., Zhao, L., . . . Yang, S. (2017). Direct selective laser sintering and melting of ceramics: a review. *Rapid Prototyping Journal*, 23(3), 611-623.

Singh, M., Haverinen, H. M., Dhagat, P., & Jabbour, G. E. (2010). Inkjet printing—process and its applications. *Advanced Materials*, 22(6), 673-685.

Smyrnioti, M., & Ioannides, T. (2017). Synthesis of Cobalt-Based Nanomaterials from Organic Precursors. In *Cobalt: InTech*.

Sousa Filho, P. C. d., Lima, J. F., & Serra, O. A. (2015). From lighting to photoprotection: fundamentals and applications of rare earth materials. *Journal of the Brazilian Chemical Society*, 26(12), 2471-2495.

Sreeja, V., Jayaprabha, K., & Joy, P. (2015). Water-dispersible ascorbic-acid-coated magnetite nanoparticles for contrast enhancement in MRI. *Applied Nanoscience*, 5(4), 435-441.

Stoianova, D., Johns, A., & Pederson, R. (2015). Olefin metathesis: Commercial applications and future opportunities. *Handbook of Metathesis*, 699-726.

Stringer, J., & Derby, B. (2009). Limits to feature size and resolution in ink jet printing. *Journal of the European Ceramic Society*, 29(5), 913-918.

Stringer, J., & Derby, B. (2010). Formation and stability of lines produced by inkjet printing. *Langmuir*, 26(12), 10365-10372.

Strnat, K., Hoffer, G., Olson, J., Ostertag, W., & Becker, J. (1967). A family of new cobalt-base permanent magnet materials. *Journal of Applied Physics*, 38(3), 1001-1002.

Strnat, K., Hoffer, G., Ostertag, W., & Olson, J. (1966). Ferrimagnetism of the Rare-Earth-Cobalt Intermetallic Compounds R_2Co_{17} . *Journal of Applied Physics*, 37(3), 1252-1253.

Suh, J., Shin, S., & Bae, D. (2015). Fabrication of tungsten-based composites by solid binder mixing and sintering. *Powder Technology*, 283, 401-405.

Sun, S., Murray, C. B., Weller, D., Folks, L., & Moser, A. (2000). Monodisperse FePt nanoparticles and ferromagnetic FePt nanocrystal superlattices. *science*, 287(5460), 1989-1992.

Takemori, M. T. (1979). Towards an understanding of the heat distortion temperature of thermoplastics. *Polymer Engineering & Science*, 19(15), 1104-1109.

Tao, Y., Li, Z., & Zhou, K. (2013). Effects of debinding atmosphere on the microstructure and sintering densification of nickel ferrite. *Ceramics International*, 39(1), 865-869.

Tedstone, A. A., Lewis, D. J., & O'Brien, P. (2016). Synthesis, properties, and applications of transition metal-doped layered transition metal dichalcogenides. *Chemistry of Materials*, 28(7), 1965-1974.

Torad, N. L., Hu, M., Ishihara, S., Sukegawa, H., Belik, A. A., Imura, M., . . . Yamauchi, Y. (2014). Direct synthesis of MOF-derived nanoporous carbon with

magnetic Co nanoparticles toward efficient water treatment. *Small*, 10(10), 2096-2107.

Torgerson, T., Harris, M., Alidokht, S., Scharf, T., Aouadi, S., Chromik, R., . . . Voevodin, A. (2018). Room and elevated temperature sliding wear behavior of cold sprayed Ni-WC composite coatings. *Surface and Coatings Technology*, 350, 136-145.

Tran, V.-H. T., & Lee, B.-K. (2017). Novel fabrication of a robust superhydrophobic PU@ ZnO@ Fe₃O₄@ SA sponge and its application in oil-water separations. *Scientific reports*, 7(1), 17520.

Uematsu, K., Ito, H., Ohsaka, S., Takahashi, H., Shinohara, N., & Okumiya, M. (1995). Characterization of particle packing in an injected molded green body. *Journal of the American Ceramic Society*, 78(11), 3107-3109.

Unger, C., Koch, J., Overmeyer, L., & Chichkov, B. N. (2012). Time-resolved studies of femtosecond-laser induced melt dynamics. *Optics express*, 20(22), 24864-24872.

Vaezi, M., Seitz, H., & Yang, S. (2013). A review on 3D micro-additive manufacturing technologies. *The International Journal of Advanced Manufacturing Technology*, 67(5-8), 1721-1754.

Vaseem, M., Lee, K. M., Hong, A.-R., & Hahn, Y.-B. (2012). Inkjet printed fractal-connected electrodes with silver nanoparticle ink. *ACS applied materials & interfaces*, 4(6), 3300-3307.

Visser, C. W., Pohl, R., Sun, C., Römer, G. W., Huis in 't Veld, B., & Lohse, D. (2015). Toward 3D printing of pure metals by laser-induced forward transfer. *Advanced Materials*, 27(27), 4087-4092.

Wadell, C., Nugroho, F. A. A., Lidström, E., Iandolo, B., Wagner, J. B., & Langhammer, C. (2015). Hysteresis-free nanoplasmonic Pd–Au alloy hydrogen sensors. *Nano letters*, 15(5), 3563-3570.

Wallace, W. E. (2012). *Rare earth intermetallics*: Elsevier.

Wang, G., Robert, C., Suslu, A., Chen, B., Yang, S., Alamdari, S., . . . Tongay, S. (2015). Spin-orbit engineering in transition metal dichalcogenide alloy monolayers. *Nature communications*, 6, 10110.

Wang, K., Chen, Y., Tian, R., Li, H., Zhou, Y., Duan, H., & Liu, H. (2018). Porous Co–C Core–Shell Nanocomposites Derived from Co-MOF-74 with Enhanced Electromagnetic Wave Absorption Performance. *ACS applied materials & interfaces*, 10(13), 11333-11342.

Wang, L. J., Deng, H., Furukawa, H., Gándara, F., Cordova, K. E., Peri, D., & Yaghi, O. M. (2014). Synthesis and characterization of metal–organic framework-

74 containing 2, 4, 6, 8, and 10 different metals. *Inorganic chemistry*, 53(12), 5881-5883.

Wang, N., Liu, G.-Q., Leong, W.-H., Zeng, H., Feng, X., Li, S.-H., . . . Cui, X.-D. (2018). Magnetic Criticality Enhanced Hybrid Nanodiamond Thermometer under Ambient Conditions. *Physical Review X*, 8(1), 011042.

Wang, R., & Zheng, Z. (2010). Rare Earth Complexes with Carboxylic Acids, Polyaminopolycarboxylic Acids, and Amino Acids. *Rare Earth Coordination Chemistry: Fundamentals and Applications*, 91-136.

Wang, Y., Luo, Y., Wang, Z., Wu, G., Xie, J., Yan, W., & Yu, D. (2018). Coercivity enhancement in Nd-Fe-B magnetic powders by Nd-Cu-Al grain boundary diffusion. *Journal of magnetism and magnetic materials*, 458, 85-89.

Wong, K. V., & Hernandez, A. (2012). A review of additive manufacturing. *ISRN Mechanical Engineering*, 2012.

Wu, H. B., Xia, B. Y., Yu, L., Yu, X.-Y., & Lou, X. W. D. (2015). Porous molybdenum carbide nano-octahedrons synthesized via confined carburization in metal-organic frameworks for efficient hydrogen production. *Nature communications*, 6, 6512.

Wu, J., Wang, R., Yu, H., Li, G., Xu, K., Tien, N. C., . . . Li, D. (2015). Inkjet-printed microelectrodes on PDMS as biosensors for functionalized microfluidic systems. *Lab on a Chip*, 15(3), 690-695.

- Wu, M. X., & Yang, Y. W. (2017). Metal–Organic Framework (MOF)-Based Drug/Cargo Delivery and Cancer Therapy. *Advanced Materials*, 29(23), 1606134.
- Xu, S., Wang, Z., Su, R., Han, N., Xie, A., Wang, L., & Li, H. (2018). Structure and magnetic properties of multi-morphological CoFe₂O₄/CoFe nanocomposites by one-step hydrothermal synthesis. *Ceramics International*.
- Xu, X., Li, H., Zhang, Q., Hu, H., Zhao, Z., Li, J., . . . Gogotsi, Y. (2015). Self-sensing, ultralight, and conductive 3D graphene/iron oxide aerogel elastomer deformable in a magnetic field. *ACS nano*, 9(4), 3969-3977.
- Yao, Z., Tian, X., Jiang, L., Hao, H., Zhang, G., Wu, S., . . . Gerile, N. (2015). Influences of rare earth element Ce-doping and melt-spinning on microstructure and magnetostriction of Fe₈₃Ga₁₇ alloy. *Journal of Alloys and Compounds*, 637, 431-435.
- Yin, W., & Lu, Z. (1998). Synthesis and characterization of complexes of rare earth with ascorbic acid. *JOURNAL-GUANGXI NORMAL UNIVERSITY NATURAL SCIENCE EDITION*, 16, 46-51.
- Yu, H., Zheng, Y., Liu, W., Zheng, J., & Xiong, W. (2010). Effect of V content on the microstructure and mechanical properties of Mo₂FeB₂ based cermets. *Materials & Design (1980-2015)*, 31(5), 2680-2683.

Yuan, H., Zou, Z., Li, Z., Ye, J., Guo, X., Jiang, L., . . . Liu, X. (2013). Effect of particle size on the performance of rare earth–Mg–Ni-based hydrogen storage alloy electrode. *International Journal of Hydrogen Energy*, 38(19), 7881-7887.

Yun, Y. H., Kim, J. D., Lee, B. K., Cho, Y. W., & Lee, H. Y. (2009). Polymer inkjet printing: Construction of three-dimensional structures at micro-scale by repeated lamination. *Macromolecular research*, 17(3), 197-202.

Yung, K., Wu, S., & Liem, H. (2009). Synthesis of submicron sized silver powder for metal deposition via laser sintered inkjet printing. *Journal of materials science*, 44(1), 154-159.

Yung, W. K., Sun, B., Huang, J., Jin, Y., Meng, Z., Choy, H. S., . . . Yang, J. (2016). Photochemical copper coating on 3D printed thermoplastics. *Scientific reports*, 6, 31188.

Yung, W. K., Sun, B., Meng, Z., Huang, J., Jin, Y., Choy, H. S., . . . Yang, J. (2016). Additive and photochemical manufacturing of copper. *Scientific reports*, 6, 39584.

Yung, W. K. C., Sun, B., Meng, Z. G., Huang, J. F., Jin, Y. D., Choy, H. S., . . . Wong, W. Y. (2016). Additive and Photochemical Manufacturing of Copper. *Scientific Reports*, 6. doi:Artn 3958410.1038/Srep39584

Zako, T., Yoshimoto, M., Hyodo, H., Kishimoto, H., Ito, M., Kaneko, K., . . . Maeda, M. (2015). Cancer-targeted near infrared imaging using rare earth ion-doped ceramic nanoparticles. *Biomaterials science*, 3(1), 59-64.

Zeng, K., Pal, D., & Stucker, B. (2012). *A review of thermal analysis methods in laser sintering and selective laser melting*. Paper presented at the Proceedings of Solid Freeform Fabrication Symposium Austin, TX.

Zenou, M., Sa'ar, A., & Kotler, Z. (2015). Laser transfer of metals and metal alloys for digital microfabrication of 3D objects. *Small*, *11*(33), 4082-4089.

Zhang, H., Peng, S., Rong, C.-b., Liu, J. P., Zhang, Y., Kramer, M., & Sun, S. (2011). Chemical synthesis of hard magnetic SmCo nanoparticles. *Journal of Materials Chemistry*, *21*(42), 16873-16876.

Zhang, S., Liu, X., Liu, B., Xia, Z., Wang, W., Yang, Q., . . . Chen, S. (2015). 3D Co (II, III) mixed-valence metal-organic framework affording field-induced slow magnetic relaxation. *Science China Chemistry*, *58*(6), 1032-1038.

Zhang, T., Blackburn, S., & Bridgwater, J. (1997). The orientation of binders and particles during ceramic injection moulding. *Journal of the European Ceramic Society*, *17*(1), 101-108.

Zhang, T., Evans, J., & Bevis, M. (1996). The control of fibre orientation in ceramic and metal composites by open-ended injection moulding. *Composites science and technology*, *56*(8), 921-928.

Zhang, Y., Yao, W., Li, H., & Mu, Y. (2012). Rare-earth-metal complexes supported by new chiral tetra-azane chelating ligands: synthesis, characterization,

and catalytic properties for intramolecular asymmetric hydroamination.

Organometallics, 31(13), 4670-4679.

Zhang, Z., Zhou, Y., Zhang, Y., Zhou, S., Xiang, S., Sheng, X., & Jiang, P. (2015).

A highly reactive and magnetic recyclable catalytic system based on AuPt nanoalloys supported on ellipsoidal Fe@ SiO₂. *Journal of Materials Chemistry A*, 3(8), 4642-4651.

Zhao, X., Iyer, A., Promopatum, P., & Yao, S.-C. (2017). Numerical modeling of the thermal behavior and residual stress in the direct metal laser sintering process of titanium alloy products. *Additive Manufacturing*, 14, 126-136.

Zheng, H., Zhang, Y., Liu, L., Wan, W., Guo, P., Nyström, A. M., & Zou, X. (2016).

One-pot synthesis of metal–organic frameworks with encapsulated target molecules and their applications for controlled drug delivery. *Journal of the American Chemical Society*, 138(3), 962-968.

Zhong, G., Liu, D., & Zhang, J. (2018). The application of ZIF-67 and its derivatives: adsorption, separation, electrochemistry and catalysts. *Journal of Materials Chemistry A*, 6(5), 1887-1899.

Zhou, H.-C., Long, J. R., & Yaghi, O. M. (2012). Introduction to metal–organic frameworks. In: ACS Publications.

Zhou, W. h., Gan, Q., Ji, J. x., Yao, N., Wang, J. g., Zhou, Z., . . . Shi, J. l. (2016).

Non-destructive identification of pigments printed on six Imperial China

Engraved Coiling Dragon stamps. *Journal of Raman Spectroscopy*, 47(3), 316-320.

Zhou, X., Zhang, Z., Xu, X., Men, X., & Zhu, X. (2013). Facile fabrication of superhydrophobic sponge with selective absorption and collection of oil from water. *Industrial & Engineering Chemistry Research*, 52(27), 9411-9416.

Zhou, Y. S., Fan, L. S., Xie, Z. Q., Jiang, L., Silvain, J.-F., & Lu, Y. F. (2015). Laser-assisted vibrational control of precursor molecules in diamond synthesis. *Current Opinion in Solid State and Materials Science*, 19(2), 107-114.

Zhu, C., Yang, H. X., Wang, Y. Z., Zhang, D. Q., Chen, Y., & Gao, L. X. (2018). Synergistic effect between glutamic acid and rare earth cerium (III) as corrosion inhibitors on AA5052 aluminum alloy in neutral chloride medium. *Ionics*, 1-12.

Zhu, H., Fuh, J., & Lu, L. (2007). The influence of powder apparent density on the density in direct laser-sintered metallic parts. *International Journal of Machine Tools and Manufacture*, 47(2), 294-298.

Zou, J., Gaber, Y., Voulazeris, G., Li, S., Vazquez, L., Liu, L.-F., . . . Bongs, K. (2018). Controlling the grain orientation during laser powder bed fusion to tailor the magnetic characteristics in a Ni-Fe based soft magnet. *Acta Materialia*, 158, 230-238.

Zywietz, U., Evlyukhin, A. B., Reinhardt, C., & Chichkov, B. N. (2014). Laser printing of silicon nanoparticles with resonant optical electric and magnetic responses. *Nature communications*, 5, 3402.

刘光华. (2007). 稀土材料学.